University of Bath

PHD

Design and Dynamic Control of Heteropolar Inductor Machines

Wu, Jingzhe

Award date:
2015

Awarding institution:
University of Bath

Link to publication

Alternative formats
If you require this document in an alternative format, please contact:
openaccess@bath.ac.uk

General rights
Copyright and moral rights for the publications made accessible in the public portal are retained by the authors and/or other copyright owners and it is a condition of accessing publications that users recognise and abide by the legal requirements associated with these rights.

- Users may download and print one copy of any publication from the public portal for the purpose of private study or research.
- You may not further distribute the material or use it for any profit-making activity or commercial gain
- You may freely distribute the URL identifying the publication in the public portal ?

Take down policy
If you believe that this document breaches copyright please contact us providing details, and we will remove access to the work immediately and investigate your claim.

Download date: 22. Jun. 2021

Design and Dynamic Control of Heteropolar Inductor Machines

Jingzhe Wu

A thesis submitted for the degree of Doctor of Philosophy

University of Bath

Department of Electronic and Electrical Engineering

November 2015

COPYRIGHT

Attention is drawn to the fact that copyright of this thesis rests with the author. A copy of this thesis has been supplied on condition that anyone who consults it is understood to recognise that its copyright rests with the author and that they must not copy it or use material from it except as permitted by law or with the consent of the author

This thesis may be made available for consultation within the University Library and may be photocopied or lent to other libraries for the purposes of consultation with effect from……………….(date)

Signed on behalf of the Faculty/School of…………………..

Abstract

The thesis focuses on a type of electrical machine with a unique structure, namely heteropolar inductor machine. Heteropolar inductor machine is characterised as having both DC field excitation windings and AC armature windings placed on stator side, while maintaining a completely passive rotor. Its robustness offers the machine the potential to serve under extreme conditions, and the thesis discusses the theory, design, control and applications of heteropolar inductor machine. The main achievements are as follows.

(1) Space vector method is successfully adopted to construct a dynamic and universal model for heteropolar inductor machine. The strong couplings of air gap permeance variation, armature mmf wave and stator-side field excitation is explained and the machine model is well linked to classical two axis theory of electrical machines with the derivations of important model parameters.

(2) The harmonic distortion in heteropolar inductor machine and its influence are addressed and analysed by finite element analysis in the thesis, and potential strategies to overcome the problem are proposed. The machine output voltage waveform and torque ripple are greatly improved by optimisations of winding configuration and rotor shaping.

(3) A field oriented control system employing an efficient and effective sensorless control strategy specifically designed for heteropolar inductor machine is proposed. The method takes advantage of the machine's structural property and estimates the rotor position and speed based on estimation of internal emf. The proposed method is proved to be of much less computational complexity compared with conventional sensorless approaches.

(4) A test machine is fabricated together with the implementation of a micro-processor based controller system with sensorless control algorithm embedded. The prototype is tested against the theories developed for both machine modelling and sensorless controller for system verification and validation.

(5) A potential application is analysed in the thesis. The overall advantages and disadvantages of heteropolar inductor machine are compared against several candidate machines. A Simulink model is constructed for heteropolar inductor machine based on the developed machine theory, and the performance of a gas turbine starter generator integrator with a heteropolar inductor machine is evaluated via simulation.

List of frequently used symbols

Symbol	**Meaning**
B	Specific magnetic loading
B_0 , B_1, B_2 $\cdots$	Magnitudes of air gap flux density harmonic components
D	Friction coefficient
d	Bore diameter
$\overrightarrow{e_S}$	Armature internal emf space vector in stationary frame
$\overrightarrow{e_S^R}$	Armature internal emf space vector in synchronous frame
$e_{S\alpha}$, $e_{S\beta}$	α β axes internal emf
g	Air gap length
i_A , i_B , i_C	Three phase armature currents
i_f	Field current
$\overrightarrow{i_f}$	Field current space vector in stationary frame
$\overrightarrow{i_f^R}$	Field current space vector in synchronous frame
$\overrightarrow{i_S}$	Armature current space vector in stationary frame
$\overrightarrow{i_S^R}$	Armature current space vector in synchronous frame
i_{Sd} , i_{Sq}	d q axes armature current
$i_{S\alpha}$, $i_{S\beta}$	α β axes armature current
J	Inertia
K	Specific electrical loading
k_{dv}	Internal emf distribution factor
$k_{dv}^{'}$	Armature reaction voltage distribution factor
k_{dpv}	Internal emf winding factor
$k_{dpv}^{'}$	Armature reaction voltage winding factor

Symbol	**Meaning**
k_{pv}	Internal emf pitch factor
$k_{pv}^{'}$	Armature reaction pitch factor
L_f	Field circuit inductance
L_{lf}	Field leakage inductance
L_{mf}	Field main inductance
L_{mfa}	Mutual inductance
L_{lS}	Armature leakage inductance
L_{mS}	Main frequency armature magnetising inductance
L_S	Armature inductance
l	Axial length
M_f	Field coil mmf
M_a	Magnitude of armature reaction mmf
m_a	Armature reaction mmf
N_f	Number of turns per field coil
N_S	Number of turns per armature winding
p	Number of rotor saliencies; Differentiation operator
R_f	Field winding resistance
R_S	Armature winding resistance
r	Bore radius
T_e	Electromechanical torque
T_m	Mechanical torque
t	Time
u_A, u_B, u_C	Three phase armature voltages
u_f	Field voltage
$\widetilde{u}_{f1}$, $\widetilde{u}_{f2}$, $\widetilde{u}_{f3}$	Field winding AC voltage
$\widetilde{\widetilde{u}}_f$	Field AC voltage space vector in stationary frame

Symbol	**Meaning**
$\overrightarrow{\widetilde{u_f}'}$	Phase shifted field AC voltage space vector in stationary frame
$\widetilde{u_{f\alpha}}'$, $\widetilde{u_{f\beta}}'$	α β axes shifted field AC voltage
$\overrightarrow{u_S}$	Armature voltage space vector in stationary frame
$\overrightarrow{u_S^R}$	Armature voltage space vector in synchronous frame
u_{Sd} , u_{Sq}	d q axes armature voltage
$u_{S\alpha}$, $u_{S\beta}$	α β axes armature voltage
γ	Angular displacement of armature reaction mmf
θ	Angular displacement along air gap circumference
$\Lambda_0, \Lambda_1, \Lambda_2 \cdots$	Magnitudes of air gap permeance harmonic components
λ_A , λ_B , λ_C	Three phase armature flux linkage
λ_f	Field flux linkage
λ_{lS}	Armature leakage flux linkage
λ_{mf1} , λ_{mf2} , λ_{mf3}	Field winding main flux linkage
$\overrightarrow{\lambda_f}$	Field AC flux linkage space vector in stationary frame
$\overrightarrow{\lambda_{mS}}$	Armature magnetising flux linkage space vector in stationary frame
$\overrightarrow{\lambda_S}$	Armature flux linkage space vector in stationary frame
$\overrightarrow{\lambda_S^R}$	Armature flux linkage space vector in synchronous frame
λ_{Sd} , λ_{Sq}	d q axes armature flux linkage
μ_0	Permeability of free space
ν	Harmonic index
ξ	Angular displacement of rotor axis
ρ	Angular displacement of q-axis
ψ	Internal power factor angle
ω_S	Synchronous speed

Contents

Abstract……………………………………………………………………………..i

List of frequently used symbols ii

Chapter 1: Introduction 1

1.1 Motivation 1

1.2 Thesis summary...3

Chapter 2: Literature Review...5

2.1 Review of armature side excited machines 5

2.1.1 Flux switching machines...5

2.1.2 Flux reversal machines..7

2.1.3 Field assisted singly excited machines...8

2.1.4 Inductor machines 9

2.1.5 Summary 12

2.2 Review of sensorless field oriented control...14

2.2.1 Field oriented control 14

2.2.2 Sensorless control..15

2.2.3 Summary 20

Chapter 3: Theories 21

3.1 Structure, simplification and assumptions...21

3.2 Internal flux linkage and no load emf...24

3.3 Armature reaction..27

3.4 Electromechanical torque 31

3.5 Space vector theory 34

3.5.1 Introduction of space vectors 34

3.5.2 Armature space vectors...35

3.5.3 Field analysis 39

3.5.4 Space vectors with field orientation 42

3.6 Experimentation 48

3.6.1 Test machine and experiment setup 48

3.6.2 Steady state experiments 50

3.6.3 Transient experiments 53

3.7 Summary and discussion 58

Chapter 4: Design 60

4.1 Stator and rotor slot combinations 60

4.2 Winding factors and winding configurations 65

4.2.1 Distributed windings and distribution factor 65

4.2.2 Pitch factor 67

4.2.3 Elimination of second time harmonic 69

4.3 Rotor shaping and cogging torque 73

4.3.1 Square rotor 73

4.3.2 Sine permeance rotor 77

4.4 Sizing equation 81

4.5 Local saturation 85

4.6 Losses 93

4.7 Summary and discussion 96

Chapter 5: Control 98

5.1 Field characteristics 98

5.2 Sensorless estimation algorithm 100

5.3 Experimentation 108

5.3.1 Experiment setup 108

5.3.2 Q-axis position estimation 109

5.3.3 Rotor speed estimation 112

5.3.4 Field weakening 113

5.4 Prototype drive system 115

5.4.1 Start-up process 115

5.4.2 PI tuning 118

5.5 Summary and discussion 125

Chapter 6: Application 127

6.1 Target specifications 127

6.2 Feasibility study 130

6.2.1 Permanent magnet synchronous machine 130

6.2.2 Wound rotor synchronous machine 131

6.2.3 Switched reluctance machine 132

6.2.4 Flux switching machine 133

6.2.5 Heteropolar inductor machine 134

6.2.6 Summary 136

6.3 Starter simulation 137

6.3.1 Starter system 137

6.3.2 Simulation results 139

6.4 Generator simulation 143

6.4.1 Generator system 143

6.4.2 Simulation results 145

6.5 Summary and discussion 150

Chapter 7: Conclusion and Future Works 151

7.1 Conclusion 151

7.2 Future works 153

Reference 154

Publications 166

Appendix 167

Appendix I: Iron magnetic property 167

Appendix II: Electronic interfaces 168

Appendix III: Simulink models for gas turbine starter generator 171

Chapter 1: Introduction

1.1 Motivation

Electrical machines and their associated drive systems have been developed for over a century and society has witnessed their widespread usage and operational advantages in industrial, business and domestic applications. Generally, nowadays the technology of conventional electrical machines and their drives is sufficiently mature and varied to easily find a suitable design for most uses. For example, the efficiency of synchronous generators in most industrial power plants can achieve from 88 per cent to as high as 97 per cent depending on the different ratings of machines, even according to the data collected in 1959 [1]. From the aspect of domestic use, a wide selection of relatively low-cost induction motors, with synchronous speed ranging from 600 to 3600 rpm and power from sub-fractional to 200 horsepower, are mass produced to meet the requirements of various domestic loads, such as electrical fans, air conditioners, refrigerators, etc. [1].

In more sophisticated, high-performance machines drive application, a revolutionary leap occurred in machine drive torque and speed control flexibility when power electronics was developed and integrated with electrical machines in the 1960s. This has greatly improved the achievable dynamic performance of each machine drive type, especially AC machines drives. Since the 1970s, high-capacity power-semiconductor power-converter configurations, controlled by microprocessor-based digital controllers, have been developed which can implement sophisticated scalar and vector control methods and make AC electrical machines adaptable to time-varying operational requirements determined by process controllers. A result of to the relatively high-frequency switching waveform synthesis now possible with power electronics and the programmable nature of its control electronics, sophisticated systems may be produced which rapidly adjust machine-winding voltage, frequency and phase, and continuously optimise AC machine current to deliver precise torque control. Consequently the application fields available for electrical machines have hugely expanded. For instance, the dynamic performance and power density of AC drives may now exceed that of DC drives; and these may be used over a wider speed range, with greater operating efficiency and reliability because AC machine rotor geometry is generally more compact and robust than in DC machines.

With the continuing development of technology and expansion of applications, however, the available conventional machines may still not satisfactorily provide the anticipated performance due to both internal (e.g. electromagnetic properties) and external (e.g. harsh environment) factors. There are certain fields, for instance, where very high unattended operating life, due to limited accessibility, is in demand. Also, some applications may require special considerations from the point of view of the relatively inaccessible application environment, while some others may demand very high mechanical strength and robustness.

For example, machines and drives for aerospace applications or deep water submarines usually have very limited accessibility, which means regular or unplanned maintenance is not possible and consequently the reliability of such machines will need to be exceptionally high.

Wind turbine generators located in deserts or off shore are at greater risk of corrosion and fouling, which can accelerate the deterioration of commutators, brushes or slip rings, i.e. sliding contact elements, which exist in most DC and AC synchronous machines and doubly-fed induction generators. This leads to a significant reduction in the time before failure. Therefore a brushless generator is preferred.

The integrated starter-generators (ISGs) for airplanes and hybrid electric vehicles (HEVs) also require special purpose machines. The candidate machines may be positioned very close to gas turbines or diesel engines for direct drive purpose, and the adverse heating effect on machines has to be taken into consideration.

In high speed locomotive and traction drives for modern transportation systems, the vehicle can be driven by a rotary machine or its linear/disk counterpart operating at remarkably high speed, thus imposing significant stress on machine parts.

Machine drives literature discusses possible methods of applying conventional electrical machines under unusually demanding conditions. However, most of the conventional electrical machine designs will face a compromise in performance when servicing demanding applications. Such compromises may include increased losses, structural risks, unreliability and so on. Noting this raises a challenge which this project aims to address: to search for a better solution to special purpose electrical machine applications, and propose an unconventional type of electrical machine that can overcome some drawbacks that exist in conventional machine designs. The proposed machine design should be able to provide enhanced robustness, reliability and better immunity from harsh environments and extreme conditions.

The armature side excited machine is an unusual type of electrical machines that fit the aims of this project. It is a special variant of the conventional rotor excited synchronous machine. As the name suggests, the field excitation of such machines is transferred to the stator side, leaving a completely passive rotor. Such a design provides the structural advantage of a completely passive rotor, while the advantages of field excitation over singly fed electrical machines are inherited.

This project will specifically focus on one of the various possible types of armature side excited synchronous machines, namely the heteropolar inductor machine. Despite the fact that the concept of heteropolar inductor machine is not novel, this type of machine is still of interest in this project, not only because of the lack of research results available in previous literature, but also due to its undiscovered potential after the advent of power electronic drives.

1.2 Thesis summary

The content and salient issues in the remainder of the thesis will now be briefly identified.

Chapter 2 briefly reviews the techniques of armature side excited machines and sensorless controllers identified in the literature. The advantages and disadvantages of different techniques will be highlighted.

Chapter 3 derives the most fundamental theories of heteopolar inductor machines since the literature related to this type of machine is very limited and seems insufficiently precise. Both steady state and transient state theories will be developed and verified experimentally.

Chapter 4 studies the design theories of heteropolar inductor machine for the purpose of generalisation and practical machine design guidance. Potential modifications will be identified and made to greatly improve the machine characteristics. Certain machine properties that are different from conventional machines (e.g. saturation and losses) are briefly discussed as well.

Chapter 5 discusses the development of a novel sensorless estimation scheme specially designed for heteropolar inductor machine based on its transient theory. The scheme contains independent sensorless position and speed estimation algorithms, and the functionality is verified by experiment. A prototype sensorless drive system is also implemented and tested. The results will be presented.

Chapter 6 studies the suitability of a special purpose, demanding application for the heteropolar inductor machines, which is a gas turbine starter generator. This is used to compare the preliminary designs of several candidate electrical machines against the target specifications, and to clearly identify and quantify advantages. Results for the dynamic performance of the simulated gas turbine starter generator based on the heteropolar inductor machine drive system will be presented.

Chapter 2: Literature Review

2.1 Review of armature side excited machines

2.1.1 Flux switching machines

The flux switching (FS) machine is an important type of armature side excited machine, and has been studied extensively. Most of the FS machines in literature are permanent magnet (PM) excited [2-5] mainly due to the large flux density available from PMs. The cross section view of a basic PM excited FS machine is shown in Fig. 2.1. It is seen that the stator of FS machine is equipped with three-phase concentrated windings with PMs inserted in each tooth, while the rotor is salient and passive.

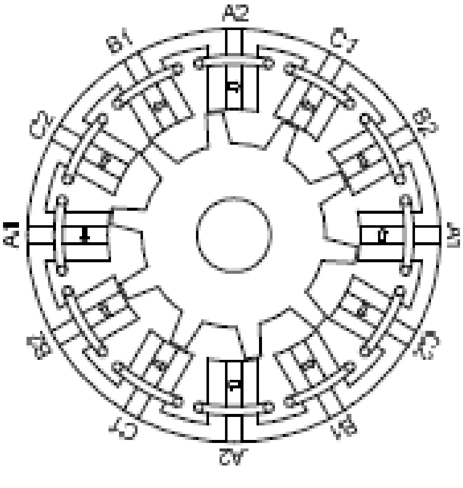

Fig. 2.1 [6] Cross section view of a 12/10 PM excited FS machine

The principle of FS machines is based on the switching of flux direction occurring when each rotor saliency passes by each stator tooth. [7] compares the topologies involving different stator and rotor slot combinations, and concludes that the torque capability is maximum when the number of rotor saliencies is similar to that of stator. The electrical speed of FS machines is the rotor speed times the number of rotor saliencies.

Similar to switched reluctance machines (SRMs), the salient stator structure and concentrated windings minimise the mutual inductance between any two phases, therefore it ensures a high level of fault tolerance. Also, the length of end turns is significantly reduced compared with machines with overlapping windings. Thus lower end winding copper loss and leakage reactance are expected.

The stator side excitation source can be replaced by field currents. Compared with its PM excited counterpart, field winding excited FS machines [8-11], as shown in Fig. 2.2, offer an economical solution and a better controllable field excitation. In order to achieve a reasonable level of power output, a field excited FS machine with segmented rotor structure is proposed [12].

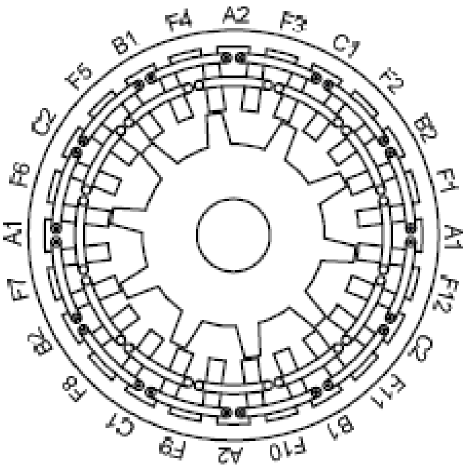

Fig. 2.2

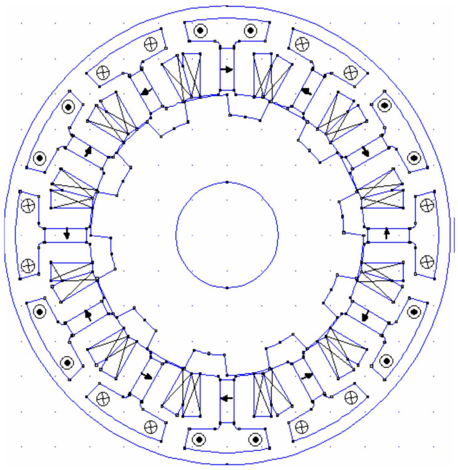
Fig. 2.3

Fig. 2.2 [6] Cross section view of a 12/10 field current excited FS machine
Fig. 2.3 [13] Cross section view of a 12/10 hybrid excited FS machine

Hybrid excited FS machines [13-15] are proposed to combine the merits of both PM and field winding excited FS machines, featuring additional field windings to assist to either enhance or diminish the flux density of PMs. They offer a boosted torque capability at low speed and a better flux weakening capability for an extended range of speed. The trade off, however, is a much more complicated stator punching structure. A cross section view of a hybrid excited FS machine is shown in Fig. 2.3.

A number of variants of conventional FS machines are discussed to suit the requirements of different applications. The FS machine with asymmetrical rotor improves the starting torque capability [16], while multi-tooth stator structure is analysed for low speed high torque traction purpose [17]. A transverse FS machine is employed for wind power generation, as discussed in [18]. The fault tolerant capability of FS machines can be improved by applying an alternate poles-wound winding configuration [19]. However it is reported that such a winding structure causes an increased level of torque ripple, reduction in average torque output, and distortion of internal emf.

2.1.2 Flux reversal machines

The flux reversal machine utilises its doubly salient structure to periodically reverse the direction of stator flux excited by stator side PMs. The concept of flux reversal machines dates back to 1955 [20], and the design is shown in Fig. 2.4. Researchers have attempted to overcome its poor material utilisation and complex structure over the past few decades. As a consequence, a three-phase flux reversal machine with PMs located on the stator teeth surface was introduced [21], as shown in Fig. 2.5.

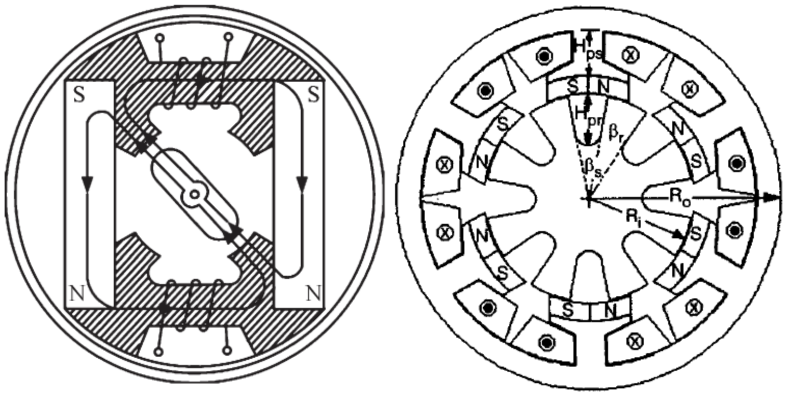

Fig. 2.4 Fig. 2.5

Fig. 2.4 [21] Cross section view of original flux reversal machine
Fig. 2.5 [21] Cross section view of flux reversal machine with PMs mounted on stator teeth surfaces

The three-phase flux reversal machine benefits from low self and mutual inductance, and is proposed for automotive purpose [22]. Instead of stator teeth surface mounted PMs, an inserted PM flux reversal machine is reported as a low speed servo drive, offering improved torque density and slightly reduced torque pulses [23].

Improvements and modification in structure can lead to better performance. For instance, concave stator poles and rotor barriers can be applied to increase winding effective flux linkage [24], and machine designs with rotor teeth pairing exhibit a smoother toque profile [25]. The cogging torque magnitude can also be minimised by introducing tapered air gap [26]. However it is reported that the performance of flux reversal machines is still more or less compromised by high magnetic eddy current loss and low power factor, as well as a considerable amount of fringing leakage flux [27]. Besides, the physical location of PMs in flux reversal machines leads to a potentially mechanically fragile structure, and a potential risk of magnet demagnetisation.

2.1.3 Field assisted singly excited machines

Although several singly excited machines, e.g. switched reluctance machine (SRM) and synchronous reluctance machine (RM), have been proven to work with satisfactory performances for various applications, they can still suffer from deficiencies caused by excitation penalty. In order to mitigate the disadvantages of single excitation, researchers have made improvements to RMs and SRMs by introducing auxiliary excitation sources (field windings, PMs etc.) on the stator side [28-32]. Fig. 2.6 and Fig. 2.7 show a field assisted SRM and a field assisted RM respectively.

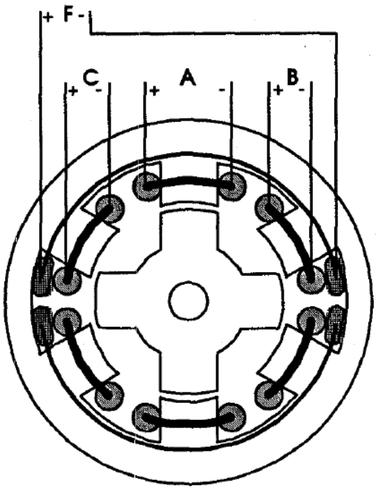

Fig. 2.6

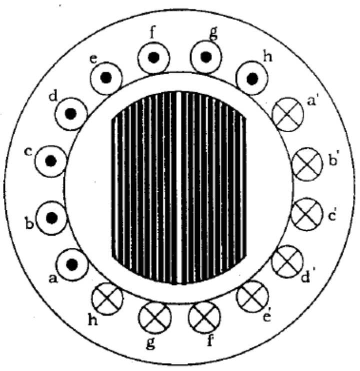

Fig. 2.7

Fig. 2.6 [29] Cross section view of a 6/4 DC assisted SRM
Fig. 2.7 [31] Cross section view of field assisted RM

Significant boosts in power density (up to 50%) and efficiency are reported by the improvements. A downside of such designs, however, is that the machines are inevitably of pulsed torque nature, resulting in a relatively unsmooth torque profile. The machine's punching structure may also be more complicated to accommodate the auxiliary field windings or the insertion of PMs into the stator yoke. Moreover, it is reported in [33] that the energy conversion of such field assisted machines is limited to first and second quadrant, instead of the four-quadrant operation in normal servo drives.

2.1.4 Inductor machines

Inductor machines are another important family of armature side excited machines, and they are subdivided into two different types: homopolar inductor machines and heteropolar inductor machines. The general principles of inductor machines were published by Walker [34] in the 1940s. Inductor machines were commonly used as high frequency generators for applications such as induction furnaces more than half a century ago, before power devices and adjustable frequency inverters were available for this application. Even so, the properties of inductor machines still remain interesting for researchers; and, in the past few decades, alternative applications for inductor machines have been more and more attempted [35].

Homopolar inductor machine

Homopolar inductor machines (Fig. 2.8) are usually composed of two equal stacks. Stators of two stacks are slotted and equipped with polyphase armature windings as for usual singly salient AC machines. Rotors are connected on a common shaft and of the shapes of SRMs. Usually the rotor in one of the stacks is displaced by 90 electrical degrees from another. In between the junction of two stacks is fitted with a concentrated field coil, providing an axially oriented magnetic flux. Owing to the saliencies on the rotors, a unidirectional pulsating flux is seen by the stator on each stack and multiphase electromotive forces (emfs) are induced in the armature windings. The period of flux pulsation spans a rotor pitch, and hence the number of rotor teeth indicates the number of pole pairs in the machines. Undoubtedly the rotor tooth and slot shapes will have an influence on the pulsating component of the flux. It is possible to improve flux concentration [36], eliminate undesired harmonic flux [37], and increase torque output [38] by employing adequate rotor modifications.

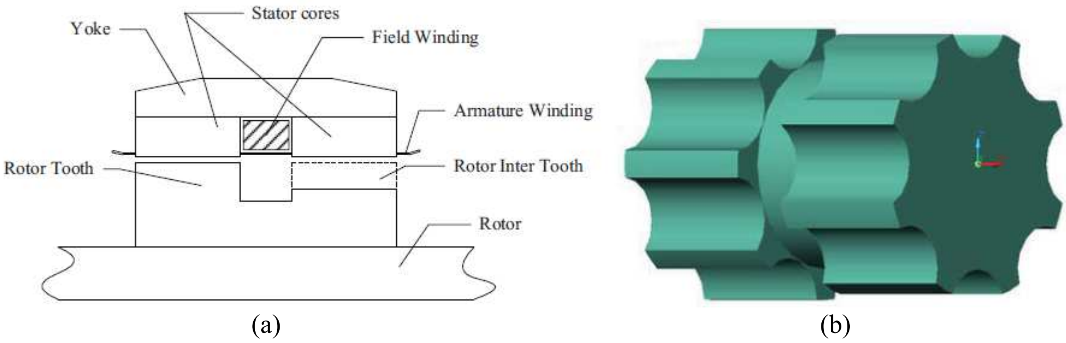

(a) (b)

Fig. 2.8 [36] The (a) side view and (b) 3D rotor structure of homopolar inductor machine

The rotor laminations used for reducing eddy current losses is no longer a necessity, since magnetic flux flowing from rotor to stator in each stack is unidirectional. Such a rotor structure, as a result, offers an even higher mechanical strength than those in SRMs and FS machines. In some literature, homopolar inductor machines provide alternatives to applications where SRMs are proposed, such as flywheel energy storage systems [39], high speed drives [40], nuclear power plant compressors [41], aerospace alternators [42], and (linear) high-speed ground transportation [43, 44] etc.

Given the fact that homopolar machines only utilize the varying components of a unidirectional flux, the size of the machines will have to be approximately doubled compared with a traditional AC machine utilizing a full flux reversal (seen by the stator windings) if the maximum allowed flux density is kept equal [45]. An example is given to compare the characteristics between a homopolar inductor machine and a PM synchronous machine with same loadings and ratings [46]. It shows that with similar stator inner and outer diameters, the total stator length of the PM synchronous machine (75 mm) is just about half of that of the homopolar inductor machine (120 mm), though the emf waveform of the homopolar inductor machine is smoother than that of the PM synchronous machine. Further, homopolar inductor machines have a relatively longer magnetic flux path since the closed path includes both an axial component and a radial component. As a consequence, the machines may require larger mmfs and experience higher associated losses especially when heavy saturation occurs. Besides, the axial flux may tend to magnetise the shaft and bearings, and reduce their lifespan.

Claw pole machines

Claw pole machines are one of the most popular solutions for HEV motors. The Lundell claw pole machine is developed from the homopolar inductor machine, and achieves a full swing of flux seen by the stator, thus increasing the output. A Lundell rotor is shown in Fig. 2.9, and it is accommodated in a conventional AC machine stator. Unidirectional magnetic flux is created by coils wound on the rotor yoke. The Bekey-Robinson claw pole machine (Fig. 2.10) takes advantage of a pair of back-to-back Lundell machines for a higher output.

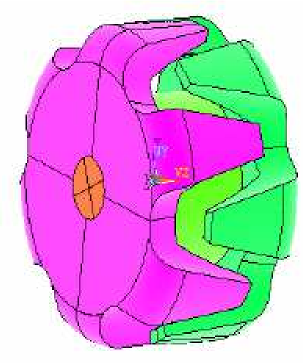

Fig. 2.9

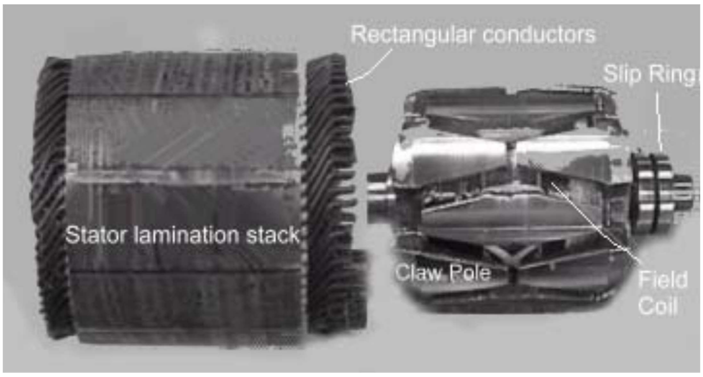

Fig. 2.10

Fig. 2.9 [47] 3D view of rotor of Lundel claw pole machine
Fig. 2.10 [48] Bekey-Robinson claw pole machine

Conventional claw pole machines suffer from deficiencies such as brush/slip ring assembly, highly complicated structure and high level of leakage flux. Researchers have managed to improve and modify machine structures in order to gain a better overall performance [49]. For example, brushless claw pole machines are developed for increased mechanical integrity, and leakage reactance can be reduced by the insertion of PMs into rotor slots. A high power-to-weight ratio modified Lundell machine for aerospace applications with a rated speed reaching 30000rpm has been reported.

Heteropolar inductor machines

Although classified as an inductor machine, the heteropoar inductor machine differs a lot from its homopolar counterparts. Literature about heteropolar inductor machines is very limited and such machines that appear in literature merely function as generators so far. Various design plans of heteropolar inductor machine were proposed by researchers [50-54], among which a three-phase design is of the simplest structure and meets the basic requirements for three-phase power supply in nowadays. A 12/7 three phase heteropolar inductor machine is shown in Fig. 2.11 and the windings with apostrophe numberings are DC field windings. The structure is similar to field winding excited FS machines, despite that they are singly salient and the winding pitches can be adjusted either long or short. Stator slots are alternatively occupied by armature and field coils and the polarities of magnetic field excited by adjacent field coils are opposite. Same as FS machines, the electrical frequency is determined by number of rotor teeth.

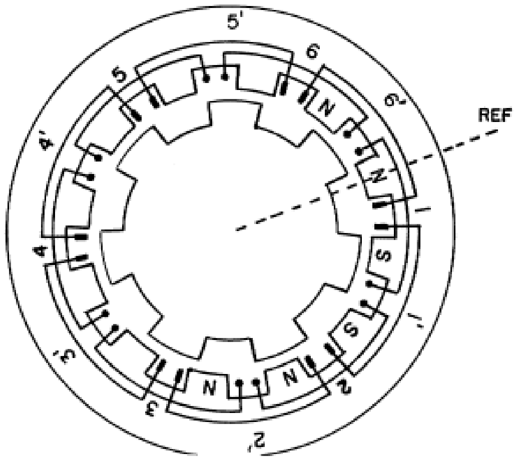

Fig. 2.11 [55] Cross section view of a 12/7 heteropolar inductor machine

The unit structure of a three phase heteropolar inductor machine stator consists of 12 slots, yet the combinations of rotor and stator slot numbers are limited for balanced three phase power generation [56]. High frequency generation can be realised by increasing the numbers of both stator and rotor slots by a same multiple. However R Nair[57] argued that the rotor tooth number does not have to increase as long as the multiplication of stator teeth is deemed as ‘separating’ concentrated windings used previously in inductor machine into distributed windings. Thus a machine with ‘high stator to rotor slot ratio’ is obtained. Based on the idea, a plan for low frequency generation can be achieved. This concept of ‘high slot ratio’ on the other hand, offers a possibility of high speed motoring application for multiphase heteropolar inductor machine.

The general theory and design aspects of three phase heteropolar inductor machines are introduced in [55] and [58], however the theories are only preliminary and several important aspects are not well explained in detail. For example, the transient theory of machine is not covered, and the analysis of armature reaction is not detailed. Besides, the selection of available stator/rotor slot combination is not generalised.

2.1.5 Summary

By reviewing the literature, multiphase heteropolar inductor machine is chosen for this project, not only because the features seem suitable for meeting the aims, but also because of the lack of exploration in this field. A multiphase heteropolar inductor machine equipped with distributed windings is proposed in this project for both motoring and generating services.

In summary, multiphase heteropolar inductor machines offer the following features to meet the requirement of this project.

(1) The robust structure of rotor is able to withstand a high speed operation and the removal of rotor winding facilitates the cooling and allows a higher electrical loading.

(2) Simplicity of structure of the machine is favoured for mass manufacturing. The stator is exactly the same as a conventional induction and synchronous machine and the rotor is similar to a reluctance machine or SRM rotor. The singly saliency also suppresses cogging torque to some extent.

(3) The nature of double excitation enhances the power density and permits the adoption of various methods of control.

(4) Compared with homopolar inductor machine, the utilisation of magnetic flux is higher and this implies a more compact size is achievable.

Nevertheless, there are several drawbacks compared with other machine types reviewed, and these drawbacks which are listed must be alleviated in the project.

(1) Much longer coil spans and end windings are associated with this type of machine. Hence copper loss and temperature rise are expected to be larger than doubly salient machines such as SRMs and FS machines which have coils wound on each stator tooth.

(2) Though the utilisation of magnetic flux is greater than homopolar inductor machines, it may be still lower than FS machines and conventional rotary field synchronous machines.

2.2 Review of sensorless field oriented control

2.2.1 Field oriented control

Field oriented control [59, 60] (FOC) is a preferred control method for electrical drives requiring rapid dynamic response, extended speed and high operational efficiency. The implementation of FOC for doubly excited machines is simple and straightforward. The rotating field excitation mmf axis on the machine cross section plane is regarded as the direct axis (d-axis), and the quadrature axis (q-axis) is orthogonal to the d-axis. Electrical machine's three phase quantities can also be projected onto d and q axes, forming magnetising and torque components respectively.

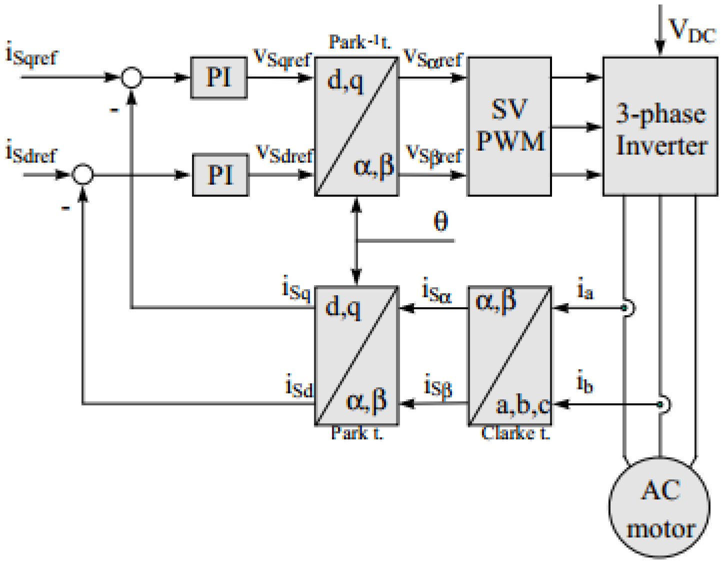
V_{DC}
i_{Sqref}
PI
v_{Sqref}
Park-¹t.
d,q
α,β
$v_{S\alpha ref}$
SV PWM
3-phase Inverter
i_{Sdref}
PI
v_{Sdref}
$v_{S\beta ref}$
-
-
θ
i_{Sq}
d,q
$i_{S\alpha}$
α,β
i_a
i_{Sd}
α,β
$i_{S\beta}$
a,b,c
i_b
Park t.
Clarke t.
AC motor

Fig. 2.12 [61] Block diagram of FOC

A schematic of FOC is shown in Fig. 2.12. The significance of FOC is that it manages to decouple three phase quantities orthogonally, and it facilitates the realisation of a variety of flexible machine control schemes by separately control the demanded d and q axis quantities. FOC is often assisted by feedback control in order to allow the precise following of controlled quantities with the references. FOC is applied for a number of motion control strategies, such as maximum torque control, maximum power factor control and maximum efficiency control etc., among which maximum torque control is the most popular and widely used. Maximum torque FOC forces d-axis current (i.e. armature magnetising current component) to be zero and the torque output can be adjusted by solely controlling q-axis current (i.e. armature torque current component). Such strategy allows maximum power output for a given current supplied, and power device ratings can be reduced to a minimum. However field weakening is necessary at extended speed range by either reducing field current supply (for wound field machines) or increasing d-axis current to counteract field mmf (for PM excited machines).

2.2.2 Sensorless control

Machine's rotor position and rotor speed are the most important information in most control systems. Rotor position creates a reference to decouple d and q orthogonal quantities and is the foundation of FOC (Park's Transform). Rotor speed, on the other hand, requires precise monitoring in most speed-related applications, and sometimes provides feedback signal for closed-loop control systems. The same as many other physical quantities, position and speed of electrical machines can be directly measured via external devices such as rotary encoders and Hall-effect devices. However such a solution is not always applicable, especially when the compromises in system robustness and simplicity caused by the introduction of external equipment must be avoided. A variety of sensorless position and speed estimation schemes have been proposed to replace sensors in advanced control techniques.

High frequency signal injection/inductance variation

High frequency signal injection, or saliency based estimation, is a preferred method for estimating salient rotor position especially at low speed and zero speed when estimations based on terminal AC variables are difficult.

Either continuous signals or transient signals can be injected and superimposed on to machine excitation. The instantaneous rotor position is estimated via the machine's electromagnetics response. Various types of high frequency signals (sinusoidal, rectangular and arbitrary) can be injected either in steady or rotating vector form [62]. The high frequency variations in d-q flux linkages caused by rotor saliency are demodulated, and the rotor position can be deduced. The transient signal injection technique, on the other hand, measures transient response of armature currents caused by a pulse voltage vector [63]. The scheme is reported to be more reliable in the presence of disturbances due to machine non-linearity.

The disadvantages of external signal injection are the requirements for auxiliary devices and the additional current ripple and losses produced. The technique of utilizing a PWM inverter input voltage to replace external transient voltage vector has been proposed, which overcomes the drawbacks mentioned [64]. As a trade-off, a more complex system is required and the accuracy is compromised since periods of pulse voltage vectors may not be fixed.

Harmonics observation

The potentiality of utilising space and time harmonics to extract rotor position and speed information is sometimes implemented in induction and brushless DC (BLDC) drives.

A number of different approaches for position and speed estimations based on parasitic effects of induction motor are summarised and compared by J Holtz [65]. A direct approach is to demodulate the slot harmonic from measured voltage by adaptive filter and phase locked loop (PLL). The rotor speed can be estimated since it is proportional to the obtained frequency which simply needs to be scaled. More advanced techniques, such as rotor resistance adaption based estimation and leakage flux measurements based estimation, have also been proposed. They are reported to increase overall performance by alleviating the possible distorted signals due to less rotor slots. Although such parasitic effect based estimations benefit from the large bandwidth and ability of satisfactorily working at zero and low speeds, the accuracy is not yet comparable with modern model based flux observers.

The simple mechanism of a BLDC machine facilitates the estimation of appropriate switching instants by observing the machine’s motional emf. It has been proven to be a low cost sensorless method by keeping track of trapezoidal emf zero crossings and shifting them by 90 degrees at commutation instants [66]. A BLDC test machine has been successfully controlled with observing fundamental emf zero crossings up to 6000rpm. Another approach estimates the BLDC switching instants by utilising the zero crossings of the 3rd harmonic voltage waveform measured between machine and load star points [67]. This method has the advantages of reduced filter sizing, improved dynamic response and extended dynamic range compared with fundamental emf based methods [68]. However it is also addressed that the method is invalid for magnetically salient machines, and error can be introduced by imbalance of three phase loads, which, unfortunately, is a common occurrence.

Observer based estimation

Flux observer

Flux observer estimation aims to estimate the instantaneous phase flux linkage of an AC machine, and the three phase flux linkage is obtained by integrating terminal voltages less resistance voltage drops. Position can be estimated from a number of approaches based on the knowledge of flux linkage. Moreover machine flux linkage is independent of speed compared with internal emf, which potentially makes flux observer based estimations suitable for estimations at low speeds.

Flux linkage (Luenberger) observers are classified into estimation with mechanical model (full order observer) and estimation without mechanical model (reduced order observer) [68]. The schematics of both estimations are shown in Fig. 2.13. Both methods compare the estimated d-q currents with measured values in order to correct the estimated position values.

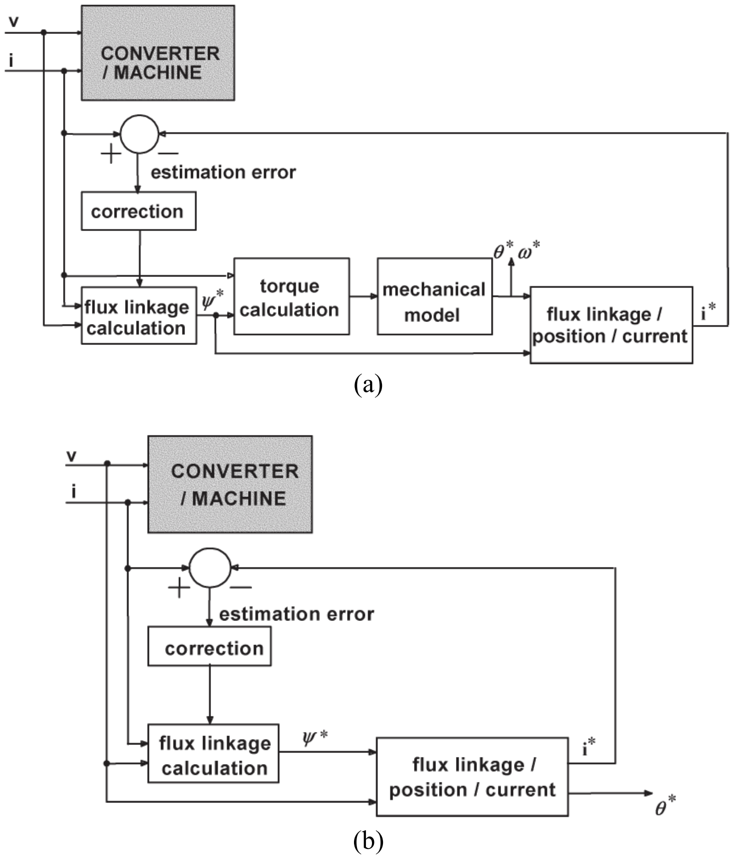
v
i
CONVERTER / MACHINE
+
−
estimation error
correction
θ^*, ω^*
torque calculation
mechanical model
flux linkage calculation
ψ^*
flux linkage / position / current
i*
v
i
CONVERTER / MACHINE
+
−
estimation error
correction
flux linkage calculation
ψ^*
flux linkage / position / current
i*
θ^*

(a)

(b)

Fig. 2.13 [68] Block diagrams of flux linkage observer based estimation (a) with mechanical model and (b) without mechanical model

Estimation based on direct flux linkage is proposed in [69], which facilitates the application of direct torque control (DTC). The principles of a number of different approaches of reduced and full order observers for PMSMs are summarised in [70]. It is concluded that although a reduced flux observer increases the system accuracy by eliminating the need for a mechanical model, its self-start and dynamic properties are compromised compared with a full order observer.

Rotor speed and rotor flux can be estimated based on a reduced order rotor flux observer for induction motor drives employing field oriented control strategy [71]. A similar approach with a full order observer for rotor and stator flux models is discussed in [72] for an induction motor with discrete time DTC.

Model reference adaptive system

In model reference adaptive system (MRAS) scheme, the electrical machine (i.e. the plant) is duplicated by a mathematical model with all parameters simulated. Given the same input data, the plant output is compared with the output from reference model, and the error is used to correct machine behaviour. The schematic of MRAS control system is shown in Fig. 2.14.

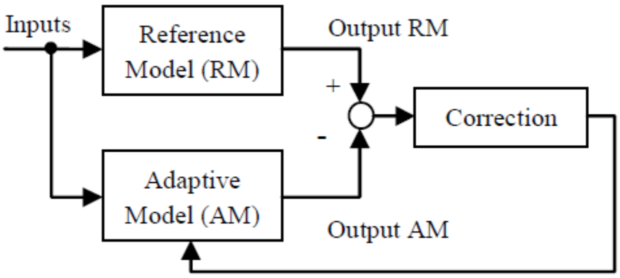

Fig. 2.14 [70] Block diagram of MRAS

An induction motor employing MRAS has been reported with advantages such as stability, simple implementation, and reasonable dynamic behaviour above 2Hz [73]. However, the method may suffer from the inaccuracy caused by drift errors introduced by open integration in the reference model and the difficulty of obtaining precise mathematical models [74].

The key to accurately replicating the plant is the implementation of online adaptive modelling with monitoring of potential parameter variations. The error convergence in the system is usually forced to be guaranteed by Popov’s hyperstability criterion. A number of adaptive algorithms are available and summarised in [75]. Recent improvements in adaptive modelling for better performance and reports of different applications (e.g. PMSM) are also available from the literature.

Kalman filtering

Observer based sensorless estimations can be greatly influenced by parameter uncertainties and noises, leading to a degradation of overall system performance. The problem can be overcome by implementing Kalman filters to the estimator, due to the fact that Kalman filter is able to predict and correct estimated future states based on knowledge of previous states. Besides, Kalman filtering based estimation has a faster transient response over other sensorless schemes and the capability of auto-correcting initial position error. Generally the machine's state space model with description of uncertainties is built first, and the states are then optimally estimated via recursive algorithms.

The estimations of flux linkage, rotor speed and rotor position are reported feasible with different variants of Kalman filter, e.g. standard Kalman Filter (KF), extended Kalman Filter (EKF) and descriptor Kalman Filter (DKF) [76, 77]. Despite the benefits, it has been pointed out that the demand for huge online matrix computing may be a great challenge for conventional fixed point processors for drive applications, and the drive can be at the risk of reverse starting due to occasional incorrect convergence [78]. Moreover the practical experimental results suggest that the accuracy of Kalman filter based method may be lower than that of flux observer due to the difficulty of processing noise covariance.

Instead of being directly used for position and speed estimation, a Kalman filter is often used to assist other estimation methods. A typical application is to provide online updates of stator and rotor resistances. A DSP based BLDC motor employing Kalman filter stator resistance estimation to compensate for the influence on flux estimation caused by temperature variation has been reviewed in [68].

Sliding mode observer

Sliding mode observer (SMO) has emerged in the past few decades as an alternative state observer scheme to Kalman filter based observers [79]. Sliding mode control is based on the non-linear variable structure nature of electrical machines. The discontinuous function of errors between observer and system actual outputs are fed as observer input, and the system states are forced to slide along the boundaries of a variable structure system by meeting Lyapunov's criterion [80].

SMO is famous for its robustness, dynamic and low speed performances, as well as its capability to be completely immune from certain classes of uncertainties with careful design. The practical examples of observers with insensitivities to different system parameter variations by altering the observer modes are illustrated in [81]. SMOs are reported to generally have a higher robustness and a greatly reduced numerical complexity than Kalman filter observers, however, the estimation accuracy can be lower if appropriate noise covariance matrices are constructed for Kalman filters [82]. Nevertheless, the SMO output must be passed through a low-pass filter to eliminate the chattering and to obtain the correct estimated states, which can lead to undesired phase lags.

2.2.3 Summary

There is a variety of approaches to obtain AC machines' rotor position and speed without mechanical sensors as introduced above. Each method offers its unique benefits, yet the disadvantages of the methods must be taken into consideration according to the requirements of applications.

High frequency signal injection takes advantage of auxiliary devices and returns reliable information of rotor magnetic saliency locations down to zero speed. Emf based estimation is simple and accurate since the emf waveform is directly related to d-q axes locations, although the estimation may not be reliable at low speeds. However the utilisation of the method is greatly limited due to the difficulty of extracting instantaneous emf values from terminal voltages, which are often modulated by armature reaction. Modern observer based estimation features satisfactory precision, wide feasibility and freedom from external devices. However, knowledge of certain system parameters (usually inductances and rotor dynamics) is necessary to set up the correct observer models. As a result, observer based methods can be sensitive to parameter variations and the strategy is more complex compared with other approaches.

Various sensorless control methods for conventional AC machines can also be applied to heteropolar inductor machines. However due to the special structure of the machine, a novel control method has been developed. Details will be discussed in Chapter 5.

Chapter 3: Theories

3.1 Structure, simplification and assumptions

To start with, a most simplified three phase inductor machine prototype is analysed. The simplest three phase armature windings occupy 6 stator slots, as in any three phase electrical machines, and 6 field winding slots in total are interleaved with armature winding slots. Hence, the minimum number of stator slot for a three phase machine is 12, as firstly indicated by J H Walker [34]. Both armature and field coil pitches are selected to be equal to 2 stator slots, and the rotor is of 4 saliencies. The sketch of the cross view of such a simplified machine is shown in Fig. 3.1.

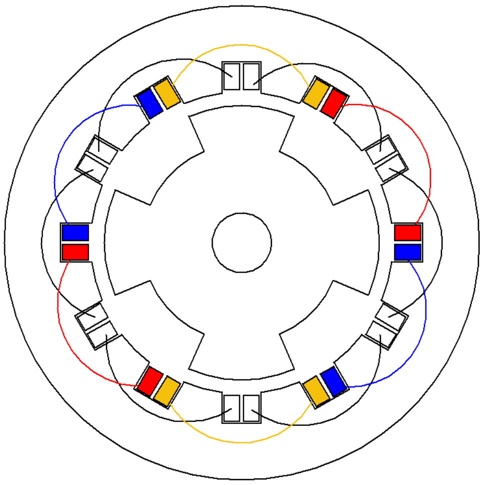

Fig. 3.1 Conceptual sketch of a 12/4 heteropolar inductor machine

As shown, the stator is non-salient, similar to those of induction motors and synchronous machine, while the rotor is similar to those of switched reluctance machines. The red, yellow and blue phases correspond to phase A, phase B and phase C coils respectively. Stator field coils are represented in black blocks. In all subsequent analysis, a 12 stator slot machine is regarded as the unit machine. Coil pitches other than 2 slots are feasible and will be discussed in Chapter 4.

For convenience, it is conventional to imaginarily 'cut' and 'unroll' an electrical machine to form a linear machine for analysis. The linear version of the machine shown in Fig. 3.1 is re-drawn in Fig. 3.2. The axis of phase A is regarded as the origin of air gap circumference and for simplicity, one of rotor saliencies coincides with the reference. Armature winding coil indices with an over bar indicate reversed currents and voltages.

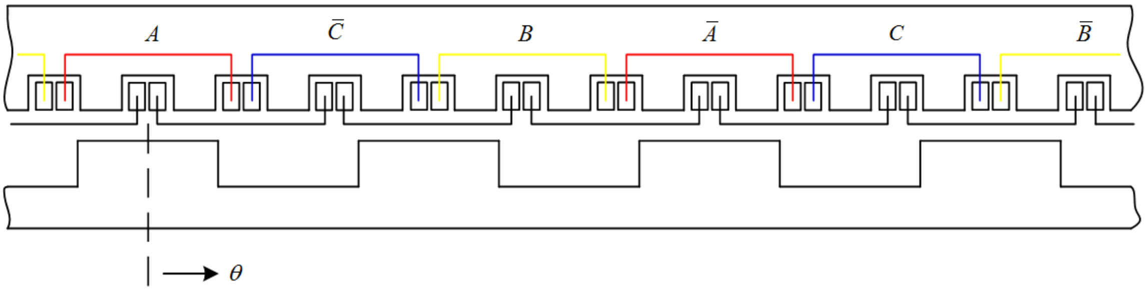

Fig. 3.2 Linearized structure of heteropolar inductor machine

The nature of salient rotor structure inevitably causes an unevenly distributed air gap magnetic permeance/reluctance. In the thesis, all the relevant analysis and calculations will be based on air gap magnetic permeance by decomposing the permeance variation resulted by rotor into a series of harmonics. Since the following analysis will all be based on 2D, only the permeance per unit area is of interest. In order to avoid confusions, the term ‘permeance’ in this thesis refers to ‘permeance per unit area’. The Fourier components of air gap permeance are expressed as

$$\Lambda(\theta)=\Lambda_0(\theta)+\Lambda_1(\theta)+\Lambda_2(\theta)+\Lambda_3(\theta)+\ldots \tag{3.1}$$

Magnetic flux density is distributed along the air gap circumference once the field windings are excited by DC, hence

$$b_f(\theta)=M_f\Lambda(\theta)=B_0(\theta)+B_1(\theta)+B_2(\theta)+B_3(\theta)+\ldots \tag{3.2}$$

In (3.1) and (3.2), b_f, M_f, and Λ are magnetic flux density, mmf excited by each field coil and air gap permeance respectively. θ represents (mechanical) angular displacement and indicates that the quantities are varying with angle. The Fourier components are indexed by the subscript and subscript 0 indicates invariant (i.e. DC) components. The values of Fourier coefficients will be derived at later stages.

A key characteristic of heteropolar inductor machines is that two adjacent field coils create magnetic flux pointing at opposite directions. A graphic illustration is shown in Fig. 3.3. The field flux reversals are expressed by the alternation of colours. Dark orange represents the regions where field-excited flux is directed from rotor to stator, while grey regions are where the flux flows reversely from stator to rotor. Crosses and dots on graph indicate the field current flows in each coil side.

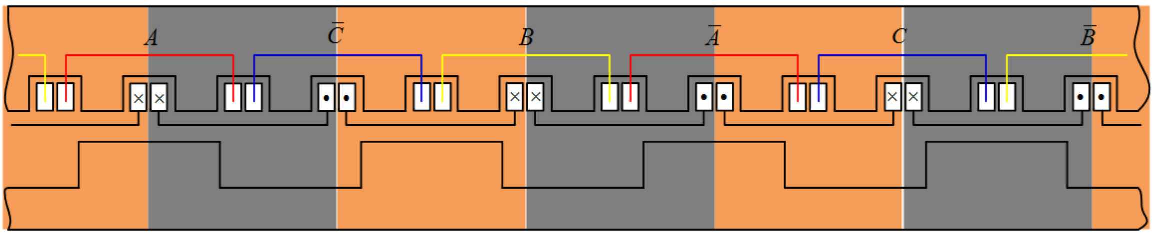

Fig. 3.3 Illustration of field flux alternation

Derivation of theories in this chapter is on the basis of the machine structure and characteristics discussed above. However, following additional simplifications and assumptions are made to facilitate the analysis.

(1) The material (iron) magnetic property is considered as linear with infinite permeability, thus magnetic saturation is not taken into consideration.

(2) The stator inner surface is considered to be ideally smooth, neglecting stator slotting. The slotting effect will be discussed in Chapter 4.

(3) The rotor is assumed in such a shape that only the invariant and fundamental air gap permeance components (i.e. Λ_0 and Λ_1) are present. In other words, only the invariant and fundamental air gap permeance components will be considered in the further analysis. Therefore the assumed air gap permeance distribution is mathematically expressed as

$$\Lambda(\theta) = \Lambda_0(\theta) + \Lambda_1(\theta) \tag{3.3}$$

The corresponding permeance waveform is plotted in Fig. 3.4.

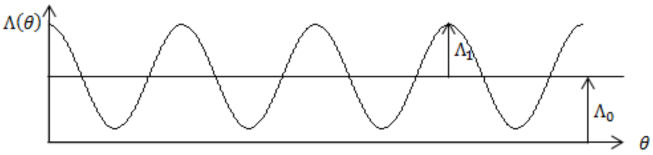

Fig. 3.4 Air gap permeance variation of ideal machine

More detailed analysis involving higher order permeance harmonics and their effects are considered in Chapter 4.

3.2 Internal flux linkage and no load emf

When the field windings of a heteropolar inductor machine are excited, the air gap flux density distribution is resultant from the alternatively reversed field mmf and the modulation effect of rotor saliencies. With the assumptions made in the previous section, the air gap magnetic flux density distribution is graphically illustrated in Fig. 3.5.

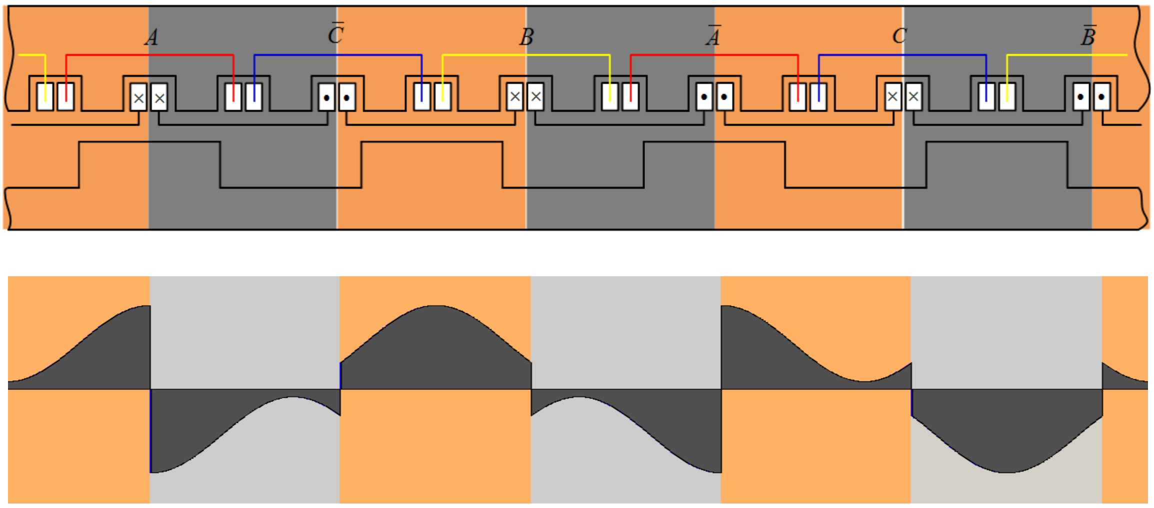

Fig. 3.5 Air gap flux density distribution of ideal machine

The shaded parts are the actual magnetic flux density waveform. It is obvious that the waveform is a segmentally reversed sinusoidal waveform with a DC offset, and that the flux density waveform is analogous to the permeance waveform shown in Fig. 3.4 if without the reversal of field. Each armature phase winding encloses a pair of reversal flux density and each stator coil spans π/3.

When the rotor is spinning at a specific angular speed ω_S with no load, the induced internal emf can be simply derived by Faraday's Law. The flux linkage linked by each phase is calculated from area-integrating the flux density in the regions enclosed by each phase winding. Since the origin of air gap circumference is referenced to phase A axis, the phase A main flux linkage can be calculated as the total magnetic flux density linked by phase A in the area covered by the phase.

$$\lambda_{fA} = N_S \int_{-\frac{\pi}{6}}^{\frac{\pi}{6}} \left[B_0 + B_1 \cos 4(\theta - \omega_S t) \right] \cdot rl d\theta \tag{3.4}$$

In (3.4), N_S denotes the total number of coil turns of phase A, i.e. sum of both A and $\bar{A}$ coil turns. B_0 and B_1 represent the magnitudes of invariant and fundamental air gap magnetic flux density components. θ and ω_S denote mechanical angle along air gap circumference and rotor mechanical angular speed respectively. r and l stand for stator bore radius and total axial length of the machine respectively. t denotes the time elapsed. The factor of 4 indicates that the fundamental air gap flux density component varies 4 times periodically along the circumference.

The air gap flux density is resulted from the interaction between field excitation and air gap permeance, and is mathematically expressed as the product of the two quantities, just as

$$B_0 + B_1 \cos 4(\theta - \omega_S t) = \begin{cases} M_f \cdot \left[\Lambda_0 + \Lambda_1 \cos 4(\theta - \omega_S t) \right], & -\frac{\pi}{6} \le \theta < 0 \\ -M_f \cdot \left[\Lambda_0 + \Lambda_1 \cos 4(\theta - \omega_S t) \right], & 0 \le \theta \le \frac{\pi}{6} \end{cases} \tag{3.5}$$

The segmental flux reversal is expressed by reversed signs of M_f in two adjacent sections.

Field mmf M_f is determined by field coil turns N_f and field DC current i_f.

$$M_f = N_f i_f \tag{3.6}$$

By solving (3.4 – 3.6), the flux linkage of phase A is expressed in a simple manner.

$$\lambda_{fA} = -\frac{3}{4} N_S N_f i_f \Lambda_1 rl \sin(4\omega_S t) \tag{3.7}$$

The emf induced in phase A e_A at no load condition is calculated according to Faraday's Law.

$$e_A = -\frac{d\lambda_{fA}}{dt} = 3\omega_S N_S N_f i_f \Lambda_1 rl \cos(4\omega_S t) \tag{3.8}$$

As indicated in (3.7) and (3.8), the invariant permeance component Λ_0 does not make any contribution to the induced internal emf. Also the electrical angular frequency is 4 times the mechanical angular speed, corresponding to the fact the electrical frequency of balanced heteropolar inductor machines is always the rotor angular frequency multiplied by the number of rotor saliencies. As a result, the heteropolar inductor machine is analogous to an 8-pole synchronous machine with a synchronous speed of ω_S.

Similarly the internal emfs induced in phase B and phase C can be calculated by the same method. Therefore

$$e_B = 3\omega_S N_S N_f i_f \Lambda_1 rl \cos\left(4\omega_S t - \frac{2\pi}{3}\right) \tag{3.9}$$

$$e_C = 3\omega_S N_S N_f i_f \Lambda_1 rl \cos\left(4\omega_S t + \frac{2\pi}{3}\right) \tag{3.10}$$

Obviously e_A leads e_B and lags e_C by $2\pi/3$ respectively. The three phase system is balanced.

3.3 Armature reaction

Once the armature windings are connected to loads or power sources, the machine terminal voltages will be modulated by the voltage components induced by conducting three phase armature currents. The phenomenon is known as armature reaction.

It is important to note that even though the rotor characteristic behaves as an 8-pole machine, the armature windings are of a 2-pole structure (i.e. only one set of three phase armature windings), as highlighted by J H Walker [34] in the very first analysis of such machines. This reveals the fact that in such a heteropolar inductor machine, the armature reaction mmf has only 2 poles. Consequently the rotational speed of armature reaction mmf must be 4 times the rotor speed. This behaviour is very different from conventional machines, in which armature reaction mmf waves normally have as many poles as field excitation pole numbers and rotate in synchronism with rotor.

If the armature currents of each phase are displaced by an electrical angle ψ (known as internal power factor angle) from the corresponding phase internal emfs, the current of phase A can be expressed as

$$i_A = \sqrt{2} I_{rms} \cos\left(4\omega_S t + \psi\right) = \sqrt{2} I_{rms} \cos 4\omega_S t \cdot \cos\psi - \sqrt{2} I_{rms} \sin 4\omega_S t \cdot \sin\psi \qquad (3.11)$$

Where I_{rms} stands for the rms magnitude of phase current.

From the point of view of the 2-pole armature reaction mmf wave, the armature windings are actually in a short pitched (i.e. chorded) manner. In other words, phase coil pitch can be regarded as decreased from full pitch π to current short pitch $\pi/3$. The effect of chording can be considered as the reduction of total number of coil turns by a pitch factor $k'_{p\nu}$. In classical electrical machine theory, $k'_{p\nu}$ is expressed as

$$k'_{p\nu} = \sin\left(\frac{\nu y'}{2}\right) \qquad (3.12)$$

ν is the index of harmonics and y' is the coil pitch in radians. In this case, the harmonic of interest is the fundamental, hence $\nu = 1$. As a result, pitch factor k'_{p1}=1/2 when y'= $\pi/3$.

With the definition of pitch factor, the resultant three phase armature reaction mmf wave is calculated as [83]

$$m_a = \frac{k'_{p1}N_S}{2}\left[i_A\cos\theta + i_B\cos\left(\theta - \frac{2}{3}\pi\right) + i_C\cos\left(\theta + \frac{2\pi}{3}\right)\right] = M_a\cos\left(\theta - 4\omega_S t - \psi\right) \quad (3.13)$$

Where

$$M_a = \frac{3\sqrt{2}}{4}k'_{p1}N_S I_{rms} \quad (3.14)$$

Same as internal emfs, phase B armature current (i_B) lags phase A by $2\pi/3$ while phase C armature current (i_C) leads phase A by $2\pi/3$. Amplitudes of three phase currents are equal if the system is ideally balanced. M_a is the magnitude of armature reaction mmf wave composed by three phase currents.

The equation (3.13) implies a travelling wave as it is a function of both angular displacement θ and time t. The speed of the travelling wave, as can be easily spotted, is 4 times the rotor speed $4\omega_S$.

Armature reaction mmf acts on air gap permeance and induces magnetic flux density distribution. The component of flux density resulted from armature reaction is denoted as b_a and calculated as

$$b_a = m_a\Lambda\left(\theta\right) \quad (3.15)$$

By combining (3.3) and (3.13 – 3.15), b_a is expressed as a function of angular displacement and time.

$$b_a = \underbrace{M_a\Lambda_0\cos\left(\theta - 4\omega_S t - \psi\right)}_{fundamental} + M_a\frac{\Lambda_1}{2}\left[\underbrace{\cos\left(3\theta + \psi\right)}_{stationary} + \underbrace{\cos\left(5\theta - 8\omega_S t - \psi\right)}_{fifth-order-harmonic}\right] \quad (3.16)$$

As shown in (3.16), the flux density distribution induced from armature reaction is composed by three terms: a 2-pole (fundamental) wave resulted from invariant permeance component Λ_0 traveling at 4 times rotor speed, a 6-pole stationary wave in space resulted from fundamental permeance component Λ_1, and a 10-pole (5th harmonic) wave resulted from fundamental permeance component Λ_1 traveling at 8/5 times rotor speed. Consequently, the first term induces an electrical frequency (i.e. $4\omega_S$) armature reaction voltage in phase windings, while the third term induces a double electrical frequency (i.e. $8\omega_S$). On the other hand the second term makes no contribution to phase winding armature reaction voltages, as it is a time-invariant 6-pole (3rd harmonic) flux density wave. Only the armature reaction voltage with electrical frequency is of interest.

Armature reaction magnetic flux linkage linking phase A with the same electrical frequency is calculated by area-integrating phase A area.

$$\lambda_{aA} = k'_{p1} N_S \int_{-\frac{\pi}{2}}^{\frac{\pi}{2}} M_a \Lambda_0 \cos\left(\theta - 4\omega_S t - \psi\right) \cdot lr d\theta \tag{3.17}$$

Phase A voltage induced by armature reaction is derived by Faraday's Law.

$$e_{aA} = -\frac{d\lambda_{aA}}{dt} \tag{3.18}$$

The expression of e_{aA} is solved by combining (3.14), (3.17) and (3.18). Hence

$$e_{aA} = 6\sqrt{2}\omega_S k_{p1}^{'2} N_S^2 \Lambda_0 I_{rms} rl \left[\cos\left(4\omega_S t - \frac{\pi}{2}\right)\cos\psi + \sin\left(4\omega_S t + \frac{\pi}{2}\right)\sin\psi \right] \tag{3.19}$$

Armature reaction voltage of phase A is rewritten in complex phasor form and denoted as $\underline{E_{aA}}$.

$$\underline{E_{aA}} = 6\sqrt{2}\omega_S k_{p1}^{'2} N_S^2 \Lambda_0 I_{rms} rl \left[\cos\psi \angle\left(4\omega_S t - \frac{\pi}{2}\right) + \sin\psi \angle\left(4\omega_S t + \frac{\pi}{2}\right) \right] \tag{3.20}$$

Similarly the phase A armature current can also be expressed as a complex phasor.

$$\underline{I_A} = \sqrt{2} I_{rms} \left(\cos\psi \angle 4\omega_S t - \sin\psi \angle 4\omega_S t\right) \tag{3.21}$$

Equations (3.20) and (3.21) are combined for armature reaction voltage phasor.

$$\underline{E_{aA}} = -jX_{ad}\underline{I_{Ad}} - jX_{aq}\underline{I_{Aq}} \tag{3.22}$$

Where

$$\underline{I_{Ad}} = -\sqrt{2} I_{rms} \sin\psi \angle 4\omega_S t \tag{3.23}$$

$$\underline{I_{Aq}} = \sqrt{2} I_{rms} \cos\psi \angle 4\omega_S t \tag{3.24}$$

$$X_{ad} = X_{aq} = 6\sqrt{2}\omega_S k_{p1}^{'2} N_S^2 r l \Lambda_0 \tag{3.25}$$

$\underline{I_A}$ is decomposed into a pair of orthogonal quantities: $\underline{I_{Ad}}$ and $\underline{I_{Aq}}$. X_{ad} and X_{aq} are known as direct axis and quadrature axis armature reaction reactance respectively, according to Blondel's two reaction theory.

Despite the structurally salient nature, the expressions of armature reaction reactance indicate that the rotor does not electrically exhibit any saliencies as they are equal to each other. The armature reaction in heteropolar inductor machines can also be analysed in a similar way as analysing the armature reaction caused by a fractional harmonic in a normal salient pole synchronous machine [84]. The results are proved to be the same as illustrated above, yet the calculation procedure is much more complicated and time consuming.

It is worth noting that (3.19 – 3.21) should contain 2nd harmonic (i.e. double electrical frequency) terms induced by the last term in (3.16), with corresponding armature reaction reactance values. Since the fundamental permeance component Λ_1 is predominant, the amplitude of such 2nd harmonic armature reaction voltage is expected to be high. The reason that the 2nd harmonic voltage is not considered here is that it is detrimental to machine characteristics and will have to be eliminated. More analysis on the 2nd harmonic and its elimination will be discussed in later sections and Chapter4.

The terminal voltage of each phase is a superimposition of both internally induced emf and armature reaction voltage.

$$u_A = e_A + e_{aA} \tag{3.26}$$

$$u_B = e_B + e_{aB} \tag{3.27}$$

$$u_c = e_C + e_{aC} \tag{3.28}$$

3.4 Electromechanical torque

A steady average torque output must be available in order to achieve a conversion of electrical power to mechanical power and vice versa in a well-designed machine. A classical method to calculate torque produced by an electrical machine is by solving the total magnetic field energy conserved in air gap.

In order to derive a generic torque equation, the rotor position and armature reaction mmf wave are considered to have an arbitrary initial displacement relative to reference axis (i.e. phase A axis). As shown in Fig. 3.6, γ_0 denotes the initial angular displacement between armature reaction mmf and the reference, and ξ_0 denotes the initial displacement between one of the rotor saliency centres and the reference.

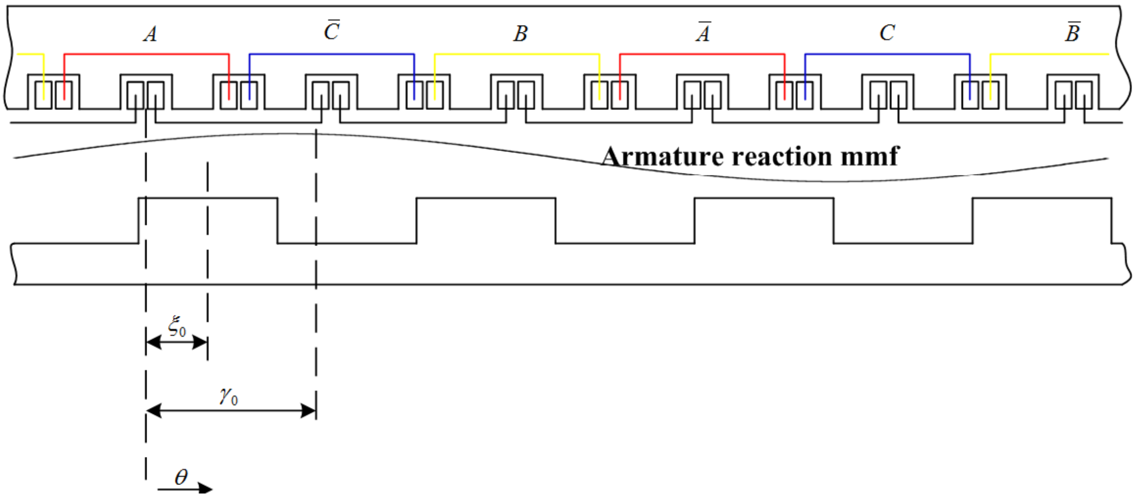

Fig. 3.6 Arbitrary initial conditions of rotor and armature reaction mmf axes

Derived from (3.5) and (3.13), the expressions of armature reaction mmf waveform m_a and rotating air gap permeance spatial distribution $\Lambda(\theta)$ are written as

$$m_a = M_a \cos\left(\theta - 4\omega_S t - \gamma_0\right) \tag{3.29}$$

$$\Lambda(\theta) = \Lambda_0 + \Lambda_1 \cos 4\left(\theta - \omega_S t - \xi_0\right) \tag{3.30}$$

The field flux reversal must be taken into consideration as mathematical constraints. Therefore the field coil mmf m_f alternates in adjacent sections and the magnitude switches between M_f and $-M_f$.

$$m_f = \begin{cases} M_f,\ \theta \in \left[\frac{\pi}{3}, \frac{2\pi}{3}\right), \left[\pi, \frac{4\pi}{3}\right), \left[\frac{5\pi}{3}, \pi\right) \\ -M_f,\ \theta \in \left[0, \frac{\pi}{3}\right), \left[\frac{2\pi}{3}, \pi\right), \left[\frac{4\pi}{3}, \frac{5\pi}{3}\right) \end{cases} \tag{3.31}$$

Total magnetic energy stored in air gap W_m is expressed as

$$W_m = \int_0^{2\pi} \frac{1}{2} \mu_0 H^2(\theta) g(\theta) lr d\theta \tag{3.32}$$

In (3.32), μ_0 is vacuum magnetic permeability and is a constant. $H(\theta)$ stands for magnetic field intensity and $g(\theta)$ is the variation of radial air gap length along bore circumference. The term $\frac{1}{2}\mu_0 H(\theta)^2$ is known as magnetic energy density. $H(\theta)$ and $g(\theta)$ are further derived as

$$H(\theta) = \frac{m_a + m_f}{g(\theta)} \tag{3.33}$$

$$g(\theta) = \frac{\mu_0}{\Lambda(\theta)} \tag{3.34}$$

By combining (3.29 – 3.34), the expression of magnetic energy stored in air gap can be solved.

$$W_m = 2lrM_f M_a \Lambda_1 \sin(\gamma_0 - 4\xi_0) - 2\pi\left(M_f^2 + \frac{M_a^2}{2}\right)\Lambda_0 \tag{3.35}$$

The conserved energy W_m in magnetic field consists of a variant component that is related to the angular relationship between armature reaction mmf wave and rotor saliencies, and an invariant component if magnitudes of armature and field currents are constant.

Internal relationship exists between angles γ_0 and $4\xi_0$ in (3.35). An initial displacement of rotor saliencies ($4\xi_0$ in electrical angle) from reference axis will lead to a corresponding initial time displacement of internal emf, hence that of phase armature current. Mathematically, the phase induced internal emf leads fundamental air gap permeance wave by π in electrical degree, because derivation of internal emf from air gap permeance includes an integration (3.4), a differentiation (3.8) and a sign reversal (3.8). On the other hand, phase current displaces from internal emf by an internal power factor angle ψ. Thus

$$\gamma_0 - 4\xi_0 = \pi + \psi \tag{3.36}$$

As a result W_m can be written with respect to angle ψ.

$$W_m = -2lrM_f M_a \Lambda_1 \sin\psi - 2\pi\left(M_f^2 + \frac{M_a^2}{2}\right)\Lambda_0 \tag{3.37}$$

The electromechanical torque can be calculated as the derivative of conserved magnetic energy with respect to ψ.

$$T_e = -4\frac{\partial W_m}{\partial \psi} = 8lrM_f M_a \Lambda_1 \cos\psi \tag{3.38}$$

The factor of 4 indicates that the machine behaves as an 8 pole characteristic (i.e. 4 pairs of poles), while the minus sign takes into account the fact that electromechanical torque is against any magnetic field energy variations. Consequently the invariant part of stored magnetic energy related to invariant permeance component Λ_0 does not generate any torque. Also the amount of torque generated is irrelevant to machine speed, but determined by phase angle relationships, similar as the way in synchronous machines.

The fundamental variation of air gap permeance Λ_1 directly affects the amount of torque delivered, it is similar to reluctance machines (RMs) to some extent and it also explains the need for salient structure on rotor. The methods for maximising saliency ratio in RMs [85] can be potentially applied in order to obtain maximised fundamental permeance swing.

A simplification is made during the analysis and calculation above as it is assumed that only armature current component with electrical frequency $4\omega_S$ exists. Nevertheless, as discussed in the previous section, the armature reaction of heteropolar inductor machine will induce a double electrical frequency $8\omega_S$ phase voltage term, which in turn creates a double electrical frequency phase current component when loaded. In reality, an oscillating torque at frequency $4\omega_S$ will respond to the double frequency current component. Such a periodical torque is undesirable as it deteriorates machine performance. Detailed analysis and appropriate measures to remove such oscillating torque are discussed in next section.

3.5 Space vector theory

3.5.1 Introduction of space vectors

The theoretical approaches of heteropolar inductor machines developed above are all based on steady state. For example the magnitude of armature current is considered to be constant, and machine speed is also assumed to stay unchanged, etc. However, in practical applications, the transient theories of an electrical machine can be even more significant as it predicts the machine's behaviour dynamically and is constructive to elaborate control systems.

Transient analysis will be based upon space vector theory in the thesis. Space vector theory transforms three phase time-variant variables (e.g. current, voltage, flux, etc.) into complex vectors (i.e. space vectors). The resultant spaces vectors are located on a same stationary complex plane coordinated by a real axis and an imaginary axis. A demonstrative space vector is plotted in Fig. 3.7.

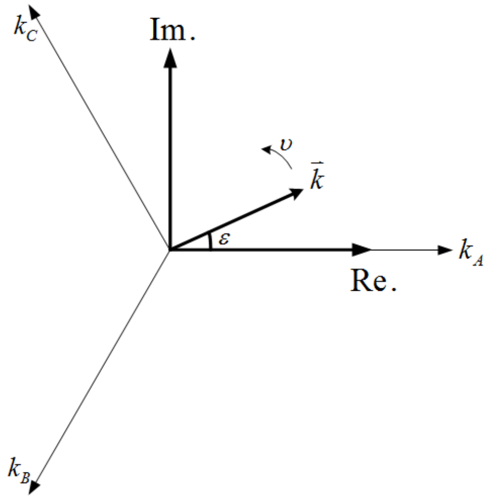

Fig. 3.7 Illustrative space vector

The space vector can be calculated and expressed in complex denotation.

$$\vec{k} = k_A + k_B e^{j\frac{2\pi}{3}} + k_C e^{-j\frac{2\pi}{3}} \tag{3.39}$$

$$\vec{k} = \left|\vec{k}\right| \cdot e^{j\varepsilon} = \left|\vec{k}\right| \cdot e^{j(\varepsilon_0 + \nu t)} \tag{3.40}$$

k_A, k_B and k_C are arbitrary three phase time-variant quantities in (3.39) and (3.40). The quantities embraced in the brackets represent the angular displacement of the vector with respect to real axis. The initial displacement of the space vector when time t is 0 is denoted as ε_0. Once the time starts elapsing, the vector acts as rotating in the complex plane at any instant angular speed of ν. The length of the vector is equal to the vector modulus.

The length, angular position and angular speed of a space vector directly link the magnitude, phase angle and instant angular frequency of corresponding three phase variables respectively. Space vectors and actual three phase quantities can be transformed bi-directionally. Moreover space vectors may be projected orthogonally to both real and imaginary axes for decoupling purposes. A series of differential equations that link various important machine quantities together can be developed, offering specific solutions to machine dynamics.

3.5.2 Armature space vectors

An arbitrary state of heteropolar inductor machine is studied. The air gap permeance wave in (3.30) can be re-written in complex form.

$$\Lambda(\theta) = \Lambda_0 + \frac{1}{2}\left(\overline{\Lambda_1} e^{-j4\theta} + \overline{\Lambda_1^*} e^{j4\theta}\right) \tag{3.41}$$

Where

$$\overline{\Lambda_1} = \Lambda_1 e^{j4\xi} \tag{3.42}$$

$$\xi = \xi_0 + \omega_S t \tag{3.43}$$

Angle ξ denotes the angular rotor displacement at any time instants. Complex vectors with an asterisk (*) represent the complex conjugate of corresponding vectors.

The field excited flux linkage of phase A (λ_{fA}) in (3.7) can be expressed in complex form, as

$$\lambda_{fA} = \frac{3}{8} N_S N_f l r \Lambda_1 \left(\overline{i_f} + \overline{i_f^*}\right) \tag{3.44}$$

Where the field current space vector is

$$\overline{i_f} = i_f e^{j\left(4\xi - \frac{\pi}{2}\right)} \tag{3.45}$$

Three phase resultant armature reaction mmf is re-written with slight modification from (3.29).

$$m_a = \frac{k'_{p1} N_S}{4} \left(\overrightarrow{i_S} e^{-j\theta} + \overrightarrow{i_S^*} e^{j\theta} \right) \tag{3.46}$$

Where

$$\overrightarrow{i_S} = i_S e^{j\gamma} = \frac{3\sqrt{2}}{2} I_{rms} e^{j\gamma} \tag{3.47}$$

$$\gamma = \gamma_0 + 4\omega_S t \tag{3.48}$$

Equations (3.46 – 3.48) are established under the assumption that three phases are balanced. The vector $\overrightarrow{i_S}$ is armature current space vector and its length is 3/2 times the amplitude of phase currents. Angle γ indicates the vector phase shift at any time instants.

The main flux linkage of phase A is the resulted by both field and armature current space vectors, hence

$$\lambda_{mA} = k'_{pv} N_S \int_{-\frac{\pi}{2}}^{\frac{\pi}{2}} m_a \Lambda(\theta) lr d\theta + \lambda_{fA} \tag{3.49}$$

A generic multi-harmonic pitch factor k'_{pv} is used in (3.49). It is because that armature reaction results in different harmonic flux density waves, and that armature windings modulate different harmonics by different pitch factors. Main flux linkage λ_{mA} is obtained by solving (3.41 – 3.49) together.

$$\begin{aligned} \lambda_{mA} = {} & \underbrace{\frac{k'^2_{p1} N_S^2}{2} lr\Lambda_0 \left(\overrightarrow{i_S} + \overrightarrow{i_S^*} \right)}_{fundamental} + \underbrace{\frac{k'_{p1} k'_{p5} N_S^2}{20} lr\Lambda_1 \left(\overrightarrow{i_{S2}} + \overrightarrow{i_{S2}^*} \right)}_{2nd-harmonic} + \underbrace{\frac{k'_{p1} k'_{p3} N_S^2}{12} lr\Lambda_1 \left(\overrightarrow{i_{S0}} + \overrightarrow{i_{S0}^*} \right)}_{stationary} \\ & + \frac{3}{8} N_S N_f lr\Lambda_1 \left(\overrightarrow{i_f} + \overrightarrow{i_f^*} \right) \end{aligned} \tag{3.50}$$

Where

$$\overrightarrow{i_{S2}} = i_S e^{j(\gamma + 4\xi)} = i_S e^{j(\gamma_0 + 4\xi_0 + 8\omega_S t)} \tag{3.51}$$

$$\overline{i_{S0}} = -i_S e^{j(\gamma - 4\xi)} = -i_S e^{j(\gamma_0 - 4\xi_0)} \tag{3.52}$$

There are four terms in (3.50). The first term is the armature reaction flux linkage with electrical angular frequency $4\omega_S$. The second term, however, exhibits a double electrical frequency $8\omega_S$ flux linkage and is resulted from a 5th harmonic magnetic flux density wave. The third term is a time-invariant flux linkage component from a stationary 3rd harmonic magnetic flux density wave. The armature reaction components correspond to the result from (3.16) in the analysis of armature reaction.

$\overline{i_{S2}}$ is a double frequency armature current space vector and $\overline{i_{S0}}$ is a DC armature current space vector. Clearly compared with conventional AC machines, the phase winding flux linkage components in heteropolar inductor machines are more complicated.

For clarification, the following inductances are defined.

$$\frac{1}{3}L_{mS} = \frac{k_{p1}^{'2} N_S^2}{2} lr\Lambda_0 \tag{3.53}$$

$$\frac{1}{3}L_{mS2} = \frac{k_{p1}^{'} k_{p5}^{'} N_S^2}{20} lr\Lambda_1 \tag{3.54}$$

$$\frac{1}{3}L_{mS0} = \frac{k_{p1}^{'} k_{p3}^{'} N_S^2}{12} lr\Lambda_1 \tag{3.55}$$

$$\frac{1}{3}L_{mfa} = \frac{3}{8} N_S N_f lr\Lambda_1 \tag{3.56}$$

$\frac{1}{3}L_{mS}$, $\frac{1}{3}L_{mS2}$ and $\frac{1}{3}L_{mS0}$ are defined as main frequency, double frequency and DC magnetising inductances per phase respectively. $\frac{1}{3}L_{mfa}$ is the phase mutual inductance. Instead of main flux linkage, phase windings are also linked by leakage flux linkage. The leakage flux linkage of phase A λ_{lA} is expressed as

$$\lambda_{lA} = \frac{1}{3}L_{lS}\left(\overline{i_S} + \overline{i_S^*}\right) + \frac{1}{3}L_{lS}\left(\overline{i_{S2}} + \overline{i_{S2}^*}\right) + \frac{1}{3}L_{lS}\left(\overline{i_{S0}} + \overline{i_{S0}^*}\right) \tag{3.57}$$

Phase leakage inductance denoted as $\frac{1}{3}L_{lS}$.With the definition of various inductance terms, phase A flux linkage λ_A is calculated by adding up both main and leakage flux linkages.

$$\lambda_A = \lambda_{mA} + \lambda_{lA} = \frac{1}{3} L_S \left(\overrightarrow{i_S} + \overrightarrow{i_S^*} \right) + \frac{1}{3} L_{S2} \left(\overrightarrow{i_{S2}} + \overrightarrow{i_{S2}^*} \right) + \frac{1}{3} L_{S0} \left(\overrightarrow{i_{S0}} + \overrightarrow{i_{S0}^*} \right) + \frac{1}{3} L_{mfa} \left(\overrightarrow{i_f} + \overrightarrow{i_f^*} \right) \quad (3.58)$$

Where

$$\frac{1}{3} L_S = \frac{1}{3} L_{lS} + \frac{1}{3} L_{mS} \quad (3.59)$$

$$\frac{1}{3} L_{S2} = \frac{1}{3} L_{lS} + \frac{1}{3} L_{mS2} \quad (3.60)$$

$$\frac{1}{3} L_{S0} = \frac{1}{3} L_{lS} + \frac{1}{3} L_{mS0} \quad (3.61)$$

Inductance terms $\frac{1}{3} L_S$, $\frac{1}{3} L_{S2}$ and $\frac{1}{3} L_{S0}$ are armature windings inductances for different current components.

Phases B and C are applied with the same method for calculating flux linkages.

$$\begin{aligned} \lambda_B = {} & \frac{1}{3} L_S \left(\overrightarrow{i_S} e^{-j\frac{2\pi}{3}} + \overrightarrow{i_S^*} e^{j\frac{2\pi}{3}} \right) + \frac{1}{3} L_{S2} \left(\overrightarrow{i_{S2}} e^{-j\frac{2\pi}{3}} + \overrightarrow{i_{S2}^*} e^{j\frac{2\pi}{3}} \right) + \frac{1}{3} L_{S0} \left(\overrightarrow{i_{S0}} + \overrightarrow{i_{S0}^*} \right) \\ & + \frac{1}{3} L_{mfa} \left(\overrightarrow{i_f} e^{-j\frac{2\pi}{3}} + \overrightarrow{i_f^*} e^{j\frac{2\pi}{3}} \right) \end{aligned} \quad (3.62)$$

$$\begin{aligned} \lambda_C = {} & \frac{1}{3} L_S \left(\overrightarrow{i_S} e^{j\frac{2\pi}{3}} + \overrightarrow{i_S^*} e^{-j\frac{2\pi}{3}} \right) + \frac{1}{3} L_{S2} \left(\overrightarrow{i_{S2}} e^{j\frac{2\pi}{3}} + \overrightarrow{i_{S2}^*} e^{-j\frac{2\pi}{3}} \right) + \frac{1}{3} L_{S0} \left(\overrightarrow{i_{S0}} + \overrightarrow{i_{S0}^*} \right) \\ & + \frac{1}{3} L_{mfa} \left(\overrightarrow{i_f} e^{-j\frac{2\pi}{3}} + \overrightarrow{i_f^*} e^{j\frac{2\pi}{3}} \right) \end{aligned} \quad (3.63)$$

Consequently the armature flux linkage space vector is calculated as

$$\overrightarrow{\lambda_S} = \lambda_A + \lambda_B e^{j\frac{2\pi}{3}} + \lambda_C e^{-j\frac{2\pi}{3}} \quad (3.64)$$

In a balanced three phase system, all the conjugate vectors and the DC component are cancelled out. The armature flux linkage space vector $\overrightarrow{\lambda_S}$ can be expressed with respect to current space vectors and relevant inductance terms,

$$\overrightarrow{\lambda_S} = L_S \overrightarrow{i_S} + L_{S2} \overrightarrow{i_{S2}} + L_{mfa} \overrightarrow{i_f} \quad (3.65)$$

The length of vector $\overrightarrow{\lambda_S}$ is 3/2 times the amplitude of flux linkage per phase. Inductance terms L_S and L_{S2} are 3/2 times corresponding armature reaction inductances of each phase. Similarly L_{mfa} is 3/2 times armature-field mutual inductance.

A voltage space vector can be formed in the same way as armature current and flux linkage space vectors.

$$\overrightarrow{u_S} = u_A + u_B e^{j\frac{2\pi}{3}} + u_C e^{-j\frac{2\pi}{3}} \tag{3.66}$$

Similarly, the length of voltage space vector $\overrightarrow{u_S}$ is 3/2 times the amplitude of phase terminal voltage. Besides, vector $\overrightarrow{u_S}$ is related to flux linkage vector $\overrightarrow{\lambda_S}$ by

$$\overrightarrow{u_S} = \overrightarrow{i_S} R_S + p\overrightarrow{\lambda_S} \tag{3.67}$$

Armature winding resistance per phase is denoted as R_S. The differentiation operator d/dt is denoted as p.

Equation (3.67) states the fact that the terminal voltage consists of a resistance voltage drop and a voltage component induced from machine flux linkage. Since the terminal voltage space vector is strongly related to flux linkage space vector, the double frequency flux linkage term $L_{S2}\overrightarrow{i_{S2}}$ will inevitably induce double electrical frequency terminal voltages. It coincides with the analysis and conclusion in previous section.

3.5.3 Field analysis

It is observed that, by re-considering Fig. 3.2 and Fig. 3.3, the field coils in the heteropolar inductor machine are distributed in a similar pattern as three phase armature windings. In other words, the 6 field coils can be grouped into 3 'phases' and the grouping of field coils is shown in Fig. 3.8.

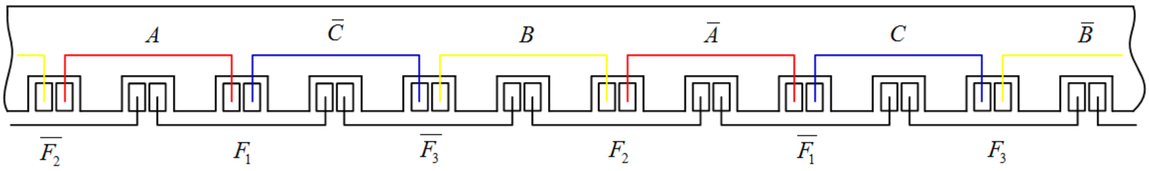

Fig. 3.8 Grouping of armature and field windings

As shown, the ‘three phase’ field windings are denoted as F_1, F_2 and F_3. The coils with overhead bars mean that their voltages and currents are reversed compared with their counterpart coils. The three phase armature windings ($A\ B\ C$ system) and ‘three phase’ field windings ($F_1\ F_2\ F_3$ system) are inter-connected in different manners, as shown in Fig. 3.9.

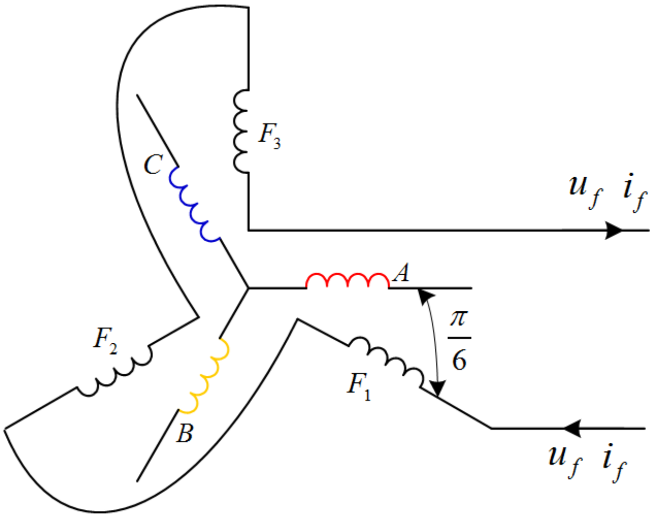

Fig. 3.9 Sketch of winding connections

u_f and i_f denote the voltage and current from the DC power source supplying the field respectively. Three phase armature windings are connected to a common point, thus forming a star connection, while the field windings are connected in series and are supplied by a single DC power source.

The main flux linkage of field winding F_1 is calculated as the combination of flux linkage excited by both field winding excitation and armature reaction,

$$\lambda_{mf1} = 2N_f lr \int_0^{\frac{\pi}{3}} \left(N_f i_f + m_a\right) \Lambda(\theta)\, d\theta \tag{3.68}$$

Equation (3.68) is solved by substituting m_a and $\Lambda(\theta)$ with (3.46) and (3.41).

$$\begin{aligned}\lambda_{mf1} = {} & \frac{2\pi}{3} N_f^2 i_f lr\Lambda_0 - \frac{\sqrt{3}}{4} N_f^2 i_f lr\left(\overrightarrow{\Lambda_1} e^{j\frac{\pi}{3}} + \overrightarrow{\Lambda_1^*} e^{-j\frac{\pi}{3}}\right) \\ & + \frac{1}{2} k_{p1}^{'} N_S N_f lr\Lambda_0 \left(\overrightarrow{i_S} e^{-j\frac{\pi}{6}} + \overrightarrow{i_S^*} e^{j\frac{\pi}{6}}\right) - \frac{1}{20} k_{p1}^{'} N_S N_f lr\left(\overrightarrow{i_S} \cdot \overrightarrow{\Lambda_1} e^{j\frac{\pi}{6}} + \overrightarrow{i_S^*} \cdot \overrightarrow{\Lambda_1^*} e^{-j\frac{\pi}{6}}\right)\end{aligned} \tag{3.69}$$

The field winding flux linkage consists of 4 terms. The first term is a constant flux linkage, representing the flux linked with air gap permeance component Λ_0. The second term is due to magnetic permeance variation caused by rotor saliencies. The last two terms are resulted from armature reaction mmf. The third term is time-varying with a fundamental electrical angular frequency, while the fourth term has a double electrical frequency variation.

The main flux linkages of field windings F_2 and F_3 are calculated similarly to (3.69).

$$\begin{aligned}\lambda_{mf2} &= \frac{2\pi}{3} N_f^2 i_f lr\Lambda_0 - \frac{\sqrt{3}}{4} N_f^2 i_f lr\left(\overrightarrow{\Lambda_1} e^{-j\frac{\pi}{3}} + \overrightarrow{\Lambda_1^*} e^{j\frac{\pi}{3}}\right) \\ &+ \frac{1}{2} k_{dp1} N_S N_f lr\Lambda_0\left(\overrightarrow{i_S} e^{-j\frac{5\pi}{6}} + \overrightarrow{i_S^*} e^{j\frac{5\pi}{6}}\right) - \frac{1}{20} k_{dp5} N_S N_f lr\left(\overrightarrow{i_S}\cdot\overrightarrow{\Lambda_1} e^{-j\frac{\pi}{2}} + \overrightarrow{i_S^*}\cdot\overrightarrow{\Lambda_1^*} e^{j\frac{\pi}{2}}\right)\end{aligned} \tag{3.70}$$

$$\begin{aligned}\lambda_{mf3} &= \frac{2\pi}{3} N_f^2 i_f lr\Lambda_0 - \frac{\sqrt{3}}{4} N_f^2 i_f lr\left(\overrightarrow{\Lambda_1} e^{j\pi} + \overrightarrow{\Lambda_1^*} e^{-j\pi}\right) \\ &+ \frac{1}{2} k_{dp1} N_S N_f lr\Lambda_0\left(\overrightarrow{i_S} e^{j\frac{\pi}{2}} + \overrightarrow{i_S^*} e^{-j\frac{\pi}{2}}\right) - \frac{1}{20} k_{dp5} N_S N_f lr\left(\overrightarrow{i_S}\cdot\overrightarrow{\Lambda_1} e^{-j\frac{7\pi}{6}} + \overrightarrow{i_S^*}\cdot\overrightarrow{\Lambda_1^*} e^{j\frac{7\pi}{6}}\right)\end{aligned} \tag{3.71}$$

As discussed, ‘three phase’ field windings are connected in series. Hence no rotating space vector is formed. The main field flux linkage is calculated by simply adding up the flux linkages of each winding.

$$\lambda_{mf} = \lambda_{mf1} + \lambda_{mf2} + \lambda_{mf3} = L_{mf} i_f \tag{3.72}$$

$$L_{mf} = 2\pi N_f^2 lr\Lambda_0 \tag{3.73}$$

It is seen from (3.72) that balanced three phase armature current excitations have no influence on total field winding flux linkage, although they induce flux linkage components in each individual field coil. The decoupling of field flux linkage from armature currents improves the machine transient property by eliminating transient reactance which occurs during the transients of conventional AC machines. Also the total field main flux linkage λ_{mf} is irrelevant to rotor saliencies. Nevertheless, λ_{mf} is proportional to the mean value of air gap permeance variation (i.e. the invariant component Λ_0).

The total field flux linkage is expressed as

$$\lambda_f = L_f i_f \tag{3.74}$$

Where

$$L_f = L_{lf} + L_{mf} \tag{3.75}$$

Field leakage inductance is denoted asL_{lf}. The field voltage u_f is composed by a resistance voltage drop and the rate of variation of flux linkage.

$$u_f = i_f R_f + p\lambda_f \tag{3.76}$$

The field circuit diagram is shown in Fig. 3.10.

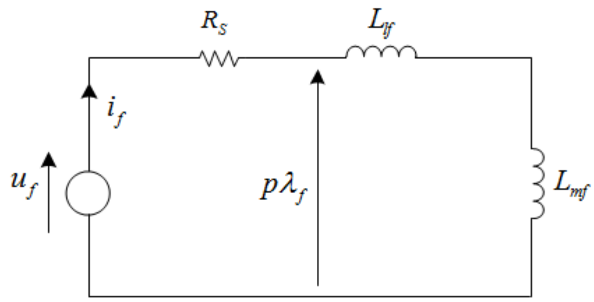

Fig. 3.10 Field equivalent circuit

3.5.4 Space vectors with field orientation

The analysis of this section so far is based on the assumption that all the space vectors are referenced to a fixed complex plane with real axis aligning with phase A axis. However, since the space vectors are all travelling at a same angular speed (except for $\overrightarrow{i_{S2}}$), it is common to reference the space vectors to a complex plane which is rotating at the same speed ($4\omega_S$). It is customary to align the real axis of the rotating frame to the field current vector. Transforming from stationary to rotating frame is known as field orientation. It decouples the complex couplings in a three-phase system by creating a fictitious two-phase system with constant inductance value on each phase axis. This approach is often used in modern motor control strategies (e.g. field oriented control).

As a result, (3.65) and (3.67) are re-written in (3.77) and (3.78) respectively when referred to the rotating frame. Current space vectors are also referenced to the rotating frame as shown in (3.78 – 3.81).

$$\overrightarrow{\lambda_S^R} = L_S \overrightarrow{i_S^R} + L_{S2} \overrightarrow{i_{S2}^R} + L_{mfa} \overrightarrow{i_f^R} \tag{3.77}$$

$$\overline{u_S^R} = \overline{i_S^R} R_S + p\overline{\lambda_S^R} + j4\omega_S \overline{\lambda_S^R} \tag{3.78}$$

Where

$$\overline{i_f^R} = i_f \tag{3.79}$$

$$\overline{i_S^R} = i_S e^{j\left(\gamma_0 - 4\xi_0 + \frac{\pi}{2}\right)} \tag{3.80}$$

$$\overline{i_{S2}^R} = i_S e^{j\left(\gamma + \frac{\pi}{2}\right)} \tag{3.81}$$

The internal emf space vector is

$$\overline{e_S^R} = j4\omega_S \overline{\lambda_S^R} \tag{3.82}$$

The superscript R indicates that the space vectors are referenced to a rotating frame. Field current space vector $\overrightarrow{i_f}$ is regarded as the real axis and the imaginary axis is orthogonal to it. As is seen, an additional rotating voltage term $j4\omega_S\overrightarrow{\lambda_S^R}$ appears in voltage vector expression after transforming the frame. The armature current space vector $\overline{i_S^R}$ stands still with respect to the frame. However vector $\overrightarrow{i_{S2}^R}$ still rotates at electrical frequency $4\omega_S$. A space vector diagram within the rotating frame is illustrated in Fig. 3.11. Double frequency armature current space vector $\overline{i_{S2}^R}$ is not shown on the graph.

Decomposition of space vectorial equations into real and imaginary axes is shown in Fig. 3.11. Vector $\overrightarrow{i_{S2}^R}$ is neglected in the equations.

$$\lambda_{Sd} = L_S i_{Sd} + L_{mfa} i_f \tag{3.83}$$

$$\lambda_{Sq} = L_S i_{Sq} \tag{3.84}$$

$$u_{Sd} = i_{Sd} R_S + p\lambda_{Sd} - 4\omega_S \lambda_{Sq} \tag{3.85}$$

$$u_{Sq} = i_{Sq} R_S + p\lambda_{Sq} + 4\omega_S \lambda_{Sd} \tag{3.86}$$

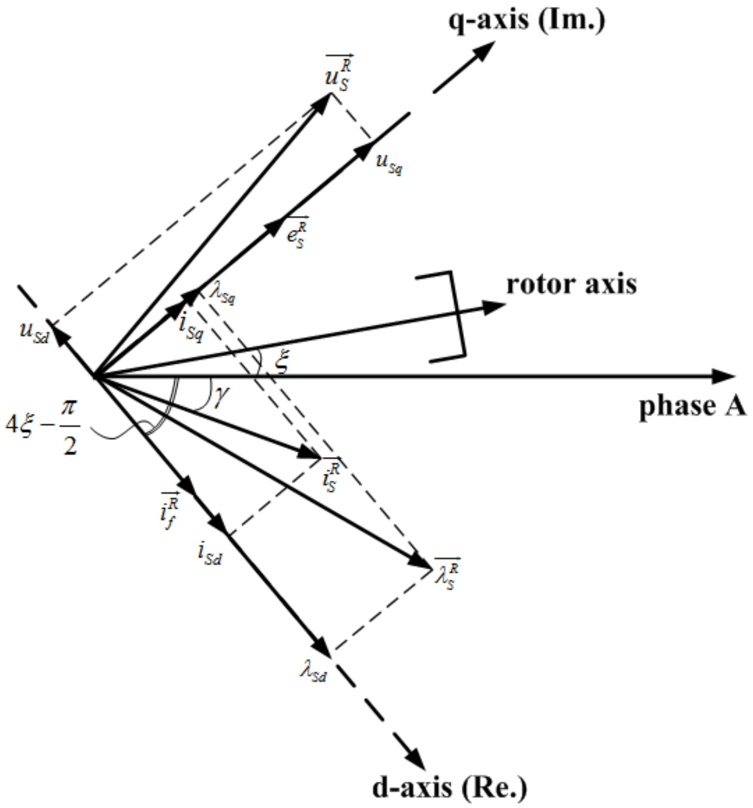
q-axis (Im.)
$\overrightarrow{u_S^R}$
u_{Sq}
$\overrightarrow{e_S^R}$
λ_{Sq}
i_{Sq}
rotor axis
u_{Sd}
ξ
phase A
γ
$4\xi-\frac{\pi}{2}$
$\overrightarrow{i_S^R}$
$\overrightarrow{i_f^R}$
i_{Sd}
$\overrightarrow{\lambda_S^R}$
λ_{Sd}
d-axis (Re.)

Fig. 3.11 Field oriented space vector diagram for various machine vectors

The quantities subscripted with d and q represent the direct (real) and quadrature (imaginary) axes components respectively. It is a same approach as Park's Transform. Relations implied in (3.83 – 3.86) are visualised by two axis equivalent circuit diagrams drawn in Fig. 3.12. Field current i_f contributes to the direct axis flux linkage λ_{Sd}, while the quadrature axis flux linkage λ_{Sq} is solely excited by armature current. However the armature main (magnetising) inductance L_{mS} is not entirely linked by field current in d-axis. As shown in Fig. 3.12 (a), the mutual inductance L_{mfa} is only a portion of L_{mS} (which is also reflected in (3.53) and (3.56)). Besides, the field excitation is regarded as a fixed current source controlled by an independent field source as the armature reaction is decoupled from the field circuit.

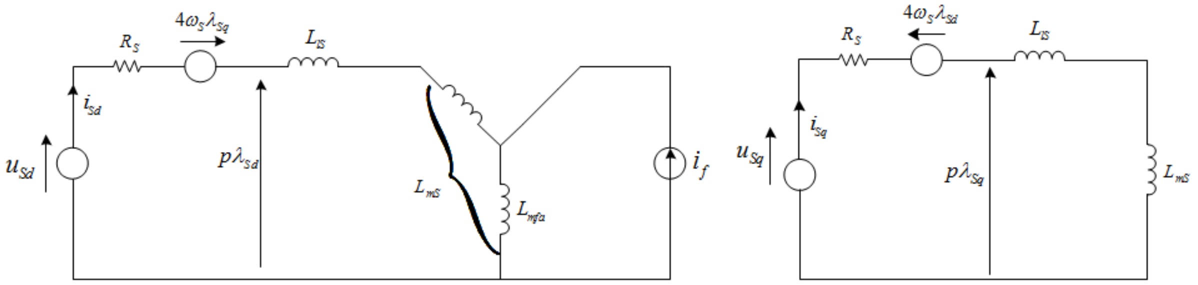
R_S
$4\omega_S\lambda_{Sq}$
L_{lS}
i_{Sd}
u_{Sd}
$p\lambda_{Sd}$
L_{mS}
L_{mfa}
i_f
R_S
$4\omega_S\lambda_{Sd}$
L_{lS}
i_{Sq}
u_{Sq}
$p\lambda_{Sq}$
L_{mS}

(a) (b)

Fig. 3.12 Equivalent circuit diagrams for (a) d-axis and (b) q-axis

Aside from the analysis of electromagnetics, the mechanics of machine is also important as both electromagnetic and mechanical behaviours of an electrical machine are closed bonded. The total instantaneous electrical power p_{elec} is the sum of total input electrical power at any instant, and the instantaneous electrical energy dW_{elec} is therefore the total electrical power in an infinitesimal time dt. Hence

$$p_{elec} = u_A i_A + u_B i_B + u_C i_C + u_f i_f = \frac{2}{3} Re\left\{\overline{u_S^{R*}} \cdot \overline{i_S^R}\right\} + u_f i_f \tag{3.87}$$

And

$$dW_{elec} = p_{elec} dt \tag{3.88}$$

By solving (3.78), (3.80), (3.87) and (3.88) together,

$$\begin{aligned} dW_{elec} = {} & \underbrace{\left(\frac{2}{3} i_S^2 R_S + i_f^2 R_f\right)}_{ohmic-loss} dt + \underbrace{\left(\frac{2}{3} Re\left\{\overline{i_S^R} \cdot p\overline{\lambda_S^{R*}}\right\} + L_f \frac{di_f^2}{dt}\right) dt}_{energy-storage} \\ & + \underbrace{\left(\frac{2}{3} Re\left\{-j4\omega_S \overline{\lambda_S^{R*}} \cdot \overline{i_S^R}\right\}\right)}_{mechanical-output} dt \end{aligned} \tag{3.89}$$

The input electrical energy dW_{elec} is converted into 3 parts, corresponding to the three terms in (3.89): ohmic loss of all windings, electrical energy for sustaining magnetic field and energy converted as mechanical output dW_{mech}. Therefore the electromechanical torque T_e can be derived from mechanical energy output as

$$dW_{mech} = \frac{2}{3} Re\left\{-j4\omega_S \overline{\lambda_S^{R*}} \cdot \overline{i_S^R}\right\} dt = T_e \omega_S dt \tag{3.90}$$

As a result

$$T_e = \frac{8}{3} Im\left\{\overline{\lambda_S^{R*}} \cdot \overline{i_S^R}\right\} = \frac{8}{3}\left[L_{mfa} i_f i_{Sq} + L_{S2} i_S \sin\left(\gamma + \gamma_0 - 4\xi_0\right)\right] \tag{3.91}$$

It is observed that the electromechanical torque is composed by a steady component and a periodical component oscillating at frequency of $4\omega_S$. The result verifies the prediction of oscillating torque if 2nd harmonic suppression measures are not taken.

In summary, the equations governing the electro-mechanics of hetreopolar inductor machines are summarised and listed in (3.92 – 3.99). The unwanted 2nd harmonic terms are neglected in the equations since they will eventually be eliminated by certain modifications, as discussed in detail in Chapter 4. Equation (3.99) presents rotor mechanical dynamics. The external mechanical load torque is denoted as T_m. Rotor's moment of inertia is J, and D is the rotational friction coefficient due to bearing friction, windage and eddy currents etc.

$$\lambda_{Sd} = L_S i_{Sd} + L_{mfa} i_f \tag{3.92}$$

$$\lambda_{Sq} = L_S i_{Sq} \tag{3.93}$$

$$u_{Sd} = i_{Sd} R_S + p\lambda_{Sd} - 4\omega_S \lambda_{Sq} \tag{3.94}$$

$$u_{Sq} = i_{Sq} R_S + p\lambda_{Sq} + 4\omega_S \lambda_{Sd} \tag{3.95}$$

$$\lambda_f = L_f i_f \tag{3.96}$$

$$u_f = i_f R_f + p\lambda_f \tag{3.97}$$

$$T_e = \frac{8}{3} L_{mfa} i_f i_{Sq} \tag{3.98}$$

$$T_e = T_m + pJ\omega_S + D\omega_S \tag{3.99}$$

A dynamic mathematical model for heteropolar inductor machines, in which quantities are all internally related and linked to each other, is built and graphically plotted in Fig. 3.13. The dynamic model not only provides a foundation of machine simulation, but also aids the analysis and prediction of machine behaviours mathematically under various conditions.

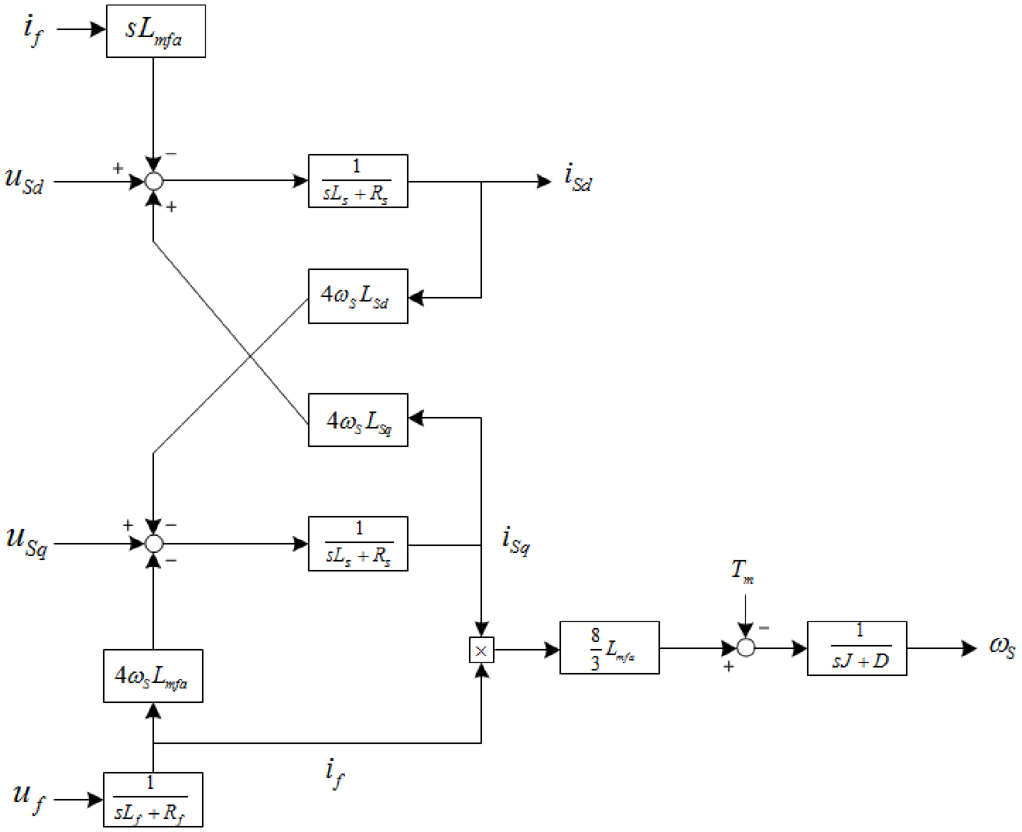
i_f
sL_{mfa}
u_{Sd}
$\frac{1}{sL_s + R_s}$
i_{Sd}
$4\omega_S L_{Sd}$
$4\omega_S L_{Sq}$
u_{Sq}
$\frac{1}{sL_s + R_s}$
i_{Sq}
T_m
$\frac{8}{3} L_{mfa}$
$\frac{1}{sJ + D}$
ω_S
$4\omega_S L_{mfa}$
u_f
$\frac{1}{sL_f + R_f}$
i_f
+
−
×

Fig. 3.13 Mathematical model of heteropolar inductor machine

3.6 Experimentation

3.6.1 Test machine and experiment setup

A test machine is designed and fabricated in order to verify the general theories developed in this chapter. The structure of the practical test machine is different from the conceptual model as in Fig. 3.1 by necessary modifications, yet the principles governing the machine nature remain unchanged.

First of all, the rotor of test machine is not as a square shape as that shown in Fig. 3.1. Instead, an improved rotor shaping exhibiting only fundamental and invariant permeance variations (Λ_0 and Λ_1) is applied to fulfil the third assumption and equation (3.3) in section 3.1. Secondly, test machine stator is of 36 semi-closed slots instead of the 12 completely open slots, for the purpose of reducing potential stator slotting effects. Thirdly, each concentrated coil in Fig. 3.1 is distributed evenly into a coil group consisting of 3 coils to fit in all 36 stator slots. The coils are laid out in a double layer winding structure. Finally, the coil pitch is adjusted in order to eliminate the detrimental 2nd harmonic voltage component induced by armature reaction.

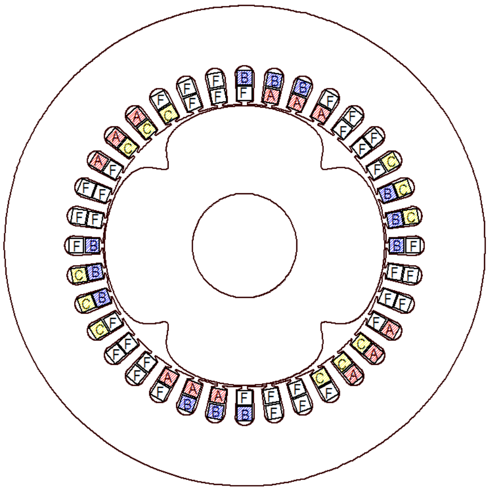

Fig. 3.14

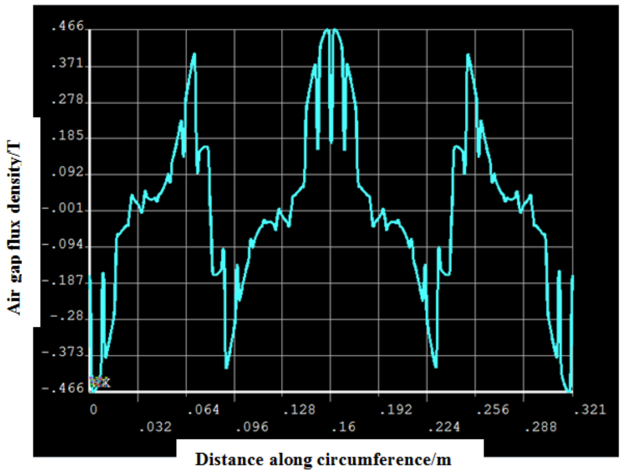

Fig. 3.15

Fig. 3.14 Cross section view of practical test machine with winding configuration highlighted
Fig. 3.15 FEA simulated air gap flux density distribution of test machine

With the practical approaches made, the cross section of test machine is shown in Fig. 3.14 with coil group marked and armature windings colour coded. The modifications make the test machine closer to the ideal conditions assumed, and are advantageous for the machine to gain better performance. Such structural modifications are covered in detail in Chapter 4 by theoretically analysing their influences in depth. Despite, the modifications made to winding structure will inevitably cause differences in machine behaviours compared with the theories developed, which are based on the concentrated winding structure. Such differences can be factorised by winding factors which will be studied in detail and systematically in Chapter 4. Due to the fact that the winding factors only make limited influence on fundamental components (≈ 1), they will be regarded as non-influential at this stage.

The air gap flux density of test machine with 2A field excitation is simulated by FEA in Fig. 3.15. The flux density distribution is similar in shape with the conceptual plot in Fig. 3.5, with slotting harmonics on top.

Test machine specifications and data are listed in Table 1. The test machine is fabricated with steel DR490-50, its magnetic property is attached in Appendix I.

Outer diameter D	170mm	Turns per phase winding N_S	150turns
Bore radius r	51.5mm	Turns per field coil group N_f	75turns
Axial length l	108mm	Rotor mass	9.5kg
Λ_1	0.96×10^{-3}H/m^2	Armature winding resistance R_S	3.2Ω
Λ_0	1.3×10^{-3}H/m^2	Field winding resistance R_f	8Ω

Table 1 Specifications of test machine

The complete test system consists of the test machine, a 2-pole synchronous machine, a DC motor and an in-shaft torque transducer (Torqsense RWT320). The complete system is photographed as shown in Fig. 3.16.

The DC motor and synchronous machine are directly coupled to a single shaft, while the test machine is couple to the same shaft via a 2:1 reduction gear combination, ensuring that both synchronous machine and test machine have a same electrical frequency. The armature windings of test machine are connected to synchronous machine armature. The DC motor functions as a drive to keep the shaft rotating.

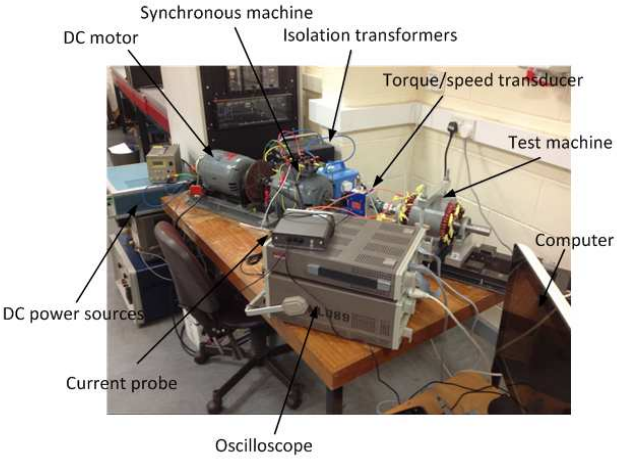
Synchronous machine
DC motor
Isolation transformers
Torque/speed transducer
Test machine
Computer
DC power sources
Current probe
Oscilloscope

Fig. 3.16 Test rig setup

The synchronous machine can be regarded either as a generator that supplies power to the test machine, or as a load that consumes power generated from the test machine. The load angle of the synchronous machine is adjusted by manipulating the gears to lock the two rotors into different relative positions. Similarly the armature current and torque can be adjusted in the same way.

3.6.2 Steady state experiments

The open circuit phase internal emf waveforms are recorded by oscilloscope when the test machine is steadily rotating at 500rpm with different field excitation currents. The recordings are plotted in Fig. 3.17, and as shown, the waveforms are close to proper sinusoid. The results coincide with the theoretical prediction either by (3.8), except that a small portion of slot harmonics is observed on the actual waveforms. It is due to unavoidable permeance fluctuations caused by slot opening and can be eliminated by skewing.

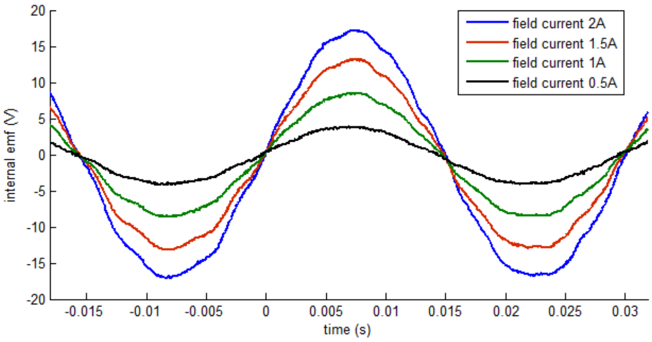

Fig. 3.17

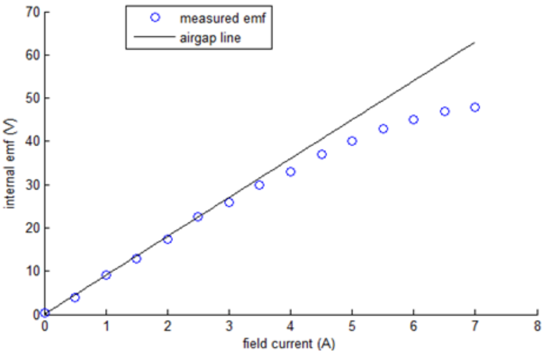

Fig. 3.18

Fig. 3.17 Internal emf waveforms of test machine recorded by oscilloscope with different field excitations
Fig. 3.18 Magnetic curve of test machine

Open circuit magnetic curve is plotted in Fig. 3.18. Field current i_f is increased from 0 to 7A with test machine speed maintained at 500rpm. The air gap line has a slope of 9V/A. The magnetic curve diverges from air gap line when i_f equals to 4A due to steel saturation, and converges to approximately 50V (peak).

The unsaturated magnetising reactance X_{ms} of test machine at 500rpm is 11.72Ω as calculated from (3.53). The estimated leakage reactance is 3.41Ω according to the classical methods [86] for AC machine leakage flux estimation. The total estimated unsaturated synchronous reactance X_S of 14.5Ω is slightly lower than the actual value of 15.7Ω calculated from test machine open circuit and short circuit characteristics. The difference may be due to the differential leakage reactance.

Heteropolar inductor machines are also subject to armature reaction, which modifies the phase terminal voltages when armature currents start conducting. Similar to conventional synchronous machines, the effects of steady state armature reaction can be analysed with the aids of external characteristic curves and V curves. Both series of curves are plotted when the test machine speed is 500rpm and phase terminal voltage is constantly sustained at 18.6V.

The external characteristics are shown in Fig. 3.19. The variations of field currents to maintain a fixed generated terminal voltage are simulated base on steady state model when phases are of different power factors. Practical measurements are taken to compare with the simulation. It is shown that armature currents with lagging and unity power factors tend to demagnetise the magnetic field of test machine as a generator, while armature current with leading power factors tend to help magnetise the test machine.

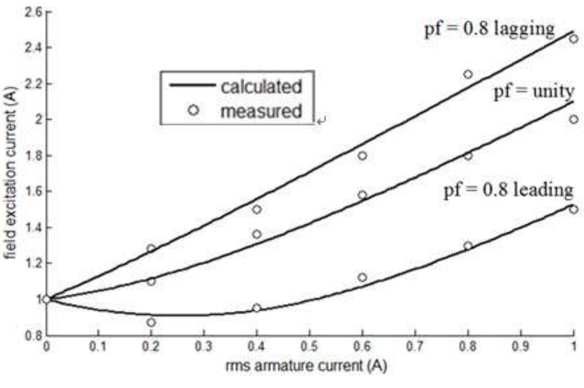

Fig. 3.19

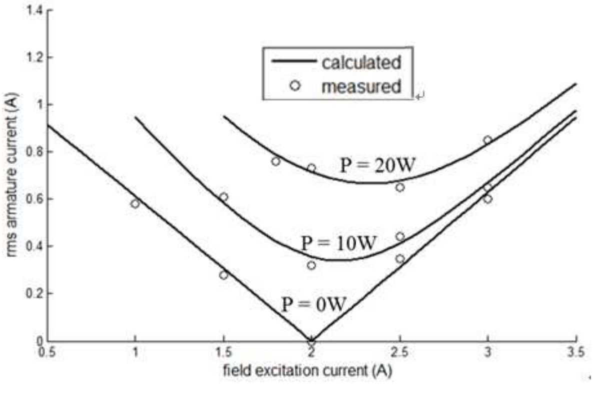

Fig. 3.20

Fig. 3.19 External characteristic of test machine with different power factor
Fig. 3.20 V curve of test machine with different output power

The V curves of the test machine (in generating mode) are simulated with different levels of power outputs, as shown in Fig. 3.20. Corresponding practical measurements prove the validity of simulations. With the increase of field excitation, the armature currents with leading power factor decrease to a minimum and then increase with lagging power factors. The minimum current points are the locus of unity power factor armature current values. An unstable region occurs at leading power factor as the field current is too low to support enough power output.

Both Fig. 3.19 and Fig. 3.20 show a resemblance with conventional synchronous machine characteristics. It is predictable from the space vector analysis as the space vector diagram is analogous to that of conventional synchronous machines. Therefore it validates the statement that heteropolar inductor machines can be regarded as a special case of synchronous machines (referred as armature side excited synchronous machine). In spite of the external properties, however, the electromagnetic properties inside heteropolar inductor machines greatly differ from conventional machines, as analysed in detail in Chapter 4.

The energy conversion starts and electromechanical torque is generated when the test machine is loaded. The relationship between steady state motoring torque and internal power factor angle ψ is explored when the test machine is supplied by 2A field current and 1.2A peak phase current, and fixed at rotation speed of 500rpm. Both predicted and measured torque-angle curves are illustrated in Fig. 3.21.

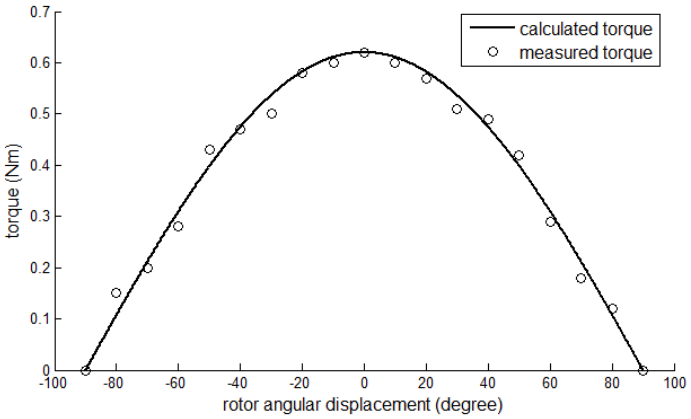

Fig. 3.21 Torque-angle curve of test mahine

It is seen from (3.98) the torque output is a sinusoidal function of load angle ψ. Therefore it is predicted that the torque-angle curve is in a sinusoidal distribution, as verified by practical measurements. The curve in Fig. 3.21 is similar to the torque curve of a non-salient synchronous machine despite the fact the test machine rotor is of salient nature. Moreover the rotor saliency is a vital factor of torque generation since the amount of torque is directly proportional to L_{mfa}, hence Λ_1.

3.6.3 Transient experiments

The transient theories developed are also verified experimentally.

The transient response of field current i_f to a step change in field source voltage u_f is analysed first. The field transient is largely dependent on the variation of field flux linkage λ_f, and the field circuit time constant τ_f is related to field inductance L_f and field resistance R_f, as

$$\tau_f = \frac{L_f}{R_f} \tag{3.100}$$

With the given test machine specifications, τ_f is approximately equal to 29.5ms.

The practical response of field current responding to a 16V step field voltage is captured by oscilloscope as shown in Fig. 3.22, while a theoretical estimation in a same situation is plotted in Fig. 3.23. The field current is measured by a Hall-effect current sensor which converts current signals into voltage signals. The vertical scale of the practical measurement is equivalent to 1 A/div. The duration of transient lasts approximately 144ms as seen from the oscilloscope screen shot. The actual field transient exhibits a characteristic of multi-effective time constants, which flattens the transient current pattern, instead of the single effective time constant shown in the ideal condition in Fig. 3.23.

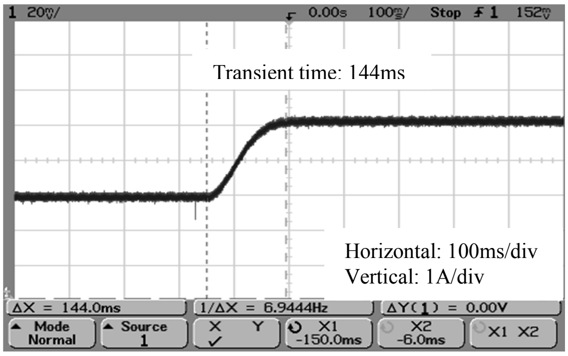

Transient time: 144ms

Horizontal: 100ms/div
Vertical: 1A/div

Fig. 3.22

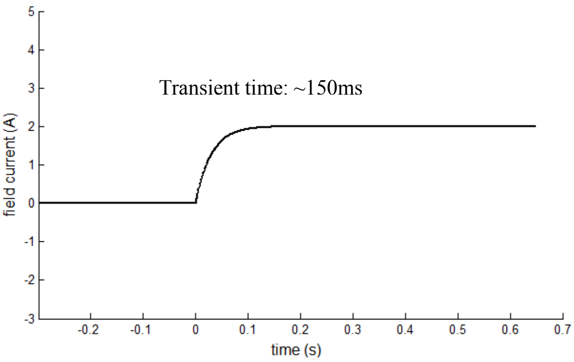

Transient time: ~150ms

Fig. 3.23

Fig. 3.22 Field transient of test machine with a 16V step field voltage recorded by oscilloscope
Fig. 3.23 Simulated field transient with a 16V step field voltage

Three phase sudden short circuit, a classical transient scenario, is also investigated for the test machine. Initially the test machine is driven at 500rpm and supplied with 2A field current. Three phase winding terminals are then shorted simultaneously at a specific instant. The waveform of phase A current and field current during the transient are captured by oscilloscope and shown in Fig. 3.24. The vertical scale for phase current is 1A/div.

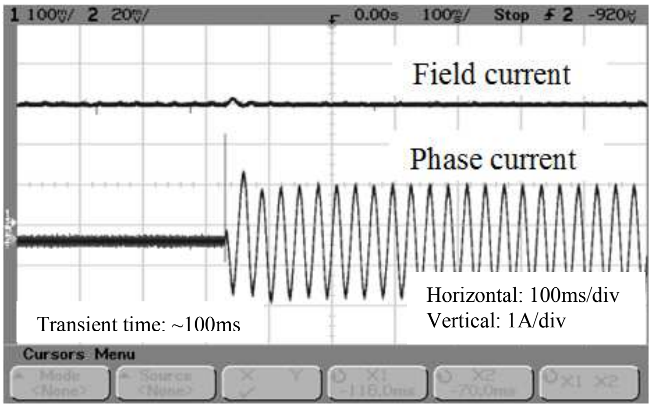

Fig. 3.24 Armature and field transients of three phase balanced shorting recorded by oscilloscope

A clear transient is observed on the phase current waveform since the waveform transitions from an offset sinusoid to a steady non-offset one. Hence the transient phase current is solely composed by a decaying DC component and a steady state short circuit component. Different from transients in conventional synchronous machines, there is no transient current component on phase current. It is due to the fact that the field circuit flux linkage is not influenced by phase winding transients, as shown in (3.96), and therefore the 'transient reactance' is not applicable. The decoupling of field and armature circuits is also proven by the recorded field current trace. The field current maintains constant without notable fluctuations influenced by armature transient, except that a slight ripple appears at the very moment of transient. The ripple occurs because of the heavy local saturation in material due to high level of armature currents at the instant of short circuit.

The DC offset at the short circuit point attempts to restore the phase flux linkage to its initial value just before short circuit occurs. The offset decays exponentially as time elapses and the decay rate is determined by phase time constant τ_S, as in (3.101), and τ_S of the test machine is 23.4ms.

$$\tau_S = \frac{L_S}{R_S} \tag{3.101}$$

It is common knowledge that the transient DC current component depends greatly on the rotor position, i.e. internal emf value, at the instant of short circuit. The offset is the greatest when internal emf is zero since phase flux linkage is maximal at the instant. On the contrary, the offset is zero when phase flux linkage is zero and internal emf reaches maximum.

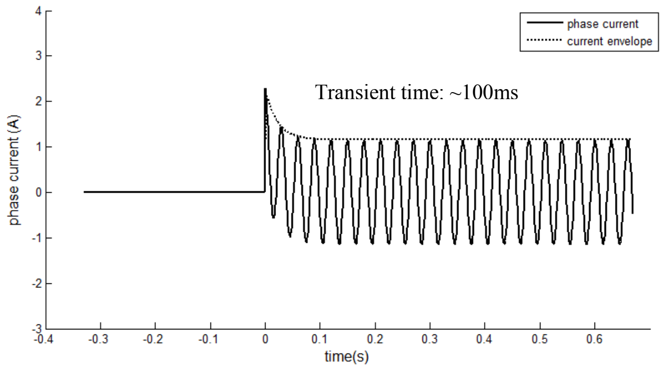

Fig. 3.25

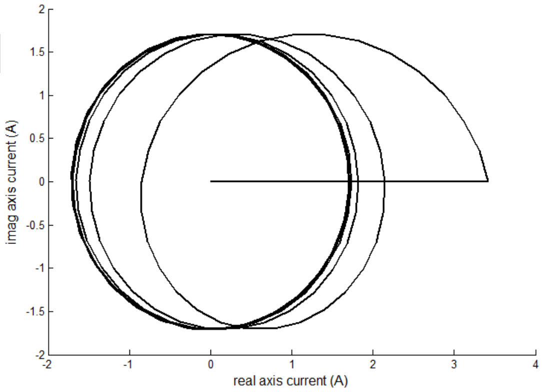

Fig. 3.26

Fig. 3.25 Simulated phase current waveform and envelope during three phase balanced shorting when initial flux linkage is maximum

Fig. 3.26 Simulated phase current locus during three phase balanced shorting when initial flux linkage is maximum

Fig. 3.25 and Fig. 3.26 plots the simulated phase short circuit transient when the flux linkage is maximum before shorting, and the locus of phase current vector $\overrightarrow{i_S}$ in complex plane, respectively. The envelope of current waveform signifies the decay of transient DC current component. Same as practical measurements, the AC current component is always its steady state without transient. From the point of view of Fig. 3.26, the decay of DC offset is represented by the horizontal shift of $\overrightarrow{i_S}$ locus leftwards to the centre of complex plane.

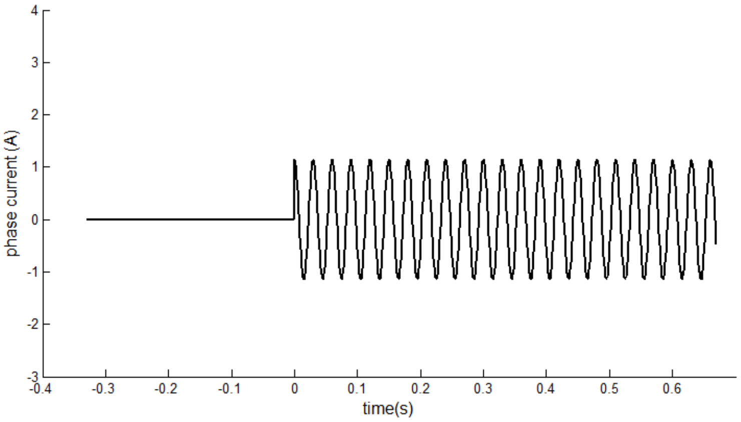

Fig. 3.27

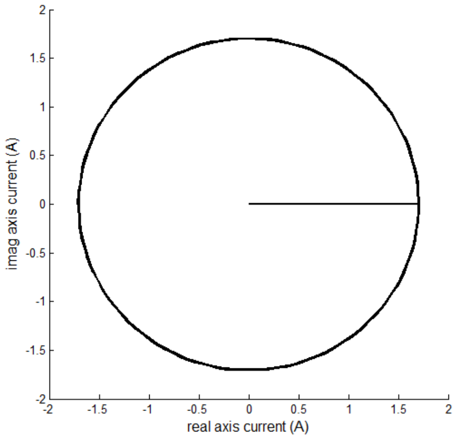

Fig. 3.28

Fig. 3.27 Simulated phase current waveform and envelope during three phase balanced shorting when initial flux linkage is zero

Fig. 3.28 Simulated phase current locus during three phase balanced shorting when initial flux linkage is zero

Similarly, the predicted phase current waveform and its locus when the flux linkage of a phase is zero before shorting are plotted in Fig. 3.27 and Fig. 3.28 respectively. Since no initial flux linkage is to be sustained, the DC transient current disappears and phase current transitions direct between two steady states without transient process. The smooth transition without transient is also observed in Fig. 3.28 as a steady state current vector is formed instantly after short circuit.

The situation of sudden loading on test machine is experimented. The test is performed by applying a step external load of 0.57Nm to the test machine operating at a specific instant. Test machine speed and field excitation are fixed at 500rpm and 2A respectively. The rotor inertia is estimated from its mass and is approximately 0.0126kg·m^2. The damping torque factor is estimated by [87]. The electromechanical torque reacting to the sudden loading is recorded by the torque transducer. The duration of recording is approximately 8s and shown in Fig. 3.29.

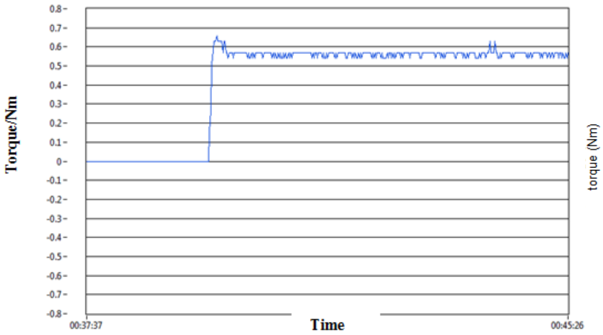

Fig. 3.29

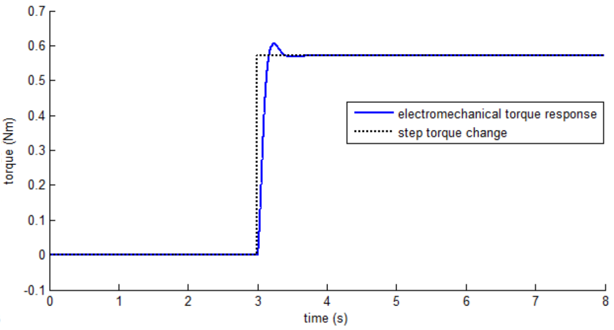

Fig. 3.30

Fig. 3.29 Electromechanical torque of test machine in response to 0.57Nm sudden loading recorded by torque transducer

Fig. 3.30 Simulated electromechanical torque in response to 0.57Nm step external torque

It is observed that a counteracting electromechanical torque is created instantly when the external torque is exerted. The torque recording displays an overshoot as the system is underdamped. The practical measurement is well predicted by simulation based on machine dynamic model, as plotted in Fig. 3.30. Moreover, the phase current waveform of phase A during the sudden loading transient is also recorded by oscilloscope and is shown in Fig. 3.31. Oscilloscope vertical scale is 1A/div and the capture lasts for 1s. The phase current response is also simulated by the mathematical model and is compared in Fig. 3.32.

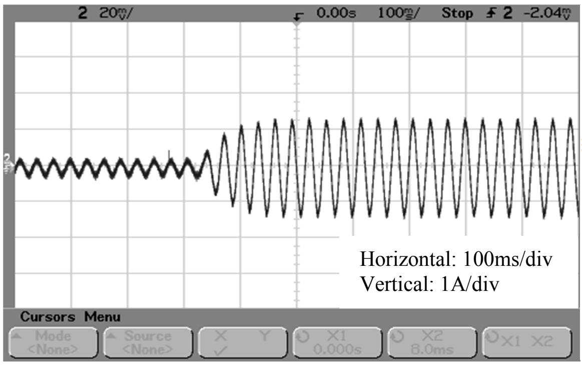
2 20mV/
0.00s 100ms/ Stop 2 -2.04mV
Horizontal: 100ms/div
Vertical: 1A/div
Cursors Menu
Mode <None>
Source <None>
X Y
X1 0.000s
X2 8.0ms
X1 X2

Fig. 3.31

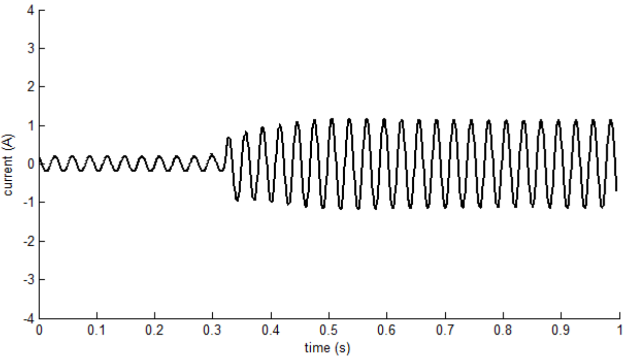

Fig. 3.32

Fig. 3.31 Phase current waveform in response to 0.57Nm external loading recorded by oscilloscope
Fig. 3.32 Simulated phase current waveform in response to 0.57Nm external loading

3.7 Summary and discussion

Both steady state and dynamic theories for three phase heteropolar inductor machine are developed in this chapter. The theories are developed on the basis of machine air gap permeance waves and several ideal assumptions are made to facilitate the mathematics.

The derivation of steady state theory takes advantages of different methods: the calculation of induced internal emf is based on Faraday’s Law, armature reaction is analysed from two-reaction theory, and the expression of steady state torque is derived from the point of view of energy conversion. The existence of 2nd harmonic in machine is addressed. Also, the expressions for armature reaction reactance and electromechanical signifies the resemblance to non-salient synchronous machine.

The transient theory is mainly developed by space vector and two axis theories. Dynamic space vector equations representing flux linkages, phase voltages and torque are illustrated in relation to various types of machine inductances. The space vectors are decomposed into two axes for field orientation. The parameters affecting unwanted 2nd harmonic are discussed, and the necessity of elimination is addressed. Two axis equivalent circuit diagrams and dynamic machine model are presented. The properties of field windings are also studied.

Test machine is fabricated with reasonable modifications to meet idealised assumptions. Experiments for theory verifications cover steady state internal emf and open circuit characteristic, external characteristics, synchronous reactance, torque angle relationship, field circuit transient, armature circuit transient and transient loading. The experimental results show good agreement with theoretical predictions.

The heteropolar inductor machine analysed in this project is a three phase machine, and it is possible to increase the number of phases. The application of multi-phase windings has certain advantages such as reduced harmonic components, improved torque profile and enhanced fault tolerance capability, etc. The space vector theory is still applicable to multi-phase systems as long as the spatial displacements are adjusted accordingly.

Other than space vector method applied in analysis, the dynamic machine theory can also be achieved by different approaches, including two-axis theory, lumped circuit model, and numerical magnetic field analysis. All the methods are able to satisfactorily solve machine transient behaviours and are internally inter-linked. The reason for selecting space vector theory is that the method commonly acts as a foundation of vector control, and also because of the physical clearness of the model.

Chapter 4: Design

4.1 Stator and rotor slot combinations

It is seen that unlike conventional AC electrical machines, heteropolar inductor machines have a special mechanism for field emf induction. The field magnetic flux density distribution is resulted from the co-effect of varying air gap permeance and the alternatively reversed field mmf, as described in Chapter 3. Obviously the number of rotor saliencies plays a significant role in magnetic density variation, and it is discovered that it cannot be chosen randomly. J H Walker discussed the topology with four rotor saliencies [34] while P K Dash reported that seven rotor saliencies are also feasible [55]. However, it is meaningful to mathematically explore the influence of different number of rotor saliencies on armature emf induction. This section discusses the possible numbers of rotor saliencies that lead to balanced three phase flux linkage swing in three phase armature windings.

Same as in Chapter 3, the very basic stator structure with 12 stator slots is analysed. The basic stator structure in a linear form is plotted in Fig. 4.1.

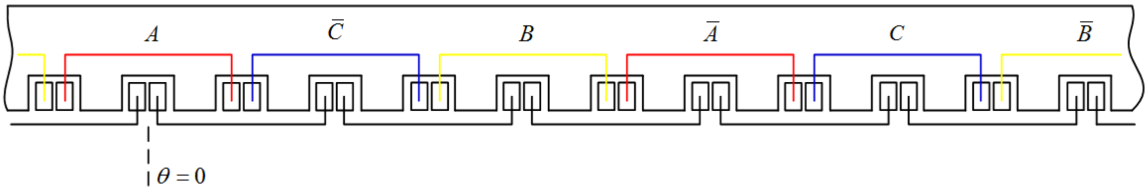

Fig. 4.1 Short pitched armature winding configuration

In Fig. 4.1, the armature and field coils are all of the same coil pitch, i.e. $\pi/3$ mechanical radian along bore circumference. However different armature winding configurations with longer armature coil pitches are also available, by extending the return coil side to the next available armature winding slot. Another two possible armature winding layouts are shown in Fig. 4.2 and Fig. 4.3.

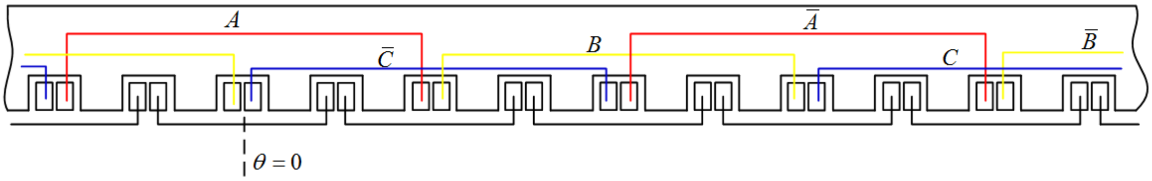

Fig. 4.2 Middle pitched armature winding configuration

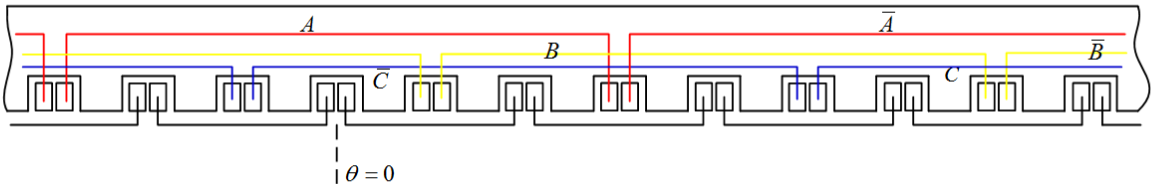

Fig. 4.3 Long pitched armature winding configuration

The armature coils in Fig. 4.2 and Fig. 4.3 span $2\pi/3$ and π respectively. For convenience, the armature coil in Fig. 4.1 is regarded as 'short pitched coil', while the armature coils shown in Fig. 4.2 and Fig. 4.3 are named as 'middle pitched coil' and 'long pitched coil' respectively. Phase A winding axes in all 3 cases are defaulted as the stator reference axes.

The number of rotor saliencies (or slots) is denoted as p. It is straightforward that the fundamental permeance variation thus has $2p$ poles per bore circumference. For simplicity of calculation, the assumptions made in the end of section 3.1 still persist and one of the rotor saliencies is initially aligned to reference axis in all 3 cases. The spatial air gap permeance with random number of rotor saliencies is mathematically expressed as

$$\Lambda(\theta) = \Lambda_0 + \Lambda_1 \cos p(\theta - \omega_S t) \tag{4.1}$$

Three phase internal emfs are calculated through the same approach as for (3.8). As a result, the phase internal emfs induced when the armature windings are long pitched are

$$e_{A(long)} = -\left(\cos\frac{\pi p}{2} - 2\cos\frac{\pi p}{3} + 1\right) \cdot 2\omega_S N_S N_f i_f \Lambda_1 rl \cos\left(p\omega_S t - \frac{\pi p}{2}\right) \tag{4.2}$$

$$e_{B(long)} = -\left(\cos\frac{\pi p}{2} - 2\cos\frac{\pi p}{3} + 1\right) \cdot 2\omega_S N_S N_f i_f \Lambda_1 rl \cos\left(p\omega_S t - \frac{7\pi p}{6}\right) \tag{4.3}$$

$$e_{C(long)} = -\left(\cos\frac{\pi p}{2} - 2\cos\frac{\pi p}{3} + 1\right) \cdot 2\omega_S N_S N_f i_f \Lambda_1 rl \cos\left(p\omega_S t - \frac{5\pi p}{6}\right) \tag{4.4}$$

Internal emfs induced in middle pitched armature windings are

$$e_{A(middle)} = \left(\sin\frac{\pi p}{3} - 2\sin\frac{\pi p}{6}\right)\cdot 2\omega_S N_S N_f i_f \Lambda_1 rl \sin\left(p\omega_S t - \frac{\pi p}{3}\right) \tag{4.5}$$

$$e_{B(middle)} = \left(\sin\frac{\pi p}{3} - 2\sin\frac{\pi p}{6}\right)\cdot 2\omega_S N_S N_f i_f \Lambda_1 rl \sin\left(p\omega_S t - \pi p\right) \tag{4.6}$$

$$e_{C(middle)} = \left(\sin\frac{\pi p}{3} - 2\sin\frac{\pi p}{6}\right)\cdot 2\omega_S N_S N_f i_f \Lambda_1 rl \sin\left(p\omega_S t - \frac{5\pi p}{3}\right) \tag{4.7}$$

Internal emfs induced in short pitched armature windings are

$$e_{A(short)} = \left(1 - \cos\frac{\pi p}{6}\right)\cdot 2\omega_S N_S N_f i_f \Lambda_1 rl \cos\left(p\omega_S t - \frac{\pi p}{6}\right) \tag{4.8}$$

$$e_{B(short)} = \left(1 - \cos\frac{\pi p}{6}\right)\cdot 2\omega_S N_S N_f i_f \Lambda_1 rl \cos\left(p\omega_S t - \frac{5\pi p}{6}\right) \tag{4.9}$$

$$e_{C(short)} = \left(1 - \cos\frac{\pi p}{6}\right)\cdot 2\omega_S N_S N_f i_f \Lambda_1 rl \cos\left(p\omega_S t - \frac{3\pi p}{2}\right) \tag{4.10}$$

Equations (4.2 – 4.4), (4.5 – 4.7) and (4.8 – 4.10) correspond to the three phase internal emf equations for winding layouts shown in Fig. 4.3, Fig. 4.2 and Fig. 4.1 respectively, with number of rotor saliency equal to p. Certain similarities are shared in (4.2 – 4.10). The electrical frequency of internal emfs is p times the rotor mechanical frequency. The number p not only links the ratio between electrical and mechanical frequency directly, but also influences the phase displacement of emfs induced in three phase windings. A key criterion of selecting appropriate values for p is to ensure that three phases are balanced, i.e. all electrical quantities are $2\pi/3$ displaced in time. Moreover, the scaling terms for emf magnitudes are also determined by p. The multiplicative scaling factors for emf magnitudes (those terms embraced in brackets) are denoted as following denotations.

$$Mag_{long} = \cos\frac{\pi p}{2} - 2\cos\frac{\pi p}{3} + 1 \tag{4.11}$$

$$Mag_{mid} = \sin\frac{\pi p}{3} - 2\sin\frac{\pi p}{6} \tag{4.12}$$

$$Mag_{short} = 1 - \cos\frac{\pi p}{6} \tag{4.13}$$

The significance of p is explicit, as it is the very determinative factor for electrical frequency and phase separation, as well as a measure of internal emf magnitude. Possible numbers of p that balance three phases up to 22 are listed in Table 1 for all three cases, together with values of magnitude scalers. p_{long}, p_{mid} and p_{short} correspond to the feasible values of p in long pitched, middle pitched and short pitched windings respectively.

p_{long}	Mag_{long}	p_{mid}	Mag_{mid}	p_{short}	Mag_{short}
4	3	4	$\frac{3\sqrt{3}}{2} \approx 2.6$	4	1.5
-	-	7	$\frac{2+\sqrt{3}}{2} \approx 1.866$	7	$\frac{2+\sqrt{3}}{2} \approx 1.866$
10	1	10	$\frac{\sqrt{3}}{2} \approx 0.866$	10	0.5
-	-	13	$\frac{2-\sqrt{3}}{2} \approx 0.134$	13	$\frac{2-\sqrt{3}}{2} \approx 0.134$
16	3	16	$\frac{3\sqrt{3}}{2} \approx 2.6$	16	1.5
-	-	19	$\frac{2+\sqrt{3}}{2} \approx 1.866$	19	$\frac{2+\sqrt{3}}{2} \approx 1.866$
22	1	22	$\frac{\sqrt{3}}{2} \approx 0.866$	22	0.5

Table 4.1 Available rotor saliency numbers for balanced three phase with corresponding magnitude scalers for three winding configurations

As shown in Table 4.1, the minimum number of rotor saliencies is 4 for balanced three phase system and the choices of available values of p are more limited in the case of long pitched winding. Different values of p lead to different emf magnitudes and the variation of the magnitudes is periodical with the increase of p. Generally the armature winding emf magnitudes are higher with longer coil pitches. It is due to the fact that coils with longer pitches embrace more air gap area and experience greater flux swings. Nevertheless it is at the cost of longer end turns.

The above analysis are based on a 'unit machine', i.e. the heteropolar inductor machine with 12 stator slots and 1 set of balanced three phase armature windings. A unit machine is a balanced machine structure that has a minimum number of repetitiveness of windings, magnets and electrical cycles. Unit machine is often used in finite element analysis to build electrical machine models. It is consequently feasible to construct other machine structures by combining multiple unit machines. For example, a heteropolar inductor machine with 24 stator slots, 8 rotor slots and 2 sets of armature windings is applicable, as it is derived from repeating a unit machine twice along the bore circumference.

A K Das Gupta also demonstrated the variety of choices of rotor teeth numbers. However the analysis and conclusion were not complete and generalised [58].

4.2 Winding factors and winding configurations

4.2.1 Distributed windings and distribution factor

The machine structures discussed in theories so far are equipped with concentrated windings. Regardless of the various possible rotor structures, the stator armature winding of each phase only consists of as many coils as the number of armature poles. The same winding configuration applies to field windings as well, considering the fact that each flux reversal is only effected by a single field coil.

As already discussed in previous section, the increase of stator slots can be realised by repeating the unit machine stator structure on stator periphery, with the increased rotor saliencies by a same repetition factor. On the other hand, the increase of stator slots can be achieved by applying distributed windings [57]. This is done by separating concentrated winding coils into a number of smaller and evenly placed coils. An illustrative distributed winding unit machine stator structure with each original coil replaced by two is shown in Fig. 4.4.

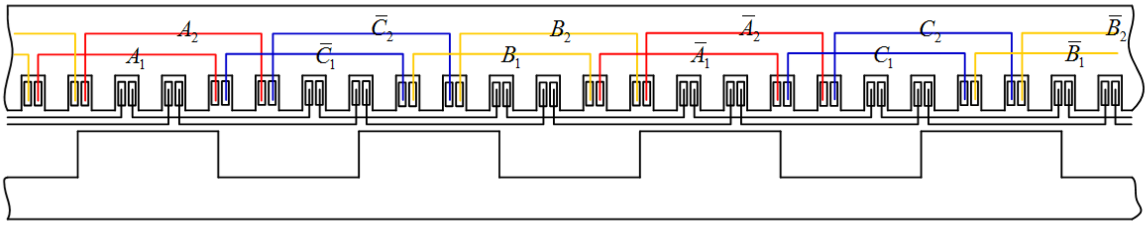

Fig. 4.4 Short pitched distributed windings with 2 coils per coil group

The original concentrated windings can also be distributed by higher factors, e.g. 3 or 4, depending on the design requirements. Distributed windings possess several advantages over concentrated winding.

(1) Distributed windings refine both internal emf and armature reaction mmf wave, suppressing harmonics and making waveforms more sinusoidally distributed.

(2) More effective cooling capability is offered by distributed windings as conductors are more evenly distributed along stator periphery.

(3) The stator core space is fully utilised by applying distributed windings.

Distributed armature windings modulate the flux linkage of each phase by suppressing each harmonic component with a distribution factor. Also the influence of distribution factor is regarded as reducing the effective winding turns for different harmonics.

The phase armature reaction voltage is induced by three phase resultant two-pole armature reaction mmf wave, and the relevant distribution factor is calculated in the same way as in conventional AC machines.

$$k_{dv}^{'} = \frac{\sin\left(q\frac{\nu\alpha'}{2}\right)}{q\sin\left(\frac{\nu\alpha'}{2}\right)} \tag{4.14}$$

The armature reaction winding distribution factor k_d' acts differently to different harmonic indices, and is a function of total number of coils per phase winding q and the electrical angular displacement between each coil α'. The angular displacement α' is calculated by considering the pole number of armature reaction wave.

Unlike armature reaction voltage, the induction of internal emf in heteropolar inductor machines is of a completely different mechanism. However, the armature distribution factor for internal emfs is still calculated as the ratio of emf induced in distributed winding to that in concentrated counterpart. Internal emf winding distribution factor is

$$k_{dv} = \frac{2}{3} + \frac{\sin\left(q\frac{\nu\alpha}{2}\right)}{3q\sin\left(\frac{\nu\alpha}{2}\right)} \tag{4.15}$$

The coil angular displacement α in (4.15) is calculated by considering the pole number of magnetic permeance variation. The distribution factor for internal emf k_d in heteropolar inductor machines, as seen, is somewhat ‘weaker’ than that in conventional AC machines, as only 1/3 of total induced emf is modulated. The factor also varies for different harmonics.

4.2.2 Pitch factor

Three possible armature winding configurations are proposed according to different coil pitches as presented before. Obviously the magnitude of internal emf in phase windings is influenced by the choice of coil pitches, as shown in Table 1. The magnitude of armature reaction voltage is also affected by armature coil pitch variations. Generally the coil pitch of armature windings influences the voltage induction by changing the integration area of magnetic flux, hence flux linkage. Such an effect is effectively regarded as a reduction of armature winding turns by a winding pitch factor.

Similar to winding distribution factor, the pitch factor for the armature reaction effect is identical to the case of conventional AC machines.

$$k'_{p\nu} = \sin\left(\frac{\nu y'}{2}\right) \tag{4.16}$$

The coil pitch length y' in (4.16) is in the form of electrical radian by considering the pole number of armature reaction mmf wave.

The pitch factor for internal emfs can also be explained by (4.16) despite the different mechanism of voltage induction. The effect of internal emf pitch factor is regarded as scaling the magnitude scaler of long pitched winding Mag_{long}. Different from $k'_{p\nu}$, the emf pitch factor is considered from the point of view of air gap permeance pole numbers. Also, a phase reversal must be added when two coil sides belong to reversed flux areas. The expression of internal emf winding pitch factor is

$$k_{p\nu} = \begin{cases} \sin\left(\dfrac{\nu y}{2}\right), flux-non-reversal \\ \sin\left[\dfrac{\nu\left(y+\pi\right)}{2}\right], flux-reversal \end{cases} \tag{4.17}$$

An example is made for a 12/4 unit machine structure. In the case of long pitched winding, the armature coil span is half of the stator bore circumference, i.e. π in mechanical radian. Correspondingly, the coil pitch in electrical angle is 4π since the rotor indicates an 8 pole structure. It is noted the field flux orientation is reversed at each coil side. Hence it is considered by adding an additional electrical angle π to the actual coil pitch. Therefore k_p for fundamental (ν=1) wave is 1 according to (4.17).

The pitch factor for middle pitched winding is calculated in the same manner, but without considering the flux reversal since the opposite coil sides are under a same direction of flux. The pitch is shortened by 1/3 and hence has a value of $8\pi/3$ in electrical angle. The corresponding k_p equals to $\sqrt{3}/2$ for fundamental wave, which also indicates the relationship between Mag_{mid} and Mag_{long}.

$$Mag_{mid} = \frac{\sqrt{3}}{2} Mag_{long} \tag{4.18}$$

Further, the short pitched windings are regarded as having a $4\pi/3$ pitch plus an additional π for the reversal of field flux. As a result, k_p for short pitched windings is 1/2 from (4.17). The relationship between Mag_{short} and Mag_{long} is

$$Mag_{mid} = \frac{1}{2} Mag_{short} \tag{4.19}$$

The relations shown in (4.18) and (4.19) can be generalised to machines with any other feasible rotor pole numbers, and it is verified by the data in Table 1.

Winding distribution factor and winding pitch factor are usually combined as a winding factor. Armature emf winding factor and armature reaction winding factor are defined in (4.20) and (4.21) respectively.

$$k_{dp\nu} = k_{d\nu} k_{p\nu} \tag{4.20}$$

$$k'_{dp\nu} = k'_{d\nu} k'_{p\nu} \tag{4.21}$$

Appropriate managements of winding factors can help suppress or eliminate certain unwanted harmonic components.

The reactance and inductance definitions introduced in Chapter 3 can be reformed with the inclusion of winding factors discussed in this section. The steady state armature reaction reactance (3.25) can be written as

$$X_{ad} = X_{aq} = 6\sqrt{2}\omega_S k'^2_{dp1} N_S^2 r l \Lambda_0 \tag{4.22}$$

Also, (3.53 – 3.56) can be rewritten as

$$\frac{1}{3}L_{mS}=\frac{k_{dp1}^{'2}N_S^2}{2}lr\Lambda_0 \tag{4.23}$$

$$\frac{1}{3}L_{mS2}=\frac{k_{dp1}^{'}k_{dp5}^{'}N_S^2}{20}lr\Lambda_1 \tag{4.24}$$

$$\frac{1}{3}L_{mS0}=\frac{k_{dp1}^{'}k_{dp3}^{'}N_S^2}{12}lr\Lambda_1 \tag{4.25}$$

$$\frac{1}{3}L_{mfa}=\frac{3}{4}k_{dp1}N_SN_flr\Lambda_1 \tag{4.26}$$

4.2.3 Elimination of second time harmonic

Despite the very importance of fundamental air gap permeance variation in emf induction and torque generation etc. in heteropolar inductor machines, certain serious side effects are also associated with the permeance swing. Analysis in Chapter 3 has theoretically demonstrated the detrimental influences led by the reaction of armature reaction and air gap permeance. For instance, a substantial 5th harmonic air gap magnetic density traveling wave caused by armature reaction tends to induce a 2nd armature reaction voltage component, as expressed mathematically in (3.16). The resulted second harmonic armature currents from second harmonic voltages, in turn, lead to a periodically oscillating electromechanical torque, as seen from (3.91). Therefore, necessary measures to suppress the second voltage harmonic to an acceptable level must be applied.

It is demonstrated that the second harmonic voltage component is strongly linked to the second harmonic main armature reaction inductance L_{mS2}.

$$L_{mS2}=\frac{3}{20}k_{dp1}^{'}k_{dp5}^{'}N_S^2lr\Lambda_1 \tag{4.27}$$

The decrease of L_{mS2} by decreasing fundamental permeance variation Λ_1 is not practically feasible, since the reduction will inevitably compromise the overall machine performance. Therefore, the only possible way to achieve the goal is by nulling the winding factor.

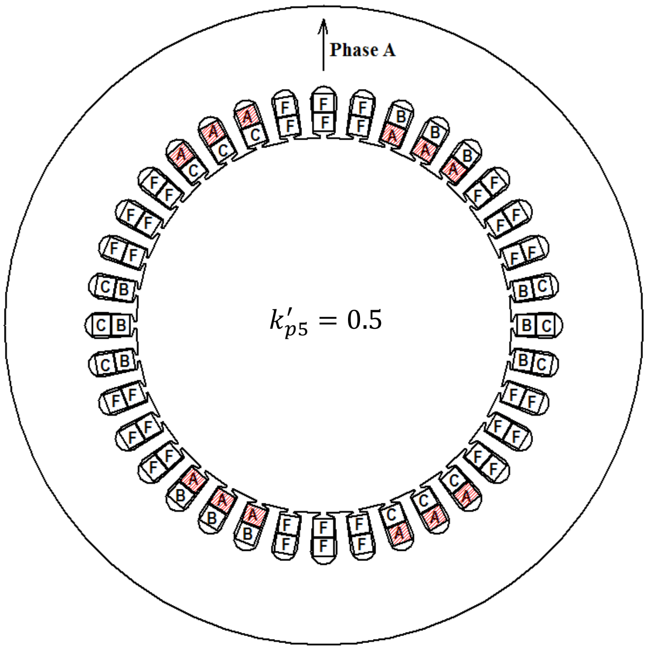
Phase A
$k'_{p5} = 0.5$

Fig. 4.5

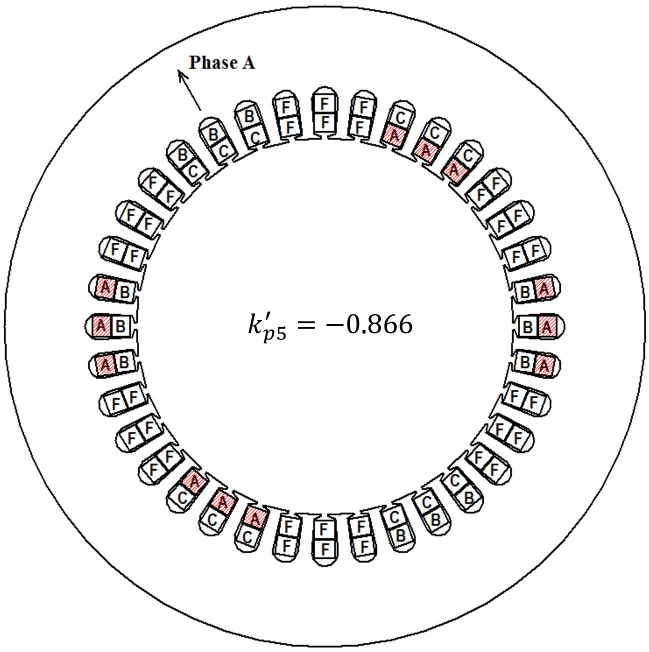
Phase A
$k'_{p5} = -0.866$

Fig. 4.6

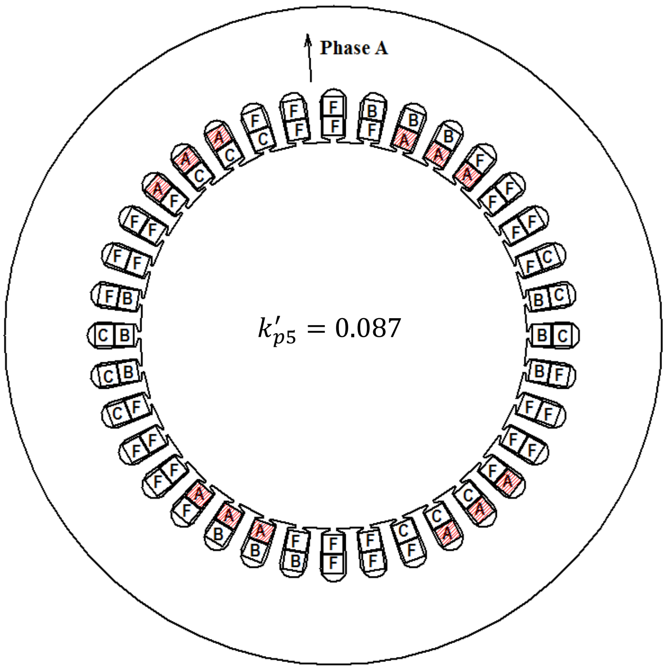
Phase A
$k'_{p5} = 0.087$

Fig. 4.7

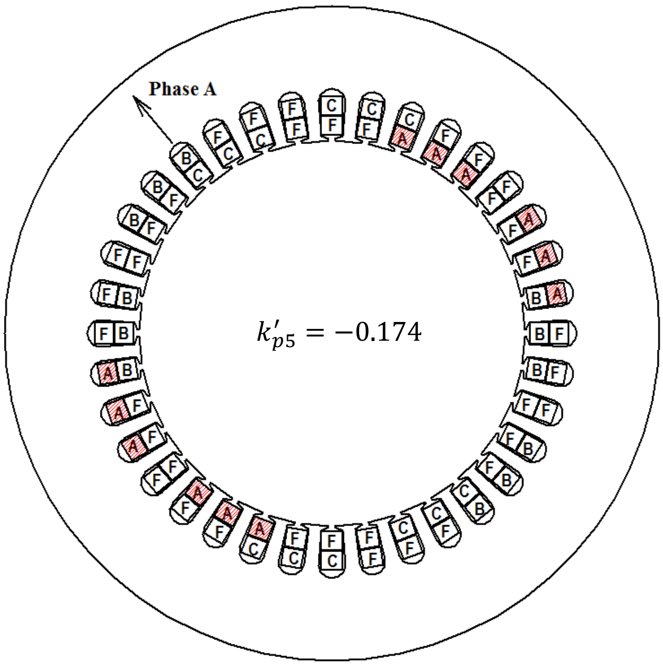
Phase A
$k'_{p5} = -0.174$

Fig. 4.8

Fig. 4.5 Short pitched stator winding configuration without 2nd harmonic suppression
Fig. 4.6 Middle pitched stator winding configuration without 2nd harmonic suppression
Fig. 4.7 Short pitched stator winding configuration with 2nd harmonic suppression by pitch adjustment
Fig. 4.8 Middle pitched stator winding configuration with 2nd harmonic suppression by pitch adjustment

As discussed, the second voltage harmonic is resulted by a 10-pole (i.e. 5th harmonic) armature reaction magnetic flux density wave. Hence it is key to select an appropriate armature coil pitch length such that 5th space harmonic is reasonably suppressed for inducing time harmonics. In other words, it is ideal that k'_{p5} is equal to zero.

The nulling of k'_{p5} may be approached by different winding design schemes. In this project, the structure of heteropolar inductor machine consists of a stator with 36 semi-closed slots equipped with distributed windings and a rotor with 4 saliencies. The distributed short pitched and middle pitched winding configurations are shown in Fig. 4.5 and Fig. 4.6 respectively with the values of k'_{p5}. As a comparison, the suppression of 2nd harmonic is achieved by extending the original coil pitches, as shown in Fig. 4.7 and Fig. 4.8.

In Fig. 4.7, the upper layer of the double layer winding is shifted by 1 stator slot, while it is shifted by 2 stator slots in Fig. 4.8. The suppression effect is considerable as k'_{p5} is reduced by more than 80 per cent.

The distributed nature of stator windings in the machines will also introduce the modulation effect of winding distribution factor. However the emf and voltage magnitudes considering distribution factor is not substantially different from those in the case of concentrated windings.

Due to the internal relevancy in machine theories, the machine with the stator structure as in Fig. 4.7 is selected for further investigations in this project. Its planar stator winding layout is illustrated in Fig. 4.9. The winding layout is similar to those of conventional AC machines equipped with lap coils. Each phase winding consists of a pair of series-connected distributed coil groups. Field winding, on the other hand, consists of six series-connected distributed coil groups as already introduced.

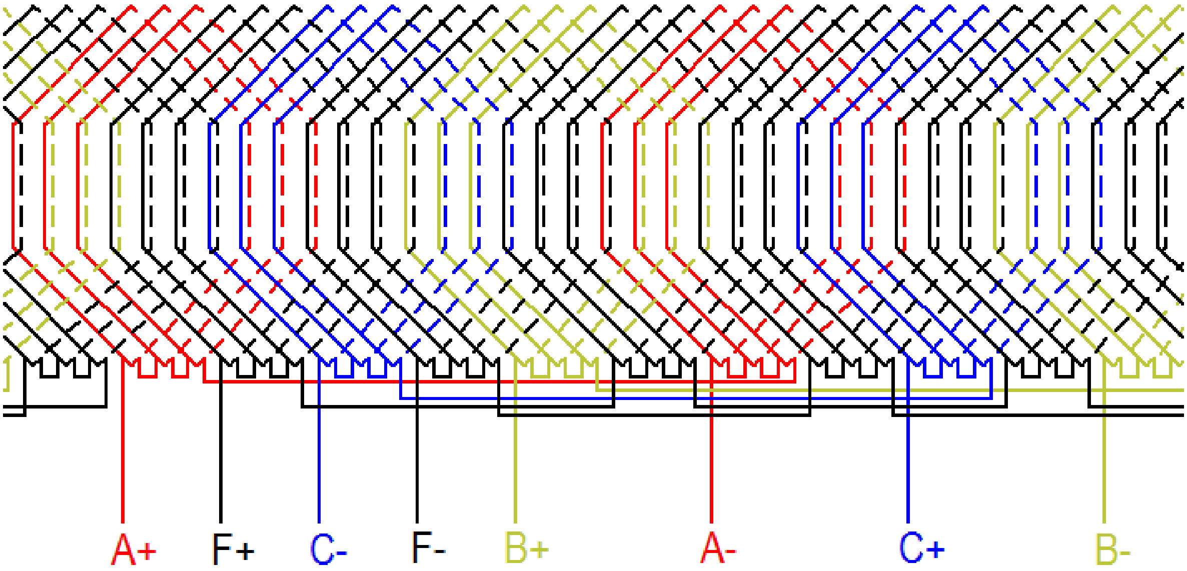

Fig. 4.9 Planar layout of test machine stator winding configuration

4.3 Rotor shaping and cogging torque

4.3.1 Square rotor

In this thesis, the rotor structure shown in Fig. 3.1 is referred as a 'square rotor', due to the fact that the shape of rotor surface is square, and that the resulting air gap permeance is square wave when the machine is analysed in a linear form, although the actual rotor shape is not geometrically square. In reality, the square rotor structure, as plotted in a linear form in Fig. 4.10, will result in an air gap permeance variation composed by higher order harmonic variations other than the fundamental. The harmonic permeance variations will also induce various harmonic voltage components in armature windings and distort the terminal waveforms from ideal sinusoid. Further, harmonics with high orders may lead to torque ripples, increasing the machine's mechanical fatigue and causing unnecessary trembling.

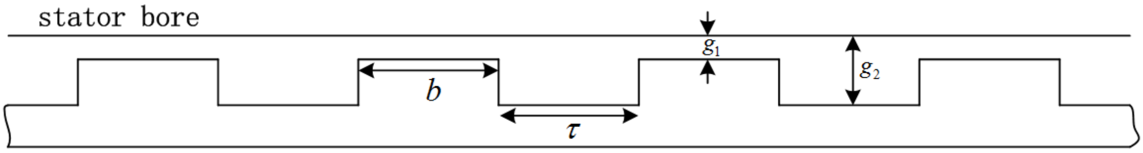

Fig. 4.10 Square rotor and its surface parameters

The Fourier series of air gap permeance components is shown in (4.28) [58], with notations from Fig. 4.11.

$$\Lambda(\nu,\theta)=\mu_0\left[\frac{1}{g_2}+\frac{b}{2\tau}\left(\frac{1}{g_1}-\frac{1}{g_2}\right)\right]+\sum_{n=1}^{\infty}\frac{2\mu_0}{\nu\pi}\left[\sin\nu\left(\frac{\pi}{2}\cdot\frac{b}{\tau}\right)\right]\cdot\left(\frac{1}{g_1}-\frac{1}{g_2}\right)\cos 4\nu\theta \quad (4.28)$$

It is possible to eliminate certain permeance harmonics by altering the length of rotor teeth and slots. For instance, all even order harmonics can be greatly reduced if *b* and *τ* are designed to be equal. On the other hand, 5th permeance harmonic can be completely eliminated if *b* is 4/5 of the length of τ.

The magnitudes of harmonic permeance components are largely dependent on the choices of small air gap g_1 and large air gap g_2. The selection of g_1 and g_2 is a trade-off between rotor saliency and mechanical robustness. The magnitudes of invariant and fundamental components of permeance wave (Λ_0 and Λ_1) with respect to selections of g_1 and g_2 are plotted in Fig. 4.11 and Fig. 4.12.

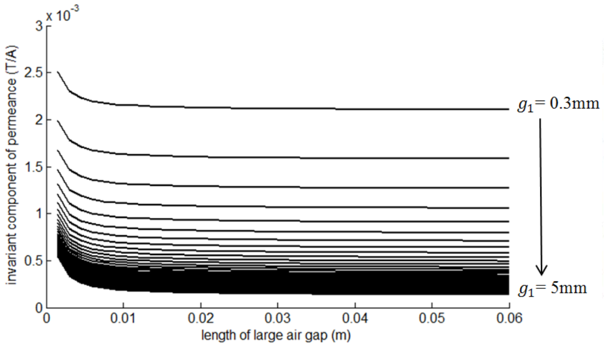

Fig. 4.11

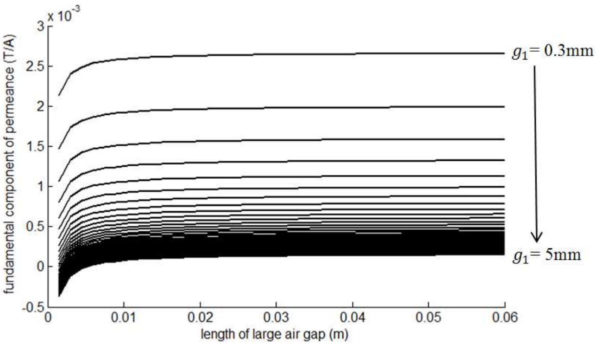

Fig. 4.12

Fig. 4.11 Variation of air gap invariant permeance component with respect to small and large air gap lengths
Fig. 4.12 Variation of air gap fundamental permeance component with respect to small and large air gap lengths

The increment of g_1 is 0.1mm in Fig. 4.11 and Fig. 4.12. As illustrated, whichever value is chosen for g_1, the magnitudes of permeance components converge at roughly g_2 equals 20mm. Also it is worth realising that saturation and stator slotting effects may increase considerably with the decrease of small air gap g_1.

A square rotor, shown in Fig. 4.13, is fabricated with the specifications listed in Table 4.2. Its air gap permeance variation when equipped with the stator introduced in previous section is plotted by FEA tool in Fig. 4.14. As expected, the permeance variation is a square wave with an offset and sharp edges rounded off. The stator slotting effect is also shown in the figure.

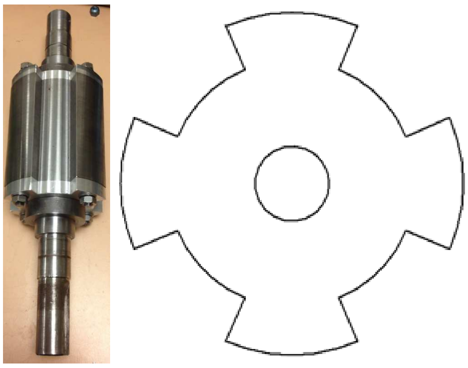

Fig. 4.13

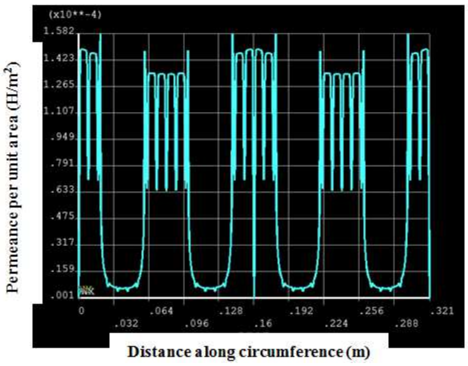

Fig. 4.14

Fig. 4.13 Square rotor for test and rotor punching sketch
Fig. 4.14 FEA simulation for air gap permeance distribution of test machine equipped with square rotor

g_1	0.6mm
g_2	14.13mm
b	40mm
τ	40mm

Table 4.2 Surface dimensions of square rotor for practical test

The actual performance of test machine installed with square rotor is tested. The open circuit emf waveform with 2A field current at 500rpm is recorded in Fig. 4.15. It is observed that the waveform is similar to a trapezoidal wave with stator slotting ripples. The waveform deviates from ideal sinusoidal waveform as unwanted odd emf harmonics (e.g. 5th and 7th harmonics) are introduced by the nature of rotor.

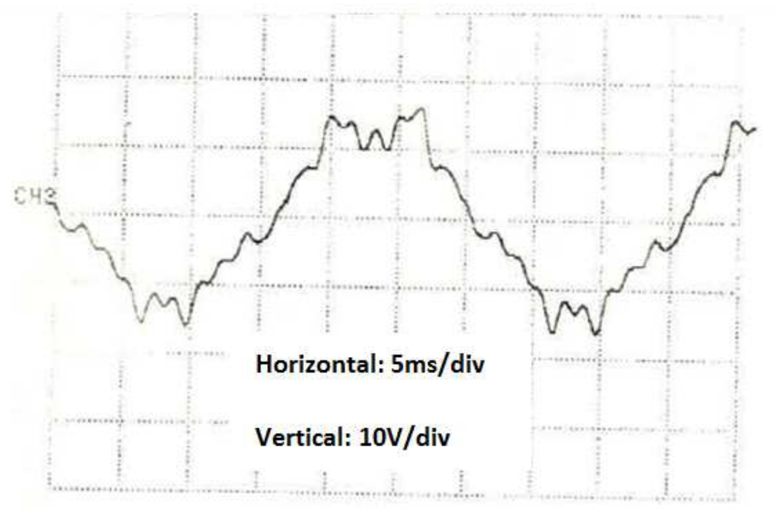

Fig. 4.15 Open circuit emf waveform of test machine with square rotor with 2A field current at 500rpm

The square rotor not only potentially distorts the output voltage waveform, but also tends to cause periodical torque oscillations. A FEA simulation is made to investigate torque generated when the machine is open-circuit with 2A field excitation and 500rpm rotor speed. A pulsating torque is observed and oscillates at a period of 30 degrees of rotor displacement, i.e. $\pi/6$ in mechanical radian. Such a pulsating torque will tend to accelerate and retard the rotor periodically, causing mechanical stress and noise. Since the armature current is not in effect, the torque is purely resulted from the machine cogging effect and is thus named as cogging torque. When armature currents start conducting, such cogging torque will superimpose onto the average electromechanical torque. The torque waveform is simulated in Fig. 4.16 and its Fourier components are shown in Fig. 4.17.

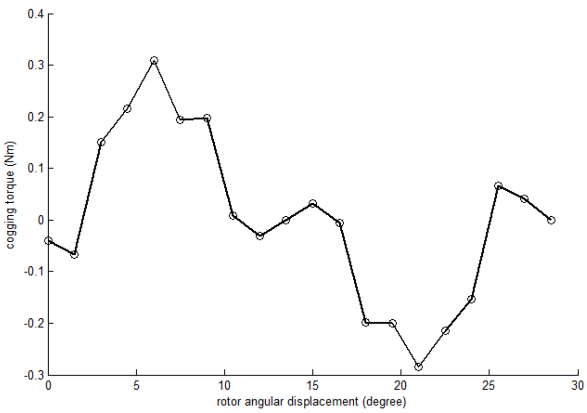

Fig. 4.16

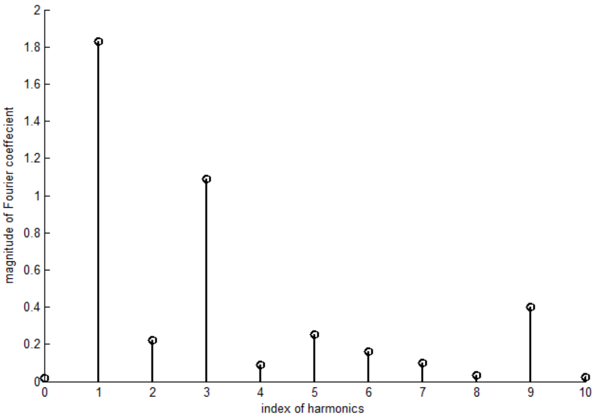

Fig. 4.17

Fig. 4.16 FEA simulation for cogging torque of test machine with square rotor with 2A field current at 500rpm
Fig. 4.17 Harmonic components of cogging torque of test machine with square rotor

The simulation results are supported by experiment when the test machine is driven at a same condition, and the torque measurement is recorded by torque transducer and plotted in Fig. 4.18. Although the relatively low sensitivity (6 samples per revolution) of the torque transducer is unable to record the detailed torque waveform as in Fig. 4.16, the recording still exhibits an oscillating nature of the cogging torque.

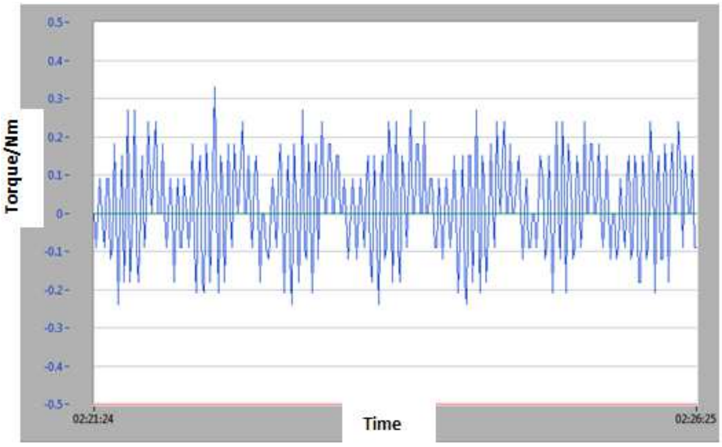

Fig. 4.18 Measurements of cogging torque of test machine with square rotor by torque transducer

From the Fourier analysis in Fig. 4.17, it is seen that the fundamental and 3rd harmonics contributes predominantly to the cogging torque. The fundamental component has a period of 30 mechanical degrees while the 3rd order component has a period of 10 mechanical degrees, i.e. stator slot pitch.

The 3rd torque harmonic is caused by the air gap inductance variation due to stator slotting effect, same as in all conventional electrical machines. It can be eliminated by skewing the rotor by one stator slot pitch. The fundamental cogging torque component, on the other hand, is a consequence of rotor slotting. However it is also related to the transition of flux reversal. More specifically, the flux reversal is no longer 'abrupt' due to the distributed field coils and the transition of field flux from a direction to another causes the mechanical effect. Fig. 4.19 is used to aid the analysis. It plots the magnitude of field magnetic flux density distribution on a pair of rotor teeth over 30 degrees of rotor rotation. F and –F are used to denote a pair of coil sides of each field coil. Blue lines indicate the absolute value of magnetic flux density over a pair of rotor teeth, presumably the stator bore is ideally smooth and the magnetic flux density over large air gaps is regarded as negligible.

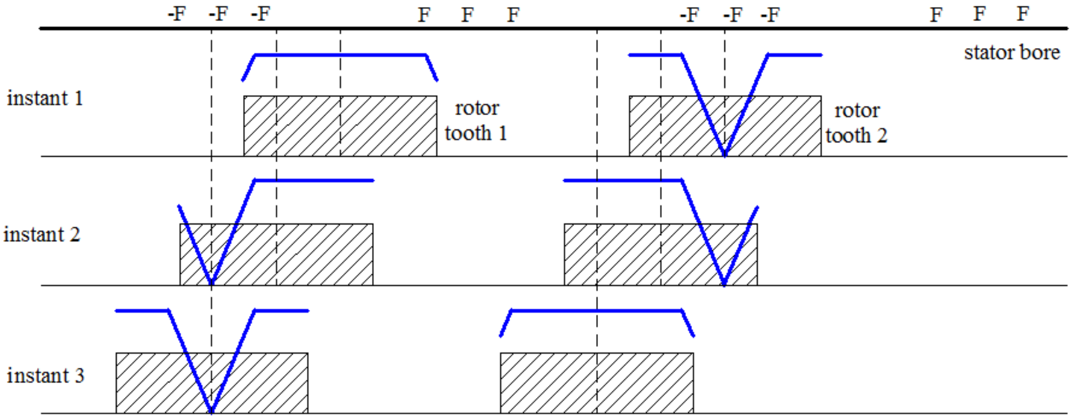

Fig. 4.19 Air gap magnetic flux density variation over a pair of rotor saliencies for rotation of 30 degrees

As seen from Fig. 4.19, there are 'dents' in the magnetic flux density distribution at the places where field flux reverses. Once the rotor rotates, a pair of rotor teeth witness a total reduction (instant 2) and rise (instant 3) of magnetic flux density in small air gap every 30 mechanical degrees. Hence the total magnetic field energy conserved in the small air gap varies accordingly. Cogging torque is generated naturally to resist the variation of energy. The other pair of rotor teeth behaves exactly in the same way.

Skewing can still be applied to eliminate the cogging torque due to rotor slotting. However in this case, the rotor must be skewed by 3 stator slots, and the skewing will reduce the main fundamental voltages by a relatively larger coefficient.

4.3.2 Sine permeance rotor

A reasonable approach is to adequately shape the geometry of rotor lamination so that unwanted air gap permeance components are forced to be cancelled, and that only fundamental component exists, as assumed in Chapter 3. The fabrication of such rotor laminations is technically feasible with the knowledge of desired values for Λ_0 and Λ_1, and a given bore diameter.

Λ_0	0.96×10^{-3}H/m^2
Λ_1	1.3×10^{-3}H/m^2
Minimum air gap	0.55mm
Maximum air gap	11.74mm

Table 4.3 Surface dimensions of sine permeance rotor for practical test

A special rotor punching with specifications listed in Table 4.3 is manufactured by laser cutting, as shown in Fig. 4.20. This type of rotor is termed as 'sine permeance rotor' in this thesis for the reason that the structure of this rotor aims to create a sinusoidal air gap permeance distribution when the machine is analysed in a linear form. FEA is used for analysing the air gap permeance pattern resulted by the rotor and it is plotted in Fig. 4.21. Compared with Fig. 4.14, the waveform in Fig. 4.21 is much closer to an offset sinusoid, though the ripple caused by stator slotting is still existent.

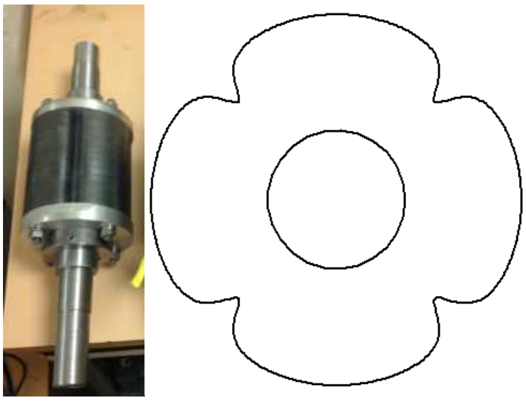

Fig. 4.20

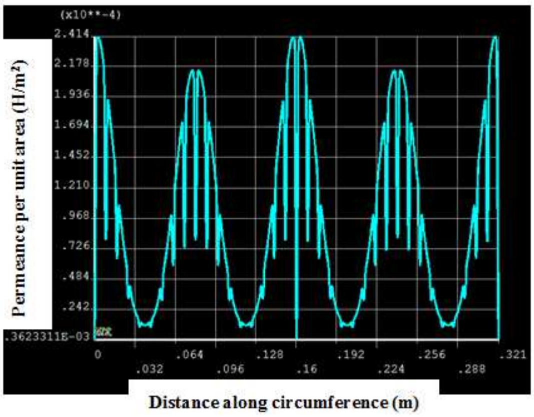

Fig. 4.21

Fig. 4.20 Sine permeance rotor for test and rotor punching sketch
Fig. 4.21 FEA simulation for air gap permeance distribution of test machine equipped with sine permeance rotor

The experiments conducted in Chapter 3 for theory verifications are based on a test machine equipped with this specific rotor to avoid the influences caused by harmonic permeance waves. It is already seen from Fig. 3.17 that the improved rotor shape manages to achieve sinusoidal emf induction. Moreover it is found that the new rotor shape is able to considerably suppress the cogging torque as analysed in the previous section, because the improved rotor structure manages to conserve air gap magnetic energy by avoiding abrupt air gap energy variations. The conclusion is supported by both FEA simulation (Fig. 4.22) and practical experiment (Fig. 4.23).

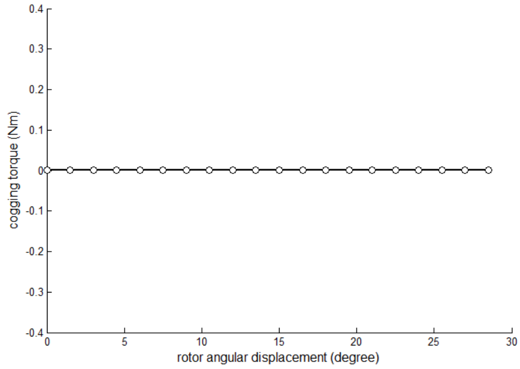

Fig. 4.22

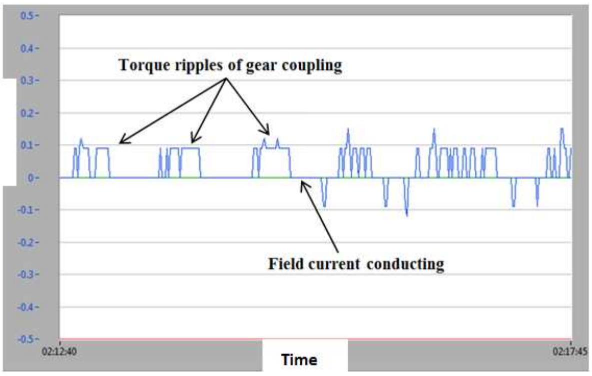

Fig. 4.23

Fig. 4.22 FEA simulation for cogging torque of test machine with sine permeance rotor with 2A field current at 500rpm
Fig. 4.23 Measurements of cogging torque of test machine with sine permeance rotor by torque transducer

The cogging torque in simulation is completely suppressed compared with Fig. 4.16. However, in practice the torque transducer still senses a small amount of no load torque ripples, which may result from the mismatch between practical and ideal rotor shapes. Nevertheless the torque ripple is greatly reduced compared with that recorded in Fig. 4.18. Conclusively, the improved rotor shape is more advantageous than the square rotor from the point of view of both waveform optimisation and ripple torque suppression, yet the performance improvements gained by sine permeance rotor are at the expense of more material/mass required per rotor punching compared with square rotor.

The experimental results discussed in Chapter 3 and all subsequent analysis are upon the basis of a test machine with the improved rotor shape shown in Fig. 4.20, and the stator and winding layout shown in Fig. 4.9. A cross section view and a 3D CAD model of the test machine are illustrated in Fig. 4.24 and Fig. 4.25 respectively.

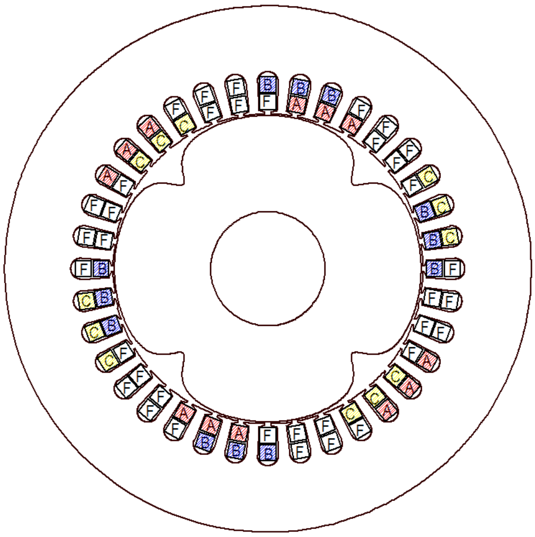

Fig. 4.24

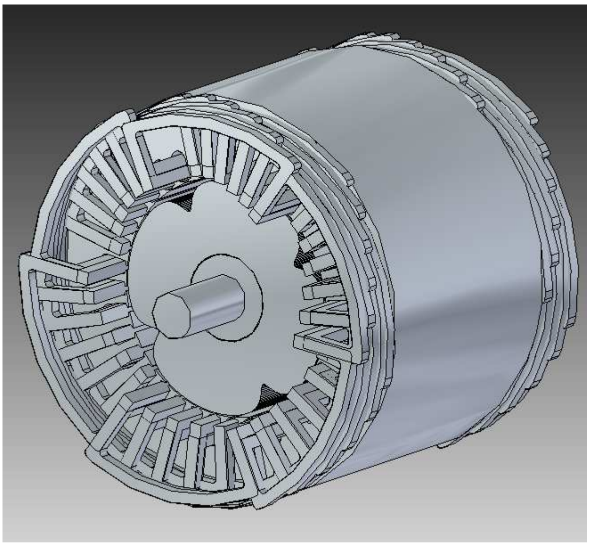

Fig. 4.25

Fig. 4.24 Cross section view of prototype machine with winding configuration highlighted
Fig. 4.25 3D CAD graph of prototype machine

4.4 Sizing equation

The relationship between electromagnetic properties and essential physical size of heteropolar inductor machines is investigated in this section.

The rms value of rated phase internal is denoted as E_n and can be directly derived from (3.8), with the bore radius r replaced by bore diameter d.

$$E_n = \frac{3}{\sqrt{2}} \omega_S k_{dp} N_S N_f i_f \Lambda_1 dl \tag{4.29}$$

A variation of magnetic field flux density is resulted by the permeance variation when field windings are excited. The fundamental swing of flux density is denoted as B_1.

$$B_1 = N_f i_f \Lambda_1 \tag{4.30}$$

Flux density component B_1 is related to the maximum flux density appearing in air gap, given that the bore is assumed to be smooth. Maximum air gap magnetic flux density occurs at the positions where air gap length is minimum, and is denoted as B. B and B_1 can be simply related via a numerical factor k_1.

$$B_1 = k_1 B \tag{4.31}$$

Maximum air gap magnetic flux density B is known as the specific magnetic loading of an electrical machine and is one of the most important design parameters. It is a measure of machine's magnetic loss due to eddy current and hysteresis loss of iron yokes. It is restricted by various design parameters, such as material permeability, shape and size of slots and permissible iron loss. In the case of sinusoidal permeance rotor,

$$k_1 = \frac{\Lambda_1}{\Lambda_0 + \Lambda_1} \tag{4.32}$$

While in the case of square rotor,

$$k_1 = \frac{2}{\pi}\left(1 - \frac{g_1}{g_2}\right)\sin\left(\frac{\pi}{2} \cdot \frac{b}{\tau}\right) \tag{4.33}$$

The internal emf will be modulated armature reaction once three phase armature currents start conducting. Aside from phase shifts, armature reaction also has an influence on the magnitude of phase voltage by increasing or decreasing the terminal voltage level. The degree of phase voltage deviation from original phase emf is known as voltage regulation. The rated voltage regulation is denoted as k_2. Hence the rms value of rated phase voltage V_n is numerically linked to E_n.

$$V_n = k_2 E_n \tag{4.34}$$

By combining (4.29 – 4.31) and (4.34), the rated phase rms terminal voltage V_n is expressed as

$$V_n = \frac{3}{\sqrt{2}} \omega_S k_{dp} k_1 k_2 N_S B d l \tag{4.35}$$

Compared with the actual currents in conductors, the total current density concentrated at a unit length on stator bore periphery is of more interest in machine design. The line current density of stator bore, also known as specific electrical loading of electrical machines, is an important measure of heating and copper loss (i.e. ohmic loss).

Specific electrical loading K is calculated as the line current density along the bore circumference, with smooth bore surface assumed.

$$K = \frac{2 \times \left(3 N_S I_n + 6 N_f I_{fn}\right)}{\pi d} \tag{4.36}$$

Rated rms armature current and rated field current are denoted as I_n and I_{fn} respectively. The multiplier 2 takes into account the fact that each coil consist of 2 coil sides. The stator bore is assumed to be ideally smooth and current density distributes evenly along bore circumference.

It is possible to refer field amp-turns to armature amp-turn by forcing I_{fn} equal to I_n, and the equivalent number of winding turns per phase is denoted as N', therefore,

$$2 \times \left(3 N_S I_n + 6 N_f I_{fn}\right) = 2 \times 3 N' I_n \tag{4.37}$$

A factor k_3 is used for representing the proportion of armature winding turns in the total turns of windings on stator. It is also a measure the portion of heating and copper loss contributed by armature currents.

$$k_3 = \frac{N_S}{N'} \tag{4.38}$$

The rated apparent power S_n of an electrical machine is calculated from the armature terminal voltages and currents for all three phases,

$$S_n = 3V_n I_n \tag{4.39}$$

The design parameters and electromagnetic characteristics of a heteropolar inductor machine are linked by combining (4.35 – 4.39). The sizing equation for heteropolar inductor machines is organised as

$$S_n = \frac{3\pi}{2\sqrt{2}} \omega_S k_{dp} k_1 k_2 k_3 B K d^2 l \tag{4.40}$$

Sizing equation plays an important role at the primary design stage of electrical machinery, which gives a preliminary estimation of machines' 'effective size' with a rough knowledge of their electromagnetic ratings and limitations. It is generally expressed in the form as

$$S_n = k \omega_S K B d^2 l \tag{4.41}$$

The notation k in the equation is usually a numerical constant which is different from case to case, depending on the types of electrical machines.

It is a fact that the maximum permissible values of K and B for various steels vary only within a narrow range. The significance of sizing equation, therefore, is that the product of a machine's axial length l and bore diameter d is more or less fixed, given the desired rated output capacity and speed. On the other hand, if the spatial limitation is a prime issue in design process, feasible values of d and l can be selected firstly to build up an internal relationship between electrical rating and operational speed. Moreover, sizing equation may be used for estimating a series of similar electrical machines, facilitating design process by referencing the knowledge and experience of a previously designed similar machine.

Due to the structural nature of heteropolar inductor machines, the sizing equation, as shown in (4.40), is much more complicated and inter-related compared with that for conventional electrical machines.

Different from conventional AC machines, heteropolar inductor machines only takes advantage of the varying component of a unidirectional field magnetic flux. It is reflected by the factor k_1 which has an upper-limit value of only 0.5, while it equals to 1 in the case of conventional machines that utilise the full swing of air gap magnetic flux density. It implies the potential ineffectiveness of magnetic flux usage in heteropolar inductor machines. Unavoidably the machine size must be larger than conventional machines of similar ratings as a consequence. During the design, k_1 must be as high as permitted by the structure. Higher values of k_1 may be achieved by applying flux guides/barriers and axial lamination.

As is known, the phase voltages induced by field and armature reaction are resulted by distinct mechanisms in heteropolar inductor machines. The estimation of terminal voltage by superimposition of air gap magnetic flux density, as in conventional AC machines, is no longer applicable. The factor k_2 is introduced to link actual phase terminal voltages with internal emfs via the machine’s external characteristics. Voltage regulation k_2 is a measure of armature reaction effect and must be considered together with armature reaction reactance and rated power factor during design. It is desirable if it is as close to 1 as possible in most situations.

A limitation of sizing equation for conventional electrical machines is that only stator-side currents are considered in the specific electrical loading K. Hence K deviates from functioning as a proper metric for heating due to the exclusion of rotor-side electrical loading. As a matter of fact, rotor currents can sometimes contribute a considerable portion of machine heating because of the poor heat dissipation in the air gap. In (4.36), however, both armature and field current densities are considered in estimating K, and both heating and copper loss are reflected more appropriately. As suggested in (4.38), the factor k_3 expresses the portion of armature current specific electrical loading in the total electrical loading on bore surface. Values of k_3 varies for different selections of armature and field winding turns, and their rated currents.

In summary, the internal complexity heteropolar inductor machine is reflected by factors k_1, k_2 and k_3. k_1 reveals the nature of magnetic induction in heteropolar inductor machines and the effectiveness of magnetic usage. k_2 implies the inconsistency of voltage induction mechanisms for internal emf and armature reaction. k_3 indicates the co-existence of both armature and field amp-turns.

4.5 Local saturation

The armature reaction of conventional synchronous machines may tend to either magnetise or demagnetise the field flux excited by rotor field windings. The magnetisation and demagnetisation effects are largely dependent on the relative positions of the field mmf and armature reaction mmf. When the armature reaction mmf (or part of it) is aligned with field mmf axis, the field mmf is enhanced. Naturally when the armature reaction mmf amplitude (or part of it) is in a reversed direction to field mmf, the field is weakened. Externally, such effects are observed from the external characteristic curves and V curves of a synchronous machine.

It is seen in Fig. 3.19 and Fig. 3.20 that the external characteristic curves and V curves of heteropolar inductor machines are in identical shapes as those of conventional synchronous machines. It can be explained by different relative positions of field current and armature current vectors in space vector theories introduced in Chapter 3. Despite the resemblance in external characteristics with conventional synchronous machines, the internal magnetisation and demagnetisation effects of heteropolar inductor machines are much more complicated.

First of all, the field and armature reaction mmfs are no longer constantly synchronised. The field windings are fixed on stator side, while the armature reaction mmf is travelling in space.

Secondly, the excitation of field windings creates alternately reversed magnetic fields along the air gap. Field mmfs of adjacent field coils are directed oppositely. Consequently, with the travelling armature reaction mmf existing in air gap, the mmf of one of field coils will be enhanced if the armature reaction mmf axis is in line (or partially in line) with this specific field coil axis and pointing to a same direction. On the contrary, an adjacent field coil mmf will be counteracted by the same armature reaction mmf at the same time. The analysis is aided by Fig. 4.26 which shows the occasions when armature reaction enhances and weakens a pair of adjacent field.

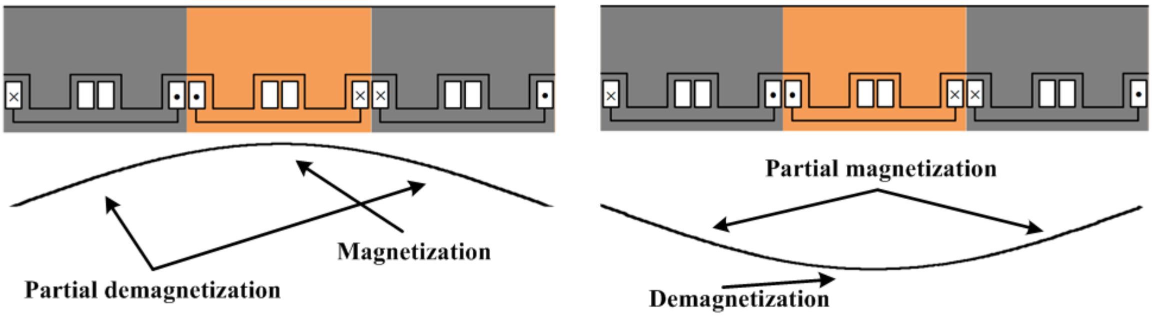

Fig. 4.26 Magnetisation and demagnetisation of field flux by armature reaction mmf

Thirdly, the unsmooth rotor surface results in a varying air gap length. With the permeance variation, it is possible that only a little magnetic field density is resulted by a field coil even if its mmf is enhanced by armature reaction. It happens when the field coil happens to have a large air gap. On the other hand, if the superimposition of field and armature mmfs happen to effect on a small air gap, regional magnetic flux density will be high and severe local saturation can appear.

Above all, the analysis of internal magnetisation and demagnetisation for heteropolar inductor machines are based on the full scale analysis of field coil mmf directions, armature reaction mmf wave and positions of rotor saliencies. It is found that the internal magnetisation and demagnetisation are greatly influenced by internal power factor angle ψ. A preliminary analysis is based on FEA to simulate the magnetic flux density distribution within the machine in the steady state conditions with different ψ.

Fig. 4.27 plots the magnetic flux density distribution of six instants of a whole electrical cycle (i.e. 90 degrees of rotor rotation) when $\psi = -\pi/2$ and rotor saliency initially aligning to phase A axis. The field current in simulation is 2A and the magnitude of three phase armature currents is 1.5A. Number of coil turns is 25.

Initially, as plotted in Fig. 4.27(a), the direction of armature mmf magnetisation is perpendicular to phase A axis, pointing to left of the plane. At this instant, the armature reaction mmf axis coincides with two field coils and is of the same direction of field coil mmfs. The two field coil magnetisation regions are marked by red circles. Also the minimum air gaps happen to be placed on the same axis. Consequently high magnetic flux density is excited in the circled regions by the superimposed mmfs, and heavy saturation occurs at certain stator teeth and the rotor surfaces on the magnetisation axis.

Next instant is analysed when the rotor revolves 15 degrees counter-clockwise, as shown in Fig. 4.27(b). In the meantime armature reaction mmf rotates 60 degrees counter-clockwise in space. The armature reaction mmf axis is thus aligned with adjacent field coils of those marked in Fig. 4.27(a), as highlighted by white circles. Since the mmf excited by white-marked field coils in Fig. 4.27(b) is in opposite direction of that excited by red-marked coils in Fig. 4.27(a), the armature reaction mmf tends to cancel out the field mmf. As a result, the resultant magnetic flux density is minimal in white regions. Additionally large air gaps are aligned to the same axis, further reducing the flux density in the regions. However the armature reaction mmf is still partially aligned to the previous field coils, as marked in red in Fig. 4.27(b), hence the mmf enhancement in red regions persists. Partial high flux density (but lower than that in Fig. 4.27(a)) and saturation are still observable in red regions.

As the rotor rotates for a further 15 degrees and armature reaction mmf travels another 60 degrees, as in Fig. 4.27(c), the situation is similar to Fig. 4.27(a). The armature reaction enhances another two field coil mmfs and causes local saturation. The magnetic flux density in regions marked in Fig. 4.27(b) returns to normal level.

When rotor rotates 45 degrees as shown in Fig. 4.27(d), the heavily saturated regions highlighted in Fig. 4.27(a) witness a cancellation of mmfs. The magnetic flux density is almost nulled. Fig. 4.27(e) and Fig. 4.27(f) show a repetitive pattern, except that the locations of flux concentration are further shifted by 120 degrees compared with Fig. 4.27(c) and 4.27(d). A new period starts when rotor rotates 90 mechanical degrees. It is observed that each field coil region experiences a huge swing of magnetic flux density variation.

The flux density variation in field coil regions shown in Fig. 4.27 can be reduced by altering ψ. In Fig. 4.28, six step simulations are performed with $\psi = \pi/2$. The excitation conditions and initial rotor position are unchanged.

Comparing with the regions circled in Fig. 4.27(a), the same regions in Fig. 4.28(a) exhibit a low flux density (also highlighted by red circles). It is due to the fact that the initial position of armature reaction mmf axis is reversed and the circled regions are demagnetised by armature reaction. The main magnetic flux circulations are located at the top and bottom of the plain. The flux density circulates via small air gap, stator teeth, stator yoke and rotor teeth surface.

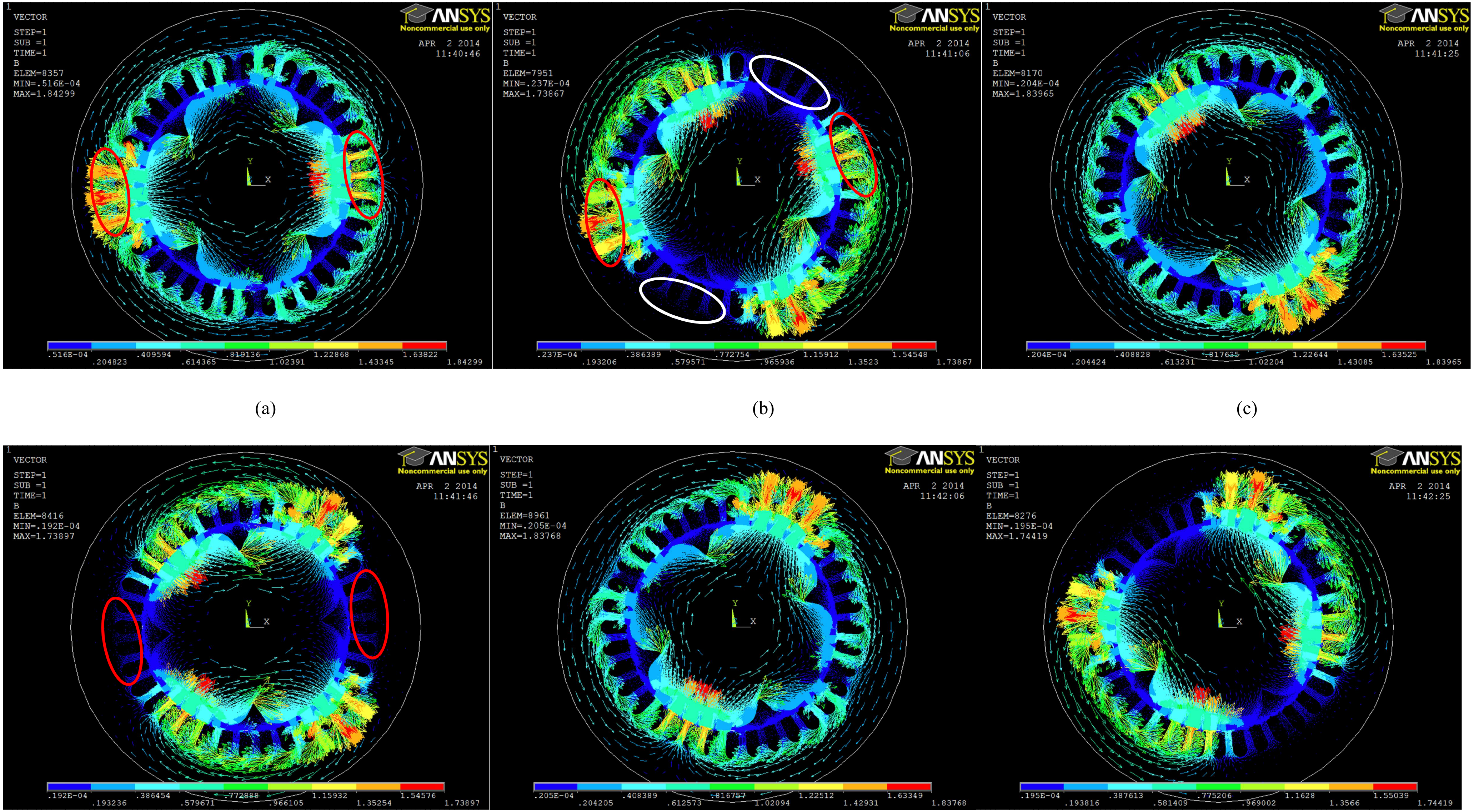

(a) (b) (c)

(d) (e) (f)

Fig. 4.27 FEA flux density vector plot for prototype machine over rotation of 90 degrees with $\psi = -\pi/2$ and rotor axis initially aligned with phase

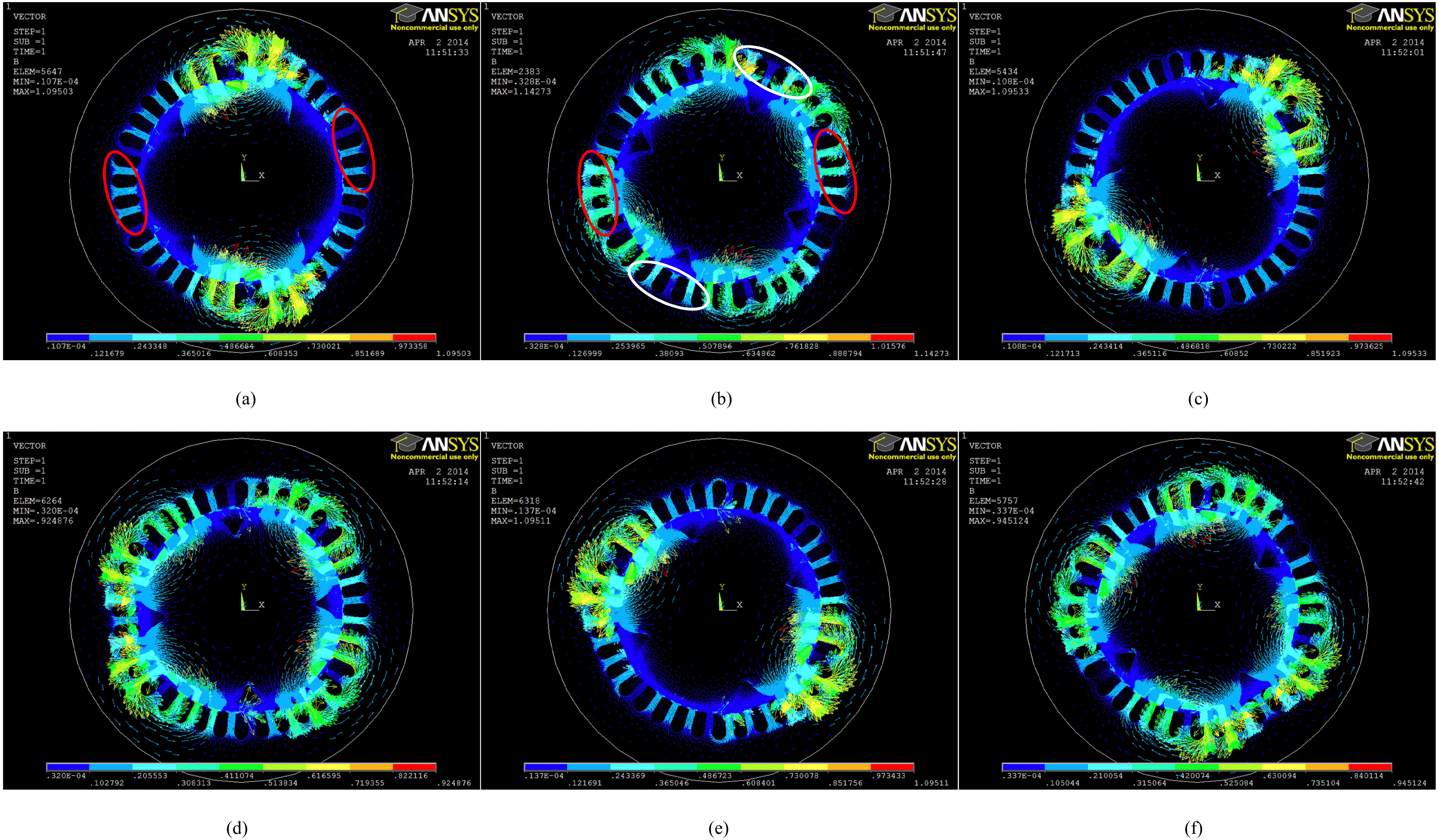

(a) (b) (c)

(d) (e) (f)

Fig. 4.28 FEA flux density vector plot for prototype machine over rotation of 90 degrees with $\psi = \pi/2$ and rotor axis initially aligned with phase A

In Fig. 4.28(b), rotor rotates 15 degrees counter-clockwise and armature reaction mmf axis is -30 degrees displaced from reference. The armature reaction mmf enhances the adjacent field coil mmfs of those considered in Fig. 4.28(a).

The enhanced field coil regions are marked with white circles. However large air gaps are also aligned to the same axis, resulting in a limited increment of flux density the regions. The flux is mostly concentrated at the areas near white-marked regions where air gaps are smaller. Moreover, partial demagnetising effect still persists on the red-marked regions.

Fig. 4.28 (c), Fig. 4.28(d), Fig. 4.28(e) and Fig. 4.28(f) show the flux density distribution for the remaining 2/3 of the electrical cycle. Each field coil in the simulation of each individual instant is shown to be demagnetised periodically by armature reaction. The enhancement of mmf is always suppressed by the large air gap aligned. Though stator teeth still experience a periodical variation in magnetic flux density due to armature reaction, the level of flux density swing is greatly reduced.

Simulations shown in Fig. 4.29 have an initial rotor position displacement of $\pi/6$ counter clockwise compared with Fig. 4.27 and Fig. 4.28. The initial armature reaction mmf axis is unchanged, resulting an internal power factor angle of $-7\pi/6$. The excitation conditions remain unchanged.

Fig. 4.29(a) shows the initial condition. The armature reaction mmf axis lies in the same position as in Fig. 4.27(a) and in line with the field coil regions circled. However the minimum air gap is no longer aligned with the same axis. Consequently, it is shown that 2/3 of the red-marked regions are faced with a larger air gap, and only 1/3 of the regions are subject to heavy saturation. Also an adjacent tooth beyond the regions experiences high flux density due to armature reaction mmf. The flux density in stator yoke is reduced compared with the result shown in Fig. 4.27(a). It is because that the field mmf at regions marked in white circles act on large air gaps and the resultant flux density is minimised.

In the next instant, as shown in 4.29(b), the armature reaction mmf counteracts the mmf created in the white-marked regions. On the other hand, the armature reaction partially magnetise the field regions highlighted by yellow circles and increases the magnetic flux density in the regions.

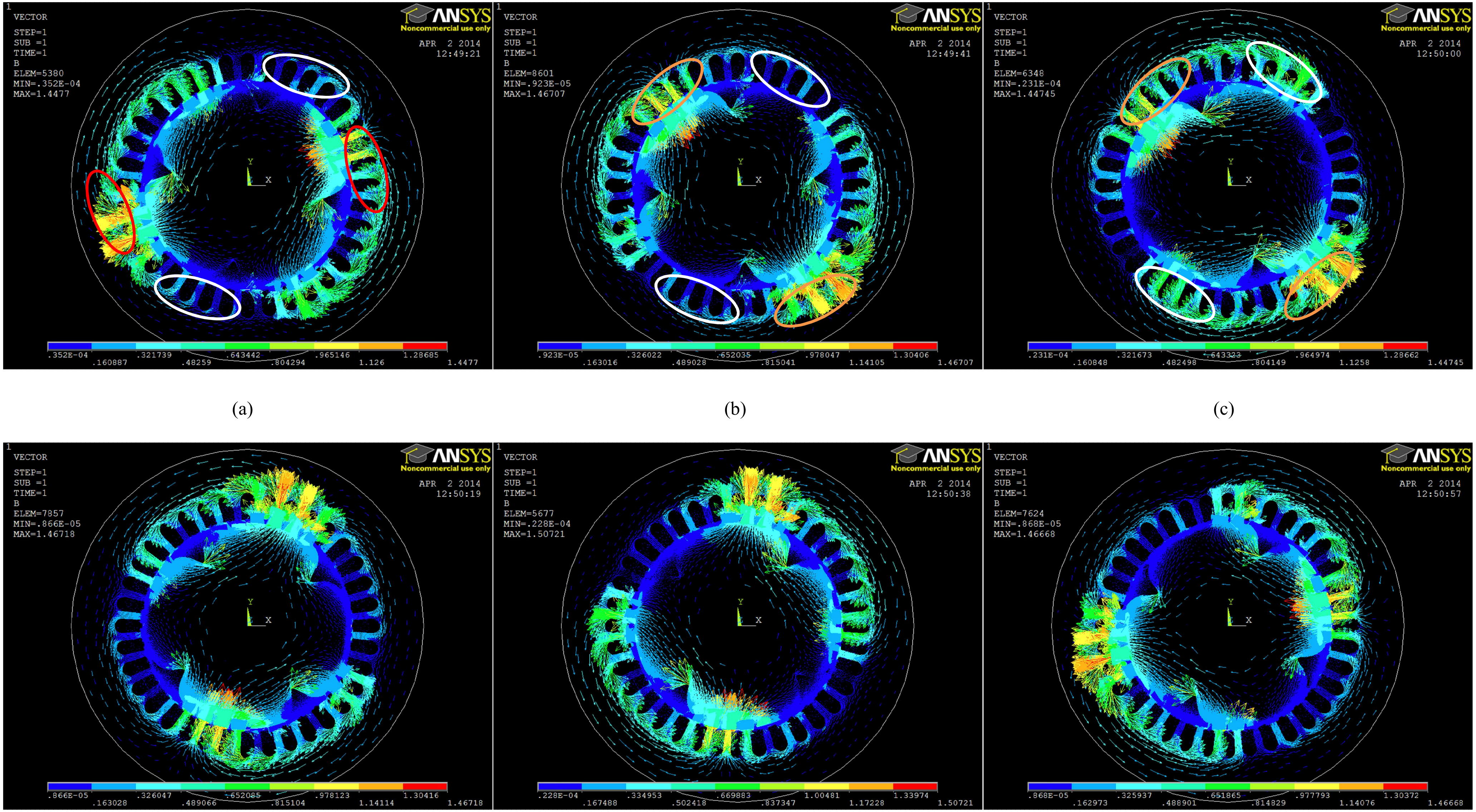

(a) (b) (c)

(d) (e) (f)

Fig. 4.29 FEA flux density vector plot for prototype machine over rotation of 90 degrees with $\psi = -7\pi/6$ and rotor axis initially displaced from phase A by $\pi/6$

In 4.29(c), the armature reaction mmf is in the same direction as the field mmfs in yellow-marked regions and the influence is the same as in red-marked regions in 4.29(a). The white-marked regions now become active and excite flux density although they are still slightly demagnetised by armature reaction.

Subsequent simulation instants shown in Fig. 4.29(d), Fig. 4.29(e) and Fig. 4.29(f) illustrate the magnetic flux density distribution in the remaining half electrical cycle, and they follow a similar pattern of distribution. Compared with Fig. 4.27, the variation of magnetic field density in field coil regions is reduced.

Above all, it is seen that although it is inevitable for stator teeth to experience periodical magnetic flux density swings, the pattern and level of the swings are predictable, even controllable with appropriate current orientation. The analysis of regional saturation and flux density is important as it is a direct source of iron loss on stator teeth and rotor surface. In certain applications in which machine efficiency is of interest, appropriate control methods may be applied for heteropolar inductor machines to optimise the regional magnetic flux variation pattern.

For loss control, the acceptable regional magnetic flux variation can be considered in design stage, and most suitable values of ψ can be found and implemented for major operational ranges. The control of angle ψ suggests the significance of sophisticated control strategy, i.e. field oriented control.

4.6 Losses

The losses of machines are classified into 4 main categories: iron loss, copper loss, stray loss and mechanical loss.

The copper loss, stray loss and mechanical loss of heteropolar inductor machine losses can be analysed exactly the same as the ways for conventional AC machines. The copper loss is due to winding resistance and is subject to heating to some extent. The stray loss is usually resulted from the eddy currents in armature conductors and housings or bolts, and flux pulsations caused by slot openings. Mechanical loss usually consists of shaft and bearing friction, windage loss and ventilation loss.

The analysis of iron loss, however, is slightly different from conventional machines. Iron loss is composed by hysteresis loss and eddy current loss. Both types of losses are directly and strongly related to the periodical variation of flux density in steel. It is seen from Figs. 4.27 – 4.29 that most magnetic flux is concentrated at stator and rotor teeth, though stator and rotor yokes also experience flux variations.

In conventional AC machines, magnetic flux density in each stator tooth periodically swings from a positive maximum magnitude to a corresponding negative maximum magnitude because of the polarities of travelling mmf waves. In the case of stator teeth of heteropolar inductor machines, the magnetic flux density variations may not be the same for each individual tooth. Fig. 4.29 is re-drawn in Fig. 4.30 with a stator tooth enclosed by a field coil and another enclosed by an armature coil highlighted by a red circle and a white circle respectively.

It is obvious that, during a full electrical cycle, the direction of magnetic flux density vector in red-marked tooth is always (or most of the time, if armature reaction is strong) pointing from air gap to tooth, while that in white-marked tooth is bi-directional. It is because of the pre-built magnetic field in field coil regions. Hence the positive and negative flux density swings in red-marked tooth can be unbalanced due to material non-linearity when the tooth is pushed to heavy saturation by superimposed mmfs. The unbalanced flux swing also changes the shape of hysteresis cycle compared with white-marked tooth. Therefore both induced eddy current and hysteresis loss in red-marked tooth is different from those in white-marked tooth.

Apart from stator iron loss, the rotor iron loss also requires further analysis. A main drawback of heteropolar inductor machines is that they exhibit high rotor iron loss, due to the fact that field and armature mmfs and resulting flux density are moving asynchronously with rotor.

Seen from one of rotor tooth surfaces, the field mmf on stator side behaves as a 6-pole trapezoidal wave travelling backward, while the 2-pole armature reaction mmf is travelling 3 times faster forward. The analysis of magnetic flux distribution in each rotor tooth at every instant must consider the instantaneous resultant mmf, the variation of air gap and the exponential decay of flux density radially into tooth depth. In other words, the estimation rotor iron loss for heteropolar inductor machines involves solving a series of complicated electromagnetic conditions.

However, the problem can be analogous to the calculation of rotor loss for salient fractional slot winding synchronous machines subject to sub-harmonics. Researchers have developed various approaches to gain appropriate approximations of factional slot winding machine rotor losses both analytically and via computer simulation [88].

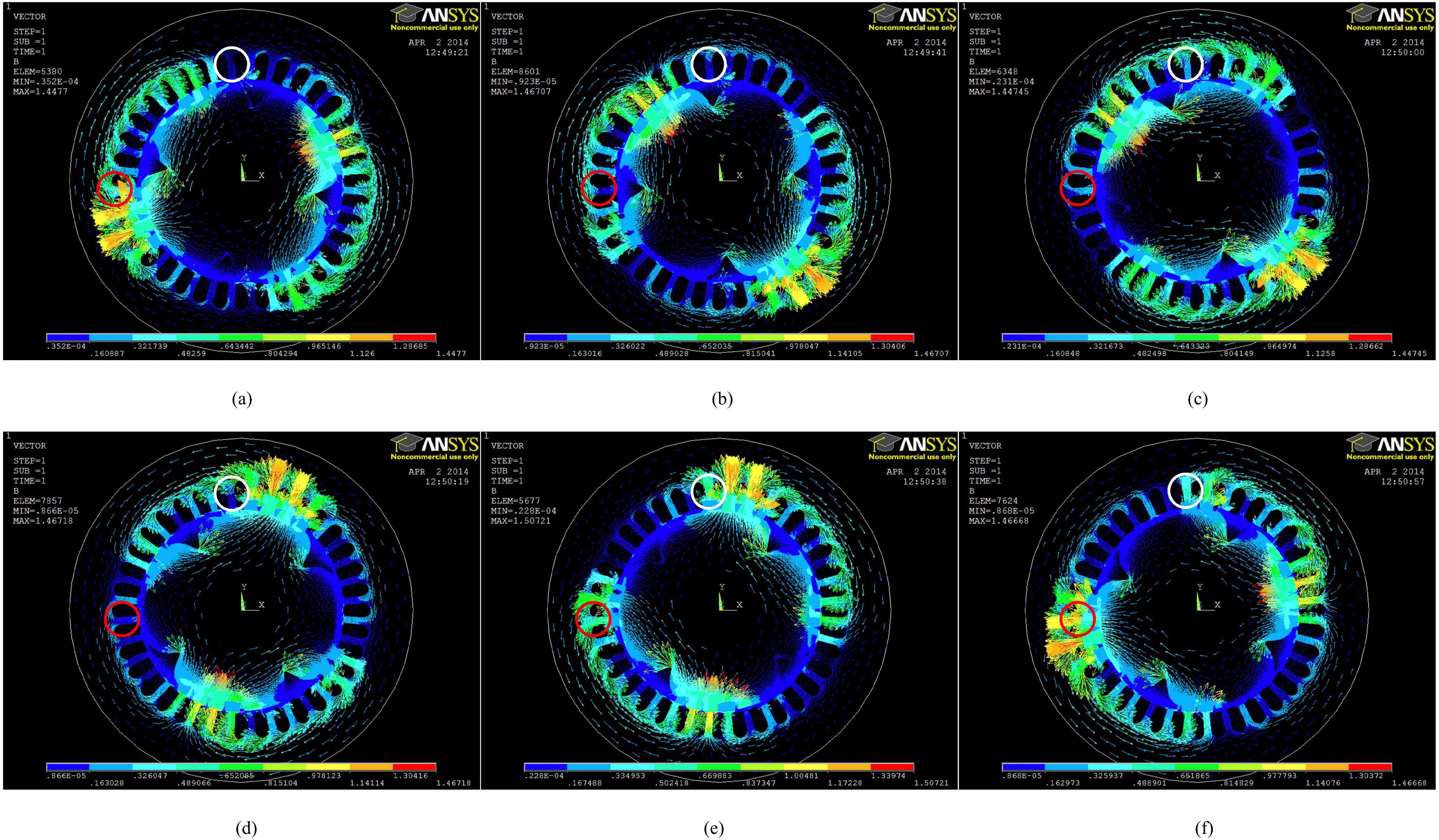
VECTOR
STEP=1
SUB =1
TIME=1
B
ELEM=5380
MIN=.352E-04
MAX=1.4477
ANSYS
Noncommercial use only
APR 2 2014
12:49:21
Y
X
.352E-04
.160887
.321739
.48259
.643442
.804294
.965146
1.126
1.28685
1.4477
VECTOR
STEP=1
SUB =1
TIME=1
B
ELEM=8601
MIN=.923E-05
MAX=1.46707
APR 2 2014
12:49:41
.923E-05
.163016
.326022
.489028
.652035
.815041
.978047
1.14105
1.30406
1.46707
VECTOR
STEP=1
SUB =1
TIME=1
B
ELEM=6348
MIN=.231E-04
MAX=1.44745
APR 2 2014
12:50:00
.231E-04
.160848
.321673
.482498
.643323
.804149
.964974
1.1258
1.28662
1.44745
VECTOR
STEP=1
SUB =1
TIME=1
B
ELEM=7857
MIN=.866E-05
MAX=1.46718
APR 2 2014
12:50:19
.866E-05
.163028
.326047
.489066
.652085
.815104
.978123
1.14114
1.30416
1.46718
VECTOR
STEP=1
SUB =1
TIME=1
B
ELEM=5677
MIN=.228E-04
MAX=1.50721
APR 2 2014
12:50:38
.228E-04
.167488
.334953
.502418
.669883
.837347
1.00481
1.17228
1.33974
1.50721
VECTOR
STEP=1
SUB =1
TIME=1
B
ELEM=7624
MIN=.868E-05
MAX=1.46668
APR 2 2014
12:50:57
.868E-05
.162973
.325937
.488901
.651865
.814829
.977793
1.14076
1.30372
1.46668

(a) (b) (c)

(d) (e) (f)

Fig. 4.30 FEA flux density vector plot for prototype machine over rotation of 90 degrees with $\psi = -7\pi/6$ and rotor axis initially displaced from phase A by $\pi/6$, stator teeth flux density highlight

4.7 Summary and discussion

This chapter focuses on the design aspects of heteropolar inductor machines. The influence of different rotor pole numbers with 12 stator slots is analysed with respect to phase separation and emf magnitude. The possible choices of rotor pole numbers for constructing balanced three phase systems are discussed and generalised.

The influences of winding separation and chording on internal emf induction and armature reaction are studied in detail. The expressions of winding factors are developed and are used for mitigating the influence of unwanted 2nd harmonic in the system. Several winding configurations with reduced 2nd harmonic component are proposed.

The performances of square rotor and sine permeance rotor are compared to highlight the importance of rotor shaping. FEA is utilised to plot the air gap permeance distributions of two rotors, as well as to analyse the cogging torque profile. It is discovered that sine permeance rotor not only suppresses the various high order emf harmonics, but also greatly reduces the cogging torque. The origin of cogging torque in heteropolar inductor machine is also analysed.

A sizing equation that governs the relationships of ratings, electromagnetic loadings, and essential dimensions is developed. The significance of several important factors in the equation is explained in detail, addressing the difference of heteropolar inductor machine from conventional AC machines from the viewpoint of design.

The characteristics of internal local saturation are briefly analysed with the aid of FEA. The special property of periodical local saturation is caused by the out-of-synchronism of rotor, armature reaction mmf and field excitation. The influence of internal factor and rotor location on local saturation is visualised by FEA plots.

The magnetic flux density variation patterns for two different stator teeth are demonstrated with the assistance of FEA. It is discovered that the flux variation in stator teeth can be either unidirectional and bidirectional, leading to the discussion of stator iron loss calculation. On the other hand, the complexity of calculating rotor iron loss is preliminarily discussed due to the out-of-synchronism between rotor rotation and mmfs.

It is theoretically demonstrated that rotors with different number of saliencies are possible to be fitted into a same stator for different operational speeds. Therefore it is possible that a motor can achieve speed change by replacing rotors only, facilitating manufacturing process.

The armature and field windings are assumed to have equal number of coils and number of turns in the analysis in precious sections. Instead, it is possible to increase or decrease the relative numbers of coils and turns for armature and field windings, with total slot number unchanged. For example, the number of coils contained in an armature coil group in Fig. 4.24 can be increased to be 4, while the number of coils for each field coil group is reduced to 2, and vice versa. Such modifications can potentially be used to adjust inductance values and to balance heat loadings.

It is seen from the theory that the machine’s performance is highly dependent on the air gap permeance variation, hence it is important at the design stage to achieve as large permeance swing as possible. Instead of utilising structurally salient rotors, other methods can also be adopted to further increase the permeance swing. Interior flux guides and barriers can be employed to enhance the flux concentration. Moreover, axial lamination technique is able to help decrease rotor saliency structurally, but increase the saliency magnetically. The reduction of rotor surface smoothness is advantageous to reduce the loss and noise associated with windage power.

The finite element analysis (FEA) in the project is based on 2D machine models, due to the fact that the main flux of heteropolar inductor machine is radial, unlike its homopolar counterpart, in which the main flux is both axial and radial. Compared with 3D modelling, 2D modelling for FEA is unable to simulate machine’s end effect, e.g. leakage flux linkage and copper loss etc. on end windings. The lack of end winding simulation inevitably compromises the accuracy of FEA, and the actual machine tends to exhibit slightly higher inductance and lower efficiency. A 3D modelling is necessary for a more precise assessment of machine’s behaviours, and should be regarded as a future work.

The analysis of internal local saturation and iron loss is only preliminarily discussed in the thesis, and the availability of relevant research in the literature is also very limited. This should be a major direction for future works aiming for proposing more quantitative analysis, more accurate modelling and the integration into control strategies.

Chapter 5: Control

5.1 Field characteristics

In the case of conventional rotor excited synchronous machines, the flux linkage linked with rotor field windings stays constant unless transient situations are undergone. However, a major difference of heteropolar inductor machines from conventional electrical machines is that the field windings are placed on stator side. The relative motion between rotor and stator will inevitably induce emf in each field winding when they are excited, due to the air gap variation. It is verified theoretically in Chapter 3. Practical measurement of open circuit emfs induced in three field windings is shown in Fig. 5.1.

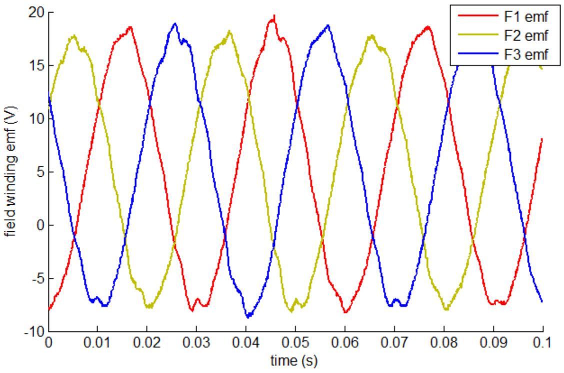

Fig. 5.1 Emfs induced in three field windings

As seen, field windings of heteropolar inductor machines also form a balanced three phase AC system, except that they are connected in series. The three phase components are superimposed on a DC component indicating resistance voltage drop. If observing from the field DC supply terminals, three phase AC components cancel out each other, leaving a pure DC terminal voltage.

The AC emf waveforms displayed in Fig. 5.1 implicitly contain rotor position information just as the case of a searching coil placed in salient rotor machines for detecting saliencies. Every point on the waveform is directly linked to a specific rotor position because of the way the emfs are induced. However, when the machine is loaded and armature currents start conducting, the situation becomes much more complicated. Armature reaction will cause the field winding voltages to deviate from no load waveforms. The voltage waveform recorded from field winding F_1 is compared with phase A armature voltage in Fig. 5.2 when the machine is supplied by switched mode power source.

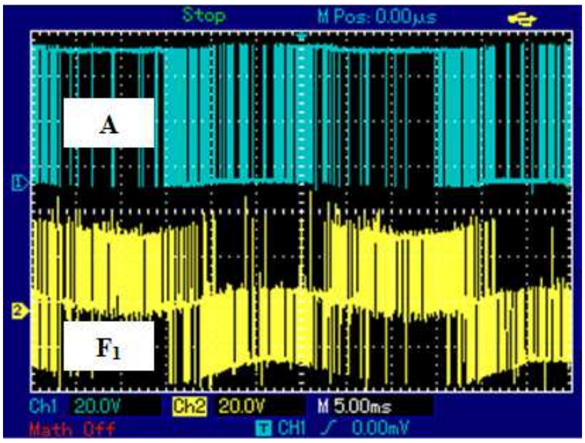

Fig. 5.2 Terminal voltage waveforms of phase A and field F_1 windings when machine is supplied by switched mode power source

The original no load field emf waveform shown in Fig. 5.1 is modulated by armature reaction components. Hence the extraction of rotor position information from field emf waveforms is no longer directly available. Nevertheless special characteristics of field windings are still worth exploring as position information is hidden implicitly in the waveforms. Appropriate demodulation methods can be applied to counteract the influence of armature reaction and to gain correct rotor position.

5.2 Sensorless estimation algorithm

Sensorless rotor angle and speed estimation schemes aim to indirectly obtain the angle speed information of electrical machines by observing measurements such as voltage, current and flux linkage. They greatly improve the robustness of a drive system by eliminating the use of mechanical encoder/resolver, which is considered to be one of the most mechanically fragile structures in the whole system. Hence the adoption of sensorless estimations is especially favourable for system with high demand in robustness, as discussed in section 2.2.2. Since the potential application area of heteropolar inductor machines is systems with high robustness and limited maintenance as introduced in section 1.1, the potentiality of developing a sensorless estimation scheme for this type of machine is worth exploring.

As discussed in Chapter 3, the ‘three phase’ flux linkages of 3 field windings are mathematically derived in (3.69 – 3.71). The equations are written in (5.1 – 5.3) with the main flux linkage and inductance terms expanded.

$$\begin{aligned}\lambda_{f1} &= \frac{1}{3}L_{lf}i_f + \frac{2\pi}{3}N_f^2 i_f lr\Lambda_0 - \frac{\sqrt{3}}{4}N_f^2 i_f lr\left(\overrightarrow{\Lambda_1}e^{j\frac{\pi}{3}} + \overrightarrow{\Lambda_1^*}e^{-j\frac{\pi}{3}}\right)\\ &+\frac{1}{2}k_{dp1}^{'}N_S N_f lr\Lambda_0\left(\overrightarrow{i_S}e^{-j\frac{\pi}{6}} + \overrightarrow{i_S^*}e^{j\frac{\pi}{6}}\right)\end{aligned} \tag{5.1}$$

$$\begin{aligned}\lambda_{f2} &= \frac{1}{3}L_{lf}i_f + \frac{2\pi}{3}N_f^2 i_f lr\Lambda_0 - \frac{\sqrt{3}}{4}N_f^2 i_f lr\left(\overrightarrow{\Lambda_1}e^{-j\frac{\pi}{3}} + \overrightarrow{\Lambda_1^*}e^{j\frac{\pi}{3}}\right)\\ &+\frac{1}{2}k_{dp1}^{'}N_S N_f lr\Lambda_0\left(\overrightarrow{i_S}e^{-j\frac{5\pi}{6}} + \overrightarrow{i_S^*}e^{j\frac{5\pi}{6}}\right)\end{aligned} \tag{5.2}$$

$$\begin{aligned}\lambda_{f3} &= \frac{1}{3}L_{lf}i_f + \frac{2\pi}{3}N_f^2 i_f lr\Lambda_0 - \frac{\sqrt{3}}{4}N_f^2 i_f lr\left(\overrightarrow{\Lambda_1}e^{j\pi} + \overrightarrow{\Lambda_1^*}e^{-j\pi}\right)\\ &+\frac{1}{2}k_{dp1}^{'}N_S N_f lr\Lambda_0\left(\overrightarrow{i_S}e^{j\frac{\pi}{2}} + \overrightarrow{i_S^*}e^{-j\frac{\pi}{2}}\right)\end{aligned} \tag{5.3}$$

It is worth expressing the field current i_f in the form of field space vector $\overrightarrow{i_f}$. With a simple complex vector manipulation, (5.1 – 5.3) can be performed in a slightly different way.

$$\lambda_{f1} = \frac{1}{3}L_{lf}i_f + \frac{2\pi}{3}N_f^2 i_f lr\Lambda_0 + \frac{\sqrt{3}}{4}N_f^2\Lambda_1 lr\left(\overline{i_f}e^{-j\frac{\pi}{6}} + \overline{i_f^*}e^{j\frac{\pi}{6}}\right)$$
$$+\frac{1}{2}k_{dp1}^{'}N_S N_f lr\Lambda_0\left(\overline{i_S}e^{-j\frac{\pi}{6}} + \overline{i_S^*}e^{j\frac{\pi}{6}}\right) \tag{5.4}$$

$$\lambda_{f2} = \frac{1}{3}L_{lf}i_f + \frac{2\pi}{3}N_f^2 i_f lr\Lambda_0 + \frac{\sqrt{3}}{4}N_f^2\Lambda_1 lr\left(\overline{i_f}e^{-j\frac{5\pi}{6}} + \overline{i_f^*}e^{j\frac{5\pi}{6}}\right)$$
$$+\frac{1}{2}k_{dp1}^{'}N_S N_f lr\Lambda_0\left(\overline{i_S}e^{-j\frac{5\pi}{6}} + \overline{i_S^*}e^{j\frac{5\pi}{6}}\right) \tag{5.5}$$

$$\lambda_{f3} = \frac{1}{3}L_{lf}i_f + \frac{2\pi}{3}N_f^2 i_f lr\Lambda_0 + \frac{\sqrt{3}}{4}N_f^2\Lambda_1 lr\left(\overline{i_f}e^{j\frac{\pi}{2}} + \overline{i_f^*}e^{-j\frac{\pi}{2}}\right)$$
$$+\frac{1}{2}k_{dp1}^{'}N_S N_f lr\Lambda_0\left(\overline{i_S}e^{j\frac{\pi}{2}} + \overline{i_S^*}e^{-j\frac{\pi}{2}}\right) \tag{5.6}$$

Although no space vector is generated for field flux linkage due to the series-connect field windings, the flux linkages of field windings still show a pattern of three phase distribution as the time-variant components separate each other by 2 π /3 in time. Therefore it is mathematically feasible to form a 'fictitious space vector' from flux linkages of field windings,

$$\overline{\lambda_f} = \lambda_{f1} + \lambda_{f2}e^{j\frac{2\pi}{3}} + \lambda_{f3}e^{-j\frac{2\pi}{3}} = \frac{3}{2}k_{dp1}^{'}N_S N_f lr\Lambda_0\overline{i_S}e^{-j\frac{\pi}{6}} + \frac{3\sqrt{3}}{4}N_f^2 lr\Lambda_1\overline{i_f}e^{-j\frac{\pi}{6}} \tag{5.7}$$

Both leakage flux linkage and time-invariant main flux linkage terms are balanced out during the formation of space vector $\overrightarrow{\lambda_f}$. Similar to the armature winding flux linkage space vector, $\overrightarrow{\lambda_f}$ is also effected by both armature and field current space vectors.

AC voltage component will be induced in each of the field windings due to flux linkage variation as shown in (5.8 – 5.10). The AC voltages of 'three phase' field windings are denoted as $\widetilde{u_{f1}}$, $\widetilde{u_{f2}}$ and $\widetilde{u_{f3}}$.

$$\widetilde{u_{f1}} = p\lambda_{f1} \tag{5.8}$$

$$\widetilde{u_{f2}} = p\lambda_{f2} \tag{5.9}$$

$$\widetilde{u_{f3}} = p\lambda_{f3} \tag{5.10}$$

AC voltages $\widetilde{u_{f1}}$, $\widetilde{u_{f2}}$ and $\widetilde{u_{f3}}$ are directly measurable via appropriate devices, and can be mathematically formed as a fictitious voltage space vector.

$$\overrightarrow{\widetilde{u_f}} = \widetilde{u_{f1}} + \widetilde{u_{f2}}e^{j\frac{2\pi}{3}} + \widetilde{u_{f3}}e^{-j\frac{2\pi}{3}} \tag{5.11}$$

Field AC voltage space vector $\overrightarrow{\widetilde{u_f}}$ can also be calculated directly from flux linkage space vector $\overrightarrow{\lambda_f}$ via differentiation.

$$\overrightarrow{\widetilde{u_f}} = p\overline{\lambda_f} = p\left(\frac{3}{2}k'_{dp1}N_S N_f lr\Lambda_0 \overline{i_S} e^{-j\frac{\pi}{6}}\right) + p\left(\frac{3\sqrt{3}}{4}N_f^2 lr\Lambda_1 \overline{i_f} e^{-j\frac{\pi}{6}}\right) \tag{5.12}$$

As already introduced in (3.67), the armature voltage space vector is composed by a resistance drop and an induction voltage resulted from armature winding flux linkage space vector $\overrightarrow{\lambda_S}$. $\overrightarrow{\lambda_S}$ is the summation of main flux linkage vector $\overrightarrow{\lambda_{mS}}$ and leakage flux linkage vector $\overrightarrow{\lambda_{lS}}$. It is fairly appropriate to approximately replace $\overrightarrow{\lambda_S}$ by $\overrightarrow{\lambda_{mS}}$, considering that the leakage flux linkage only occupies a very little portion of total armature winding flux linkage. Hence armature voltage space vector $\overline{u_S}$ can be written as

$$\overline{u_S} \approx \overline{i_S}R_S + p\overline{\lambda_{mS}} = \overline{i_S}R_S + p\left(\frac{3}{2}k'^2_{dp1}N_S^2 lr\Lambda_0 \overline{i_S}\right) + p\left(\frac{9}{4}k_{dp1}N_S N_f lr\Lambda_1 \overline{i_f}\right) \tag{5.13}$$

The prototype heteropolar inductor machine being analysed has an equal number of armature and field winding turns. It is worth noting that the denotation N_S in the equations represents the total number of turns of armature winding per phase, while N_f is the number of turns of one field coil (half field winding). In other words,

$$N_S = 2N_f \tag{5.14}$$

Moreover both winding factors k_{dp1} and k'_{dp1} are approximately equal to 1/2, as discussed in Chapter 4. Therefore

$$k_{dp1} \approx k'_{dp1} \approx \frac{1}{2} \tag{5.15}$$

Equations (5.12) and (5.13) can be modified by (5.14) and (5.15) with appropriate denotation for inductances.

$$\overrightarrow{u_f} = p\left(L_{mS}\overrightarrow{i_S}e^{-j\frac{\pi}{6}}\right)+\frac{\sqrt{3}}{3}\overrightarrow{e_S}\cdot e^{-j\frac{\pi}{6}} \tag{5.16}$$

$$\overrightarrow{u_S} = \overrightarrow{i_S}R_S + p\left(L_{mS}\overrightarrow{i_S}\right)+\overrightarrow{e_S} \tag{5.17}$$

Where

$$L_{mS} = \frac{3}{8}N_S^2 lr\Lambda_0 \tag{5.18}$$

$$L_{mfa} = \frac{9}{16}N_S^2 lr\Lambda_1 \tag{5.19}$$

And

$$\overrightarrow{e_S} = p\left(L_{mfa}\overrightarrow{i_f}\right) \tag{5.20}$$

Armature winding main inductance L_{mS} and field-armature mutual inductance L_{mfa} are the same as defined in previous chapters. Space vector $\overrightarrow{e_S}$ is denoted as internal emf space vector, and is calculated from three phase internal emfs. Hence,

$$\overrightarrow{e_S} = e_A + e_B\cdot e^{j\frac{2\pi}{3}} + e_C\cdot e^{-j\frac{2\pi}{3}} = e_S\cdot e^{j\rho} \tag{5.21}$$

The angular displacement ρ of vector $\overrightarrow{e_S}$ is directly related to rotor position. It indicates the location of q-axis in field orientation of machine.

It is easily spotted that (5.16) and (5.17) share certain similarities. Both armature and field current space vectors in (5.16) are shifted in phase by - $\pi/6$. The first term in (5.16) is exactly the same as the second term in (5.17), while the second term in (5.16) differs from the third term in (5.17) by merely a numeric factor. Therefore, the influence of armature reaction flux linkage vector can be eliminated if (5.16) is firstly shifted by $\pi/6$ in complex plain and then subtracted by (5.17). Only the internal emf space vector term and armature resistance drop term (sometimes negligible) are left after the process, and the angular position of field current vector $\overrightarrow{i_f}$ can be deduced.

The phase shift of vector $\overrightarrow{\widetilde{u_f}}$ is realised by multiplying the vector with complex number $e^{j\frac{\pi}{6}}$.

$$\overline{\widetilde{u}}_f{}' = \overline{\widetilde{u}}_f e^{j\frac{\pi}{6}} = p\left(L_{mS}\overline{i}_S\right) + \frac{\sqrt{3}}{3}\overline{e}_S \tag{5.22}$$

The original space vecter $\overrightarrow{\widetilde{u_f}}$ is shifted by $\pi/6$ and becomes a new space vector $\overrightarrow{\widetilde{u_f}}'$. The phase shift in (5.22) is a complex number arithmetic which can be processed within a micro-processer.

The purpose of phase shift is regarded as eliminating the time shift between armature voltage space vector $\overrightarrow{u_S}$ and field AC voltage vector $\overrightarrow{\widetilde{u_f}}$. The two space vectors are then regarded as being synchronised to same time instants. The vector diagrams of $\overrightarrow{\widetilde{u_f}}'$ and $\overrightarrow{u_S}$ are plotted in Fig. 5.3.

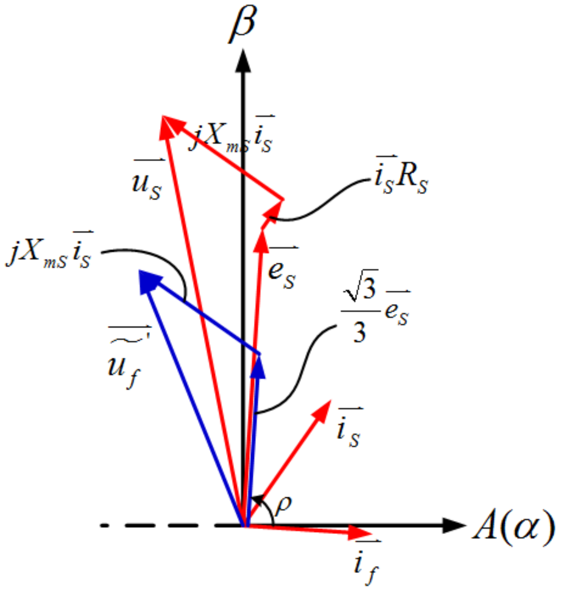
β
$jX_{mS}\overline{i}_S$
$\overline{i}_S R_S$
$\overline{u}_S$
$jX_{mS}\overline{i}_S$
$\overline{e}_S$
$\frac{\sqrt{3}}{3}\overline{e}_S$
$\overline{\widetilde{u}}_f{}'$
$\overline{i}_S$
ρ
$A(\alpha)$
$\overline{i}_f$

Fig. 5.3 Vector diagram of $\overrightarrow{\widetilde{u_f}}'$ and $\overrightarrow{u_S}$

As discussed, the armature reaction voltage space vector is cancelled by subtracting (5.17) by (5.22).

$$\overline{u}_S - \overline{\widetilde{u}}_f{}' = \overline{i}_S R_S + \left(1 - \frac{\sqrt{3}}{3}\right)\overline{e}_S \tag{5.23}$$

Equation (5.23) can be decoupled by being decomposed into the stationary complex frame coordinated by α axis (real axis) and β axis (imaginary axis). α axis coincides with machine's reference axis (i.e. phase A axis), while β axis is orthogonal to α axis. The two axis equations are

$$\begin{cases} u_{S\alpha} - \widetilde{u_{f\alpha}}' - i_{S\alpha}R_S = \left(1 - \dfrac{\sqrt{3}}{3}\right) e_{S\alpha} \\ u_{S\beta} - \widetilde{u_{f\beta}}' - i_{S\beta}R_S = \left(1 - \dfrac{\sqrt{3}}{3}\right) e_{S\beta} \end{cases} \tag{5.24}$$

The projection of internal emf space vector onto two stationary axis ($e_{S\alpha}$ and $e_{S\beta}$) are solved by rearranging (5.24),

$$\begin{cases} e_{S\alpha} = \dfrac{u_{S\alpha} - \widetilde{u_{f\alpha}}' - i_{S\alpha}R_S}{1 - \dfrac{\sqrt{3}}{3}} \\ e_{S\beta} = \dfrac{u_{S\beta} - \widetilde{u_{f\beta}}' - i_{S\beta}R_S}{1 - \dfrac{\sqrt{3}}{3}} \end{cases} \tag{5.25}$$

Under certain circumstances, current measurements are not absolutely necessary for the estimation. For instance, in large electrical machines, armature winding resistance is small and often negligible. In this case (5.25) can be further reduced to (5.26) without any substantial compromise to the estimation algorithm.

$$\begin{cases} e_{S\alpha} = \dfrac{u_{S\alpha} - \widetilde{u_{f\alpha}}'}{1 - \dfrac{\sqrt{3}}{3}} \\ e_{S\beta} = \dfrac{u_{S\beta} - \widetilde{u_{f\beta}}'}{1 - \dfrac{\sqrt{3}}{3}} \end{cases} \tag{5.26}$$

Obviously $e_{S\alpha}$ and $e_{S\beta}$ are orthogonal quantities and are governed by orthogonal trigonometric functions. The angular position ρ of internal emf space vector $\overrightarrow{e_S}$ in complex plain can be derived with the assistance of inverse trigonometric arithmetic. Hence,

$$\rho = \begin{cases} \sin^{-1}\left(\dfrac{e_{S\beta}}{\sqrt{e_{S\alpha}^2 + e_{S\beta}^2}}\right), & e_{S\alpha} \geq 0 \\ \pi - \sin^{-1}\left(\dfrac{e_{S\beta}}{\sqrt{e_{S\alpha}^2 + e_{S\beta}^2}}\right), & e_{S\alpha} < 0 \end{cases} \tag{5.27}$$

The waveforms of estimated $e_{S\alpha}$ and $e_{S\beta}$ are plotted in Fig. 5.4 with zero-crossing points emphasised. $e_{S\alpha}$ and $e_{S\beta}$ are assumed to have constant amplitude and frequency.

The waveforms of $e_{S\alpha}$ and $e_{S\beta}$ cross zero alternately, and the separation of each zero-crossing is $\pi/2$ in electrical radian. The average electrical speed between adjacent zero-crossings is thus estimated by dividing $\pi/2$ by the total time spent between adjacent points.

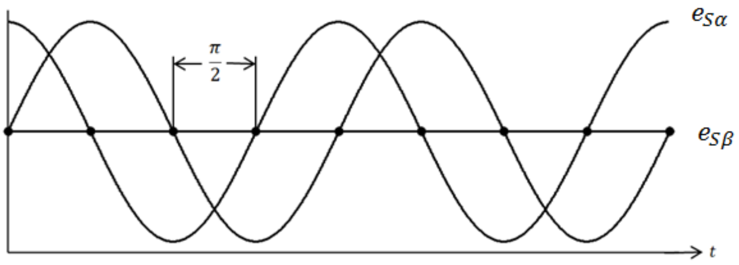

Fig. 5.4 Conceptual waveforms of $e_{S\alpha}$ and $e_{S\beta}$ with zero-crossings

The actual rotor mechanical speed is 1/4 of the electrical speed and the proposed speed estimation method provides 16 speed updates per rotor revolution. This will generally meet the speed control purposes if the precision of speed sensing is not highly demanded. Demonstrative speed estimation during the machine acceleration process is shown in Fig. 5.5. It is shown that the speed trajectory is in a step form, and a filter may be applied to smoothen it.

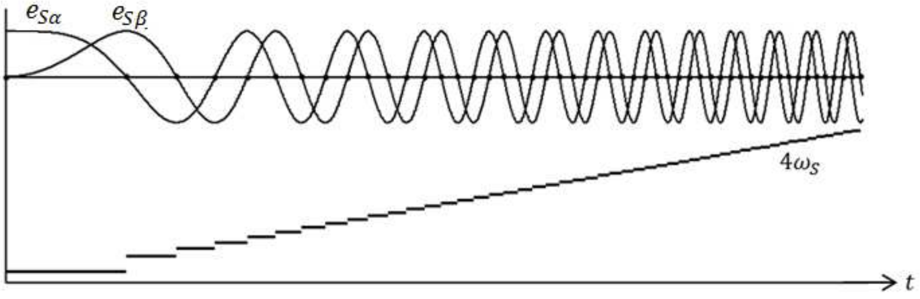

Fig. 5.5 Deduction of electrical speed from waveforms of $e_{S\alpha}$ and $e_{S\beta}$

Overall, the block diagram of the sensorless position and speed estimation scheme discussed is plotted in Fig. 5.6.

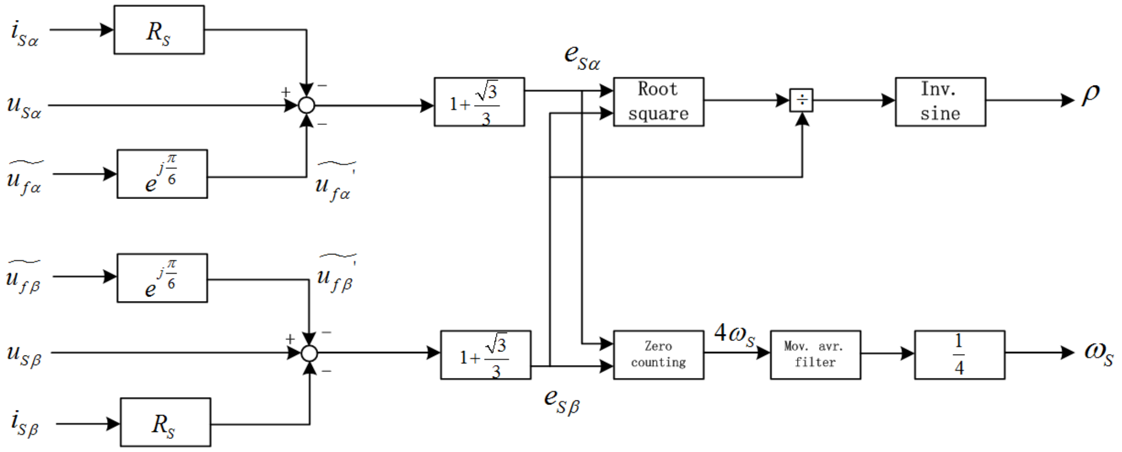
$i_{S\alpha}$
R_S
$u_{S\alpha}$
$\widetilde{u_{f\alpha}}$
$e^{j\frac{\pi}{6}}$
$\widetilde{u_{f\alpha}}'$
$1+\frac{\sqrt{3}}{3}$
$e_{S\alpha}$
Root square
÷
Inv. sine
ρ
$\widetilde{u_{f\beta}}$
$e^{j\frac{\pi}{6}}$
$\widetilde{u_{f\beta}}'$
$u_{S\beta}$
$1+\frac{\sqrt{3}}{3}$
Zero counting
$4\omega_S$
Mov. avr. filter
$\frac{1}{4}$
ω_S
$e_{S\beta}$
$i_{S\beta}$
R_S
+
−

Fig. 5.6 Block diagram of proposed sensorless position and speed estimation

There are several potential advantages associated with the proposed position and speed estimation strategy.

(1) As discussed before, the acquisition of position and speed information is free from any external sensors or auxiliary signal injection devices for saliency detection. The quantities are estimated from the measured voltages and currents. The algorithm is programmed and processed within a single micro-controller chip.

(2) Unlike many other sensorless estimation schemes, the proposed method only involves simple mathematical operations e.g. sum, subtraction, multiplication, division and square root. The inverse trigonometric operations are realized by pre-programmed look-up tables in the program. Therefore, the accuracy of estimation is improved by eliminating the possibility of potential integration drift. Both position and speed estimations are updated every time the calculation subroutine is called and as a result, previous estimations will have zero influence on current estimation.

(3) The estimations are mainly based on voltage measurements and are insensitive to variations of machine parameters (e.g. resistance, inductance) that are potentially caused by temperature rise and saturation.

5.3 Experimentation

5.3.1 Experiment setup

The test machine experimented in this chapter is slightly different from that in the previous chapters. The stator side provides additional terminals for measuring field winding emf. The controller/drive system consists of a micro-processor (Texas Instruments Launchxl-F28027), several ADC and DAC interfaces, an IGBT gate drive (International Rectifier IRAMS10UP60B), a DC buck converter, an optical encoder (Bourns ENC1J-D28-L00128L) and a number of Hall-effect current sensors (LEM LTSR 6-NP). The circuit designs for electronic interfaces and buck converter is attached in Appendix II. The system frequency is 10kHz and the voltage ranges for both ADC and DAC pins of micro-controller are 0 to 3.3V. The complete experiment setup is as shown in Fig. 5.7.

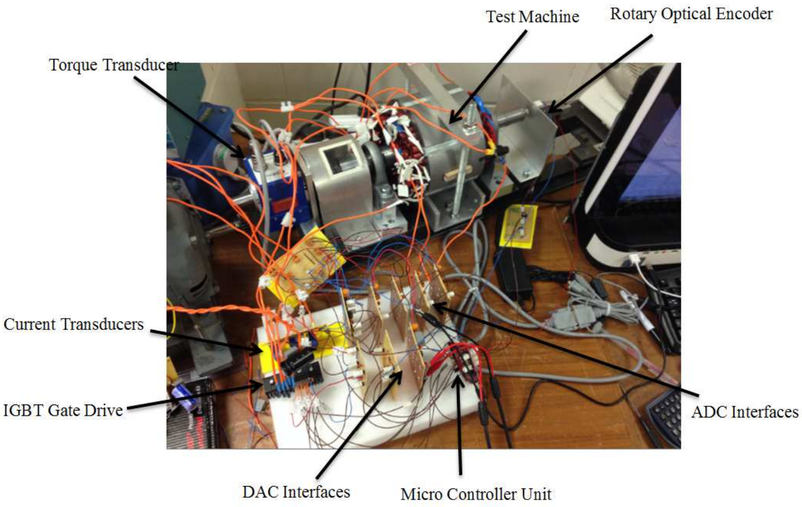
Test Machine
Rotary Optical Encoder
Torque Transducer
Current Transducers
IGBT Gate Drive
ADC Interfaces
DAC Interfaces
Micro Controller Unit

Fig. 5.7 Set-up of experimental drive system

The experimental results for validating the sensorless position and speed estimations are discussed in this section. The waveforms are regulated to be within the range of -1 to +1 p.u. They are output from DAC pins of the micro-controller and picked up by oscilloscope probes via the DAC interfaces. The p.u. system and base quantity values are introduced in detail in next section.

5.3.2 Q-axis position estimation

The field current i_f for this part of experiments is fixed at 2A.

As shown in the previous section, the sensorless position estimation algorithm is designed to locate the position of q-axis, i.e. the angle internal emf space vector ρ. The mathematical expression of internal emf space vector $\overrightarrow{e_S}$ in complex form can be derived from (5.20).

$$\overrightarrow{e_S} = p\left(L_{mfa}\overrightarrow{i_f}\right) = j4\omega_S L_{mfa}\overrightarrow{i_f} = 4\omega_S L_{mfa} i_f e^{j4\xi} \tag{5.28}$$

Therefore

$$\rho = 4\xi \tag{5.29}$$

The q-axis position is 4 times the rotor saliency axis position ξ, also implying that the speed of q-axis rotation (i.e. electrical speed) is 4 times the actual rotor rotation speed (i.e. mechanical speed).

The estimated q-axis position and actual rotor axis position under 2 different speeds are compared in Fig. 5.8. The rotor axis position is measured by the in-shaft optical encoder. It is observed that in both high speed (500rpm) and low speed (150rpm) cases, q-axis experiences 4 periods while the rotor finishes a full revolution.

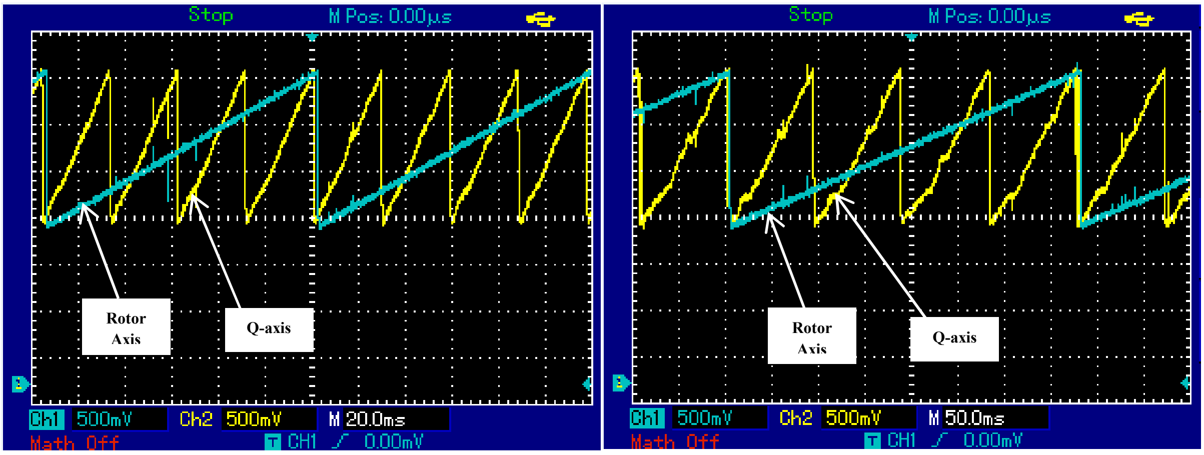

(a) (b)

Fig. 5.8 Comparison between estimated q-axis position and actual rotor position at (a) 500rpm and (b) 150rpm

The estimated q-axis position waveform is compared with the reference q-axis position to evaluate the accuracy of the estimation. The estimated and reference positions when the machine is running with no load at two different speeds are compared in Fig. 5.9, with the estimation error highlighted.

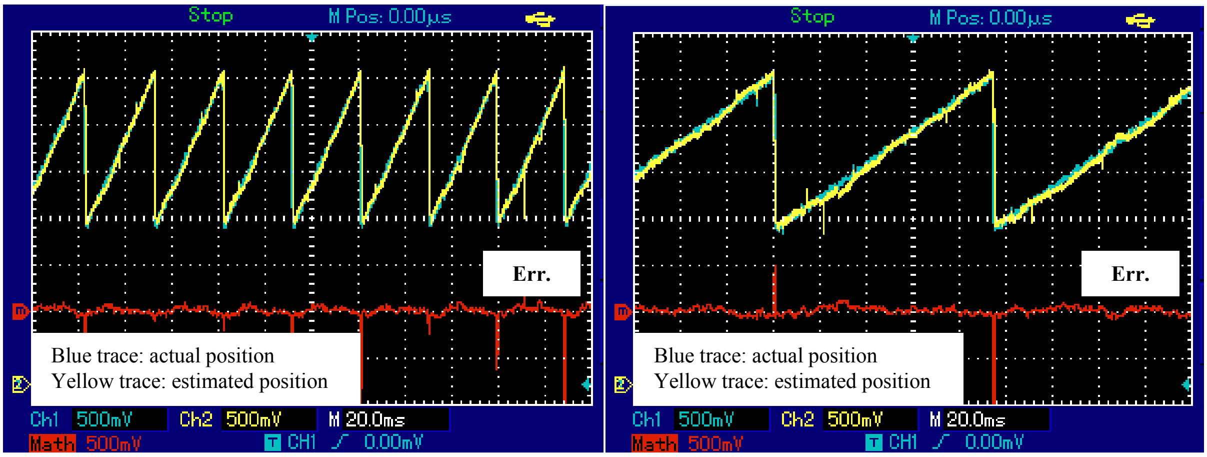

(a) (b)

Fig. 5.9 Comparison between estimated and actual q-axis positions with no load at (a) 500rpm and (b) 150rpm

It is seen from Fig. 5.9 that the waveforms of estimated (yellow) and reference (blue) q-axis are almost indistinguishable under both speeds. Their differences are plotted in red lines. Generally the estimation error is restricted below 10% of the waveform amplitude. The spikes appearing on the error waveforms are due to the transitions from 2π to 0 of the position saw tooth waveforms.

The q-axis position waveforms estimated and measured when the machine is loaded (i_q= 1.5A) are compared in Fig. 5.10. The estimation error at high speed (500rpm) is not considerably affected by loading to the machine, and is well maintained within 5%. However the maximum estimation error at low speed (150rpm) is increased to approximately 15% when the machine is loaded. It is because that the armature resistive voltage drop at high machine speed is negligible compared with the internal emf, while it becomes influential in the case of low machine speed.

The position estimation performance is also evaluated with transient loading conditions. It is realised by applying a sudden load (i_q= 1.5A) to the machine while it is under steady state no load operation. Fig. 5.11 evaluates the position estimations with sudden loading at two different speeds.

.

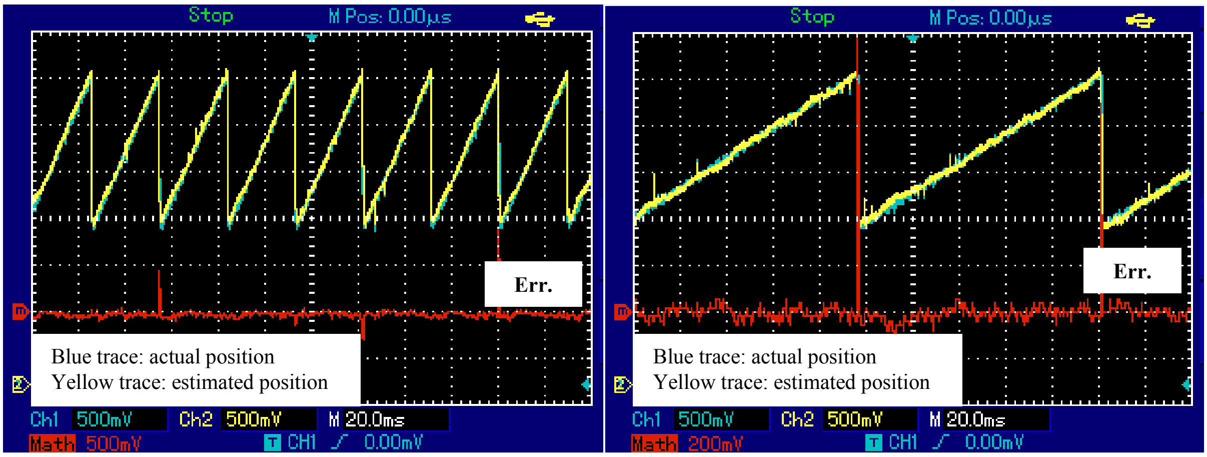

(a) (b)

Fig. 5.10 Comparison between estimated and actual q-axis positions with load at (a) 500rpm and (b) 150rpm

The deviation of estimated q-axis position from the reference is increased during the transient of sudden loading. As indicated in Fig. 5.11, the transient estimation error is more or less doubled for both high speed and low speed modes. The error at 500rpm is increased from approximately 5% to 10%, while it is increased from approximately 8% to a maximum of 20% when the test machine is operating at 150rpm. Even through, the position error is still within acceptable range and it decays after the machine transitions from transient state to steady state.

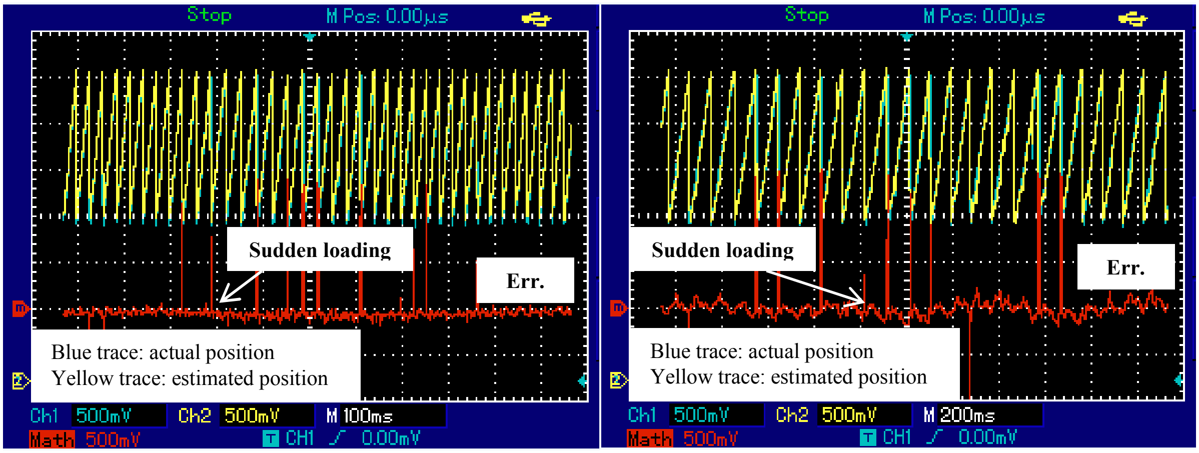

(a) (b)

Fig. 5.11 Comparison between estimated and actual q-axis positions with transient load at (a) 500rpm and (b) 150rpm

In summary the q-axis position estimation is satisfactory under various conditions, compared with measured actual q-axis position. It is also worth noting that the estimation error is, to some extent, subject to quantisation error introduced by optical encoder and calibration of ADC interfaces.

5.3.3 Rotor speed estimation

The field current i_f for this part of experiments is fixed at 2A.

As discussed, rotor speed estimation is implemented by counting zeroes for the orthogonal internal emf waveforms (i.e. $e_{s\alpha}$ and $e_{s\beta}$). It is therefore vital for speed estimation that the estimations of $e_{s\alpha}$ and $e_{s\beta}$ are obtained correctly. The waveforms of $e_{s\alpha}$ and $e_{s\beta}$ at two different machine speeds are recorded in Fig. 5.12. The two waveforms are scaled to p.u. values and output via ADCs.

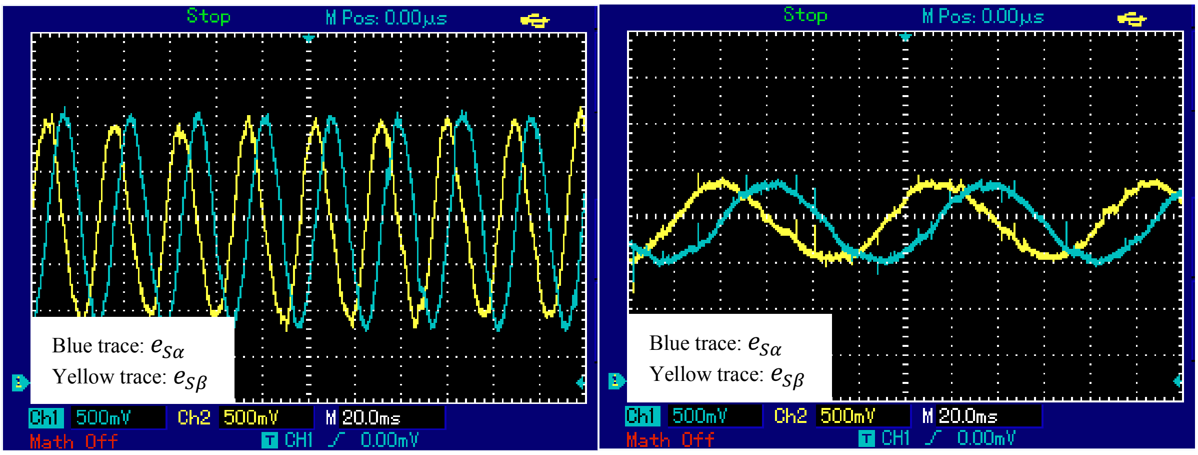

(a) (b)

Fig. 5.12 Actual waveforms of $e_{s\alpha}$ and $e_{s\beta}$ at (a) 500rpm and (b) 150rpm

The amplitude and frequency of emf waveforms are proportional to the rotor speed, as seen by comparing the waveforms at different speeds. It is shown in Fig. 5.12 that $e_{s\alpha}$ and $e_{s\beta}$ are orthogonal sinusoidal waveforms with a small amount of ripple superimposed.

Steady state speed estimation is compared with measured actual rotor speed in Fig. 5.13. A digital moving average filter is implemented in the processor to attenuate speed ripples. Three speed steps are performed. The speed estimation exhibits good correspondence with reference speed (i.e. actual speed) even at low speed range. The average error is controlled within less than 5%.

Transient speed estimation capability is also explored. The estimated and reference rotor speeds are recorded when a considerable sudden load is applied to the steadily running machine and causes a substantial transient speed drop. The results are plotted in Fig. 5.14.

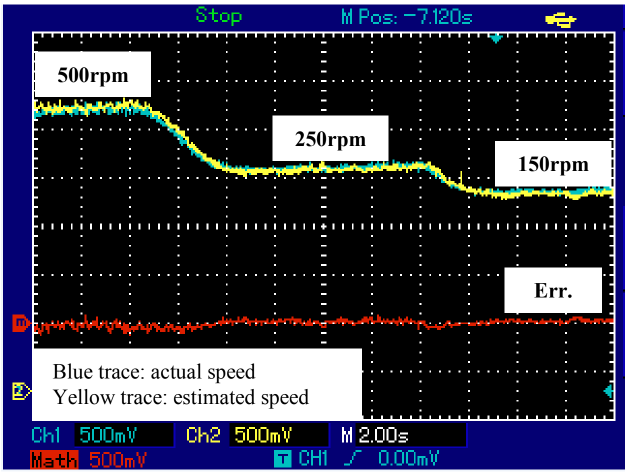

Fig. 5.13 Comparison between estimated and actual steady state rotor speeds at 500rpm, 250rpm and 150rpm

In both high speed and low speed cases, estimated and reference rotor speeds experience a significant speed drop in response to the sudden loading on the shaft. Generally, the speed estimation under steady rotor speed coincides well with reference speed. However, there is an obvious lag of estimated speed response during the transient compared with the actual speed response. It is due to the time delay introduced by the moving average filter. The amount of lag is determined by the time constant of the filter.

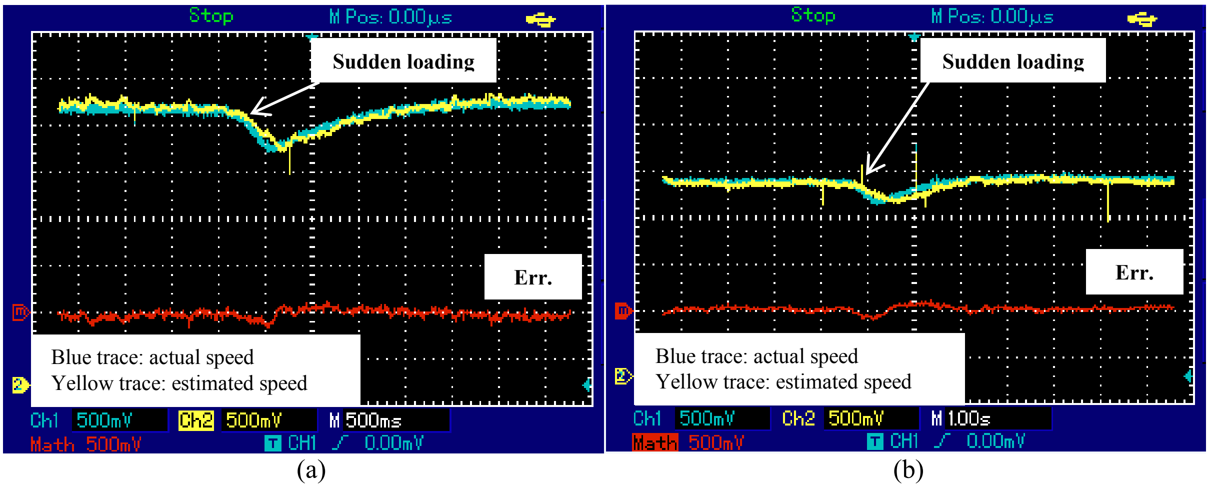

Fig. 5.14 Comparison between estimated and actual rotor speeds with transients at (a) 500rpm and (b) 150rpm

5.3.4 Field weakening

The experiments conducted so far are based on a fixed field current value (i.e. i_f=2A). However, in practical applications, a reduction of field excitation, known as field weakening, is often necessary for the machine to enter constant power operation mode and to extend operational speed range. It is therefore important that the sensorless controller scheme functions appropriately during field weakening.

The field supply for test machine is controlled by a DC-DC buck converter. Field weakening is realised by varying the duty cycle of the power switch. In the experiment, the field voltage is controlled to decrease from 16V to 8V within 160ms, resulting in a field current drop from 2A to 1A. The resultant field current drop is recorded in Fig. 5.15.

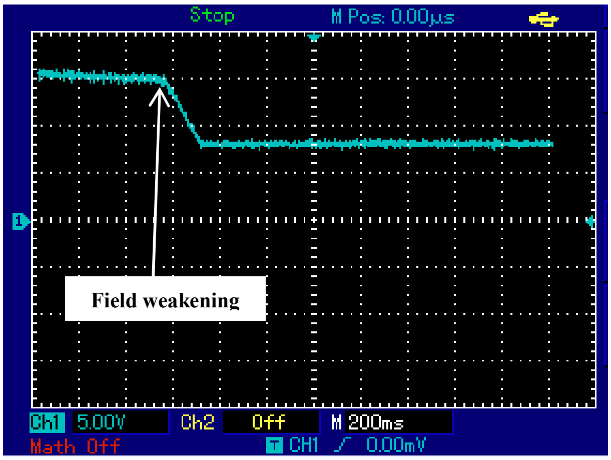

Fig. 5.15 Field current supply during field weakening

The position estimation is evaluated for field weakening transient, as shown in Fig. 5.16. The error level maintains more or less the same before, during, and after field weakening. Hence it is concluded that variation in field voltage/current has no significant influence on the sensorless estimation algorithm.

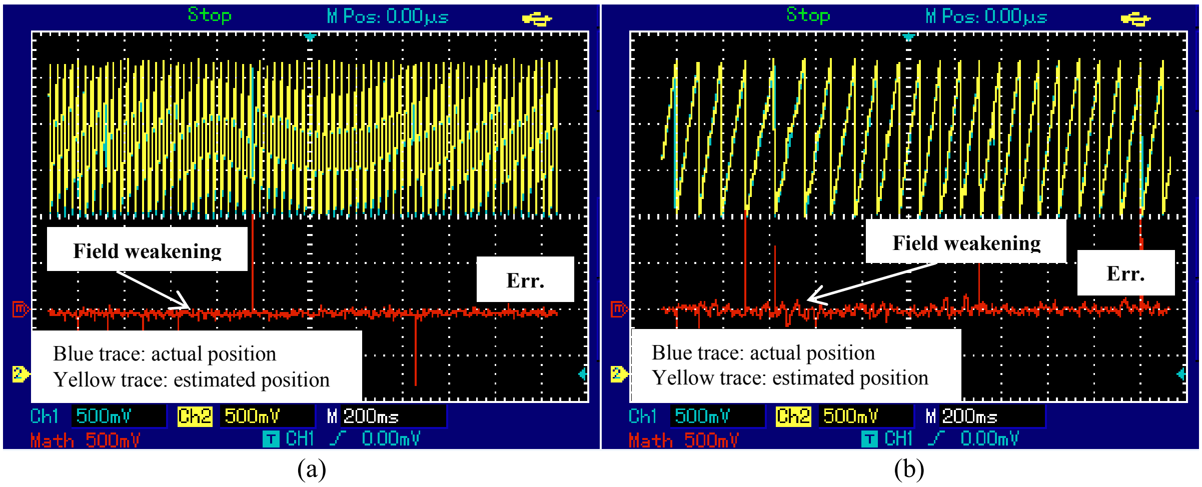

Fig. 5.16 Comparison between estimated and actual q-axis positions with field weakening at (a) 500rpm and (b) 150rpm

5.4 Prototype drive system

5.4.1 Start-up process

A controller and drive system is designed, aiming to enable the test machine to start up from stand-still to a nominal speed, as in most motor drive applications. The system block diagram is shown in Fig. 5.17.

The sensorless position and speed estimation algorithm is programmed in the micro-controller as a module. Field oriented control strategy is implemented in the system. Two feedback loops are seen from Fig. 5.17. Armature current measurements are passed through Clarke's Transform block and are compared with reference signals. Current differences are fed to current hysteresis controllers for appropriate IGBT drive switching patterns. The actual machine speed is fed back to form an outer speed control loop. The speed difference is passed through a PI controller for creating reference q-axis current signal.

The sensorless estimation block plays a significant role in both feedback loops. The estimated q-axis position is used as an angular reference for the inverse Park's Transform, while the estimated rotor speed closes the speed feedback loop. Armature current signals are also input into the estimation block due to the fact that resistance in test machine cannot be neglected.

All quantities processed within the micro-controller are in p.u. system to avoid exceeding digital length limit. The base values of important quantities are listed in Table 5.1.

Base quantity	***Base value***
Base apparent power S_b	270 VA
Base voltage V_b	30 V
Base current I_b	3 A
Base rotor speed ω_{Sb}	70 rad/s
Base torque T_b	3.86 Nm
Base impedance Z_b	10 Ω
Inertia Constant H	0.11 s

Table 5.1 Base values for p.u. system of the drive system

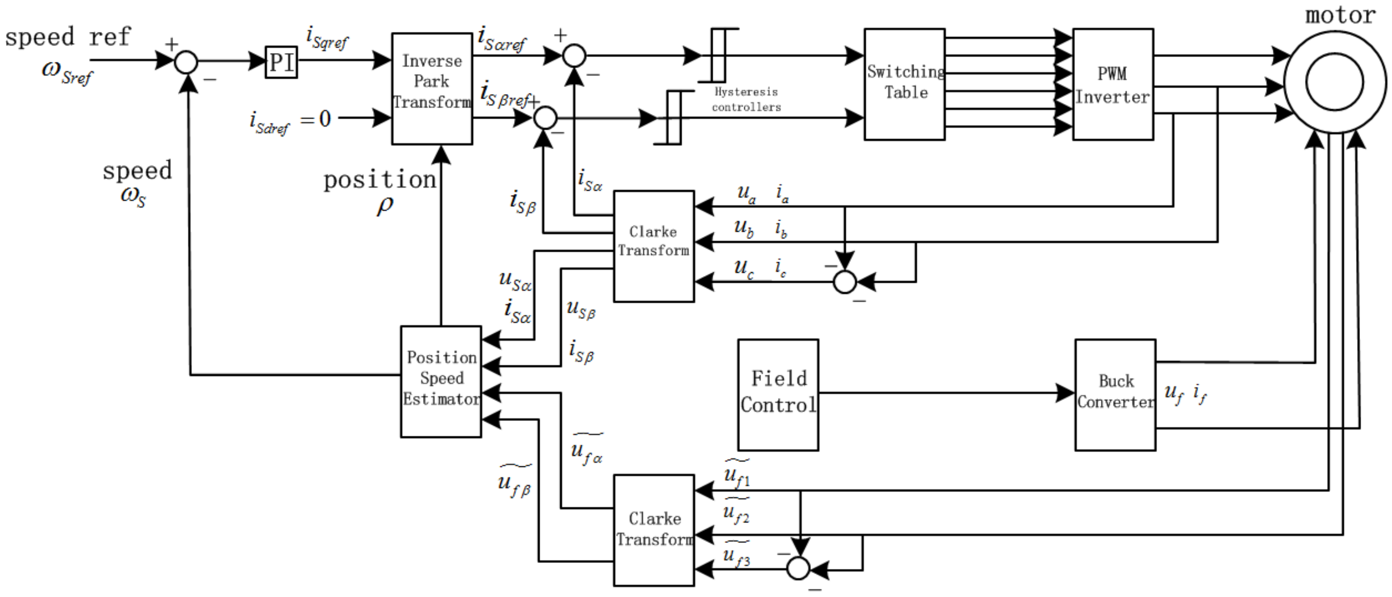
speed ref
ω_{Sref}
+
−
PI
i_{Sqref}
$i_{Sdref} = 0$
Inverse Park Transform
$i_{S\alpha ref}$
$i_{S\beta ref}$
+
−
Hysteresis controllers
Switching Table
PWM Inverter
motor
speed
ω_S
position
ρ
$i_{S\beta}$
$i_{S\alpha}$
Clarke Transform
u_a i_a
u_b i_b
u_c i_c
$u_{S\alpha}$
$i_{S\alpha}$
$u_{S\beta}$
$i_{S\beta}$
Position Speed Estimator
Field Control
Buck Converter
u_f i_f
$\widetilde{u_{f\alpha}}$
$\widetilde{u_{f\beta}}$
Clarke Transform
$\widetilde{u_{f1}}$
$\widetilde{u_{f2}}$
$\widetilde{u_{f3}}$

Fig. 5.17 Block diagram for closed loop field oriented control of prototype drive system

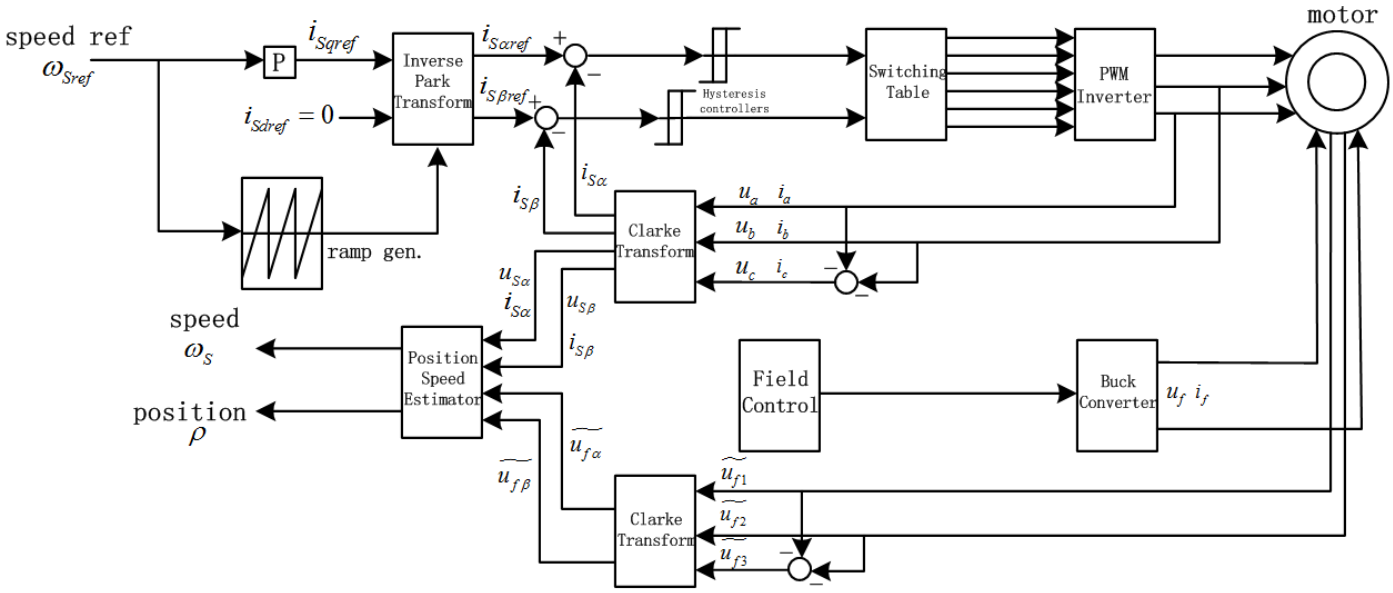
speed ref
ω_{Sref}
P
i_{Sqref}
$i_{Sdref} = 0$
Inverse Park Transform
$i_{S\alpha ref}$
$i_{S\beta ref}$
+
−
Hysteresis controllers
Switching Table
PWM Inverter
motor
ramp gen.
speed
ω_S
position
ρ
$i_{S\beta}$
$i_{S\alpha}$
Clarke Transform
u_a i_a
u_b i_b
u_c i_c
$u_{S\alpha}$
$i_{S\alpha}$
$u_{S\beta}$
$i_{S\beta}$
Position Speed Estimator
Field Control
Buck Converter
u_f i_f
$\widetilde{u_{f\alpha}}$
$\widetilde{u_{f\beta}}$
Clarke Transform
$\widetilde{u_{f1}}$
$\widetilde{u_{f2}}$
$\widetilde{u_{f3}}$

Fig. 5.18 Block diagram for open loop field oriented control of prototype drive system

By analyzing the position and speed estimation algorithms, it is shown that the method is voltage based. This poses a problem as the position and speed estimations are ineffective when the rotor speed is zero and no voltage is induced. Moreover, when the rotor is at a relatively low speed, the accuracy of estimation is compromised due to the influence of dominant resistive voltage drop. Hence it is necessary to start up the machine before the estimator plays the role appropriately.

A simple open loop start-up method is implemented in the project [89]: the test machine is driven by open loop control firstly and the feedback cuts in once the estimator is able to function effectively. Initially the three phase IGBT drive is controlled to inject three phase currents that form a slowly accelerating current space vector in the direction of rotation. Due to the energy variation in air gap, the rotor will tend to follow the current vector. Finally the rotor is pulled up to a designated initial speed for closed loop operation. The block diagram of open loop start-up control is shown in Fig. 5.18.

Field oriented open loop control is used for the initial start-up process, and the angle information referenced by inverse park transform block is generated by an internal angle generator in micro-processor. For the reason that the d-q axes are not directly derived from actual rotor positions, the q axis current may not coincide with the actual q axis and the field oriented control risk a compromise in performance. This situation can be mitigated by presetting an initial rotor position before starting up. The rotor can be locked initially to phase A axis by injecting a DC current into phase A windings only, and the air gap permeance variation forces the rotor saliency to align.

It is of extreme importance that the test machine speed is correctly estimated before the feedback signal cuts in, as failure to do so will lead to wrong error speed signals and such fault can accumulate. In other words, the position and speed estimator must become functional within the region of open loop start-up process. Consequently the selection of speed ramp slope and total start up time of the open loop process is determined by the shortest time for obtaining satisfactory estimations. After repetitive experiments with prototype machine, it is found that speed estimations can always successfully function if the speed reference of open loop start up process lasts for approximately 3s with a final speed of approximately 100 rpm.

Overall, the experimental drive system firstly accelerates the machine to 100rpm within 3s by open loop start-up method, and the machine continues to accelerate final speed of 500 rpm once the speed feedback cuts in. In closed loop control stage, the ramp of speed reference increases considerably and lasts for another 3s. The speed reference ω_{Sref} for the whole process from standstill to 500 rpm is shown in Fig. 5.19.

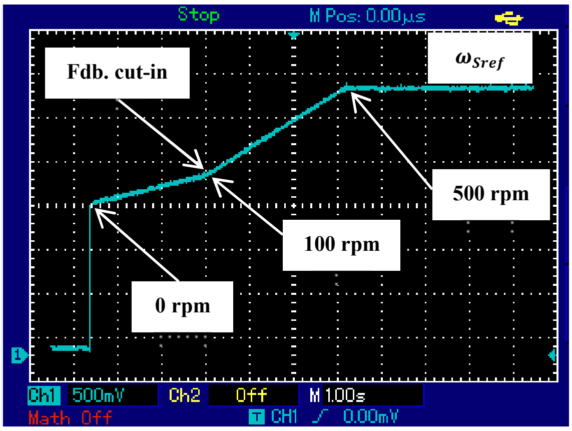

Fig. 5.19 Speed reference of complete start-up process for the drive system

5.4.2 PI tuning

The speed loop response is governed by a proportional-integral (PI) controller block and its internal structure is sketched in Fig. 5.20. The estimated actual speed (fdb) is compared with the reference value (ref) at each sampling instant and the error (err) between two speeds enters the PI controller to create a torque reference (out). The saturation block (sat.) protects the system from over-rated outputs. The proportional gain and integral gain of controller are denoted as k_p and k_i.

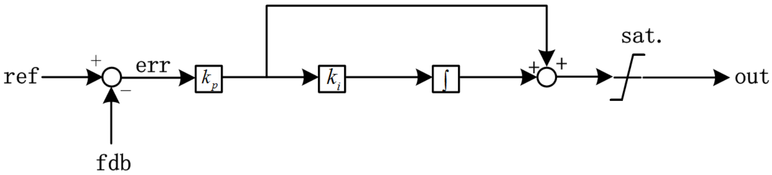

Fig. 5.20 Sketch of PI controller

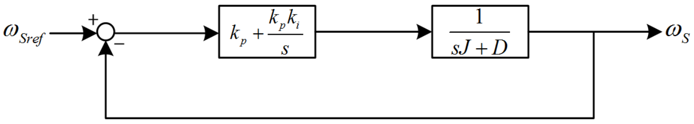

Fig. 5.21 Simplified block diagram of control system

By reasonably assuming that the mechanical time constant is much greater than the electrical time constant, the speed feedback control block diagram is simplified as shown in Fig. 5.21. The effect of saturation and is neglected in the block diagram.

The resulting transfer function of the system in s-domain is

$$T(s)=\frac{\frac{k_p(s+k_i)}{J}}{s^2+\frac{D+k_p}{J}s+\frac{k_pk_i}{J}} \tag{5.30}$$

The natural oscillation frequency ω_n and damping factor σ are expressed as

$$\omega_n=\sqrt{\frac{k_pk_i}{J}} \tag{5.31}$$

$$\sigma=\frac{D+k_p}{2\sqrt{k_pk_iJ}} \tag{5.32}$$

The transfer function $T(s)$ indicates that the system is a second order system and the dynamic response of the system is largely dictated by the combination of k_p and k_i. The influences of different k_p and k_i values on the experiment system are discussed in this section.

The PI controller downgrades to a pure proportional controller if k_i is absent, and the system shown in Fig. 5.21 becomes a first order system. Proportional controller can only output reference torque value when there is an error. Therefore, as shown in Fig. 5.22, the estimated actual speed (yellow line) of the test machine in this case will always pose a steady state error compared with the reference (blue line).

It is also observed that the speed estimation is not fully functional at the beginning of the starting process. However, the speed estimator manages to correctly estimate the rotor speed before entering acceleration stage, at a time between 2s and 3s.

The steady state error can be completely eliminated by the involvement of k_i, hence forming a second order system at the risk of instability. Fig. 5.23 shows the dynamic response of rotor speed when k_i is too large. As shown, the actual speed deviates from the reference by an overshoot immediately after the speed estimation is managed and feedback loop cuts in. The system is underdamped. On the other hand, the estimated actual speed keeps track of the reference eventually, with the absence of steady state speed error.

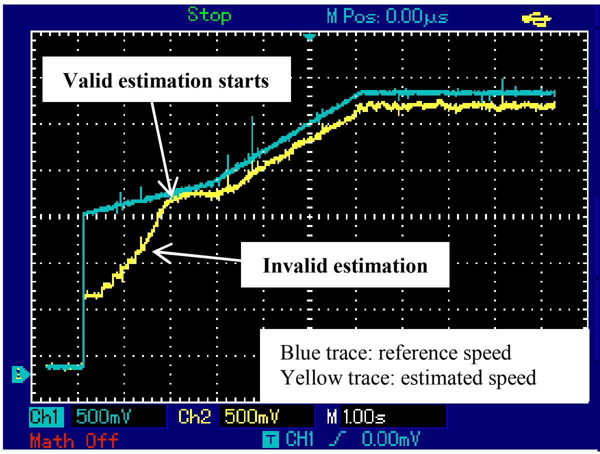

Fig. 5.22

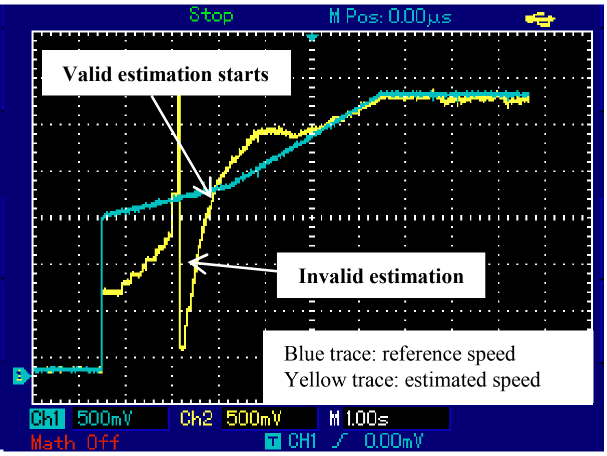

Fig. 5.23

Fig. 5.22 Comparison between actual and reference speeds with k_p only in control system
Fig. 5.23 Comparison between actual and reference speeds with large k_i in control system

The proportional gain k_p can still affect the performance of a second order system. Fig. 5.24 and Fig. 5.25 illustrate the situations when small and large values of k_p are in effect respectively. For a small value of k_p, the speed error has to be increased for outputting demanded torque during the acceleration region.

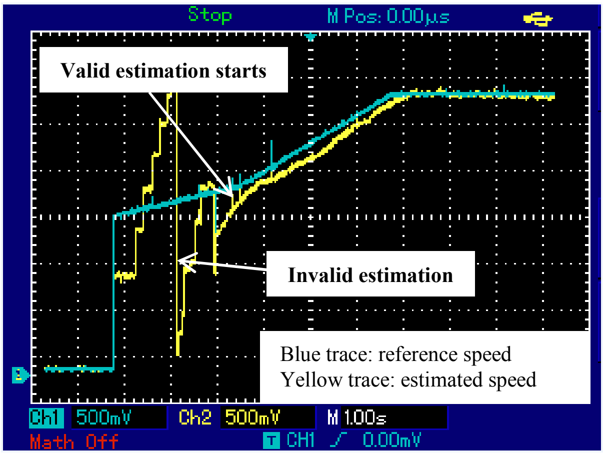

Fig. 5.24

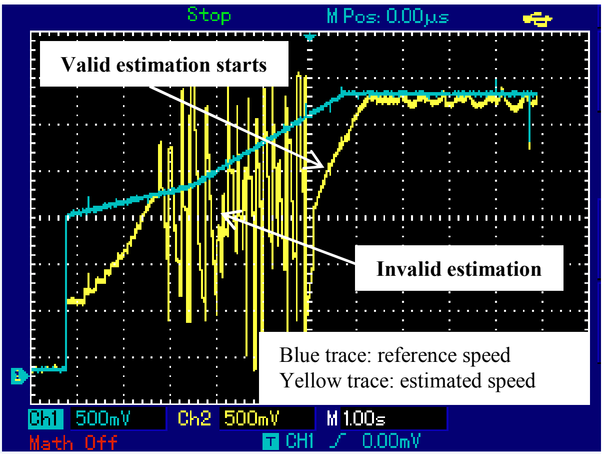

Fig. 5.25

Fig. 5.24 Comparison between actual and reference speeds with small k_p in control system
Fig. 5.25 Comparison between actual and reference speeds with large k_p in control system

It is observed on Fig. 5.24 that the speed difference is greatest in the middle of acceleration region and reduces gradually afterwards. It is because that the integral controller output becomes greater and greater as the errors of past instants keep accumulating. The analysis proves that the effect of k_i is lagging as it is based on past values. It is important to select a moderate value for k_p as it is responsible for instantaneous torque reference generation.

When the k_p is too large, as shown in Fig. 5.25, the speed estimation in the whole acceleration region is corrupted even though the open loop speed is successfully estimated before feedback loop cuts in. Due to the large value of k_p, even a tiny deviation of speed from reference will cause an excessively large torque reference and result in rapid speed oscillation. The instantaneous speed is so large that it may exceed the range of numeric limits of micro-processor program and the DAC output range. The spikes in Fig. 5.25 indicate the data overflow and under such a condition, the speed estimation fails. Oscillations still exist in the region of steady speed when little deviation occurs.

It is mentioned that the integral controller is based on past information in an accumulating manner. Controller error will occur when the accumulated error is not neutralized promptly. For example, when a sudden large load disturbance occurs and disappears quickly, machine speed will drop and rapidly recover with considerable speed error accumulated by the integrator. However, the integral controller will continue outputting a torque reference even if the speed recovers, because that the accumulated errors in integrator cannot be nulled, or unwound, instantly. Therefore, a speed overshoot is expected. Fig. 5.26 shows the speed response when a sudden load is exerted on the test machine. An overshoot is clearly seen after speed bounces back due to the so called integrator windup.

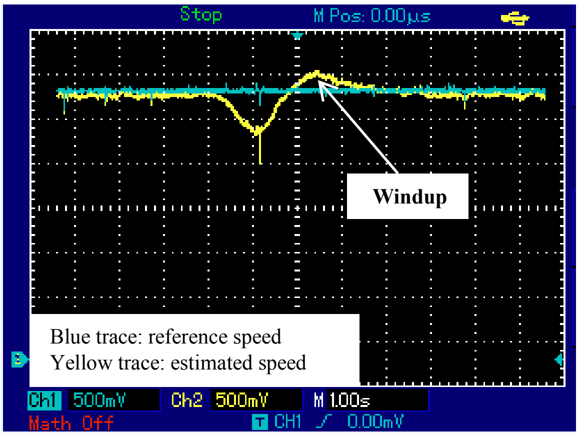

Fig. 5.26 Integrator windup effect during speed transient

In order to overcome the integrator windup for a better transient performance, necessary anti-windup strategy is applied. An improved PI controller is sketched in Fig. 5.27. As shown, anti-windup strategy is added by introducing a third controllable parameter: saturation correction gain k_c. The pre- and post- saturation output values are compared and fed back to modulate original output.

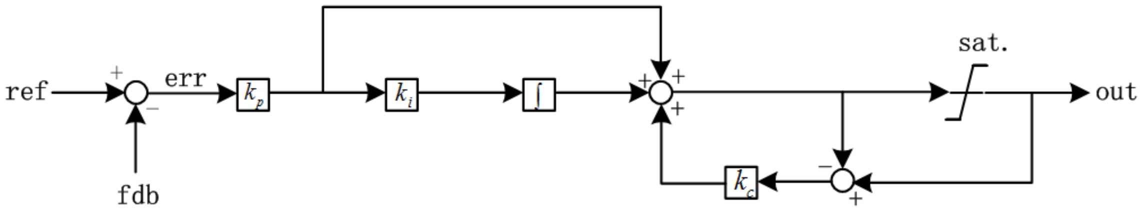

Fig. 5.27 Sketch of PI controller with anti-windup feedback

An appropriate choice of k_c will effectively damp the windup overshoot, as shown in Fig. 5.28. Nevertheless, the system will become overdamped if the value of k_c is too large, as shown in Fig. 5.29.

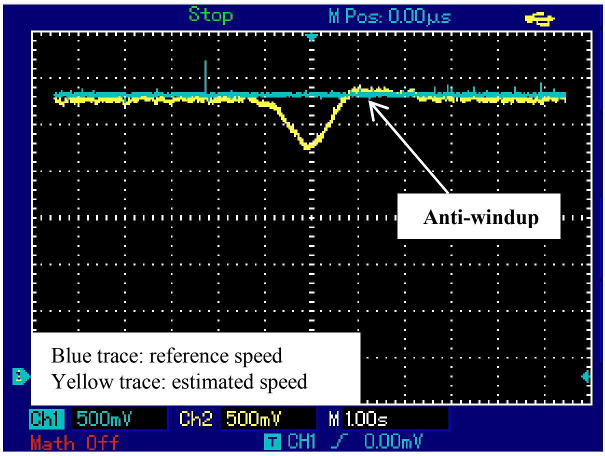

Fig. 5.28

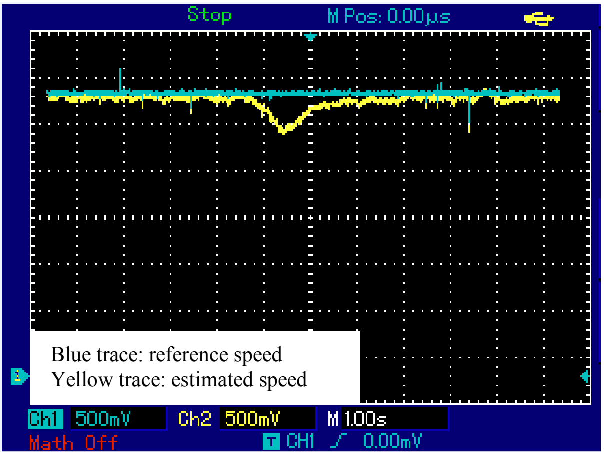

Fig. 5.29

Fig. 5.28 Comparison between actual and reference speeds during transient with anti-windup strategy
Fig. 5.29 Comparison between actual and reference speeds during transient with large k_c

The influence of PI controller parameters to the system is demonstrated. Eventually a finely tuned PI controller is integrated into the system. Its parameters are listed in Table 5.2.

k_p	2.5
k_i	0.4
k_c	0.6

Table 5.2 Actual PI control parameters for the experimental drive system

The reference and estimated speeds are recorded for the starting process of the drive system, as shown in Fig. 5.30. The machine estimated speed is correctly updated from approximately 2.5s of open loop start-up. At the beginning of closed loop operation, the actual speed loses track of the reference and deviates by a small amount. Even though, the speed manages to follow the reference just after 1s, without overshoot. A tiny overshoot appears when the test machine transitions from acceleration to final speed, and the speed falls back to steady value soon.

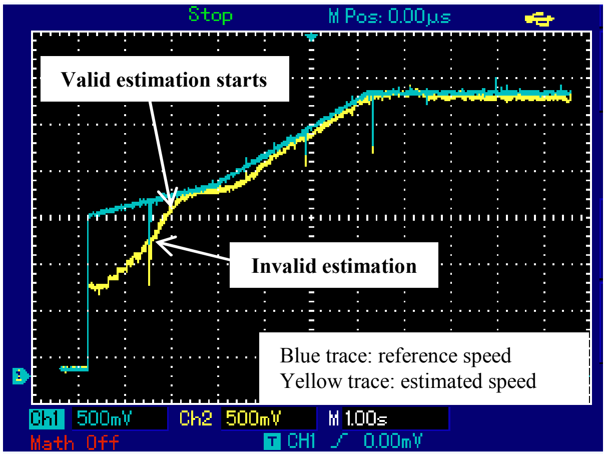

Fig. 5.30 Comparison between actual and reference speeds for the experimental drive system with appropriate tuning of PI controller

The reference q-axis current signal i_{qref} in the whole process is recorded in Fig. 5.31. A fixed reference is created during the open loop start up for obtaining valid speed estimations before end of the stage. The q-axis current reference in the acceleration region corresponds to the actual speed response observed in Fig. 5.30. The actual phase (phase A) current waveform during the process is plotted in Fig. 5.31.

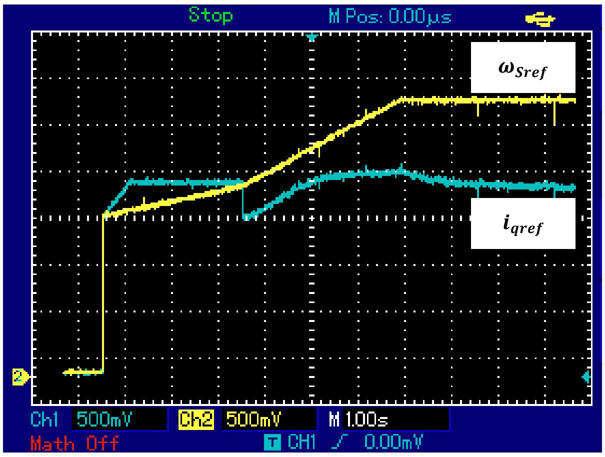

Fig. 5.31

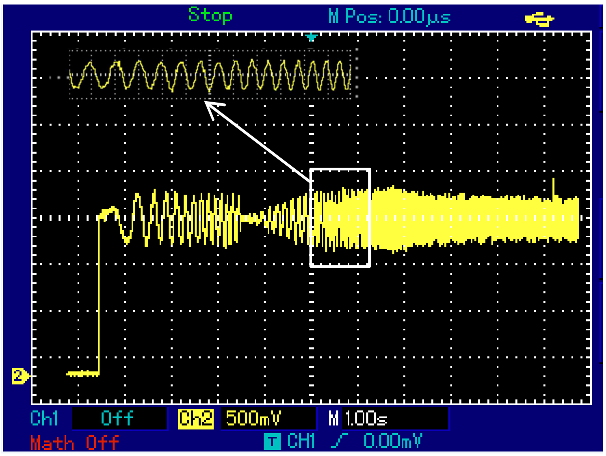

Fig. 5.32

Fig. 5.31 Reference q-axis current during the complete start-up process of the drive system
Fig. 5.32 Actual q-axis current during the complete start-up process of the drive system

As a summary, this section validates the feasibility of applying the proposed sensorless position and speed estimation algorithm and appropriate PI controller to a potential field oriented machine drive application.

5.5 Summary and discussion

This chapter concentrates on the machine control system and relevant control theories. The characteristic of field windings and the influence of armature reaction on field voltages are practically demonstrated firstly. A sensorless position and speed estimation method is then developed based on the space vector theory of heteropolar inductor machine. The sensorless q-axis position estimation is based on the comparison between the voltage and flux linkage vectors constructed from armature and field measurements. The sensorless speed estimation is realised by counting the zero-crossings of orthogonal internal emf vector components. The system blocks and several advantages over conventional sensorless schemes are illustrated.

The performances of both position and speed estimations are compared with actual measurements. The system is tested with different conditions such as no load, steady loading, transient loading and field weakening at different speeds. It is shown that the estimation error is generally maintained below 10% for various conditions.

A micro-processor based prototype heteropolar inductor machine drive system employing field oriented sensorless control is implemented for starting up the machine from standstill to a designated speed within a limited time. System block diagrams are illustrated. The necessity of starting up before estimators are functional is discussed. Initial rotor positioning and open loop starting are implemented in the drive system. Besides, the importance of gaining correct estimations at open loop operation stage is addressed. The influences of proportional, integral and correction gains of PI controller on the drive system are demonstrated with the actual speed recordings during starting up. Lastly the performances of an appropriately tuned system are recorded.

The sensorless q-axis position and speed estimations introduced are developed based on the machine configuration shown in Fig. 4.24. However, estimations for machines with different values of k_{dp}, k'_{dp}, winding turns and coil pitches etc. can also be achieved by similar steps. It is essential that the armature reaction terms in both armature voltage vector and field AC voltage vector are balanced out. This can be done by appropriately factorizing the vector $\overrightarrow{\overline{u_f}}$ if the armature reaction terms are of different magnitudes.

As discussed, the rotor speed estimation applies zero-crossing technique. However there are some restrictions that hinder the ideal estimation. A major consideration is that the $e_{S\alpha}$ and $e_{S\beta}$ waveforms may exhibit multiple zero-crossings around zero value due to possible ripples on the waveforms. As a result, spikes will appear in speed estimation waveforms. Besides, the performance of zero crossing detection may be compromised since the waveforms are discretized inside micro-controller, and may not possess an exact zero value. In practice, the actual zero crossing points are replaced by narrow regions around zero crossings. The waveforms are regarded as crossing zero points once they enter the regions.

Another limitation of zero-crossing is that its accuracy depends on the accuracy of internal emf estimation. The voltage measurements are passed into micro-controller via ADC interfaces, and error may be introduced at this stage. Each ADC interface is a series of amplifying circuit with appropriate voltage offsets. The difference in amplifier gains and voltage offset of each individual component can cause certain offset in estimated emf waveforms. Such an estimation error can be seen from Fig. 5.12 (b), and the speed estimation is compromised.

Instead of applying zero-counting method, the speed can also be calculated from the derivative of angular position estimation, which offers a higher sensitivity in speed changes. This method is experimented practically. However the performance is far from satisfactory since ripples on position estimation waveforms are hugely magnified. The speed estimation is spiky and spikes can be 10 times greater than the actual speed value. A method to mitigate position estimation ripple can be extracting position information from a phase locked loop, instead of from inverse trigonometric calculation [90].

The drive system employs field oriented control strategy for the purpose of maximum torque per ampere (MTPA) control. An alternative of the system can be made by applying direct torque control technique. Direct torque control avoids the necessity of coordinate transforms, thus simplifying the algorithm and increasing the processing speed. Nevertheless it is reported that direct torque control systems generally exhibit a higher level of torque ripples. The current hysteresis controller in Fig. 5.17 and Fig. 5.18 can be replaced by PI controllers for smoother torque output at the expense of complexity.

Chapter 6: Application

6.1 Target specifications

The potential application of heteropolar inductor machine as a gas turbine starter generator is discussed in this chapter. Alternative solutions employing different types of electrical machines will also be compared.

The starter generator is assumed to be coupled to a CFM 56-5C aircraft engine which is commonly used to power medium sized passenger aircrafts such as Boeing 737 and Airbus A340. CFM 56-5C engine is a typical double-spool turbofan engine. The high pressure (HP) spool consists of a six-stage compressor and a one-stage turbine, while the low pressure (LP) spool consists of a one-stage compressor (i.e. the fan) and a five-stage turbine. Both spools are co-axial. The physical dimensions and operational facts are detailed in the official European Aviation Safety Agency (EASA) document [91]. The speed limits for HP and LP spools are 15000rpm and 5000rpm respectively.

The electrical starter generator is directly coupled to the HP spool of the gas turbine. At the starting stage, the machine provides a forward rotating torque to assist the HP spool to accelerate from stand-still to the ignition speed (normally approximately 20% of nominal operational speed). The HP turbine is able to supply certain forward torque once the combustion chamber is ignited. However the torque supplied by the turbine at this stage is too low to support continuous rotation without the assistance of starter. Hence the starter continues to help accelerate the turbine until it reaches a speed that the turbine can finally sustain a continuous rotation without assistant. The speed value is known as self-sustaining speed, and is usually approximately 50% of HP turbine nominal operational speed. Once the turbine can be self-sustained, the starter ceases to supply torque, and the acceleration to full speed is completed by the turbine itself. In the meantime, the function of electrical machine transitions to generator mode since the gas turbine is able to provide torque to the starter generator beyond the self-sustaining speed. The LP spool is started spontaneously by the air flow when the engine is ignited.

During the starting period, the starter provides a constant torque to overcome the inertia of HP compressors and turbine (usually the inertia of starter generator is negligible compared with gas turbine), as well as the windage friction which increases with speed. The torque profile of CFM 56-5C engine during starting period is estimated as shown in Fig. 6.1. The target speed for HP spool is assumed to be 10000rpm.

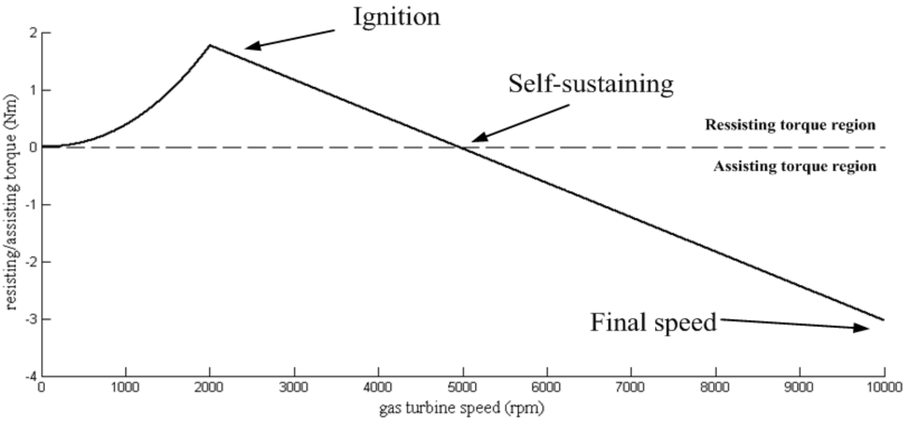

Fig. 6.1 Resisting and assisting torque of gas turbine during turbine starting

It is seen from Fig. 6.1 that before the gas turbine is ignited, the resisting torque of the gas turbine increases parabolically with speed, and is mainly contributed by windage power. After ignition (2000rpm), the resisting torque starts to reduce almost linearly until it is completely overcome by the assisting torque provided by the gas turbine itself (5000rpm). The starter is offline and waits to enter generator mode.

The starter generator is in turn driven by the gas turbine after starting process ends. It operates in constant power (field weakening) mode during generating period. The voltage of DC link on board is monitored and fed back, and the generator is responsible for maintaining the voltage at certain level. The DC link voltage can be passed through solid state components to be inverted or stepped down in order to meet different power requirements for electrical loads.

In order to compare various starter generator plans, the target specifications for the designs are listed below.

- Aircraft DC power source/auxiliary power unit (APU) voltage 270V.
- HP spool moment of inertia $1kg\cdot m^2$
- Full speed 10000rpm.
- Starting process duration up to 1 minute to full speed.

- Constant starting torque 25Nm.
- Constant generating power 3kW.
- Environmental temperatures range from -50°C to 125°C.

It is seen from the target specifications that there is a mismatch of power ratings between starter mode and generator mode. Therefore the oversizing of electrical machine is unavoidable to meet the motoring requirement. Class H insulation and above (thermal class 180 and above) is in demand to meet the requirements of ambient temperature upper limit and allowable hotspot.

Aside from the specifications listed, it is also important that the starter generator is supported by back up units to cope with faults and malfunctions, especially when the starting process is finished and the aircraft is in cruise. Besides, the starter generator must be fail-safe under faulty conditions to ensure successful cut-out from the system.

6.2 Feasibility study

6.2.1 Permanent magnet synchronous machine

The preliminary design data of a permanent magnet synchronous machine (PMSM) meeting the target specifications is listed in Table 6.1. The number of poles is selected as 8 (i.e. 4 pairs of poles), considering that best flux concentration is offered by the number of pole pairs ranging from 3 to 6 [92]. The design is based on both electromagnetic and thermal considerations, as well as empirical size relationships [93].

Number of pole pairs	4
Bore diameter	105mm
Outer diameter	160mm
Stack length	70mm
Air gap length	0.4mm
Magnetic loading	~ 1T
Electrical loading	~ 32000A/m

Table 6.1 Preliminary design of PMSM meeting target specifications

PMSMs are commonly characterised as compact size, high power density and high efficiency, owing to the attractive merits of PMs. The thickness of PMs contributes to equivalent air gap length, and armature reaction effect can be mitigated. Among various types of PMSMs, interior permanent magnet (IPM) machine is of the most interest in high speed applications since it offers the best extended speed performance [94]. Additional reluctance torque is also available to assist the motoring process [95], and to increase overload capability [96].

PMs may suffer from the poor ventilation in air gap, as they are sensitive to the ambient temperature and will encounter irreversible demagnetisation when the temperature exceeds the Curie Temperature. Besides, contaminated air and dust particle can also permanently damage the PMs [48].

Another major disadvantage associated with PMSM is the lack of field control. Sophisticated field oriented control must be applied and field flux can be countered by d-axis mmf. As a result, a portion of armature current is used to weaken the flux for constant power operation, and therefore the torque capability in flux weakening region is compromised. The inability to disable the field also raises safety issues, although remedy can be made by applying armature windings with 1 p.u. phase inductance to greatly limit the short circuit currents [11].

6.2.2 Wound rotor synchronous machine

A set of initial design data for a wound rotor synchronous machine (WRSM) is shown in Table 6.2. Same as its PM counterpart, a pole number of 8 is selected. A relatively low number of poles will result in an unsatisfactorily reduction in cranking torque, while a large pole number limits the space available for accommodating field windings.

Number of pole pairs	4
Bore diameter	115mm
Outer diameter	165mm
Stack length	70mm
Air gap length	0.4mm
Magnetic loading	~ 0.7T
Electrical loading	~ 25000A/m

Table 6.2 Preliminary design of WRSM meeting target specifications

The advantage of WRSM is the controllable field supply, which enables full and direct control of field flux excitation. Field weakening in constant power region is achieved by simply reducing field current supply. Hence the power converter VA rating and associated loss in the region are reduced compared with PM machines [97], since d-axis current component is not necessary. Further, the controllable field supply ensures immediate cut-off of field excitation, which makes the machine fail-safe. It is reported that the power factor of WRSM as a starter generator always remains at a high level, facilitating the deployment of a smaller DC link capacitor bank [98].

The major drawback of WRSM is its rotor mechanical complexity, leading to a compromise in robustness. Traditionally the rotor field winding is supplied by external exciter via brush/slip-ring assembly, which increases the overall mechanical vulnerability and fault possibility of the machine. Modern field supply to WRSM employs rotating rectifiers and brushless exciters or rotary transformer. However such strategy further increases the rotor complexity and contributes extra weight to the rotor. Moreover it is reported that the machine efficiency is reduced compared with WRSM with slip-rings [98].

6.2.3 Switched reluctance machine

The output equation of switched reluctance (SRM) is derived in [99], and a preliminary design of a SRM is shown in Table 6.3. Three phase 12/8 SRM structure is selected, considering its higher thermally limited torque capability [100] and lower acoustic noise due to shorter flux linkage path [101], compared with a 6/4 structure.

Number of stator saliencies	12
Number of rotor saliencies	8
Bore diameter	140mm
Outer diameter	180mm
Stack length	85mm
Air gap length	0.25mm
Magnetic loading	~0.7T
Electrical loading	~30000A/m

Table 6.3 Preliminary design of SRM meeting target specifications

SRM has been regarded as a competitive candidate for starter generator applications by researchers due to its robust structure and stability, suitable for high temperature and high speed operations. With appropriate rotor design to diminish rotor stress, a SRM is proposed and tested to work steadily under extreme conditions (400°C, 15000rpm) [102].

The robustness of SRM is also reflected by its superb fault tolerant capability. As is known, each concentrated stator winding in SRM is free from mutual flux linkage, implying that the flux linkage of each healthy phase is not affected even if some other phases are in fault. By improving the design of drive system, a SRM is able to continue working when one or more phases are disabled due to fault [103]. SRM is also fail-safe. The whole machine can be shut down by disconnecting the power source since it is singly excited.

Another merit of SRM is that a unipolar power supply is sufficient for the operation of an SRM, unlike three phase sinusoidal power supplies where current flow is bidirectional, or bipolar. Such a property halves the power electronic devices in each phase leg in an SRM drive, offering a more reliable and less faulty system.

The most undesirable characteristic of SRM is its torque ripple caused by current distortion due to back emf. The vibration and noise associated are disadvantageous factor for passenger flights consideration. Several measures can be taken to reduce the torque ripple, such as periodical multi-phase excitation [104] and application of bipolar current excitation [105], etc. However, such improvements compromise the simplicity of drive system.

The lack of field excitation in SRM not only reduces the controllability of the machine, but also reduces its power density, since the magnetising current carried by stator windings is not converted to mechanical output. An equivalent power factor is suggested in [106] for SRM. It appears that, according to computer model, the value of the equivalent power factor is limited to a range of 0.432 to 0.5. The VA rating of drive for a specific power output is thus increased. A torque reduction of more than 10% is reported in [107] when the power devices is to match a PMSM power converter. The efficiency of SRM is also reported to be relatively lower [108].

6.2.4 Flux switching machine

The general design theory of FS machines is discussed in [109], in which an optimal split ratio of 0.55 is suggested. It is revealed that, similar to heteropolar inductor machines, the removal of excitation source from rotor is at the cost of increased size. The initial design of a 12/10 FS machine with all poles wound winding configuration is listed in Table 6.4 to meet the requirements of the target specifications.

Number of stator saliencies	12
Number of rotor saliencies	10
Bore diameter	125mm
Outer diameter	225mm
Stack length	80mm
Air gap length	0.35mm
Magnetic loading	~1T
Electrical loading	~30000A/m

Table 6.4 Preliminary design of PM excited FS machine meeting target specifications

The existence of PMs in the FS machine implies that a high flux density is available, and that copper loss from field excitation is eliminated. The torque density is comparable with PMSM even though the PMs on stator side results in a reduced available copper area [110]. Moreover the passive nature of rotor enhances the robustness of the machine working in harsh environments and the operational speed is less constrained.

FS machines exhibit similar limitations associated with PMs as conventional PMSMs, such as narrow thermal range and lack of direct field control. Yet possibility of irreversible PM demagnetisation is almost eliminated [111], and the PM eddy current loss is lowered compared with that in PMSMs [112]. Placement of PMs on stator side and generally reduced PM losses, to some extent, facilitate the cooling of PM materials.

Similar to heteropolar inductor machines, the main mmf wave in the FS machine is asynchronous to the rotor rotation [113]. Inevitably it causes local saturation and rotor iron loss due to main flux wave, as discussed in Chapter 4. Considering the fact that the electrical speed is 10 times the rotor speed, the rotor loss is generally high. Besides, the doubly salient and flux switching nature of FS machines implies that they are prone to torque ripples especially when strong field and saturation are present [114]. Also, FS machines suffer from poor utilisation of material. A comparative study [115] shows that the total weight of PMs mounted in a FS machine is more than twice of that in a PMSM for the similar performances. This property can be disadvantageous for designs with tight budget.

A low cost plan is to replace the PMs by field coils. Predictably such an alternative causes a decrease of torque density and an increase of copper consumption. For a given copper loss, the torque density of a wound field FS machine is over 50% lowered compared with its PM excited counterpart [11]. Another study reports a massive reduction in torque output even when the field current density reaches as high as $20A/mm^2$, due to the fact that the narrow salient stator teeth are heavily saturated [8]. With these considerations, the wound field FS machine has to be of a larger size for achieving equal performances.

6.2.5 Heteropolar inductor machine

A set of preliminary sample design data of a heteropolar inductor machine is shown in Table 6.5. The winding configuration is as shown in Fig. 4.8 for higher power output compared with the test machine analysed in previous chapters.

Number of rotor saliencies	4
Bore diameter	135mm
Outer diameter	175mm
Stack length	80mm
Air gap length	0.35mm
Magnetic loading	~0.7T
Electrical loading	~30000A/m

Table 6.5 Preliminary design of heteropolar inductor machine meeting target specifications

Heteropolar inductor machine offers an alternative to a simple, robust, low cost and highly controllable solution of electrical machinery. Despite its passive rotor structure, the full control of field excitation is directly available, providing an improved power factor regulation and constant power operation. Besides, the machine is fail-safe since the electrically supply field can be cut out immediately when fault occurs. The saturation is greatly reduced due to the non-salient nature of stator, and an increased power density compared with wound field FS machine is predicted. Also torque ripples caused by current distortion and flux switching are eliminated.

As demonstrated in the transient analysis in Chapter 3, the absence of transient reactance, to some degrees, limits the level of current surge during fault. Hence the machine can be better protected. Yet the heteropolar inductor machine almost does not possess any fault tolerant capability, since electromagnetic couplings exist among each armature winding, even between armature and field windings. Consequently the machine is highly unlikely to operate satisfactorily with fault, and back-up machines are demanded.

The replacement of PMs by field coils unavoidably compromises the power density of heteropolar inductor machines. Higher current loading is therefore required for a designated output. As a result, the copper loss is likely to be higher, together with the fact that field current flows contribute to additional losses.

Even though a careful winding design is able to suppress the 2nd harmonic components greatly (as introduced in Chapter 4), the machine may still suffer from a small portion of 2nd harmonic current remaining. Such a current component will lead to additional losses, heating and torque ripples, as well as increase in generation distortion ratio.

Similar to FS machines, the removal of rotor side excitation to trade for reliability results in a penalty in machine size. As analysed in Chapter 4, the greater machine dimensions are foreseen from the partial utilisation of air gap magnetic flux swing.

6.2.6 Summary

Different types of proposed electrical machine are compared in 6.6 with regard to various properties. It is shown that heteropolar inductor machine offers a moderate compromise among various considerations.

		Robustness	Cost	Power density	Controllability	Safety
Wound field synchronous machine		Low	Medium	High	Armature and field	Fail-safe
Permanent magnet synchronous machine		Medium	High	High	Armature	Not fail-safe
Switched reluctance machine		High	Low	Medium	Armature	Fault tolerant
Flux switching machine	Permanent magnet excited	Medium	High	High	Armature	Not fail-safe
	Field winding excited	High	Low	Low	Armature and field	Fail-safe
Heteropolar inductor machine		High	Low	Medium	Armature and field	Fail-safe

Table 6.6 Comparison of various machines for gas turbine starter generator application

6.3 Starter simulation

6.3.1 Starter system

The block diagram for gas turbine starting process is shown Fig. 6.1. The closed loop control strategy is similar to Fig. 5.17 and Fig. 5.18. Feedback signals for speed and position can be obtained either via sensors or by sensorless estimation schemes. The open loop control block can be neglected when sensors are in use. Current hysteresis controllers may be replaced by current loop PID controllers, leading to a smoother torque output. The resisting/assisting mechanical torque of gas turbine is denoted as T_m, and gas turbine moment of inertia as J (electrical machine rotor inertia is neglected). The implementation of model in Simulink is shown in Appendix III.

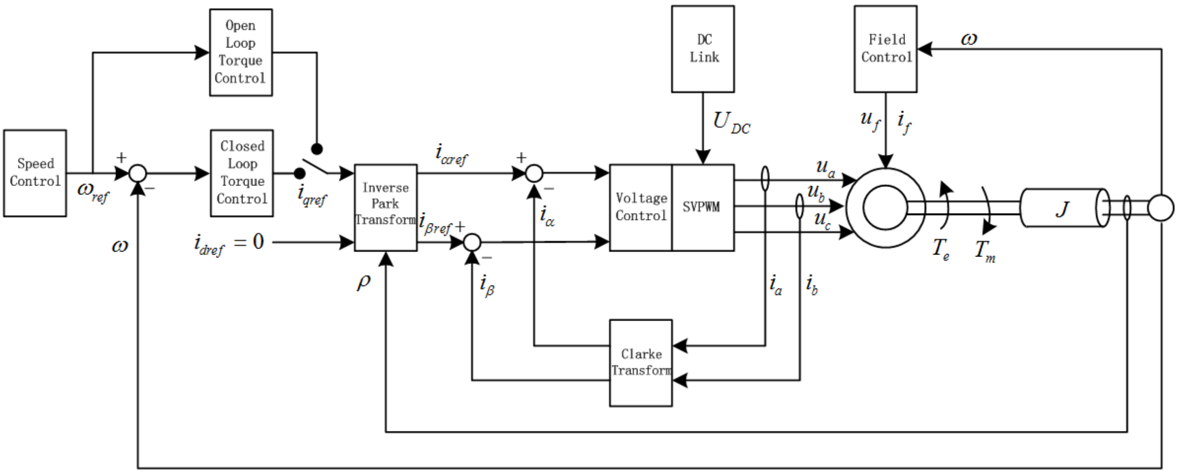
Open Loop Torque Control
DC Link
Field Control
ω
Speed Control
Closed Loop Torque Control
U_{DC}
u_f i_f
$i_{\alpha ref}$
+
−
ω_{ref}
i_{qref}
Inverse Park Transform
Voltage Control
SVPWM
u_a
u_b
u_c
J
i_α
$i_{\beta ref}$
ω
$i_{dref} = 0$
T_e
T_m
ρ
i_β
i_a
i_b
Clarke Transform

Fig. 6.1 Block diagram of starter control system

Machine model

Heteropolar inductor machine is selected as the candidate machine for the starter generator application. The detailed machine parameters are given in Table 6.7, and are used for the simulation of machine performance.

Λ_1	1×10^{-3}H/m^2	L_{mfa}	1.5mH
Λ_0	1.2×10^{-3}H/m^2	L_{mS}	0.25mH
Turns per phase winding N_S	6	Rotor moment of inertia	0.04kg·m^2
Turns per field coil group N_f	21	Armature winding resistance R_S	0.1Ω
Stator slot number	36	Field winding resistance R_f	0.5Ω

Table 6.7 Detailed design data of heteropolar inductor machine meeting target specifications

Both fundamental and invariant permeance components (Λ_1 and Λ_0) are similar to the values of the test machine in Chapter 1. The low armature winding turns lead to low self-inductance (0.25mH), as well as the capacity for much higher current conduction. The low inductance value is essential especially at high speeds, since it reduces the electrical time constant and facilitates the injection of current from source to machine. The selection of number of field coil turns is based on the trade-off between DC current level and induced field AC voltage. Field AC magnitude is approximately 103V.

Machine flux model in Simulink is based on the two-axis mathematical model for heteropolar inductor machines (Fig. A3.1). The simulation frequency is 10kHz, and field current supply in constant torque region is 50A. In addition, it is seen that the estimated rotor moment of inertia (0.04kg·m^2) is negligible compared with the moment of inertia of gas turbine HP spool (1kg·m^2).

Windage effect

The estimation of windage torque is based on the gas turbine weight model, skin friction coefficient, and the Reynolds Number for rotating disks [116, 117]. The resisting windage torque is represented by a function block of speed in Simulink model.

DC link and inverter

In starter simulation, the DC link voltage is assumed to be constant 270VDC. Switching device (IGBT) on state resistance is assumed to be 0.05Ω, and the forward voltage drop is 0.7V. The inverter link current is simulated on the basis of energy conversion and estimated from the values of three phase voltages and currents, link voltage etc.[118]. Inverter switching pattern for each phase is read from a look-up table corresponding to the outputs of current hysteresis controller.

Starting commands

The starter aims to accelerate the gas turbine to its self-sustaining speed (5000rpm) within 40 seconds. The speed reference signal during the period is illustrated in Fig. 6.2. Sensorless control strategy is simulated. As suggested in Chapter 5, the sensorless field oriented starting process will require initial rotor alignment, open loop start-up, and finally closed loop acceleration. The gas turbine is then able to accelerate itself without assistance once it is self-sustained after 40s.

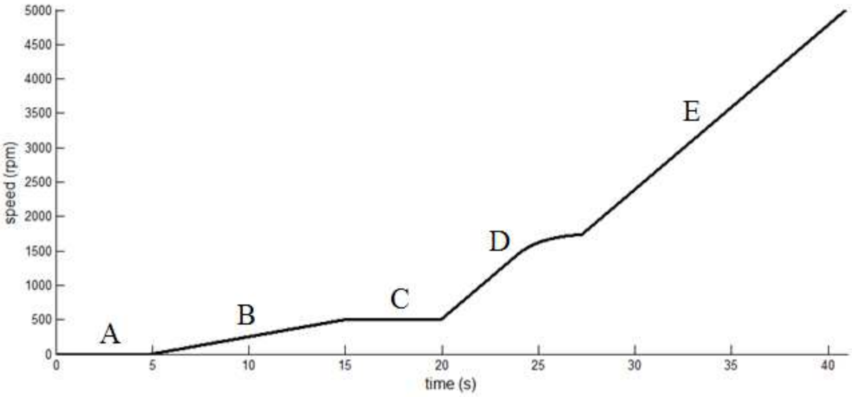

Fig. 6.2 Speed reference for gas turbine starting process

The starting process, as shown in Fig. 6.2, is divided into 5 stages [119]:

- Stage A: The initial rotor position at stand-still is calibrated.
- Stage B: The starter is driven by open loop control with a mild speed reference ramp, until the sensorless estimations are satisfactory, and ready to cut in.
- Stage C: The system is being transitioned from open loop control to closed loop control, and the speed is maintained at the final speed of open loop operation stage.
- Stage D: The slope of the closed loop acceleration speed reference is initially steep, and decreased gradually to zero to stabilise the speed for ignition process. Gas turbine is ignited at the end of this stage.
- Stage E: The speed reference is at a constant, relatively steep rate until target speed of 5000rpm is reached.

6.3.2 Simulation results

Actual and reference system speeds for starting operation up to 5000rpm are compared in Fig. 6.3. Although the actual speed trajectory (black line) almost overlaps the speed reference (red line), distinction can be observed between 5s and 20s. The speed difference in stage B results from the open loop operation and the lack of feedback information. It is corrected within the next 5s (stage C) once the feedback loop cuts in.

The q-axis current reference is shown in Fig. 6.4. The open loop reference current is fixed at 25A, for the purpose of starting the machine to a closed loop speed. The current reference rises to the upper limit of 200A in order to reduce the speed difference immediately after feedback signal and speed error PI controller cut in. During the main starting stages (stages D and E), the q-axis current reference is maintained at approximately 130A, expect for the end of stage D where the speed slope converges to zero to facilitate gas turbine ignition. Besides, it is seen that the machine is regenerating with negative reference current at stage C, in order to compensate for the over-speed occurs at 15s.

Actual q-axis and d-axis currents are plotted in Fig. 6.5 and Fig. 6.6 respectively. q-axis current follows its reference with certain ripples, while the average value of d-axis current is constantly kept at zero.

Fig. 6.7 shows the actual three phase currents recorded for the starting process up to self-sustaining speed. During the first 5s of the process, only phase A is conducted with 5A DC in order to align the rotor to an appropriate initial position. The current waveforms at both low and high speeds are enlarged. Low speed current waveforms pose a higher level of switching harmonics due to hysteresis control. The harmonic ripples, however, are greatly reduced at high speed, as the waveform period is much shortened.

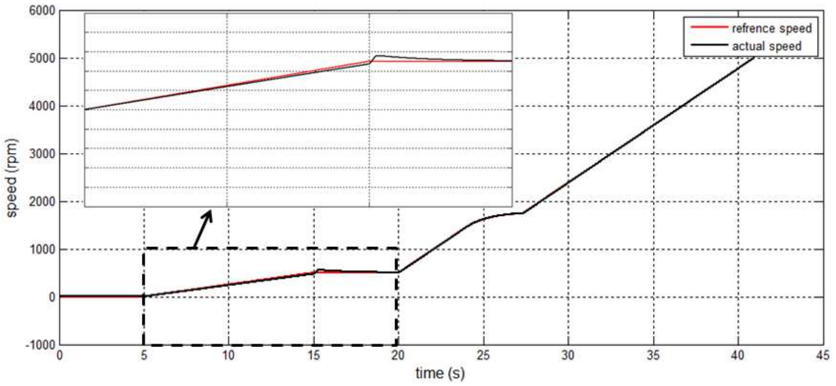

Fig. 6.3 Comparison between reference and actual speeds during gas turbine starting process

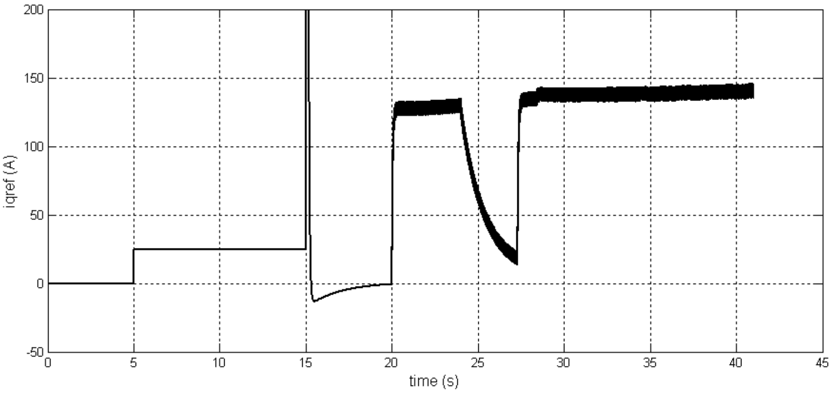

Fig. 6.4 Reference q-axis current signal during gas turbine starting process

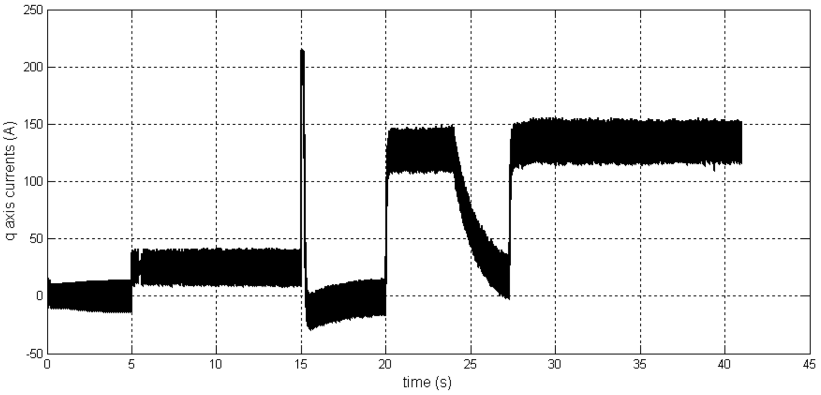

Fig. 6.5 Actual q-axis current signal during gas turbine starting process

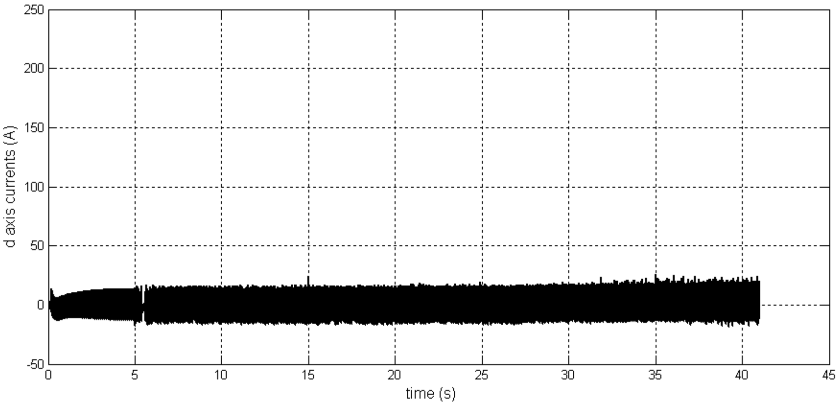

Fig. 6.6 Actual d-axis current signal during gas turbine starting process

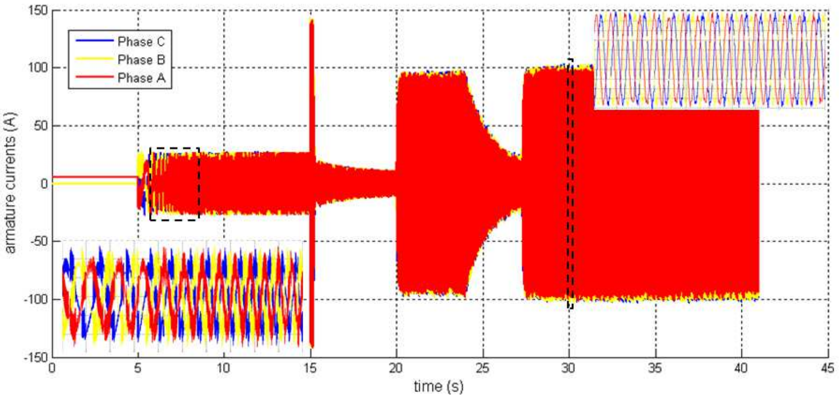

Fig. 6.7 Three phase currents during gas turbine starting process

6.4 Generator simulation

6.4.1 Generator system

The block diagram for generating process is shown in Fig. 6.8. There is an extra DC link voltage control loop compared with starter block diagram. DC link (battery) voltage is constantly measured and fed back to control the required mechanical torque input. Electrical machine is controlled in the same way as starter simulation, except that the gas turbine is acting as a prime mover. The implementation of generation model in Simulink is shown in Fig. A3.2.

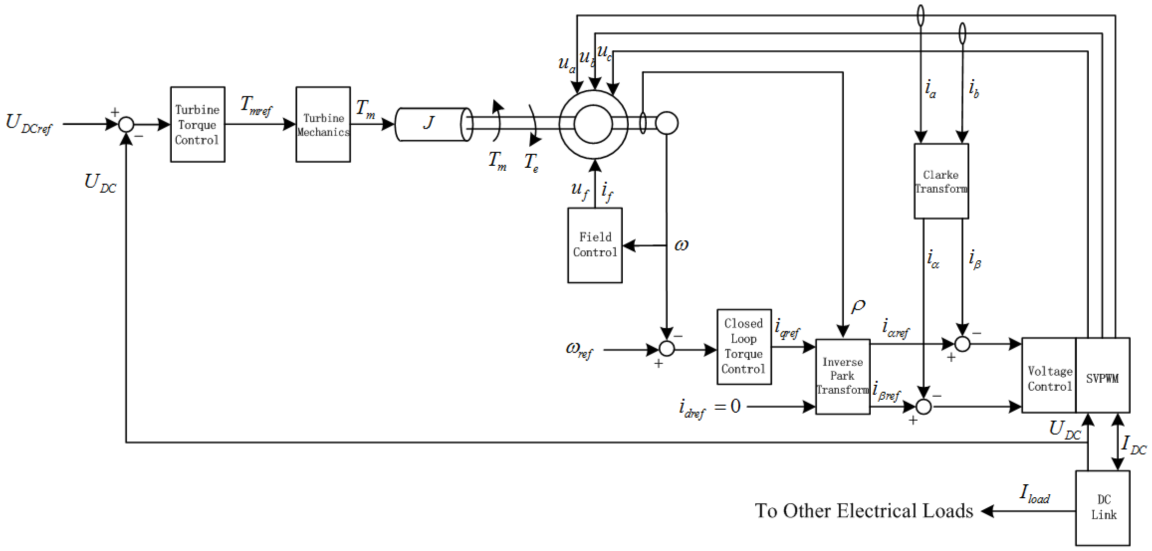

U_{DCref}
+
−
Turbine Torque Control
T_{mref}
Turbine Mechanics
T_m
J
T_m
T_e
U_{DC}
u_a
u_b
u_c
u_f
i_f
Field Control
ω
i_a
i_b
Clarke Transform
i_α
i_β
ω_{ref}
Closed Loop Torque Control
i_{qref}
ρ
Inverse Park Transform
$i_{\alpha ref}$
$i_{\beta ref}$
$i_{dref} = 0$
Voltage Control
SVPWM
U_{DC}
I_{DC}
I_{load}
DC Link
To Other Electrical Loads

Fig. 6.8 Block diagram of generator control system

Battery

Considering the key advantages of modern 270V DC aircraft power systems [120, 121], such as stability and weight saving, a 270V Nickel Cadmium battery is assumed in the simulation as the on board power source. The battery mechanism is based on a simplified Shepherd model [122], as shown in (6.1).

$$V_{bat} = E_c - K_p \frac{Q}{Q-q} q - i_{bat} R_{bat} + A_{bat} e^{-B_{bat} \cdot q} \tag{6.1}$$

$$q = \int i_{bat} dt \tag{6.2}$$

In the above equations, V_{bat} and i_{bat} correspond to instantaneous battery terminal voltage and output current respectively. The battery current consists of inverter DC link current and current supplied to other DC loads. The instantaneous battery charge is denoted by q. The battery discharge curve can be therefore defined with the Shepherd model parameters listed in Table 6.8.

Battery constant voltage E_c	271V
Polarisation voltage K_p	0.5V
Battery capacity Q	9.6Ah
Battery internal resistance R_{bat}	0.001Ω
Exponential zone amplitude A_{bat}	20V
Exponential zone time constant inverse B_{bat}	5Ah^{-1}

Table 6.8 Parameters for battery simulation

The battery block in Simulink is shown in Fig. 6.9. Battery state of charge (SOC) is also calculated and output from the simulation block.

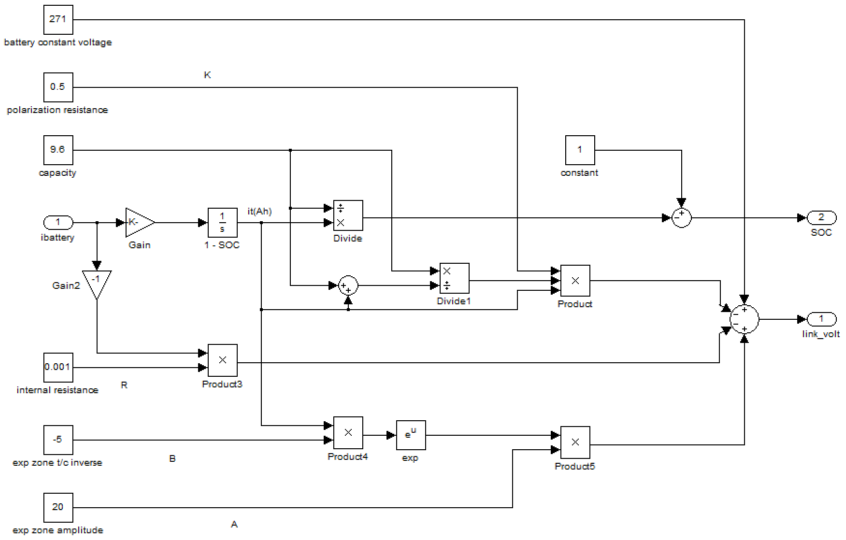
271
battery constant voltage
K
0.5
polarization resistance
9.6
capacity
1
constant
1
ibattery
K-
Gain
1/s
1 - SOC
it(Ah)
Divide
2
SOC
Gain2
-1
Divide1
Product
1
link_volt
0.001
internal resistance
R
Product3
-5
exp zone t/c inverse
B
Product4
e^u
exp
Product5
20
exp zone amplitude
A

Fig. 6.9 Simulink model of battery

Gas turbine

Once the battery output current is increased, the driving torque of gas turbine must also increase accordingly to balance the energy, and vice versa. The demanded driving torque is controlled by the link voltage loop as shown in Fig. 6.8. However the practical gas turbine response to the commands experiences a series of complex mechanical processes, including valve action, fuel inlet etc. The gas turbine action [123] is modelled with certain key parameters listed in Table 6.9, and thermal control is not considered for simplicity.

Valve positioner time constant	0.05s
Fuel system time constant	0.4s
Combustion chamber reaction delay	0.01s
Compressor discharge time constant	0.2s

Table 6.9 Parameters for simulating gas turbine mechanics

Generator field supply

The field current of generator is halved compare with that in starter mode due to the constant power operation required after starting process. The field control block is represented by a function of turbine speed, and field current is inversely proportional to rotor speed. Generator field current in simulation is maintained at around 25A at speed around 10000rpm.

6.4.2 Simulation results

A generation process is simulated when initial battery is around 269.6V. The difference between reference DC voltage value (270V) and the actual value commands the generator system to charge the battery. It is plotted in Fig. 6.10 that the battery voltage keeps raising over the simulation period of 15s. The mechanical torque reference generated to correct error DC voltage is plotted in Fig. 6.11. The positive demanded torque signifies the fact that mechanical power is converted into electrical power (current) and stored in battery.

Fig. 6.12 shows the DC link current rectified by three phase PWM rectifier from generator. An average DC current of approximately 10A is observed (except for the initial 1s). The SOC of battery (Fig. 6.13) also increases with the injection of current.

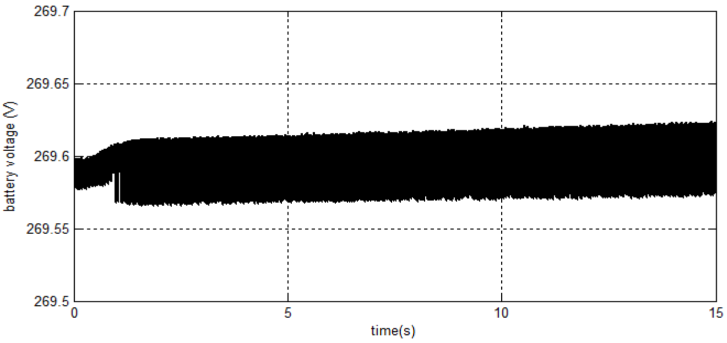

Fig. 6.10 Battery voltage during generation process

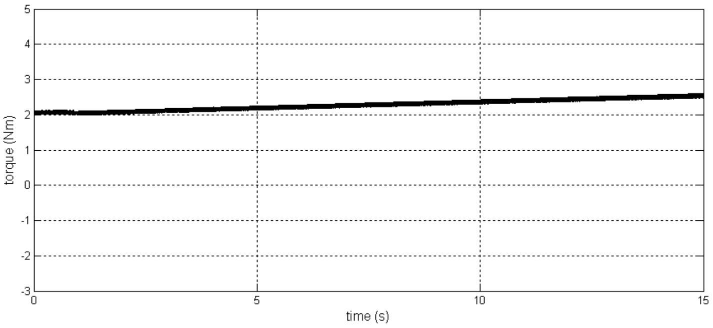

Fig. 6.11 Torque reference for turbine system during generation process

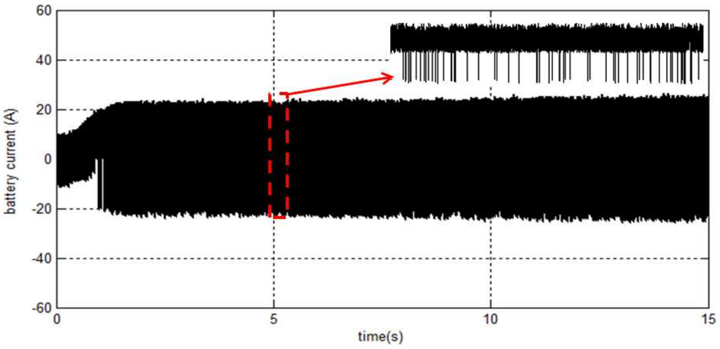

Fig. 6.12 DC link current of PWM rectifier during generation process

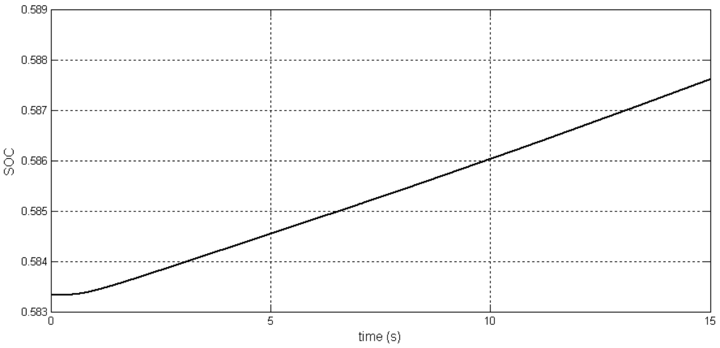

Fig. 6.13 Battery SOC during generation process

The actual mechanical and electro-mechanical torque reacting to the torque reference is compared in Fig. 6.14. A significant delay of turbine mechanical torque is seen when compared with the reference in Fig. 6.11, because of the delays and time constants of turbine mechanics. The electro-mechanical torque of generator is controlled by speed loop, and its average value follows the mechanical torque as shown. Despite the electro-mechanical torque ripple, the system speed (Fig. 6.15) is well maintained at 10000rpm, owing to the large moment of inertia of gas turbine. The torque ripple partly results from current hysteresis control, and can be mitigated by utilising current PID controllers.

The influence of battery DC loading is analysed. The load current is added in the form of an intermittent load starting from 5s to 10s, as shown in Fig. 6.16, with other parameters unchanged.

Corresponding battery terminal voltage and battery SOC are illustrated in Fig. 6.17 and Fig. 6.18 respectively. It is observed that the battery voltage drops during the loading period, due to the fact that the converted electrical power from starter generator is unable to fully support the load. Consequently the SOC of battery inevitably drops for outputting electricity between 5s and 10s. Hence the main generator or auxiliary power unit (APU) must cut in to balance the load under the circumstance.

The torque profiles under loading condition are recorded in Fig. 6.19. It is seen that both turbine mechanical and electro-mechanical torques increase slightly during loading period since the difference between reference and actual battery voltages increases. The rotor speed remains almost constant as shown in Fig. 6.20.

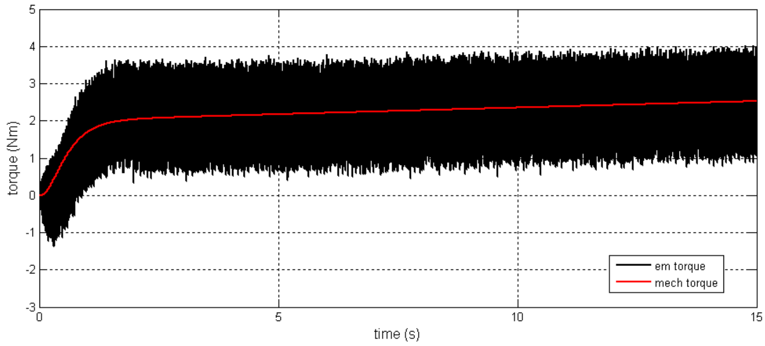

Fig. 6.14 Comparison between turbine mechanical torque and generator electro-mechanical torque during generation process

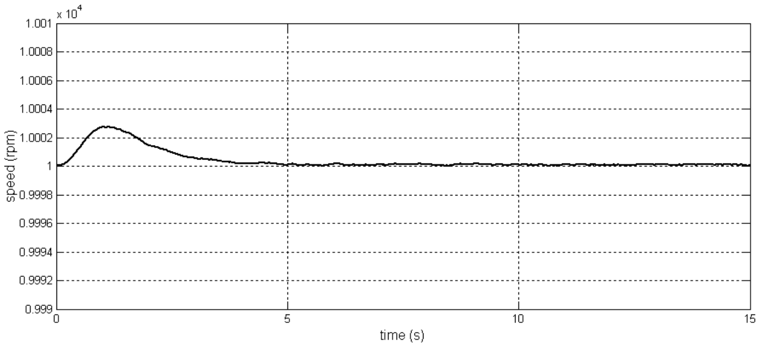

Fig. 6.15 Generator speed variation during generation process

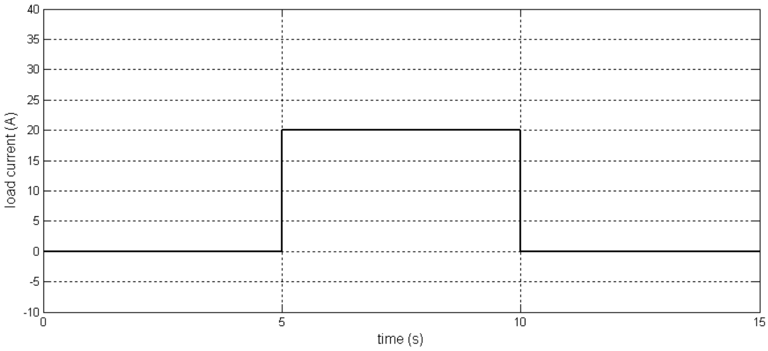

Fig. 6.16 Intermittent DC loading of battery

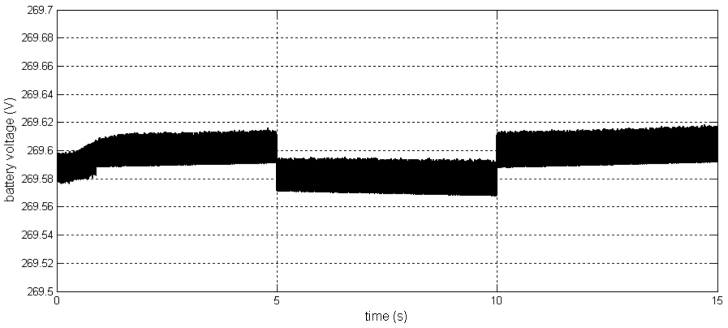

Fig. 6.17 Battery voltage during generation process with intermittent DC loading

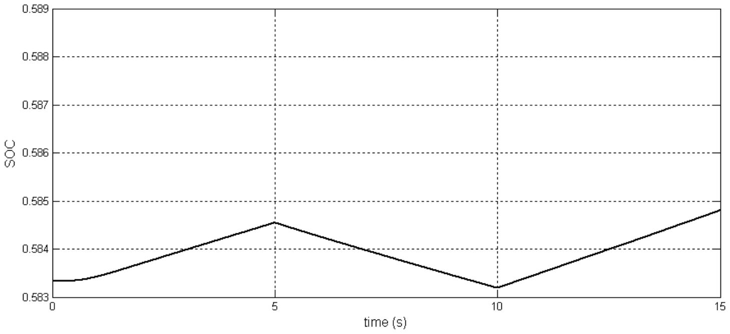

Fig. 6.18 Battery SOC during generation process with intermittent DC loading

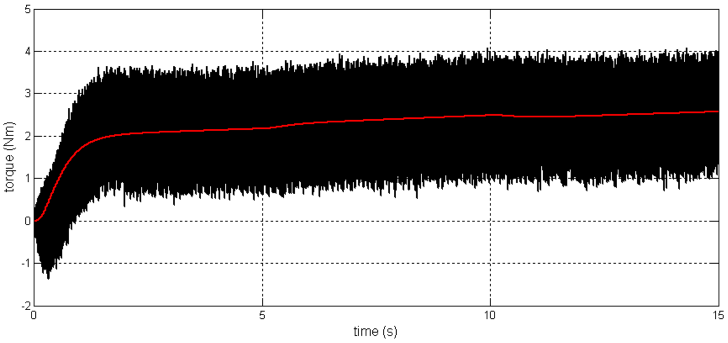

Fig. 6.19 Comparison between turbine mechanical torque and generator electro-mechanical torque during generation process with intermittent DC loading

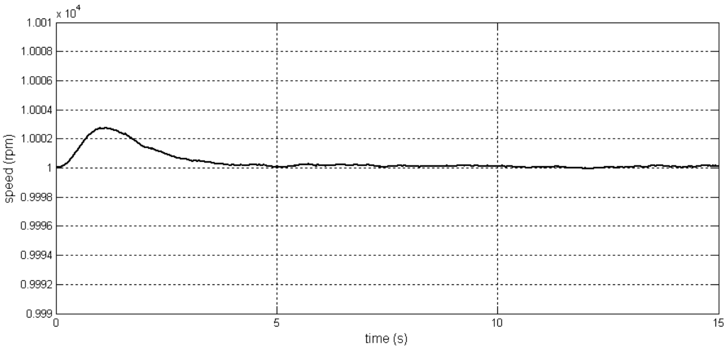

Fig. 6.20 Generator speed variation during generation process with intermittent DC loading

6.5 Summary and discussion

The operational process of a gas turbine starter generator is detailed, together with the target specifications and requirements for the starter generator application. The feasibility study of a number of electrical machines is performed considering the target specifications as well as machines' own advantages and disadvantages. A lateral comparison is made for candidate machines regarding certain important issues of starter generator.

The performance of a starter generator system based on heteropolar inductor machine is simulated. The starting and generating processes are simulated individually with illustration of system block diagrams. In starter simulation, the build-up of several important models (e.g. machine model, inverter model and windage block etc.) are detailed, and the speed reference for starting process is elaborated. The starter simulation focuses on the actual speed in the process compared with the reference, as well as the profiles of d and q axes currents. The generator simulation firstly introduces the set-up of models for battery and gas turbine mechanics. Field weakening requirement is also mentioned. The battery voltage, battery SOC, DC link current, electromechanical torque and generator speed are simulated for generation process. The scenario of intermittent loading on battery is also considered and simulated, and the responses during loading transient are analysed.

Chapter 7: Conclusion and Future Works

7.1 Conclusion

The thesis discusses an in-depth research for the principles, control and some design issues of heteropolar inductor machine. The research makes contributions to generic machine theory, construction of machine mathematical model, design optimisation and proposition of potential sensorless control scheme, in order to further disclose the operational principles of heteropolar inductor machine, as well as to improve the machine's performance, robustness and controllability.

The main contents and conclusions of the thesis are summarised as follows.

(1) Steady state and transient theories are developed for heteropolar inductor machine, and the complex inter-relationship of air gap permeance variation, armature mmf wave and stator-side field excitation is addressed and explained. Space vector method is used for constructing a dynamically flexible model for heteropolar inductor machine to align with classical approaches in dynamic analysis of electrical machines.

(2) The requirements of designing a balanced three-phase heteropolar inductor machine are discussed. The effects and influences of harmonics in the machine are addressed and analysed by finite element analysis (FEA), and potential strategies to overcome the issues and to improve performance are proposed. The analysis of structural optimisation including winding configuration and rotor shaping is also covered.

(3) By taking advantage of the unique structural properties of heteropolar inductor machine, sensorless field oriented control strategy is proposed, featuring effectiveness and simplicity. The performances of sensorless angle and speed estimations are assessed by comparing with actual measurements.

(4) Both developed theories and control system are practically validated, and the prototype is built on both hardware and software levels. A test machine is fabricated together with the

implementation of a micro-processor based controller system with sensorless control algorithm embedded. Prototypes with different machine structures and controller calibrations are compared to highlight the proposed optimisations.

(5) The potential application of gas turbine starter generator employing heteropolar inductor machine is discussed in the thesis. The overall advantages and disadvantages are compared with several candidate machines from the literature. A Simulink model is constructed based on the developed machine model as well the mechanical model of gas turbine, and the performance of such system is evaluated.

The main contributions of the thesis are concluded as follows.

(1) The development of theories for heteropolar inductor machines based on space vector method overcomes the difficulty of mathematically analysing the machine due to the structural complexity, and unifies heteropolar inductor machine with classical electrical machine theories.

(2) The modifications to original heteropolar inductor machine structure are proposed to facilitate the high speed motoring operation and to eliminate unwanted harmonics, which potentially expands the application area.

(3) A high level design approach for heteropolar inductor machine is developed, and a sizing equation linking internal electromagnetic correlations and external mechanical structure is derived.

(4) A simple yet effective sensorless control strategy is designed and implemented for a heteropolar inductor machine drive system, and the system is proven to work even at low speed down to 150rpm.

7.2 Future works

Although a number of research works have been done for heteropolar inductor machine as outlined by this thesis, several fields can still be further investigated and improved due to the limitations of equipment, time and manpower.

(1) During imbalanced operation, e.g. imbalanced short circuit, the negative phase components cannot be cancelled during the formation of space vector. Hence the space vector analysis should be supplemented with the case of imbalance. Also, the machine's behaviour under imbalanced supply is not systematically evaluated, and worth investigating.

(2) The FEA in this thesis is based on 2D models, which inherently neglects end windings in simulation. The construction of a complete 3D model in the future allows a more precise FEA simulation for heteropolar inductor machine.

(3) A preliminary analysis for the internal saturation and iron loss distribution is put forward in the thesis. More detailed study should be conducted in the future to fully understand the influence and patterns. Moreover relevant analytical approaches can be made as the basis of advanced control strategy that takes saturation and losses into consideration.

Reference

[1] J. H. H. Kuhlmann, "Design of electrical apparatus," Third ed: Wiley, 1959, pp. 299-302.

[2] Z. Q. Zhu and J. T. Chen, "Advanced Flux-Switching Permanent Magnet Brushless Machines," *Magnetics, IEEE Transactions on,* vol. 46, pp. 1447-1453, 2010.

[3] Y. Amara, E. Hoang, M. Gabsi, M. Lécrivain, and S. Allano, "Design and comparison of different flux-switch synchronous machines for an aircraft oil breather application," *European Transactions on Electrical Power,* vol. 15, pp. 497-511, 2005.

[4] A. S. Thomas, Z. Q. Zhu, R. L. Owen, G. W. Jewell, and D. Howe, "Multiphase Flux-Switching Permanent-Magnet Brushless Machine for Aerospace Application," *Industry Applications, IEEE Transactions on,* vol. 45, pp. 1971-1981, 2009.

[5] Z. X. Fang, Y. Wang, J. X. Shen, and Z. W. Huang, "Design and analysis of a novel flux-switching permanent magnet integrated-starter-generator," in *Power Electronics, Machines and Drives, 2008. PEMD 2008. 4th IET Conference on*, 2008, pp. 106-110.

[6] Z. Q. Zhu, "Switched flux permanent magnet machines &#x2014; Innovation continues," in *Electrical Machines and Systems (ICEMS), 2011 International Conference on*, 2011, pp. 1-10.

[7] J. T. Chen and Z. Q. Zhu, "Winding Configurations and Optimal Stator and Rotor Pole Combination of Flux-Switching PM Brushless AC Machines," *Energy Conversion, IEEE Transactions on,* vol. 25, pp. 293-302, 2010.

[8] J. T. Chen, Z. Q. Zhu, S. Iwasaki, and R. Deodhar, "Low cost flux-switching brushless AC machines," in *Vehicle Power and Propulsion Conference (VPPC), 2010 IEEE*, 2010, pp. 1-6.

[9] B. Gaussens, E. Hoang, O. de la Barriere, J. Saint-Michel, M. Lecrivain, and M. Gabsi, "Analytical Approach for Air-Gap Modeling of Field-Excited Flux-Switching Machine: No-Load Operation," *Magnetics, IEEE Transactions on,* vol. 48, pp. 2505-2517, 2012.

[10] L. McGrow and C. Pollock, "Low cost brushless generators," in *Industry Applications Conference, 1999. Thirty-Fourth IAS Annual Meeting. Conference Record of the 1999 IEEE*, 1999, pp. 1229-1236 vol.2.

[11] A. Zulu, B. C. Mecrow, and M. Armstrong, "A Wound-Field Three-Phase Flux-Switching Synchronous Motor With All Excitation Sources on the Stator," *Industry Applications, IEEE Transactions on,* vol. 46, pp. 2363-2371, 2010.

[12] J. F. Bangura, "Design of high-power density and relatively high-efficiency flux-switching motor," *Energy Conversion, IEEE Transactions on,* vol. 21, pp. 416-425, 2006.

[13] E. Hoang, M. Lecrivain, and M. Gabsi, "A new structure of a switching flux synchronous polyphased machine with hybrid excitation," in *Power Electronics and Applications, 2007 European Conference on*, 2007, pp. 1-8.

[14] E. Sulaiman, T. Kosaka, N. Matsui, and M. Z. Ahmad, "Design improvement and performance analysis of 12Slot-10Pole permanent magnet flux switching machine with field excitation coils," in *Power Engineering and Optimization Conference (PEOCO), 2011 5th International*, 2011, pp. 202-207.

[15] E. Hoang, M. Lecrivain, S. Hlioui, and M. Gabsi, "Hybrid excitation synchronous permanent magnets synchronous machines optimally designed for hybrid and full electrical vehicle," in *Power Electronics and ECCE Asia (ICPE & ECCE), 2011 IEEE 8th International Conference on*, 2011, pp. 153-160.

[16] Y. Chen, S. Chen, Z. Q. Zhu, D. Howe, and Y. Y. Ye, "Starting Torque of Single-Phase Flux-Switching Permanent Magnet Motors," *Magnetics, IEEE Transactions on,* vol. 42, pp. 3416-3418, 2006.

[17] Z. Q. Zhu, J. T. Chen, Y. Pang, D. Howe, S. Iwasaki, and R. Deodhar, "Analysis of a Novel Multi-Tooth Flux-Switching PM Brushless AC Machine for High Torque Direct-Drive Applications," *Magnetics, IEEE Transactions on,* vol. 44, pp. 4313-4316, 2008.

[18] Y. Jianhu, L. Heyun, H. Yunkai, L. Hengchuan, and Z. Q. Zhu, "Magnetic field analysis of a novel flux switching transverse flux permanent magnet wind generator with 3-D FEM," in *Power Electronics and Drive Systems, 2009. PEDS 2009. International Conference on*, 2009, pp. 332-335.

[19] R. L. Owen, Z. Q. Zhu, A. S. Thomas, G. W. Jewell, and D. Howe, "Fault-Tolerant Flux-Switching Permanent Magnet Brushless AC Machines," in *Industry Applications Society Annual Meeting, 2008. IAS '08. IEEE*, 2008, pp. 1-8.

[20] S. E. Rauch and L. J. Johnson, "Design Principles of Flux-Switch Alternators [includes discussion]," *Power Apparatus and Systems, Part III. Transactions of the American Institute of Electrical Engineers,* vol. 74, 1955.

[21] C. Wang, S. A. Nasar, and I. Boldea, "Three-phase flux reversal machine (FRM)," *Electric Power Applications, IEE Proceedings -,* vol. 146, pp. 139-146, 1999.

[22] C. X. Wang, I. Boldea, and S. A. Nasar, "Characterization of three phase flux reversal machine as an automotive generator," *Energy Conversion, IEEE Transactions on,* vol. 16, pp. 74-80, 2001.

[23] I. Boldea, Z. Jichun, and S. A. Nasar, "Theoretical characterization of flux reversal machine in low-speed servo drives-the pole-PM configuration," *Industry Applications, IEEE Transactions on,* vol. 38, pp. 1549-1557, 2002.

[24] K. Tae Heoung and L. Ju, "A study of the design for the flux reversal machine," *Magnetics, IEEE Transactions on,* vol. 40, pp. 2053-2055, 2004.

[25] K. Tae Heoung, W. Sung-Hong, B. Ki, and L. Ju, "Reduction of cogging torque in flux-reversal machine by rotor teeth pairing," *Magnetics, IEEE Transactions on,* vol. 41, pp. 3964-3966, 2005.

[26] K. B. Jang, W. Sung-Hong, K. Tae Heoung, and L. Ju, "Starting and high-speed driving of single-phase flux-reversal motor for vacuum cleaner," *Magnetics, IEEE Transactions on,* vol. 41, pp. 3967-3969, 2005.

[27] D. G. Dorrell, I. Chindurza, and F. Butt, "Operation, theory and comparison of the flux reversal machine - is it a viable proposition?," in *Power Electronics and Drive Systems, 2003. PEDS 2003. The Fifth International Conference on*, 2003, pp. 253-258 Vol.1.

[28] F. Liang, Y. Liao, and T. A. Lipo, "A new variable reluctance motor utilizing an auxiliary commutation winding," in *Industry Applications Society Annual Meeting, 1992., Conference Record of the 1992 IEEE*, 1992, pp. 219-225 vol.1.

[29] L. Yue, J. D. Lloyd, and G. E. Horst, "Switched reluctance motor with DC assisted excitation," in *Industry Applications Conference, 1996. Thirty-First IAS Annual Meeting, IAS '96., Conference Record of the 1996 IEEE*, 1996, pp. 801-807 vol.2.

[30] M. Barnes and C. Veerapraditsin, "Analysis of DC bias switched reluctance winding configuration," in *Power Electronics, Machines and Drives, 2004. (PEMD 2004). Second International Conference on (Conf. Publ. No. 498)*, 2004, pp. 475-480 Vol.2.

[31] J. D. Law, A. Chertok, and T. A. Lipo, "Design and performance of the field regulated reluctance machine," in *Industry Applications Society Annual Meeting, 1992., Conference Record of the 1992 IEEE*, 1992, pp. 234-241 vol.1.

[32] L. Yuefeng, F. Liang, and T. A. Lipo, "A novel permanent magnet motor with doubly salient structure," *Industry Applications, IEEE Transactions on,* vol. 31, pp. 1069-1078, 1995.

[33] C. Ming, H. Wei, Z. Jianzhong, and Z. Wenxiang, "Overview of Stator-Permanent Magnet Brushless Machines," *Industrial Electronics, IEEE Transactions on,* vol. 58, pp. 5087-5101, 2011.

[34] J. H. Walker, "The theory of the inductor alternator," *Electrical Engineers - Part II: Power Engineering, Journal of the Institution of,* vol. 89, pp. 227-241, 1942.

[35] R. K. Lay, "The history and changing fortunes of the inductor alternator," *Electronics and Power,* vol. 14, pp. 484-487, 1968.

[36] Z. Lou, K. Yu, Z. Ren, and C. Ye, "Analysis of homopolar inductor alternator for high reliability high power density applications," in *Power Electronics and Motion Control Conference, 2009. IPEMC '09. IEEE 6th International*, 2009, pp. 841-844.

[37] X. Fu, J. Zou, and X. Jiang, "Influence of rotor tooth shape on air-gap magnetic field in Homopolar Inductor Alternator," in *Electromagnetic Field Computation (CEFC), 2010 14th Biennial IEEE Conference on*, 2010, pp. 1-1.

[38] D. Gerling and M. Pyc, "Optimisation of a homopolar machine," in *Power Electronics, Electrical Drives, Automation and Motion, 2008. SPEEDAM 2008. International Symposium on*, 2008, pp. 1297-1299.

[39] T. Perry, M. Senesky, and S. R. Sanders, "An integrated flywheel energy storage system with homopolar inductor motor/generator and high-frequency drive," *Industry Applications, IEEE Transactions on,* vol. 39, pp. 1710-1725, 2003.

[40] J. A. N. Msekela, P. N. Materu, and A. H. Nzali, "Development of a homopolar electrical machine for high power density high speed applications," in *AFRICON, 1996., IEEE AFRICON 4th*, 1996, pp. 184-187 vol.1.

[41] H. Jin and L. Feng, "A high frequency high power IGBT inverter drive for 45 HP/16,000 RPM brushless homopolar inductor motor," in *Industry Applications Conference, 1995. Thirtieth IAS Annual Meeting, IAS '95., Conference Record of the 1995 IEEE*, 1995, pp. 9-15 vol.1.

[42] E. A. Erdelyi, F. S. V. Ahamed, and R. E. Hopkins, "Design Considerations and Optimization of Homopolar Inductor Alternators of Aerospace Power Systems," *Aerospace and Electronic Systems, IEEE Transactions on,* vol. AES-2, pp. 106-115, 1966.

[43] E. Levi, L. Birenbaum, and Z. Zabar, "Concerning the design of inductor synchronous motors fed by current source inverters," *Magnetics, IEEE Transactions on,* vol. 13, pp. 1421-1423, 1977.

[44] J. F. Eastham, "Iron-cored linear synchronous machines," *Electronics and Power,* vol. 23, pp. 239-242, 1977.

[45] V. B. Honsinger, "Sizing Equations for Electrical Machinery," *Energy Conversion, IEEE Transactions on,* vol. EC-2, pp. 116-121, 1987.

[46] M. Hippner and R. G. Harley, "High speed synchronous homopolar and permanent magnet machines comparative study," in *Industry Applications Society Annual Meeting, 1992., Conference Record of the 1992 IEEE*, 1992, pp. 74-78 vol.1.

[47] Z. Fengge, B. Haijun, H. P. Gruenberger, and E. Nolle, "Comparative Study on Claw Pole Electrical Machine with Different Structure," in *Industrial Electronics and Applications, 2007. ICIEA 2007. 2nd IEEE Conference on*, 2007, pp. 636-640.

[48] W. Cai, "Comparison and review of electric machines for integrated starter alternator applications," in *Industry Applications Conference, 2004. 39th IAS Annual Meeting. Conference Record of the 2004 IEEE*, 2004, p. 393.

[49] Q. Wang, Y. Ni, and G. Li, *Structure, Theory and Application of Claw Pole Machines (in Chinese)*: Press of University of Science and Technology of China, 2006.

[50] J. H. Walker, "High-Frequency alternators," *Electrical Engineers - Part II: Power Engineering, Journal of the Institution of,* vol. 93, pp. 67-80, 1946.

[51] E. J. Davies and A. M. Higginson, "Airgap and stator flux distribution in Guy-type medium-frequency inductor generators," *Electrical Engineers, Proceedings of the Institution of,* vol. 122, pp. 377-386, 1975.

[52] E. J. Davies and R. K. Lay, "Performance of Lorenz-type medium-frequency inductor alternators on load," *Electrical Engineers, Proceedings of the Institution of,* vol. 115, pp. 1791-1800, 1968.

[53] N. Iwabuchi, A. Kawahara, T. Kume, T. Kabashima, and N. Nagaska, "A novel inductor type high-torque motor with rare-earth magnet," in *Industry Applications Society Annual Meeting, 1991., Conference Record of the 1991 IEEE*, 1991, pp. 115-120 vol.1.

[54] S. I. Deaconu, M. Topor, L. Tutelea, G. N. Popa, and C. Abrudean, "Modeling and experimental investigations of a reactive homo-heteropolar brushless synchronous machine," in *Industrial Electronics, 2009. IECON '09. 35th Annual Conference of IEEE*, 2009, pp. 1209-1216.

[55] P. K. Dash and A. K. Das Gupta, "Design Aspects of Three-Phase Inductor Alternators," *Power Apparatus and Systems, IEEE Transactions on,* vol. PAS-88, pp. 1718-1724, 1969.

[56] A. K. D. Gupta, "Analytical Method to Find the Best Number of Stator and Rotor Teeth of Inductor Alternator for 3-Phase Sinusoidal Voltage Generation," *Power Apparatus and Systems, Part III. Transactions of the American Institute of Electrical Engineers,* vol. 79, pp. 674-678, 1960.

[57] R. Nair, "Inductor generators for alternative energy schemes," in *Electrical Machines and Drives, 1993. Sixth International Conference on (Conf. Publ. No. 376)*, 1993, pp. 499-504.

[58] A. K. D. Gupta, "Mathematical Analysis of Inductor Alternators," *Power Apparatus and Systems, Part III. Transactions of the American Institute of Electrical Engineers,* vol. 79, pp. 684-689, 1960.

[59] P. K. Kovács, *Transient phenomena in electrical machines*: Elsevier, 1984.

[60] W. Leonhard, *Control of Electrical Drives*: Springer Berlin Heidelberg, 2001.

[61] "Field Orientated Control of 3-Phase AC-Motors," in *Texas Instruments Literature Number BPRA073*, ed, 1998.

[62] A. Ravikumar Setty, S. Wekhande, and K. Chatterjee, "Comparison of high frequency signal injection techniques for rotor position estimation at low speed to standstill of PMSM," in *Power Electronics (IICPE), 2012 IEEE 5th India International Conference on*, 2012, pp. 1-6.

[63] M. Schroedl, "Sensorless control of AC machines at low speed and standstill based on the &ldquo;INFORM&rdquo; method," in *Industry Applications Conference, 1996. Thirty-First IAS Annual Meeting, IAS '96., Conference Record of the 1996 IEEE*, 1996, pp. 270-277 vol.1.

[64] R. Leidhold, "Position Sensorless Control of PM Synchronous Motors Based on Zero-Sequence Carrier Injection," *Industrial Electronics, IEEE Transactions on,* vol. 58, pp. 5371-5379, 2011.

[65] J. Holtz, "Sensorless control of induction motors-performance and limitations," in *Industrial Electronics, 2000. ISIE 2000. Proceedings of the 2000 IEEE International Symposium on*, 2000, pp. PL12-PL20 vol.1.

[66] K. Iizuka, H. Uzuhashi, M. Kano, T. Endo, and K. Mohri, "Microcomputer Control for Sensorless Brushless Motor," *Industry Applications, IEEE Transactions on,* vol. IA-21, pp. 595-601, 1985.

[67] J. C. Moreira, "Indirect sensing for rotor flux position of permanent magnet AC motors operating over a wide speed range," *Industry Applications, IEEE Transactions on,* vol. 32, pp. 1394-1401, 1996.

[68] P. P. Acarnley and J. F. Watson, "Review of position-sensorless operation of brushless permanent-magnet machines," *Industrial Electronics, IEEE Transactions on,* vol. 53, pp. 352-362, 2006.

[69] I. Boldea, M. C. Paicu, G. Andreescu, and F. Blaabjerg, "&#x201C;Active Flux&#x201D; DTFC-SVM Sensorless Control of IPMSM," *Energy Conversion, IEEE Transactions on,* vol. 24, pp. 314-322, 2009.

[70] R. Bojoi, M. Pastorelli, J. Bottomley, P. Giangrande, and C. Gerada, "Sensorless control of PM motor drives &#x2014; A technology status review," in *Electrical Machines Design Control and Diagnosis (WEMDCD), 2013 IEEE Workshop on*, 2013, pp. 168-182.

[71] H. Tajima and Y. Hori, "Speed sensorless field-orientation control of the induction machine," *Industry Applications, IEEE Transactions on,* vol. 29, pp. 175-180, 1993.

[72] J. Maes and J. A. Melkebeek, "Speed-sensorless direct torque control of induction motors using an adaptive flux observer," *Industry Applications, IEEE Transactions on,* vol. 36, pp. 778-785, 2000.

[73] C. Schauder, "Adaptive speed identification for vector control of induction motors without rotational transducers," *Industry Applications, IEEE Transactions on,* vol. 28, pp. 1054-1061, 1992.

[74] J. Holtz, "Speed estimation and sensorless control of AC drives," in *Industrial Electronics, Control, and Instrumentation, 1993. Proceedings of the IECON '93., International Conference on*, 1993, pp. 649-654 vol.2.

[75] H. Chang-chieh and P. Parks, "Comparative studies of model reference adaptive control systems," *Automatic Control, IEEE Transactions on,* vol. 18, pp. 419-428, 1973.

[76] M. Barut, S. Bogosyan, and M. Gokasan, "Speed-Sensorless Estimation for Induction Motors Using Extended Kalman Filters," *Industrial Electronics, IEEE Transactions on,* vol. 54, pp. 272-280, 2007.

[77] F. Alonge, F. D'Ippolito, and A. Sferlazza, "Sensorless Control of Induction-Motor Drive Based on Robust Kalman Filter and Adaptive Speed Estimation," *Industrial Electronics, IEEE Transactions on,* vol. 61, pp. 1444-1453, 2014.

[78] M. C. Huang, A. J. Moses, and F. Anayi, "The comparison of sensorless estimation techniques for PMSM between extended Kalman filter and flux-linkage observer," in *Applied Power Electronics Conference and Exposition, 2006. APEC '06. Twenty-First Annual IEEE*, 2006, p. 6 pp.

[79] Y. Zhang and V. Utkin, "Sliding mode observers for electric machines-an overview," in *IECON 02 [Industrial Electronics Society, IEEE 2002 28th Annual Conference of the]*, 2002, pp. 1842-1847 vol.3.

[80] V. Utkin, J. Guldner, and M. Shijun, *Sliding Mode Control in Electro-mechanical Systems*: Taylor & Francis, 1999.

[81] C. Lascu, I. Boldea, and F. Blaabjerg, "A Class of Speed-Sensorless Sliding-Mode Observers for High-Performance Induction Motor Drives," *Industrial Electronics, IEEE Transactions on,* vol. 56, pp. 3394-3403, 2009.

[82] F. Chen and M. W. Dunnigan, "Comparative study of a sliding-mode observer and Kalman filters for full state estimation in an induction machine," *Electric Power Applications, IEE Proceedings -,* vol. 149, pp. 53-64, 2002.

[83] A. E. Fitzgerald, C. Kingsley, and S. D. Umans, "Electric Machinery," ed: McGraw-Hill, 2003, pp. 203 - 206.

[84] R. E. Doherty and C. A. Nickle, "Synchronous machines I : An extension of Blondel's two-reaction theory," *A.I.E.E., Journal of the,* vol. 45, pp. 974-987, 1926.

[85] D. A. Staton, T. J. E. Miller, and S. E. Wood, "Maximising the saliency ratio of the synchronous reluctance motor," *Electric Power Applications, IEE Proceedings B,* vol. 140, pp. 249-259, 1993.

[86] M. Liwschitz-Garik and C. C. Whipple, "A-C machines," ed: D. Van Nostrand company, inc., 1946.

[87] E. Schlemmer, "Damping of synchronous machines -analytical estimations versus finite element results," in *Clean Electrical Power, 2009 International Conference on*, 2009, pp. 751-754.

[88] N. Bianchi, M. D. Prè, and L. Alberti, *Theory and Design of Fractional-slot Pm Machines*: CLEUP, 2007.

[89] T. Quang-Vinh, C. Tae-Won, L. Hong-Hee, K. Heung-Geun, and N. Eui-Cheol, "Simple starting-up method of BLDC sensorless control system for vehicle fuel pump," in *Power Electronics Conference (IPEC), 2010 International*, 2010, pp. 2244-2248.

[90] W. Staffler and M. Schrodl, "Extended mechanical observer structure with load torque estimation for sensorless dynamic control of permanent magnet synchronous machines," in *Power Electronics and Motion Control Conference (EPE/PEMC), 2010 14th International*, 2010, pp. S1-18-S1-22.

[91] "E.003 CFM International S.A. - CFM56-5Band5C series engines," *European Aviation Safety Agency,* 2012.

[92] Z. Chao-hui, Q. Haihong, and Y. Yang-guang, "Analysis of the Pole Numbers on Flux and Power Density of IPM Synchronous Machine," in *Power Electronics and Drives Systems, 2005. PEDS 2005. International Conference on*, 2005, pp. 1402-1407.

[93] E. Levi and Z. Zabar, "Basic Design of Electrical Machines," *Power Apparatus and Systems, IEEE Transactions on,* vol. PAS-104, pp. 1513-1518, 1985.

[94] W. L. Soong and T. J. E. Miller, "Field-weakening performance of brushless synchronous AC motor drives," *Electric Power Applications, IEE Proceedings -,* vol. 141, pp. 331-340, 1994.

[95] S. Morimoto, M. Sanada, and Y. Takeda, "Performance of PM-assisted synchronous reluctance motor for high-efficiency and wide constant-power operation," *Industry Applications, IEEE Transactions on,* vol. 37, pp. 1234-1240, 2001.

[96] G. Pellegrino, A. Vagati, B. Boazzo, and P. Guglielmi, "Comparison of Induction and PM Synchronous Motor Drives for EV Application Including Design Examples," *Industry Applications, IEEE Transactions on,* vol. 48, pp. 2322-2332, 2012.

[97] A. Girardin and G. Friedrich, "Optimal control for a Wound Rotor Synchronous starter generator," in *Industry Applications Conference, 2006. 41st IAS Annual Meeting. Conference Record of the 2006 IEEE*, 2006, pp. 14-19.

[98] G. Friedrich and A. Girardin, "Integrated starter generator," *Industry Applications Magazine, IEEE,* vol. 15, pp. 26-34, 2009.

[99] R. Krishnan, R. Arumugan, and J. F. Lindsay, "Design procedure for switched-reluctance motors," *Industry Applications, IEEE Transactions on,* vol. 24, pp. 456-461, 1988.

[100] H. C. Lovatt and J. M. Stephenson, "Influence of number of poles per phase in switched reluctance motors," *Electric Power Applications, IEE Proceedings B,* vol. 139, pp. 307-314, 1992.

[101] T. J. E. Miller, "Optimal design of switched reluctance motors," *Industrial Electronics, IEEE Transactions on,* vol. 49, pp. 15-27, 2002.

[102] D. J. Powell, G. W. Jewell, D. Howe, and K. Atallah, "Rotor topologies for a switched-reluctance machine for the 'more-electric' aircraft engine," *Electric Power Applications, IEE Proceedings -,* vol. 150, pp. 311-318, 2003.

[103] C. M. Stephens, "Fault detection and management system for fault-tolerant switched reluctance motor drives," *Industry Applications, IEEE Transactions on,* vol. 27, pp. 1098-1102, 1991.

[104] A. Jin-Woo, P. Sung-Jun, and L. Dong-Hee, "Hybrid excitation of SRM for reduction of vibration and acoustic noise," *Industrial Electronics, IEEE Transactions on,* vol. 51, pp. 374-380, 2004.

[105] J. M. Miller, A. R. Gale, P. J. McCleer, F. Leonardi, and J. H. Lang, "Starter-alternator for hybrid electric vehicle: comparison of induction and variable reluctance machines and drives," in *Industry Applications Conference, 1998. Thirty-Third IAS Annual Meeting. The 1998 IEEE*, 1998, pp. 513-523 vol.1.

[106] A. V. Radun, "Design considerations for the switched reluctance motor," *Industry Applications, IEEE Transactions on,* vol. 31, pp. 1079-1087, 1995.

[107] A. G. Jack, B. C. Mecrow, and J. A. Haylock, "A comparative study of permanent magnet and switched reluctance motors for high-performance fault-tolerant applications," *Industry Applications, IEEE Transactions on,* vol. 32, pp. 889-895, 1996.

[108] M. R. Harris and T. J. E. Miller, "Comparison of design and performance parameters in switched reluctance and induction motors," in *Electrical Machines and Drives, 1989. Fourth International Conference on (Conf. Publ. No. ??)*, 1989, pp. 303-307.

[109] H. Wei, C. Ming, Z. Q. Zhu, and D. Howe, "Design of Flux-Switching Permanent Magnet Machine Considering the Limitation of Inverter and Flux-Weakening Capability," in *Industry Applications Conference, 2006. 41st IAS Annual Meeting. Conference Record of the 2006 IEEE*, 2006, pp. 2403-2410.

[110] Y. Pang, Z. Q. Zhu, D. Howe, S. Iwasaki, R. Deodhar, and A. Pride, "Comparative study of flux-switching and interior permanent magnet machines," in *Electrical Machines and Systems, 2007. ICEMS. International Conference on*, 2007, pp. 757-762.

[111] Z. Q. Zhu, Y. Pang, D. Howe, S. Iwasaki, R. Deodhar, and A. Pride, "Analysis of electromagnetic performance of flux-switching permanent-magnet Machines by nonlinear adaptive lumped parameter magnetic circuit model," *Magnetics, IEEE Transactions on,* vol. 41, pp. 4277-4287, 2005.

[112] K. Atallah, D. Howe, P. H. Mellor, and D. A. Stone, "Rotor loss in permanent-magnet brushless AC machines," *Industry Applications, IEEE Transactions on,* vol. 36, pp. 1612-1618, 2000.

[113] M. van der Geest, H. Polinder, J. A. Ferreira, and D. Zeilstra, "Machine selection and initial design of an aerospace starter/generator," in *Electric Machines & Drives Conference (IEMDC), 2013 IEEE International*, 2013, pp. 196-203.

[114] H. Wei, C. Ming, and Z. Gan, "A Novel Hybrid Excitation Flux-Switching Motor for Hybrid Vehicles," *Magnetics, IEEE Transactions on,* vol. 45, pp. 4728-4731, 2009.

[115] C. Ruiwu, C. Mi, and C. Ming, "Quantitative Comparison of Flux-Switching Permanent-Magnet Motors With Interior Permanent Magnet Motor for EV, HEV, and PHEV Applications," *Magnetics, IEEE Transactions on,* vol. 48, pp. 2374-2384, 2012.

[116] M. R. Etemad, K. Pullen, C. B. Besant, and N. Baines, "Evaluation of Windage Losses for High-Speed Disc Machinery," *Proceedings of the Institution of Mechanical Engineers, Part A: Journal of Power and Energy,* vol. 206, pp. 149-157, August 1, 1992 1992.

[117] F. Sahin, "Design and Development of a High-speed Axial-flux Permanent-magnet Machine," ed: Technische Universiteit Eindhoven, 2001, pp. 132, 133.

[118] D. Logue, P. T. Krein, U. o. I. D. o. Electrical, C. Engineering, G. C. f. E. Machinery, and Electromechanics, *Design and Implementation of a MATLAB/SIMULINK Based Simulator for Electric Machines and Drives with Loads*: University of Illinois, Department of Electrical and Computer Engineering, 1999.

[119] B. S. Bhangu and K. Rajashekara, "Electric Starter Generators: Their Integration into Gas Turbine Engines," *Industry Applications Magazine, IEEE,* vol. 20, pp. 14-22, 2014.

[120] B. H. Nya, J. Brombach, and D. Schulz, "Benefits of higher voltage levels in aircraft electrical power systems," in *Electrical Systems for Aircraft, Railway and Ship Propulsion (ESARS), 2012*, 2012, pp. 1-5.

[121] J. Brombach, T. Schroter, A. Lucken, and D. Schulz, "Optimized cabin power supply with a &#x002B;/&#x2212; 270 V DC grid on a modern aircraft," in *Compatibility and Power Electronics (CPE), 2011 7th International Conference-Workshop*, 2011, pp. 425-428.

[122] O. Tremblay, L. A. Dessaint, and A. I. Dekkiche, "A Generic Battery Model for the Dynamic Simulation of Hybrid Electric Vehicles," in *Vehicle Power and Propulsion Conference, 2007. VPPC 2007. IEEE*, 2007, pp. 284-289.

[123] M. S. R. Murty, "Modelling of Gas Turbine and Its Control System."

Publications

Jingzhe Wu; Balchin, M.J., "Analysis of heteropolar inductor machines based on space vectors," *Electric Power and Energy Conversion Systems (EPECS), 2013 3rd International Conference on* , vol., no., pp.1,6, 2-4 Oct. 2013

Jingzhe Wu; Balchin, M.J., "A novel sensorless position and speed estimation method for heteropolar inductor machines," *Power Electronics and Applications (EPE'14-ECCE Europe), 2014 16th European Conference on* , vol., no., pp.1,10, 26-28 Aug. 2014

Appendix

Appendix I: Iron magnetic property

Silicon iron DR490-50 is used for fabricating test machines, and its magnetic property is also considered in FEA simulations. The iron magnetising curve is plotted in Fig. A1.1 and magnetising data listed in Table A1.1.

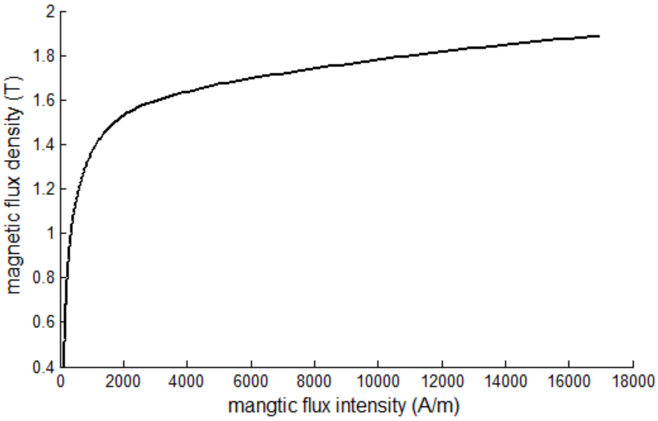

Fig. A1.1 Magnetisation curve of silicon iron DR490-50

H(A/m)	B(T)	H(A/m)	B(T)	H(A/m)	B(T)	H(A/m)	B(T)	H(A/m)	B(T)	H(A/m)	B(T)
137	0.4	200	0.69	347	0.98	746	1.27	2350	1.56	14100	1.85
138	0.41	203	0.7	355	0.99	768	1.28	2500	1.57	14800	1.86
140	0.42	206	0.71	363	1	790	1.29	2680	1.58	15500	1.87
142	0.43	209	0.72	371	1.01	814	1.3	2860	1.59	16200	1.88
144	0.44	212	0.73	379	1.02	840	1.31	3070	1.6	17000	1.89
146	0.45	216	0.74	388	1.03	868	1.32	3300	1.61		
148	0.46	220	0.75	397	1.04	896	1.33	3560	1.62		
150	0.47	223	0.76	406	1.05	926	1.34	3820	1.63		
152	0.48	227	0.77	416	1.06	958	1.35	4110	1.64		
154	0.49	231	0.78	426	1.07	986	1.36	4400	1.65		
156	0.5	235	0.79	437	1.08	1020	1.37	4700	1.66		
158	0.51	239	0.8	448	1.09	1060	1.38	5000	1.67		
160	0.52	243	0.81	460	1.1	1100	1.39	5350	1.68		
162	0.53	248	0.82	472	1.11	1140	1.4	5750	1.69		
164	0.54	252	0.83	486	1.12	1180	1.41	6150	1.7		
166	0.55	257	0.84	500	1.13	1230	1.42	6600	1.71		
168	0.56	262	0.85	514	1.14	1280	1.43	7050	1.72		
170	0.57	267	0.86	529	1.15	1330	1.44	7500	1.73		
172	0.58	273	0.87	544	1.16	1380	1.45	7970	1.74		
175	0.59	279	0.88	560	1.17	1440	1.46	8450	1.75		
177	0.6	285	0.89	576	1.18	1500	1.47	8950	1.76		
179	0.61	291	0.9	592	1.19	1570	1.48	9470	1.77		
181	0.62	297	0.91	610	1.2	1640	1.49	10000	1.78		
184	0.63	303	0.92	628	1.21	1720	1.5	10500	1.79		
187	0.64	310	0.93	646	1.22	1800	1.51	11000	1.8		
190	0.65	317	0.94	665	1.23	1890	1.52	11600	1.81		
192	0.66	324	0.95	685	1.24	1990	1.53	12200	1.82		
194	0.67	331	0.96	705	1.25	2090	1.54	12800	1.83		
197	0.68	339	0.97	725	1.26	2210	1.55	13400	1.84		

Table A1.1 Magnetisation data of silicon iron DR490-50

Appendix II: Electronic interfaces

Voltage signal ADC interface

The voltage input range for micro-processor is limited to 0 to 3.3V. Armature phase voltage measurements and field winding voltage measurements are passed through amplification circuits which downscale -60 to +60V voltage range to 0 to 3.3V, as shown in Fig. A2.1.

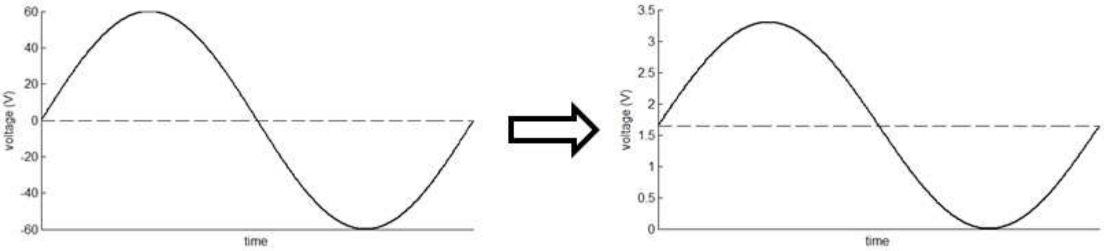

Fig. A2.1Change of waveform voltage range by voltage ADC interfaces

The schematic of voltage ADC interfaces is plotted in Fig. A2.2. The circuit is composed by two cascaded inverting amplifiers with offset and gain adjustments. TL071 low noise op-amps are used.

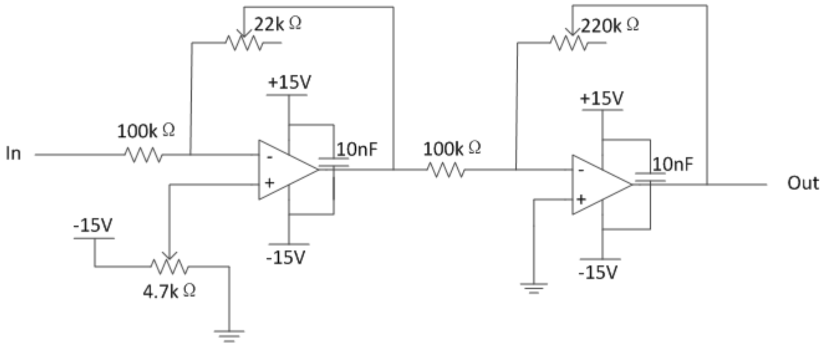

Fig. A2.2 Circuit layout of voltage ADC interfaces

Current signal ADC interface

Voltage output range from LEM Hall-effect current sensors is 2.5±0.625V for ±3A current. The curent sensor interfaces are designed to scale the 1.875 to 3.125V range to 0 to 3.3V, as shown in Fig. A2.3.

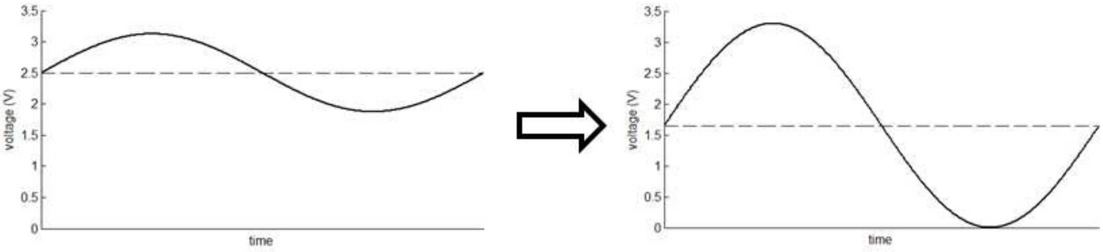

Fig. A2.3 Change of waveform voltage range by current ADC interfaces

The schematic of current ADC interfaces is plotted in Fig. A2.4. The circuit is a non-inverting amplifier with offset and gain adjustments. TL071 low noise op-amps are used.

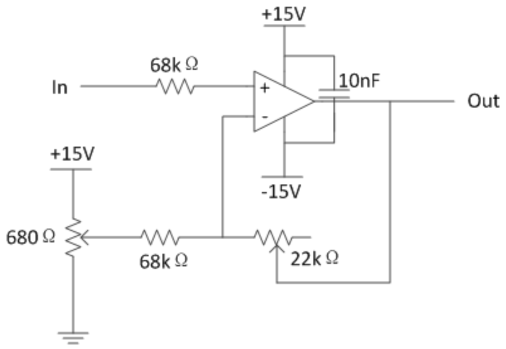

Fig. A2.4 Circuit layout of current ADC interfaces

DAC interface

Any p.u. variables and quantities in the micro-controller can be exported to PWMDAC pins and observed through an oscilloscope. The PWMDAC signals are formed by PWM signals with amplitude of 3.3V and frequency of 60 kHz. Low pass filters are interfaced between the PWMDAC pins and the oscilloscope to filter out high output frequency components. Second order active low pass Butterworth filters with Sallen-Key topology are employed, and the sketch is shown in Fig. A2.5. TL071 low noise op-amp is used.

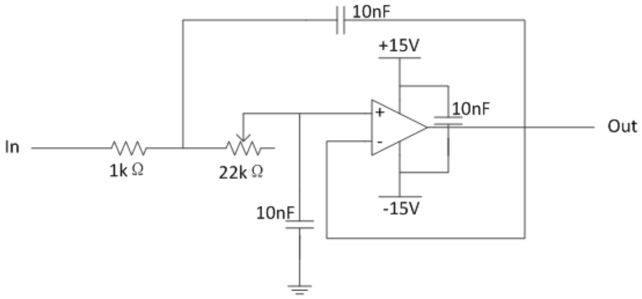

Fig. A2.5 Circuit layout of DAC interfaces

Buck converter

The buck converter for field control is designed on the basis of a DC stabilizer (National Semiconductor LM2679-ADJ). The converter circuit is shown in Fig. A2.6. A MOSFET switch is in series with one of the feedback resistors, which latches the output voltage to two states (20V and 1.21V) by the on and off of MOSFET. Switch duty cycle is control by micro-controller PWM to adjust buck converter output accordingly. The input voltage into the circuit is 30VDC.

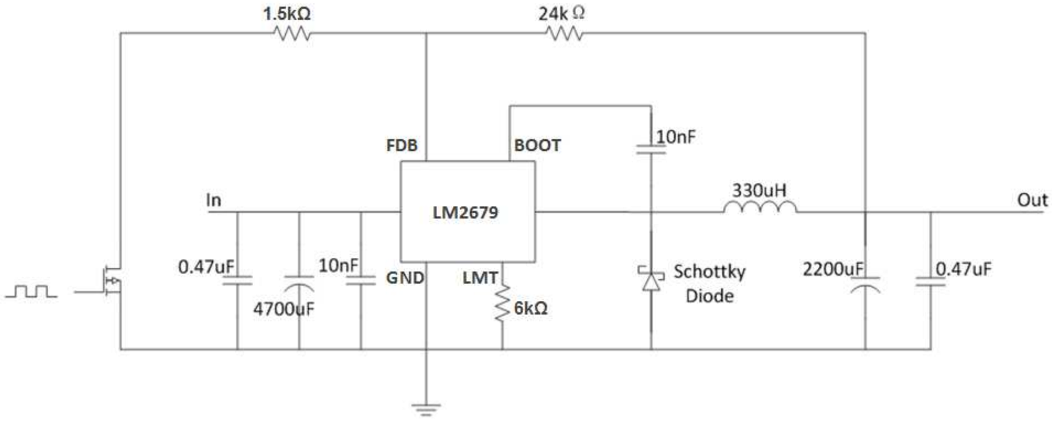
1.5kΩ
24k Ω
FDB
BOOT
10nF
In
LM2679
330uH
Out
0.47uF
10nF
GND
LMT
Schottky
Diode
2200uF
0.47uF
4700uF
6kΩ

Fig. A2.6 Circuit layout of buck converter based on LM2679 voltage regulator

Appendix III: Simulink models for gas turbine starter generator

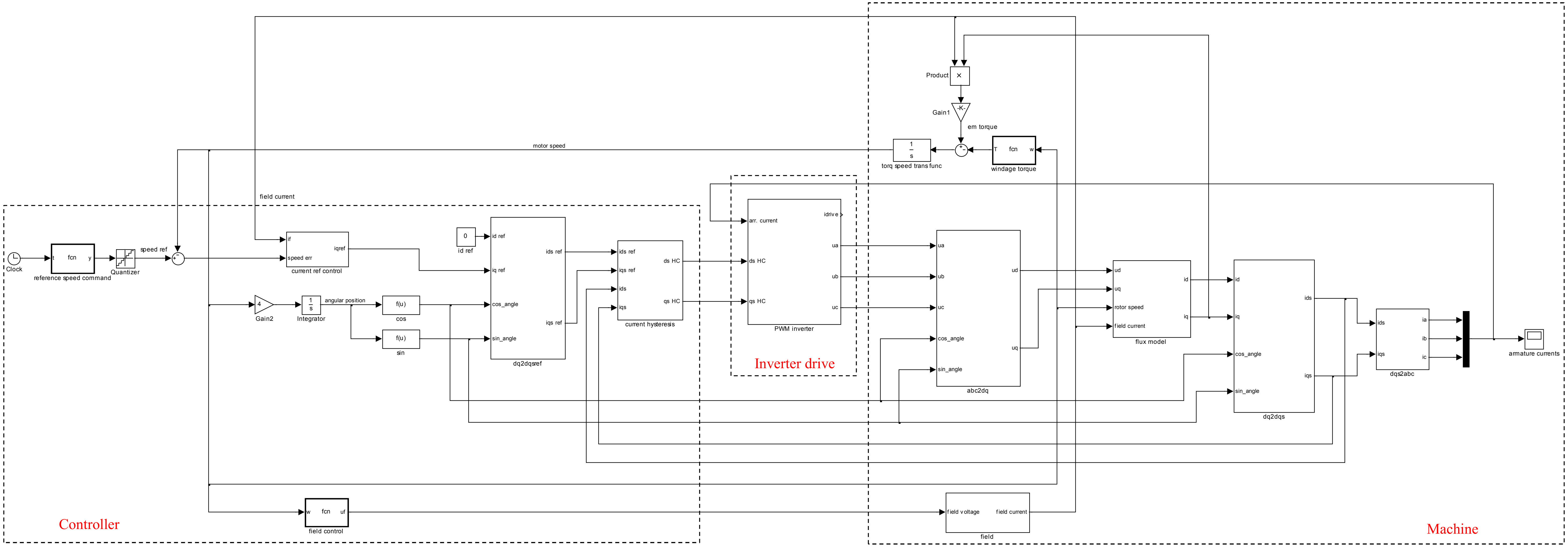
Product
×
Gain1
-K-
em torque
1
s
torq speed trans func
T
fcn
w
windage torque
motor speed
field current
Clock
t
fcn
y
reference speed command
Quantizer
speed ref
if
iqref
speed err
current ref control
0
id ref
id ref
ids ref
iq ref
cos_angle
sin_angle
iqs ref
dq2dqsref
ids ref
iqs ref
ids
iqs
ds HC
qs HC
current hysteresis
arr. current
idrive
ds HC
qs HC
ua
ub
uc
PWM inverter
Inverter drive
4
Gain2
1
s
Integrator
angular position
f(u)
cos
f(u)
sin
ua
ub
uc
cos_angle
sin_angle
ud
uq
abc2dq
ud
uq
rotor speed
field current
id
iq
flux model
id
iq
cos_angle
sin_angle
ids
iqs
dq2dqs
ids
iqs
ia
ib
ic
dqs2abc
armature currents
w
fcn
uf
field control
field voltage
field current
field
Controller
Machine

Fig. A3.1 Simulink model for gas turbine starter system

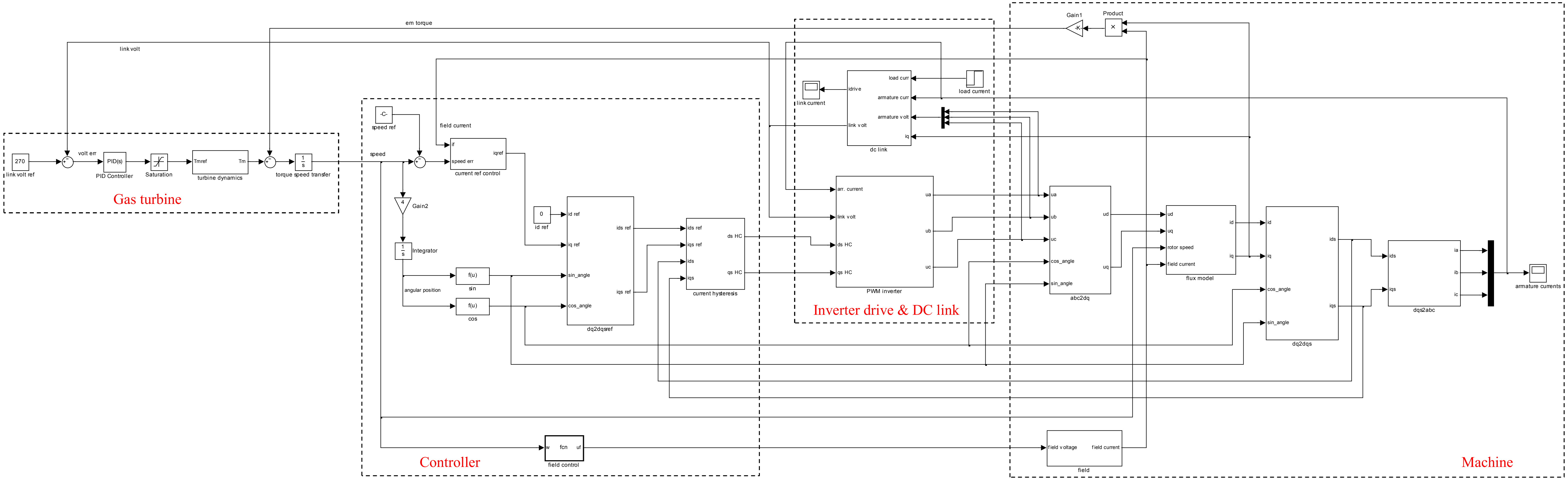
em torque
link volt
Gain1
-K-
Product
×
270
link volt ref
volt err
PID(s)
PID Controller
Saturation
Tmref
Tm
turbine dynamics
1/s
torque speed transfer
Gas turbine
-C-
speed ref
field current
speed
if
iqref
speed err
current ref control
4
Gain2
1/s
Integrator
angular position
f(u)
sin
f(u)
cos
0
id ref
id ref
iq ref
sin_angle
cos_angle
ids ref
iqs ref
dq2dqsref
ids ref
iqs ref
ids
iqs
ds HC
qs HC
current hysteresis
w
fcn
uf
field control
Controller
link current
idrive
link volt
load curr
armature curr
armature volt
iq
dc link
load current
arr. current
link volt
ds HC
qs HC
ua
ub
uc
PWM inverter
Inverter drive & DC link
ua
ub
uc
cos_angle
sin_angle
ud
uq
abc2dq
ud
uq
rotor speed
field current
id
iq
flux model
id
iq
cos_angle
sin_angle
ids
iqs
dq2dqs
ids
iqs
ia
ib
ic
dqs2abc
armature currents
field voltage
field current
field
Machine

Fig. A3.2 Simulink model for gas turbine generator system